GROUND MONITORS TO SUPPORT NAVIGATION OPERATIONS OF ARAIM AND GBAS

BY

JAYMIN HARSHADKUMAR PATEL

Submitted in partial fulfillment of the
requirements for the degree of
Doctor of Philosophy in Mechanical and Aerospace Engineering
in the Graduate College of the
Illinois Institute of Technology

Approved ________________________
Adviser

Chicago, Illinois
December 2023

ACKNOWLEDGMENT

First and foremost, I want to thank my academic advisor and dissertation committee chair Professor Boris Pervan for his endless support and entrusting me in pursuing this research. His enthusiasm for this research was contagious and motivational for me. I must also thank my advisor and committee member, Professor Samer Khanafseh, for his technical expertise, endless availability for mentoring me in this research. I would also like to extend my deepest gratitude to the rest of my committee: Professors Seebany Datta-Barua, Ankit Srivastava, and Yongyi Yang.

I would like to thank my fellow colleagues in the Navigation and Guidance Laboratory, both past and present: Professor Mathieu Joerger, Dr. Cagatay Tanil, Dr. Santiago Perea Diaz, Dr. Roohollah Parvizi, Dr. Yawei Zhai, Dr. Stefan Stevanovic, Dr. Adriano Canolla, Elisa Gallon, Birendra Kujur, Sahil Ahmed, Wengxiang Zhao, Kana Nagai, Anas Darwich, Batiste Alliaire, Shahriar Kiarash who made my tenure as a PhD candidate as memorable as possible.

AUTHORSHIP STATEMENT

I, Jaymin Harshadkumar Patel, attest that the work presented in this thesis is substantially my own.

In accordance with the disciplinary norm of Mechanical and Aerospace Engineering (see IIT Faculty Handbook, Appendix S), the following collaborations occurred in the thesis:

Professor Boris Pervan served as my PhD adviser and is the principal investigator of ARAIM and GBAS project. Under his guidance, all of thesis work is carried out. Also, he has contributed substantially in both projects, and his prior work is cited accordingly.

Professor Samer Khanafesh has provided guidance and bring me in the GBAS project. All my GBAS work was directly under his supervision, and we collaborated closely.

Dr. Yawei zhai and Prof. Mathieu Joerger has contributed to ARAIM project prior to my contributions. Their MATLAB codes were taken as an initial reference for developing a prototype to estimate GPS orbit and clock biases. The final MATLAB prototype was delivered to FAA Technical center as a project delivery; all MATLAB codes are the property of Navigation and guidance lab.

Over the course of my study, several conference papers and journal articles were published in order to share the results with scientific communities. Text from these papers is used where indicated.

J. Patel and B. Pervan, "Accurate GPS LNAV parameters and clock biases for ARAIM offline monitoring," in IEEE Transactions on Aerospace and Electronic Systems. DOI: 10.1109/TAES.2023.3241897.

J. Patel, S. Khanafseh, B. Pervan, “GNSS Satellite Orbit and Clock Truth Generation for ARAIM Offine Monitoring," Proceedings of the PNT Conference, Honolulu, HI, April 2019.

J. Patel, Y. Zhai, S. Kiarash, S. Khanafseh, M. Joerger, B. Pervan, “Prototyping an ARAIM Offline Ground Monitor Using Experimental Data," Proceedings of Institute of Navigation GNSS+ Conference, Miami, FL, Sep 2018.

J. Patel and B. Pervan, “Analyzing Satellite Orbit Error for ARAIM Offline Monitoring," 2020 IEEE/ION Position, Location and Navigation Symposium (PLANS), Portland, OR, USA, 2020.

J. Patel, S. Khanafseh, B. Pervan, “Spatial Gradient Monitor for GBAS," Proceedings of IEEE/ION PLANS, Monterey, CA, April 2018. **(Best Student Paper Award)**

J. Patel, S. Khanafseh, B. Pervan, “Detecting Hazardous Spatial Gradients at Satellite Acquisition in GBAS," in IEEE Transactions on Aerospace and Electronic Systems, vol. 56, no. 4, pp. 3214-3230, Aug. 2020, DOI: 10.1109/TAES.2020.2969541.

TABLE OF CONTENTS

LIST OF TABLES

Table Page

LIST OF FIGURES

Figure Page

LIST OF ABBREVIATIONS

Abbreviation	Term
AAIM	Aircraft Autonomous Integrity Monitoring
ABAS	Aircraft Based Augmentation System
AL	Alert Limit
ANSP	Air Navigation Service Provider
APC	Antenna Phase Center
APV	Approach operations with Vertical guidance
ARAIM	Advanced Receiver Autonomous Integrity Monitoring
CDDIS	Crustal Dynamic Data Information System
CDF	Cumulative Distribution Function
CIF	Correct Integer Fix
CMC	Code Minus Carrier
CNAV	Civil NAVigation message
CODE	Center for Orbit Determination in Europe
COM	Center of Mass
CSP	Constellation Service Provider
DCB	Differential Code group delay Bias
DF	Dual Frequency
ECEF	Earth-Center Earth-Fixed
EU	European Union
FA	False Alarm
FAA	Federal Aviation Administration
FOGMP	First Order Gauss Markov Process
GAST-D	GBAS Approach Service Type D
GBAS	Ground Based Augmentation System
GDV	Group Delay Variation
GF	Ground Facility
GNSS	Global Navigation Satellite System
GPS	Global Positioning System
GPT2w	Global Pressure and Temperature 2 wet
HAL	Horizontal Alert Limit
IF	Ionospheric-Free
IGM	Ionospheric Gradient Montior

IGS	International GNSS Service
ILS	Instrumental Landing System
ISD	Integrity Support Data
IS	Information Smoother
ISM	Integrity Support Message
KF	Kalman Filter
LL	Local Level
LNAV	Legacy NAVigation message
MD	Missed Detection
MLA	Multipath Limiting Antennas
NANU	Notice Advisory to Navstar Users
NGA	National Geospatial-Intelligence Agency
OFM	Offline Monitoring
PL	Protection Level
PRN	Pseudo Random Noise
PSD	Power Spectral Density
PWU	Phase Wind Up
RAIM	Receiver Autonomous Integrity Monitoring
RGS	Reference Ground Station
RINEX	Receiver Independent Exchange Format
RNM	Receiver Noise and Multipath
RPC	Radial Plus Clock bias
SARP	Standards and Recommended Practices
SBAS	Satellite Based Augmentation System
SET	Solid Earth Tide
SF	Single Frequency
SIS	Signal In Space
SISRE	Signal In Space Range Error
SV	Satellite Vehicle
TTA	Time to Alert
U.S.	United States
VAL	Vertical Alert Limit
WIF	Wrong Integer Fix
ZTD	Zenith Troposheric Delay

ABSTRACT

Receiver Autonomous Integrity Monitoring (RAIM) currently provides safe horizontal navigation guidance to en route civil aircraft using the GPS L1 frequency. As an evolution of RAIM, Advanced RAIM (ARAIM) is being developed to provide vertical guidance in addition to horizontal using multiple constellations and dual frequency thus facilitating precision approach without ground support for civil aircraft. However, navigation guidance during zero-visibility (Category III) precision landing requires an additional support in real time from a Ground Based Augmentation System (GBAS). To improve the aircraft navigation solution, GBAS broadcasts a differential correction and monitors any failure on transmitted satellite signals. This dissertation contributes to ARAIM and GBAS to improve existing navigation operations in order to enable precision approach and landing.

The achievable performance of ARAIM is highly dependent on the assumptions on a constellation's nominal Signal-In-Space (SIS) error models and a *priori* fault probability. In the framework of ARAIM, an Integrity Support Message (ISM) is envisioned to carry the required SIS error-model parameters and fault statistics for users. The ISM is generated and validated through offline monitoring, and disseminated along the navigation message. The first dissertation contribution is to provide necessary satellite positions and clock biases as a truth product to evaluate nominal SIS range errors (SISREs). An estimator is developed to generate accurate ephemeris parameters to provide these truth products. The estimator's performance is demonstrated for the Global Positioning System (GPS) constellation by utilizing the International GNSS Service (IGS) ground network to collect dual-frequency raw GPS code and carrier phase measurements. The resulting SISREs from the estimator are predicted to have a standard deviation of 0.5 m. When estimated ephemeris parameters and clock biases are compared with precise IGS orbit and clock products, the resulting SISREs are within $\pm 2\sigma$ at all times. In the second contribution, a new approach is proposed to generate the ISM by modeling the ephemeris parameter errors directly. In preliminary analysis, an ephemeris parameter error model is developed for the broadcast GPS legacy navigation message (LNAV) under nominal conditions. Then, the proposed approach is demonstrated to provide the nominal bias and standard deviation on GPS SISREs.

As a part of fault monitoring in the GBAS, a ground monitor is developed to detect ephemeris failures, incorrect broadcast satellite positions, and hazardous ionosphere storms using either single- or dual frequency. The monitor also addresses the challenge of fault-free differential correction when satellites are rising, newly acquired, and re-acquired. The monitor utilizes differential code and carrier phase measurements across multiple reference receiver antennas as the basis for detection. Finally, the analytical performance of the monitor is demonstrated to meet Category III precision approach and landing requirements.

CHAPTER 1

INTRODUCTION

The Global Navigation Satellite System (GNSS) consists of satellites that orbit the Earth and broadcast their locations along with ranging signals toward the Earth surface. By simply collecting the signals from satellites, any users near the Earth surface can determine their location with an accuracy of meters. The Global Positioning System (GPS) is a well-known GNSS from the United States that has successfully provided worldwide position, navigation, and timing solutions. Currently, GPS is utilized in commercial aviation for en route operations but it lacks the ability to support safety-critical landing phases of a flight. With upcoming new GNSSs, it is envisioned that aircraft navigation can completely rely on GNSS from takeoff through final approach to landing. More details about existing aircraft navigation algorithms and architectures are discussed in this introduction. This dissertation is focused towards enabling the precise approach and landing of an aircraft.

1.1 Navigation metrics for aviation application

Unlike typical systems, an aircraft navigation system requires more than high accuracy. This is because degradation or failure of the navigation system without a notice would lead to a catastrophic event. There are four metrics that describe the requirements on different navigation phases for aircraft [1].

Accuracy is the measure of the navigation output, position and/or velocity solution, deviation from truth under fault-free conditions. Accuracy is related to statistical features and is often built from the statistical distribution of the errors. The accuracy specifications are often given at a certain percentile of the Cumulative Distribution Function (CDF) (e.g., 95th percentile).

Integrity is defined as the measure of trust that can be placed in the correctness of the information supplied by a navigation system. It also includes the ability of the navigation system to provide timely warning to users when the system should not be used for navigation. Integrity risk is the probability of an undetected navigation system error or failure that results in hazardously misleading information being sent to the navigation system user.

Continuity is the likelihood that the navigation system supports the accuracy and integrity requirements for the duration of an intended operation, presuming that the system was available at the beginning of the operation. Continuity risk is the probability of a detected but unscheduled navigation function interruption after the operation has been initiated.

Availability is an indication of the ability of the system to provide a reliable usable navigation service within a specified coverage area while meeting all three of the other requirements. The availability of a navigation system is the percentage of time that the services of the system are usable by the navigator.

The above discussed parameters are important for designing a navigation system and must meet predefined requirements. Table 1.1 lists out the navigation requirements for a civil aircraft during three operational phases: en route, approach and landing. Depending on an aircraft's decision height above the runway, approach and landing operations are further divided into Approach operations with Vertical guidance (APV) I/II and Category I/II/III landings, respectively. The important and clear thing is that the required accuracy becomes more strict as you move toward the Category III landing. Similarly, all requirements have bounds, especially the Time to Alert (TTA) for Category III where a system must notify any navigation failure within 2 s.

In real time, navigation users compute a Protection Level (PL) instead of evaluating integrity risk and continuity risk directly. The PL provides an upper bound on the position errors for a given integrity requirement. The PL is a part of the navigation system output along with position solutions, and it will be discussed further in the following sections. Figure 1.1(a) illustrates a nominal operation where the PL is within the predefined Alert Limit (AL)—the system is safe to use. Usually, the PL is split into horizontal PL (HPL) and vertical PL (VPL) forming a cylindrical bound on the aircraft position; the last two rows of Table 1.1 provide Horizontal Alert Limit (HAL) and Vertical Alert Limit (VAL) requirements. If a PL exceeds the AL in any direction, the system becomes unavailable, for example Figure 1.1(b), and the user must rely on other alternative navigation systems.

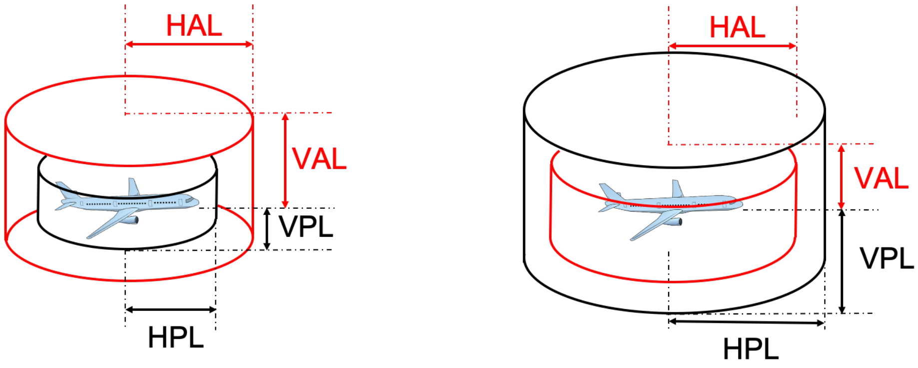

(a) Navigation system is available
(b) Navigation system is unavailable

Figure 1.1. Two examples of Protection Levels at aircraft to indicate availability of a navigation system

Table 1.1. Navigation requirements during different aircraft operations

Operation	En route[1]	Approach[1]		Landing[2]		
		APV I	APV II	Category I	Category II	Category III
Horizontal accuracy (95 percentile)	3.7 km	16 m (52 ft)	16 m (52 ft)	16 m (52 ft)	5 m (16 ft)	5 m (16 ft)
Vertical accuracy (95 percentile)	N/A	20 m (66 ft)	8 m (26 ft)	6 m to 4 m (20 ft to 13 ft)	2.9 m (9.5 ft)	2.9 m (9.5 ft)
Integrity (in each operation)	10^{-7}/h	2×10^{-7}/150 s	2×10^{-7}/150 s	2×10^{-7}/150 s	1×10^{-9}/15 s	1×10^{-9}/15 s
TTA	5 min	10 s	6 s	6 s	2 s	2 s
Continuity	10^{-4}/h to 10^{-8}/h	8×10^{-6}/15 s	8×10^{-6}/15 s	8×10^{-6}/15 s	8×10^{-6}/15 s	2×10^{-6}/15 s
HAL	7.4 km	40 m (130 ft)	40 m (130 ft)	40 m (130 ft)	17 m (55 ft)	17 m (55 ft)
VAL	N/A	50 m (164 ft)	20 m (66 ft)	35 m to 10 m (115 ft to 33 ft)	10 m (33 ft)	10 m (33 ft)

1.2 Augmented navigation systems

Since GNSS signals do not carry any information regarding their integrity, it is up to GNSS users to ensure integrity on position solutions (if required for the intended application). In the framework of civil aviation, three augmented systems have been proposed to enable integrity checks on aircraft position solutions.

(1) Aircraft Based Augmentation System (ABAS)

(2) Satellite Based Augmentation System (SBAS)

(3) Ground Based Augmentation System (GBAS)

1.2.1 ABAS. As the name suggests, this augmented system checks the position solution integrity by means of additional on-board navigation sensors or by exploiting GNSS-signal redundancy. The former approach is known as Aircraft Autonomous Integrity Monitoring (AAIM). When a barometer sensor is utilized with the GPS L1 signal, AAIM can support precise approach up to 350-ft decision height above the runway [3]. The latter approach is widely known as Receiver Autonomous Integrity Monitoring (RAIM) which is operational for horizontal guidance in civil aircraft using the GPS L1 frequency [4, 5, 6].

The major limitation of ABAS is that it cannot provide vertical guidance by using GPS alone. The continued advancement of GPS performance and new GNSS (i.e., GLONASS, Galileo, and Beidou) have opened the possibility to support vertical guidance in addition to horizontal as more measurements are available. Therefore, considerable effort has been invested, especially in the European Union (EU) and the United States (U.S.), to develop new dual-frequency multi-constellation Advanced Receiver Autonomous Integrity Monitoring (ARAIM) [7, 8, 9, 10, 11]. It is expected that ARAIM will support worldwide Category I landing requirements [10].

1.2.2 SBAS. This augmented system utilizes a geostationary satellite and a ground network to perform integrity checks on GNSS signals, and it provides timely warnings and corrections to aviation users. The SBAS ground segment uses accurately-surveyed ground stations, widely spaced over a large area, to collect ranging measurements and prepares nominal differential corrections and integrity parameters for each satellite [12, Chapter 12]. An encoded SBAS message is then prepared and uploaded to a geostationary satellite. This operation is performed in real-time and provides timely alerts to the end user when a fault is present in GNSS signals. By means of the geostationary satellite, the SBAS message could be available to a wide area or a continent. Currently, multiple SBASs exist globally to support regional aircraft navigation and enable safety-of-life operations [13]. For example, the Wide Area Augmentation System (WAAS), the U.S. implementation of SBAS, has been certified for Category I precision approach in the continental U.S., Canada, and Alaska since July 2003 [14].

1.2.3 GBAS. This system is designed to address the limitation of the SBAS by focusing navigation service to a local area such as an airport. As shown in Figure 1.2, multiple accurately-surveyed antennas are installed at the local airport to collect ranging measurements [15]. Then, the GBAS Ground Facility (GF) generates precise differential corrections and integrity parameters specifically for nearby GNSS users. The information from the GF is disseminated through a very high-frequency data broadcast transmitter. Similar to SBAS, GBAS operates in real-time to provide differential range corrections and a timely alert on faults. GBAS has been certified for Category I precision approach service since 2009 [16], but the most ambitious GBAS service, the Category III (zero visibility) precision landing, is under development.

The major benefit of GBAS is that significant airport infrastructure can be alleviated compared to the currently operational Instrumental Landing System (ILS) that enables precision landing. For example, the ILS hardware must be installed for each runway direction, while the GBAS GF enables precision landing in all directions and may also support near by airports.

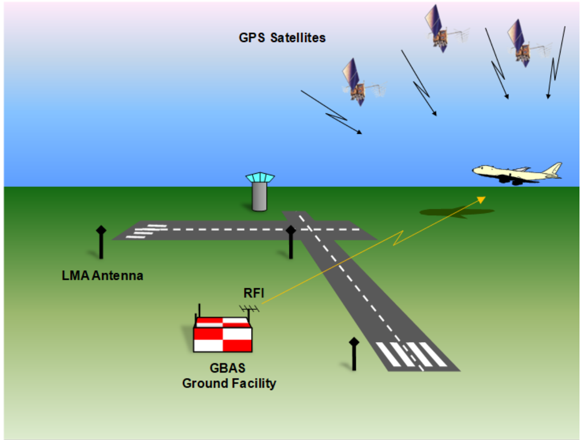

Figure 1.2. GBAS local ground facility at an airport

1.3 Research objective

This dissertation is focused on ARAIM and GBAS to enable next generation navigation service for precision approach and landing. Specifically, unaddressed challenges are resolved in the ARAIM and GBAS ground segments which are responsible for generating integrity parameters and for fault detection; ARAIM does not require real-time communication between the ground segment and the aircraft (more details in the next paragraph). The ARAIM and GBAS navigation user (airborne) algorithms are outside the scope of this dissertation; reader can find them in [7, 16]. By improving the ground segments' performance, GNSS users navigation solutions will have high accuracy and high integrity.

Since ARAIM exploits GNSS signal redundancy for integrity, its performance is highly dependent on the signal quality, including the nominal Signal In Space (SIS) range error model and a *priori* fault probability. In conventional RAIM, this information on GPS signals is hard-coded within the receiver and is consistent with the commitments of the GPS Constellation Service Provider (CSP). As an evolution of RAIM, ARAIM will use constellations which are not as mature as GPS. Therefore, Offline Monitoring (OFM) is envisioned on the ground to generate and validate the required information, dubbed Integrity Support Data (ISD), for all constellations. The generated ISD is made available to users through an Integrity Support Message (ISM) from the GNSS satellites. This dissertation contributes to the OFM by providing an independent source to evaluate GPS range error and proposing a new approach to generate the nominal range error model.

The GBAS GF is responsible for the integrity check on GNSS signals and provides a differential range correction to nearby GBAS users. Under nominal conditions, the GF will generate the differential corrections and integrity parameters by collecting ranging measurements and broadcasting them as discussed in [17]. However, in the event of a satellite or constellation fault, the GBAS GF must detect and inform GBAS users. This dissertation contributes to the GBAS GF by detecting broadcast satellite position faults and hazardous ionospheric storms. If any fault is detected, the integrity parameters on the faulty signal are increased such that a computed PL at GBAS users will be inflated. If the PL exceeds the predefined AL, the GBAS service becomes unavailable—integrity is assured.

1.4 Previous work and motivation

This section describes the existing research work in the ground segments of ARAIM and GBAS. There has been significant effort to make these systems operational as we will see in the following subsection.

1.4.1 ARAIM OFM.

As a part of EU and U.S. cooperation to develop the ARAIM algorithm, the OFM architecture is intensively investigated [9, 10, 18]. There was discussion to consider an 'online' architecture to generate the ISD and deliver to users in real time, but the OFM is preferred to eliminate the connectivity risk between users and ground segment [19, 20]. Basically, the OFM utilizes historically collected broadcast GNSS navigation messages and evaluates errors by comparing to “truth" satellite positions and clock biases. Using the precise International GNSS Service (IGS) orbit and clock products as the truth, the performance of GPS and Galileo constellations were evaluated, and nominal range error models were developed in [21, 22, 23, 24]. The error models are a part of the ISD, which contains nominal measurement biases and standard deviations of the ephemeris and clock errors. The two remaining ISD parameters, prior probabilities of satellite- and constellation-wide faults, are carefully determined for each constellation [25]. Sensitivity analysis on the ISD parameters was carried out in [26] to indicate potential benefits in navigation service once new constellations become mature.

The major limitation of the current OFM is that it heavily relies on the external IGS and National Geospatial-Intelligence Agency (NGA) organizations for the truth satellite positions and clock biases. Since ARAIM is intended to operate over several decades, the Air Navigation Service Provider (ANSP) dependencies on external organizations should ideally be avoided. Indeed, none of these organizations make specific commitments on the reliability of their products or on the process used to obtain them. Furthermore, data gaps exist especially during satellite fault events, which are crucial for the ISD fault statistics. These external products must, therefore, be carefully validated before use in the OFM [27, 28, 24]. To directly address this limitation in the OFM, an independent satellite position and clock bias generation was proposed and analyzed in [29] through a covariance analysis. In response, this dissertation brings the covariance analysis into reality by prototyping the satellite position and clock bias generation.

Once the ISD is prepared by the OFM, it must be valid for a certain duration, which requires ranging errors to be stationary over a given time period. In simple words, stationarity in the wide sense implies that the mean and standard deviation of errors must remain constant over the specific time window. In the absence of stationary errors, the generated ISM will not represent a realistic distribution of actual errors, and the computed PL at ARAIM users will not provide accurate position error bounds. In [30], the temporal behavior of satellite position and clock errors, showing time-correlated range errors, was exposed and a method was proposed to generate the ISD from sample range errors. However, GNSS users only have access to satellite positions through a broadcast ephemeris parameter set. Nominal errors in the ephemeris set would result in *completely* time-correlated satellite position errors until a new ephemeris set is available. Therefore, the randomness in ephemeris sets themselves is analyzed in this dissertation, and a new technique to prepare the ISD is proposed.

1.4.2 Fault detection in the GBAS GF. Comprehensive descriptions about all fault types and monitoring techniques in the GBAS GF are available in [12, §31.3.3]. This dissertation focuses on the two most hazardous fault modes: a broadcast ephemeris fault and unusual ionospheric activity. The former fault is categorized into different types depending on satellite maneuvers and incorrect ephemeris upload events [31]. Each type of ephemeris failure is monitored under different processing schemes [32, 33, 34, 31, 35]. The latter fault mode is simply due to abnormally sharp electron density which results in an ionospheric gradient. Unlike ephemeris faults, the ionospheric gradient size depends on location, being steepest in the equatorial regions, and significant research efforts have been made to modeling and detection [36, 37, 38, 39, 40].

An aircraft on Category III GBAS Approach Service Type D (GAST-D) cannot tolerate differential ranging errors larger than 2.75 m [41]. The largest observed ionospheric gradient size is 850 mm/km, and this results in a 7.65-m range error [42]. Detecting these gradients is so difficult that the GF must utilize the carrier wave that is intended to deliver actual pseudo-range (code) measurements to users for ranging. On its own, the carrier signal is useless due to an unknown initial cycle count, but when combined with an another close-by antenna to form a differential carrier phase measurement, it provides significant fault detection capability [36]. Since the GF has multiple antennas and receivers for hardware redundancy, multiple monitoring strategies based on differential carrier phase measurements have been proposed [43, 44, 44].

Previously developed monitors in the above mentioned citations detect both ephemeris faults and ionospheric gradients, but the absence of faults are not guaranteed when a satellite is rising, newly acquired, or re-acquired in the GBAS. The current monitors do not solve the unknown cycle ambiguity for differential carrier measurements. As a consequence, when a fault causes differential range errors that are close to the carrier cycle, the fault goes undetected. In other words, initial differential corrections from the GF lack the validation of the fault-free case. This dissertation specifically addresses the acquisition challenge and provides a new fault-detection strategy for both ephemeris failures and ionospheric gradients.

1.5 Contributions

The contributions of this dissertation are grouped and summarized into three following subsections. Each subsection is further addressed in subsequent chapters to facilitate identification of concept and implementation steps. Chapter 2 contains detailed information about GNSS signals and concepts of estimation and fault-detection.

1.5.1 Accurate GPS ephemeris parameters and clock biases generation.

A new computationally efficient information smoother, an estimator, is developed to independently provide transparent satellite position generation through ephemeris parameters and clock biases (Chapter 3). The performance of the estimator is demonstrated through experimental data, which also includes step-by-step guidance for prototyping, and the resulting SIS range errors from the estimator have an accuracy of 0.5 m (Chapter4).

1.5.2 Analyzing GPS ephemeris parameter errors. Since, for the first time, accurate ephemeris parameters will be available due to the first contribution, an effort is made to characterize the true error source of range errors by directly analyzing broadcast ephemeris parameter errors. Using experimental data, broadcast ephemeris errors are characterized to prepare a nominal ephemeris-error model under the nominal condition. Then, a new method is proposed to generate ISD directly from the developed ephemeris-error model. The preliminary result closely matches prior work and provides more insight into time-correlation of errors (Chapter 5.

1.5.3 Detecting ephemeris failures and ionospheric gradients. A GBAS ground monitor is developed to detect anomalous SIS spatial gradients caused by ephemeris faults and ionospheric gradients for rising, newly acquired, and re-acquired satellites using either single- or dual-frequency GNSS signals. The monitor uses differential carrier phase measurements across multiple reference antennas as the basis for detection, where cycle ambiguities are obtained in less than 10 min such that monitoring operation can start quickly. The analytical performance of the monitors is demonstrated to meet Category III precision approach and landing requirements (Chapters 6, 7, and 8).

CHAPTER 2

CONCEPTS FOR SAFETY-CRITICAL NAVIGATION SYSTEM

This chapter is a short overview of available GNSS measurements for users and how GNSS is used for safe navigation. Three sections provide basic descriptions of GNSS measurements, the positioning algorithm, and fault-detection concept. Overall, this chapter facilitates the concept of positioning and fault-detection theory before applying these to specific aircraft navigation applications.

2.1 GNSS measurements

In radio communication, a transmitter broadcasts useful information by modulating it over a carrier frequency. Then, a receiver collects signals in the range of the carrier frequency and decodes (demodulates) the broadcast information. Similarly, each GNSS satellite broadcasts a unique Pseudo Random Noise (PRN) code along navigation parameters over predefined carrier frequencies in the L-band. Each PRN code is unique to each satellite for clear identification, and navigation parameters contain useful information for positioning such as satellite location at the transmission time. By simply collecting satellite signals, GNSS receivers decode the PRN code to form code measurements, also known as pseudorange measurements, which provide a distance between satellite to receiver. At the same time, carrier wave, used for transmission, is tracked, and carrier phase measurement is formed. The usage of carrier phase measurement is limited due to unknown integer count at the transmission, but is helpful in certain cases (more detail in Subsection 2.1.2).

Currently, large numbers of GNSS measurements are available worldwide from multiple constellations. Some constellations have the capability to broadcast over multiple frequencies as well as multiple types of PRN codes over the same frequency.

For example, the GPS constellation broadcasts signals over the L1, L2 and L5 bands, and within the L1 band, three types of code measurement, L1 C/A, L1C and L1 P(Y), exist for navigation [45, 46]; the L2 carrier band and P(Y) code types are reserved for military purposes. Here in this chapter, we will focus only on one type of code measurement for navigation, with dual-frequency measurements being used in other chapters.

2.1.1 Code measurement. Equation (2.1) shows a generic description of code measurement at time epoch k, which is formed in receiver j and transmitted by satellite j over carrier frequency f.

$$\rho^{i,j}_{f,k} = r^{i,j}_{k} + c(dt^{j}_{k} - dt^{i}_{k}) + T^{i,j}_{k} + I^{i,j}_{f,k} + \varepsilon_{mp,\rho^{i,j}_{f,k}} + \varepsilon_{th,\rho^{i,j}_{f,k}} \tag{2.1}$$

where,

c, f	are the speed of light and the transmission frequency,
$r^{i,j}_{k}$	is the true range between satellite's transmitting Antenna Phase Center (APC) to receiving APC at user,
dt^{i}_{k}, dt^{j}_{k}	are the clock biases at satellite i and in receiver j, respectively,
$T^{i,j}_{k}$	is the tropospheric delay while signal passed through Troposphere,
$I^{i,j}_{k}$	is the ionospheric delay while signal passed through Ionosphere,
$\varepsilon_{mp,\rho^{i,j}_{f}}$	is colored multipath on code measurement,
$\varepsilon_{th,\rho^{i,j}_{f}}$	is effective white receiver thermal noise on code measurement.

Knowledge of the majority of these terms is available from the navigation message and/or a priori developed error models. For example, satellite position and its clock bias knowledge is available via ephemeris parameters and quadratic clock parameters; users will remove its contributions as discussed in [45]. Ionospheric delay contribution is removed via available Klobuchar model parameters in the navigation message, while the tropospheric delay model is usually hard-coded in receivers [47]; Ionosphere being very dynamic compared to troposphere is usually monitored and predicted by CSP. Multipath and thermal noise, being the property of local antenna environments and receiver characteristics, are treated as a noise term in determining position.

Worldwide, GNSS self-sufficiently provides position solutions with meter-level accuracy. However, depending on applications, external information can be used instead of the navigation message. For example, a user may use the IGS satellite position and clock bias product to reduce an error contribution from the navigation message. Table 34.1 of [12] provides more accurate models to externally improve error contribution in code measurements, which is not necessary in general applications.

2.1.2 Carrier phase measurement.

Equation (2.2) shows a generic description of carrier phase measurement at time epoch k, which is formed in receiver j and transmitted by satellite j over carrier frequency f.

$$\phi^{i,j}_{f,k} = r^{i,j}_{k} + c(dt^{j}_{k} - dt^{i}_{k}) + T^{i,j}_{k} - I^{i,j}_{f,k} + \lambda_f n^{i,j}_{f} + PWU^{i,j}_{f,k} + \varepsilon_{mp,\phi^{i,j}_{f,k}} + \varepsilon_{th,\phi^{i,j}_{f,k}} \tag{2.2}$$

where,

$n^{i,j}_{f}$	is the integer cycle ambiguity on carrier signal f for satellite i and receiver j,
$PWU^{i,j}_{k}$	is an additional range error due to Phase Wind Up (PWU) on carrier phase measurement for satellite i and receiver j.

Similar to code measurements, carrier phase measurements have almost identical terms except for a negative sign in the ionospheric delay term and an additional cycle ambiguity term. Unlike code phase being delayed in the ionosphere, carrier phase experiences an advance thus the negative sign is presented in Equation (2.2) [48, Subsection 5.3.1]. As mentioned earlier, the carrier wave is simply used for transmission so the integer cycle count from transmission is unavailable. In addition to cycle ambiguity, a small fraction of phase change exists due to the nature of circularly polarized electromagnetic waves, which is known as Phase Wind Up (PWU).

Direct use of carrier phase measurement in position and/or navigation solutions is limited due to unknown integer count at transmission time. However, it can be useful in certain applications. Three example applications are provided here for displaying possible advantages. First, small variations in carrier phase measurements are used to reduce the large-code-noise impact on code measurements. This approach is well known as the hatch filter [49], and accuracy on position solution can be improved. Second, Real-Time Kinematic positioning is a technique where carrier phase measurements are used to provide centimeter level position solutions [12, Section 26.3]; here, the user needs to wait for at least half an hour to resolve cycle ambiguity. Third, carrier phase measurements are used in fault-detection applications; Chapter 6 develops carrier phase-based fault-detection monitors.

2.2 Positioning algorithm

Multiple techniques are employed to determine user location using GNSS measurements, and sometimes external sensors are also used to improve user location. However, this section specifically covers obtaining user location using single frequency code measurements and navigation-message parameters. To determine three-dimensional user location, at least three code measurements would be necessary as single code measurement provides only range information. In addition, receiver clock bias is treated as an additional unknown to avoid any receiver clock instability and to align local receiver time with GPS time. Thus, four code measurements are necessary to determine user location and receiver clock bias.

In general, estimation theory is employed to determine unknown information from available measurements. For example, least-square estimation and Kalman-filter are widely used techniques. First, a linear relationship is formed between measurements and unknown parameters, and then any estimation technique can be used to determine unknowns. In aircraft navigation, the least-square estimator is used to determine user location at each time k. Thus, linear measurement sets will be formed first.

In a first step, the nonlinear range term ($r_k^{i,j}$) is linearized at an approximate user location $X_0^{*,j}$. The knowledge of $X_0^{*,j}$ does not need to be accurate as it is mainly needed for linearization; one can start with (0,0,0) as well. Then, tje approximate range term ($r_0^{*,i,j}$) is computed based on broadcast satellite position (X^i) (available from navigation message) and $X^{*,j}$. The third line of Equation (2.3) indicates the range term ($r_k^{i,j}$) with resulting range error ($\delta r|_{X_0^{*,j}}$) due to error in initial guess ($\delta X^j = X^j_{\text{true}} - X_0^{*,j}$).

$$\begin{aligned} r^{i,j} &= \|X^i - X^j\| \\ &= \|X^i - X_0^{*,j}\| + \delta r|_{X_0^{*,j}} \\ &= r_0^{*,i,j} + \delta r|_{X_0^{*,j}} \\ &= r_0^{*,i,j} + (-\,{}^{i,j}e_0^T \delta X_0^j) \end{aligned} \tag{2.3}$$

Now, the relation between additional range term (δr) and unknown user location relative to $X^{*,j}$ is visualized in Figure 2.1 as a projection of δX on the line-of-sight vector; theoretical derivation using Taylor series expansion is available in [48, Subsection 5.1.1]. As a result, the linear relationship between range term and unknown user location is established.

In the next step, the relationship between linear code measurement and unknown states will be established. The known range term ($r_0^{*,i,j}$) and other error contributions from navigation parameters will be corrected in the code measurement. The first line in Equation (2.4) shows the residual code measurement after removing the known quantities, and the second line indicates remaining unknowns, to be found,

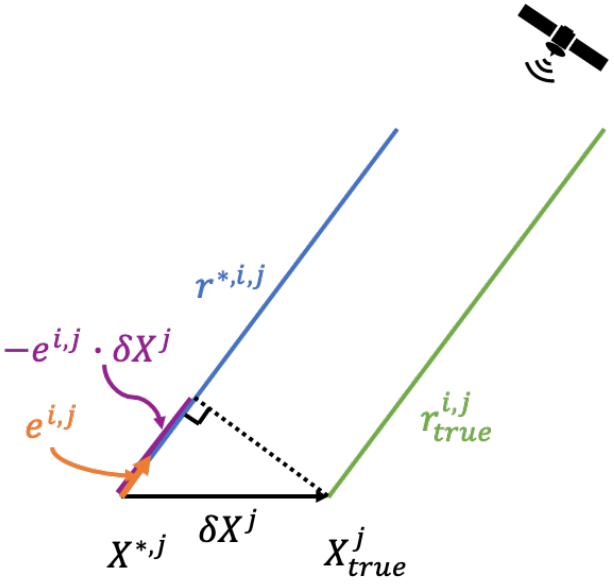

Figure 2.1. Graphic representation of linearizing range term at approximate user location.

in the residual code measurement.

$$\begin{aligned}\delta\rho^{i,j}_{f,0} &= \rho^{i,j}_f - r^{*,i,j}_0 + cdt^i - T^{i,j} - I^{i,j}_f - \delta t^{SV} \\ &= -\,{}^{i,j}e_0^T\delta X_0^j + cdt^j + \varepsilon_{mp,\rho_f^{i,j}} + \varepsilon_{th,\rho_f^{i,j}} \\ &= -\,{}^{i,j}e_0^T\delta X_0^j + cdt^j + \varepsilon_{\mathrm{RNM},\rho_f^{i,j}}.\end{aligned} \tag{2.4}$$

$\varepsilon_{mp,\rho_f^{i,j}}$ depends on the environment of user antenna and its characteristics while $\varepsilon_{th,\rho_f^{i,j}}$ depends on receiver characteristics and its internal design. Usually, the receiver manufacturer will provide a thermal noise model. However, the multipath model is application specific as it is very dynamic as shown in [50]. Here, we simply consider the combined Receiver Noise and Multipath (RNM) model used in aviation [51].

$$\varepsilon_{\mathrm{RNM}} \sim (0, V) = (0, \sigma^2_{\mathrm{RNM}}) \tag{2.5}$$

where, σ_{RNM} is available from [51].

Similarly, all visible satellites are linearized to form a stack of linear code measurements with unknown user location and receiver clock bias. Equation (2.6) indicates the general equation where N visible satellites are stacked, and different terms are identified as the typical measurement equation of an estimator.

$$\begin{bmatrix} \delta\rho_{f,0}^{i=1,j} \\ \vdots \\ \delta\rho_{f,0}^{i=N,j} \end{bmatrix} = \begin{bmatrix} -\,{}^{i=1,j}e_0^T & c \\ \vdots & \vdots \\ -\,{}^{i=N,j}e_0^T & c \end{bmatrix} \begin{bmatrix} \delta X_0^j \\ dt^j \end{bmatrix} + \begin{bmatrix} \varepsilon_{\mathrm{RNM},\rho_f^{i,j}} \\ \vdots \\ \varepsilon_{\mathrm{RNM},\rho_f^{i,j}} \end{bmatrix} \tag{2.6}$$

$$\mathscr{y}_0 = \mathscr{H}_0 \mathscr{x}_0 + \mathscr{v}$$

where, $\mathscr{y}$ is measurement vector, $\mathscr{H}$ is observation matrix, $\mathscr{x}$ is state vector containing user location (δX^j) and receiver clock bias (dt^j), and $\mathscr{v}$ is measurement noise vector.

Now, an unknown state vector ($\mathscr{x}_0$) is found using the least-square estimation (Equation (2.7)); more details about least-square estimation are available in [52, Chapter 3]. Along with the estimated state ($\hat{\mathscr{x}}_0$), covariance (1-σ) on estimated states is available, which indicates uncertainty in estimation due to measurement noise.

$$\begin{gathered} \hat{P}_0 = (\mathscr{H}_0^T V^{-1} \mathscr{H}_0)^{-1} \\ \hat{\mathscr{x}}_0 = \hat{P}_0 \mathscr{H}_0 \mathscr{y}_0 \end{gathered} \tag{2.7}$$

From Equations (2.3) through (2.6), approximate $X_0^{*,j}$ leads to $\hat{X}_0^j = (X_0^{*,j} + \delta\hat{X}_0^j)$, which is the end result of the first iteration at time-epoch k. In the next iteration, approximate user location would be $X_1^{*,j} = \hat{X}_0^j$, and the least-square estimator is repeated again. During the iteration process, the non-linearity errors caused by approximate state ($X^{*,j}$) are reduced, and once it converges, resulting $\delta\hat{X}^j$ will be much smaller. Usually, the normalized estimate error, such as $(\hat{X}_0^j - X_0^{*,j})^T P_{\hat{X}_0^j} (\hat{X}_0^j - X_0^{*,j})$

value, is monitored to check its convergence. Once the normalized estimate error becomes acceptable, we can terminate the iteration process, and user location at time-epoch k will be available as $X^{*,j}_{\text{last iteration}}$. The covariance value on the estimated state would remain the same as there is no change in the used measurements for iterations; minor variation would occur due to improved line-of-sight vector but it would negligible.

Simply using single-frequency code measurement for a given time-epoch, user location can be determined as we have shown. The accuracy of user location can be improved further by integrating signals over time. However, the integration would require a Kalman Filter with an accurate error model in the time-correlation sense. Otherwise, user location may not be accurate due to unfitted error model. The current section discussed the positioning algorithm in the general sense. Specifically in aircraft positioning, an integrity check is necessary as discussed in Chapter 1. [53, Appendix E], [54, Appendix J.1] and [55, Appendix I] provide details of the actual positioning algorithms implemented in RAIM, SBAS, and GBAS, respectively. The current-form of the ARAIM algorithm is available in [7, 56].

2.3 Fault detection

The fault-detection concept is used in different applications to identify unexpected events in a system. Particularly, in aircraft navigation, the information used in positioning must be monitored against possible fault events. For example, in the previous section, we directly assumed that satellite position (X^i) is accurate from the navigation parameter; in the past, faults were observed [57, Figure 1]. This section is intended to discuss the general detection concept with a simple example. Typical GNSS users may not be concerned with a fault, but it is very critical for aircraft navigation operation as any fault in a GNSS system could lead to a catastrophic event.

Within aircraft navigation, different approaches exist to monitor a fault event such as a residual-based monitor, a solutions-separation monitor, and an innovation-based monitor. The first two monitors are almost the same as both of them observe the impact of faults in the parity space of measurements. [58] provides a detailed comparison of the residual versus solution separation approaches. The innovation-based monitor employs additional information either from external sensors or from previously estimated states to detect a fault event. Regardless of which detection approach, the basic idea is to monitor a test-statistic, designed for a specific event, against a pre-determined threshold. Once the test-statistic exceeds the threshold, a fault event is identified, and the system will take appropriate action. However, the design of the test-statistic and threshold requires careful consideration as any false event would impact the continuity of a system while any undetected fault impacts the integrity of a system.

Here, a simple satellite fault monitor, consisting of test statistics and threshold, is going to be developed; a detailed description of the problem statement is in the next paragraph. The development of a fault monitor consists of three steps. First, available measurements and/or information is used to form a test statistic. Second, a threshold value is selected for test-statistics based on continuity requirement; this step is known as false-alarm analysis. Third, simulated faults are injected to observe detection performance for the test-statistic—threshold pair. All three steps are discussed below with actual numbers.

Problem statement: Develop a test-statistic—threshold pair to detect a fault in satellite positions for a given time epoch k using single-frequency code measurement. Considering the aircraft operation requirement, a continuity risk of 10^{-7} needs to be allocated in designing the threshold, and then fault magnitudes are determined which could result in integrity risk higher than 10^{-8}. One can assume that user location and receiver clock bias are accurately provided externally, and navigation message is fault-free for satellite clock bias and ionospheric delay.

2.3.1 Defining test statistic.

A test statistic can be envisioned as a simple variable which behaves differently in the presence of faults when compared to their absence. Based on theoretical understanding of faults, we will define a test-statistic for detecting specific types of faults. Here, we proceed via an example.

In our problem statement, we want to detect satellite faults. Thus, in the first step, we will find out how a satellite position fault would impact a range term. Just like in Equation (2.3), the range term is linearized using broadcast satellite position X^i_{eph}, and remaining range error can be visualized as a projection of the satellite-fault vector along a line-of-sight vector (Figure 2.2). When broadcast navigation parameters represent accurate satellite position, δX^i_{eph} will be zero (close to zero in reality), and so on, resulting in range error. Any orthogonal satellite faults to line-of-sight would have negligible impact. Thus, magnitude of range error will be more important to monitor than faulty satellite position vector.

$$\begin{aligned} r^{i,j} &= \|X^i_{\text{true}} - X^j\| \\ &= \|X^i_{\text{eph}} - X^j\| + \delta r|_{\delta X^i_{\text{eph}}} \\ &= r^{i,j}_{\text{eph}} + {}^{i,j}e^T \delta X^i_{\text{eph}}, \end{aligned} \tag{2.8}$$

where, δX^i_{eph} indicates a fault vector from broadcast satellite position from ephemeris (X^i_{eph}) to true position (X^i_{true}).

Based on available knowledge and known relation in Equation (2.8), we will define test statistics as,

$$\begin{aligned} q^i_{\rho,eph,k} &= \rho^{i,j}_{f,k} - r^{i,j}_{eph} - c(dt^j_k - dt^i_k) - T^{i,j}_k - I^{i,j}_{f,k} \\ &= {}^{i,j}e^T \delta X^i_{\text{eph}} + \varepsilon_{mp,\rho^{i,j}_f} + \varepsilon_{th,\rho^{i,j}_f} \\ &= {}^{i,j}e^T \delta X^i_{\text{eph}} + \varepsilon^{i,j}_{\text{RNM}}. \end{aligned} \tag{2.9}$$

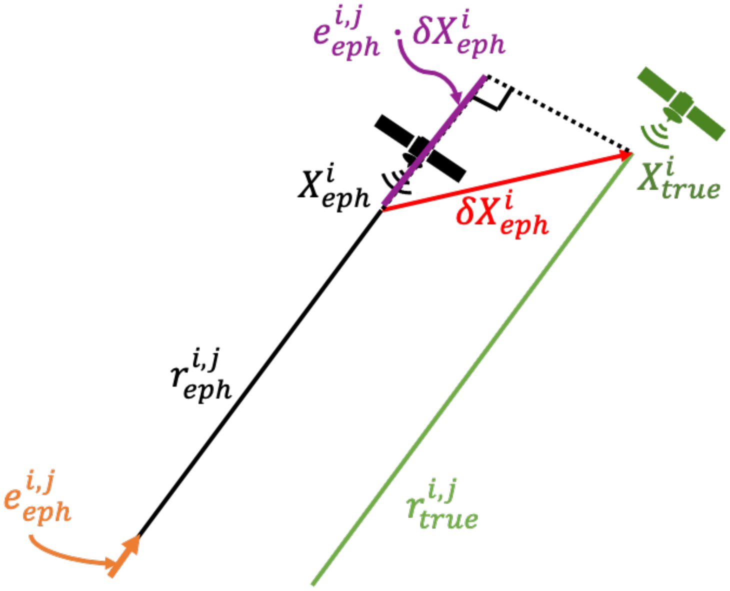

Figure 2.2. Graphic representation of range error due to incorrect satellite position

The first line indicates the computation of test-statistic in real-time using known quantities, while the second line indicates the relationship of test statistics to faults and underlying noise terms.

Once a test-statistic is defined, its distribution under the fault-free case needs to be understood for defining a threshold. Here, Gaussian distribution is considered for simple visualization. From Equation (2.9), the test-statistic seems to be affected by RNM noise. However, the used broadcast satellite position in Equation (2.9) has an uncertainty even if it is close to true. In the navigation message, σ_{URA} term is available to inform the standard deviation of resulting range error due to broadcast satellite position, and we will use it as possible uncertainty in X^i_{eph}. Thus, the test-statistic is written mathematically as,

$$q^i_{\rho,\text{eph},k} \sim \mathscr{N}\left({}^{i,j}e^T \delta X^i_{\text{eph}}, \sigma^2_{q_{\rho,\text{eph}}} \right) = \mathscr{N}\left({}^{i,j}e^T \delta X^i_{\text{eph}}, \sqrt{\sigma^2_{\text{URA}} + \sigma^2_{\text{RNM}}} \right) \tag{2.10}$$

where, $\mathscr{N}$ is normal distribution.

In our example case, it is assumed that satellite clock bias, receiver clock bias, ionosphere delay and tropospheric delay are completely accurate, and only uncertainty in broadcast satellite position needs to be considered. If any term has an uncertainty, then $\sigma_{q_{\rho,\text{eph}}}$ needs to be adjusted. Otherwise, it would cause unexpected false alarms.

2.3.2 Determining threshold. This step is straightforward if the definition of test-statistic is accurate and clear. Usually, this step is revisited after evaluating detection performance as ultimately a tighter threshold would help in better detection; sometimes, previously developed test-statistics may need to be modified.

Under fault-free conditions, the test-statistic would be $q^i_{\rho,\text{eph},k} \sim \mathcal{N}(0, \sigma^2_{q_{\rho,\text{eph}}})$. To evaluate the threshold, σ_{URA} and σ_{RNM} are needed such that the actual uncertainty in $q^i_{\rho,\text{eph}}$ can be bounded. Here, σ_{URA} of 2.4 m is simply taken from the GPS navigation message [45]. Similarly, σ_{RNM} of 0.5 m is assumed for typical GNSS receiver noise and multipath. Thus, $\sigma_{q_{\rho,\text{eph}}}$ would be 2.45 m ($= \sqrt{2.4^2 + 0.5^2}$). Figure 2.3 illustrates the probability of False Alarm (FA) (P_{FA}) in blue to indicate a chance of the test-statistic being outside the threshold due to the tail of a distribution. If a threshold value is placed towards zero-mean, P_{FA} would be higher, while placing a threshold far-away would reduce the possibility of the fault being outside the threshold at all. For the earlier continuity requirement (P_{FA}) of 10^{-7}, the exact threshold is computed by inverse Cumulative Distribution Function (CDF); for example, a MATLAB command `P_FA=cdf('norm',-T,0,sigma_q)+(1-cdf('norm',T,0,sigma_q))`. $T_{q^i_{\rho,\text{eph}}}$ would be 13.059 m for our case when $\sigma_{q_{\rho,\text{eph}}} \sim (0, (2.45\text{m})^2)$. In a typical application, false-alarm requirement will not be as low as 10^{-7}, and in such a case, the threshold could be tightened to improve detection performance.

In this section, we made two implicit assumptions. The first assumption is that the used error models for σ_{RNM} and σ_{URA} are accurately bounding the cumulative distribution of errors. In general, error models mostly look at root-mean-square

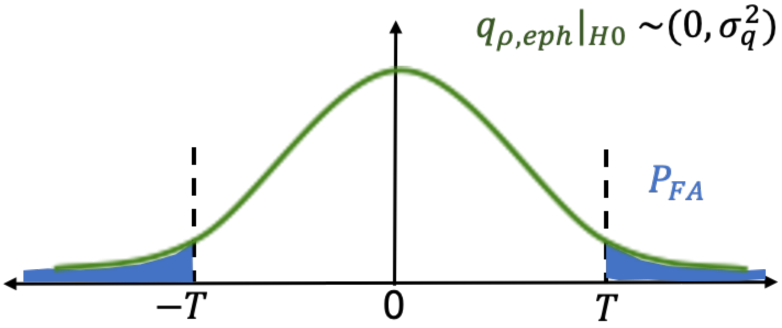

Figure 2.3. Illustration of false-alarm events for a hypothetical threshold against the test-statistic distribution.

or 95 percentile. However, given the high continuity requirement of 10^{-7}, an inaccurate error model would directly contribute to false alarms even if faults are absent. The second assumption is that the modeling of code measurement is accurate enough that no unexpected event would cause false-alarm. Code measurement is well modeled in literature, and all possible modeling error can be considered in defining a test-statistic. However, once carrier phase measurement is being used, more accurate modeling would be necessary [12, Chapter 19]. For example, received GNSS signals at Antenna Phase Center (APC) are usually different from geometric center, and sometimes orientation and placement of antenna would also contribute an error. Thus, it is ideal to collect measurements in the real environment, and check if the theoretical expected distribution of the test-statistic matches with the actually observed distribution.

2.3.3 Detection performance. The previous two subsections are sufficient to detect a fault event. In this subsection, we are interested in evaluating the detection performance of our developed $q^i_{\rho,\text{eph},k}$ and $T_{q^i_{\rho,\text{eph}}}$. By injecting simulated faults, we will determine the capability of detection in terms of Missed Detection (MD).

In general, a system has an integrity-risk budget, and different fault categories have subsequent budgets in terms of acceptable missed detection; this requires detailed study and is known as fault-tree analysis. In our case, we directly allocate integrity risk of 10^{-8} as the acceptable probability of MD. Before actual computation, a graphical representation is discussed to share why the risk of MD always exists. Figure 2.4 illustrates the test-statistic distribution under the fault-free case and two fault events. First, the fault-free case is represented by the green distribution centered at zero; T_q is obtained from Subsection 2.3.2. Under a fault case, the distribution will be driven in the positive or negative direction as a fault would impact the mean of the distribution; Equation (2.10). For illustration purpose, only the positive fault magnitude is displayed in Figure 2.4. If a fault magnitude is very large compared to threshold ($\mu_1 >> T_q$), then the faulty distribution is far away from the threshold and detection is guaranteed. This case is displayed as the red distribution in Figure 2.4. However, a fault magnitude being slightly higher than threshold is not guaranteed to be detected. For example, the orange distribution in Figure 2.4 is shifted by more than T_q due to fault magnitude μ_2, but due to the left tail distribution, probability of the test-statistic being inside the threshold does exist. Thus, the probability of MD exists due to the distribution of the test-statistic, and a system designer should be aware of a proposed test-statistic limitation.

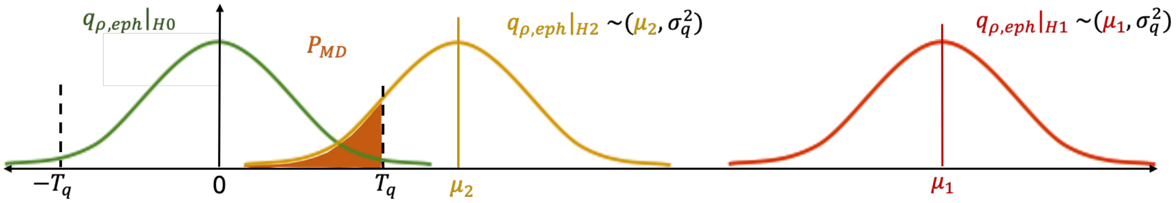

Figure 2.4. Graphical representation of test-statistic distribution under three hypothesis: (1) fault-free case (green), (2) a fault being close to designed threshold (orange), and (3) a very large fault magnitude compared to designed threshold (red)

Since the $q^i_{\rho,\text{eph},k}$ distribution and threshold $T_{q^i_{\rho,\text{eph}}} = 13.059$ m is known, we can evaluate the probability of MD for each satellite fault magnitude via inverse CDF. Specifically, a magnitude of ${}^{i,j}e^T\delta X^i_{\text{eph}}$ will be varied instead of the actual δX^i_{eph} vector for simple visualization; ultimately, resulting range error is important for GNSS users. Figure 2.5 indicates resulting P_{MD} for positively increasing fault magnitude; a matlab command "`P_MD=cdf('norm',T_q,mu,sigma_q)-cdf('norm',-T_q,mu,sigma_q)`" is used in the evaluation. Similar to Figure 2.4, the $q^i_{\rho,\text{eph},k}$ distribution is shifted towards the right side. Thus, P_{MD} would be one (10^0) when ${}^{i,j}e^T\delta X^i_{\text{eph}}$ is close to zero. The increase in ${}^{i,j}e^T\delta X^i_{\text{eph}}$ would reduce P_{MD}. One can simply read Figure 2.5 to decide if fault magnitude has an acceptable MD risk. In any case where detection performance is not acceptable or requirements are changed, Subsections 2.3.1, 2.3.2 and 2.3.3 will be executed again with a new design.

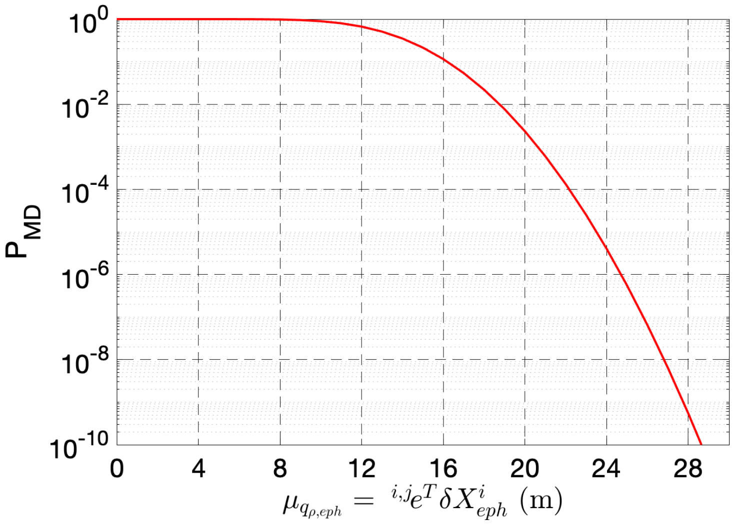

Figure 2.5. Probability of missed detection for a resulting range error due to satellite position faults

To sum up, this chapter discussed the navigation operation performed at the user from GNSS signals. First, available GNSS code and carrier phase measurements are discussed in detail with contributing errors in them. Then, a simple position algorithm is explained to obtain the navigation solution from single frequency code measurement. Lastly, the fault-detection concept is briefly discussed to ensure a safe navigation solution. In the following chapters, the discussed concepts will be used in ARAIM and GBAS applications.

CHAPTER 3

ESTIMATION OF SATELLITE ORBIT AND TIME

This chapter contributes to the ARAIM OFM which has the responsibility to monitor range-error statistics of GNSS signals. To enable independent and transparent monitoring, a method to estimate satellite orbit and clock biases is proposed here. This chapter is limited to the theoretical development of the estimator and elaborates its key elements; covariance results are presented to demonstrate achievable accuracy of the estimated orbit and clock product. Experimental results will be shown for the GPS constellation in the next chapter.

This chapter is divided into four sections. First, the required accuracy of the orbit and clock product is defined for the ARAIM OFM application. Second, a comprehensive description of the estimator design is provided. Third, the necessary steps to validate the estimated orbit and clock product are outlined. Lastly, the achievable accuracy of the estimated orbit and clock product is quantified using nominal measurement error models[1].

3.1 Required accuracy of orbit and clock product for the ARAIM OFM

Since the newly generated orbit and clock product will be used to compute nominal range errors and fault statistics, it must be accurate enough to observe actual errors in the satellite-broadcast ephemeris. An upper bound on the standard deviation of broadcast satellite orbit and clock errors is provided by the CSP as σ_{URA}. Supposing that the generated orbit and clock product has an accuracy of σ_{OFM}, the

---

[1] ©2023 IEEE. Reprinted, with permission, from J. Patel, “Accurate GPS LNAV parameters and clock biases for ARAIM offline monitoring", *IEEE Transactions on Aerospace and Electronic Systems*, Aug 2023. [59].

resulting standard deviation of perceived orbit and clock errors would be

$$\text{Validated } (\sigma_{\text{URA}}) = \sqrt{\sigma_{\text{URA}}^2 + \sigma_{\text{OFM}}^2} \tag{3.1}$$

where Validated (σ_{URA}) would be part of the ISD and is disseminated through the ISM to ARAIM users.

Currently, no requirement exists on σ_{OFM}, but for illustration purposes, we consider different magnitudes of σ_{OFM} to expose its effects. Typically, GPS satellites broadcast σ_{URA} of 2.4 m or higher, but prior work [21, 22] has shown that the orbit and clock errors in the GPS and Galileo constellations are closer to 1 m, and it is reasonable to expect that the broadcast σ_{URA} will be lowered accordingly in the future. Thus, Figure 3.1 shows the resulting Validated (σ_{URA}) for a 1-m σ_{URA}. The gradual increase in Validated (σ_{URA}) is visible as σ_{OFM} increases, but the achievable Validated (σ_{URA}) is still only 1.12 m even if σ_{OFM} reaches 0.5 m. A 1.12-m Validated (σ_{URA}) is still feasible in ARAIM to support the most ambitious LPV-200 approach [10]. Thus, we aim to provide satellite orbit and clock product having σ_{OFM} accuracy of at least 0.5 m.

3.2 Estimator design to generate satellite orbit and clock product

We employ a Kalman Filter (KF) over a certain duration to fit satellite positions through a well-established parametric orbital model: the GPS legacy model detailed in Section 5.1. The GPS legacy model uses Legacy NAVigation message (LNAV) parameters that are broadcast to GPS users. Considering the fidelity of the LNAV parameters, a four-hour filtering window is selected for the KF [29]. Because satellite clock error is not always smooth, we avoid the use of clock models in the KF and instead estimate the satellite clock biases instantaneously. The same is also true for the receiver clocks of Reference Ground Stations (RGSs). We therefore estimate satellite clock biases, receiver clock biases and LNAV parameters in a single

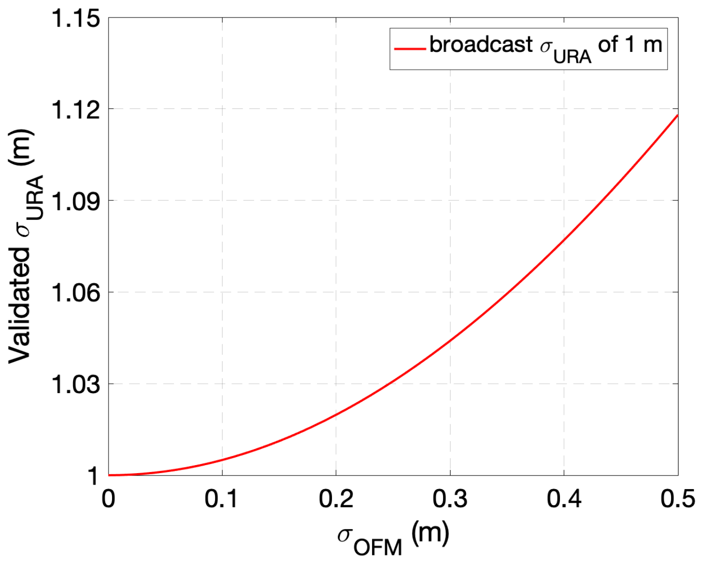

Figure 3.1. Effect of generated orbit and clock product (σ_{OFM}) on Validating (σ_{URA})

KF for all satellites and RGSs. In [29], the preliminary KF design was demonstrated and concluded that the use of a clock model has negligible effect on the accuracy of estimated orbit and clock product.

Since multiple SBAS ground networks are operational worldwide, those facilities would ideally be utilized for ARAIM OFM. Figure 3.2 shows the locations of current operational RGSs from different SBASs. In [29], it was shown that only 20 SBAS RGSs are sufficient for the proposed orbit and clock determination approach if each satellite is visible to four RGSs at all times. From a SBAS RGS, we need only dual-frequency raw code and carrier phase measurements and precise antenna location. There are other requirements, such as broadcast ephemerides and measurement error models, but those could be retrieved from an archive database.

Equations (3.2) and (3.3) below are the measurement inputs to the KF from RGS j and for Satellite Vehicle (SV) i at time epoch k. Dual-frequency raw code and

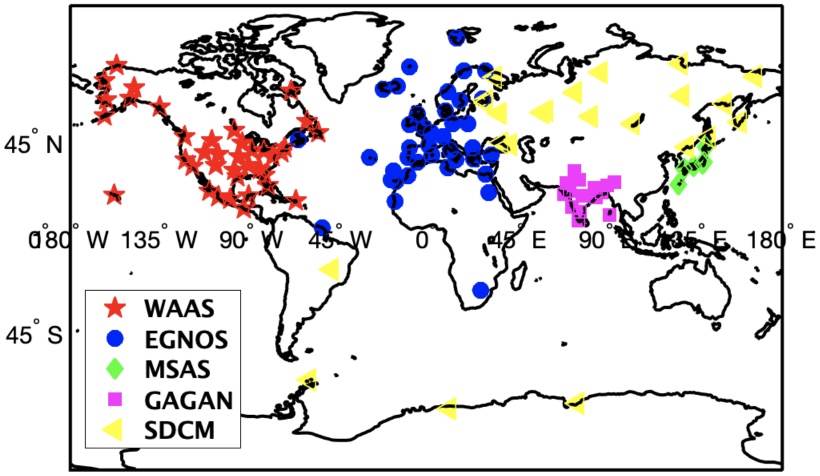

Figure 3.2. ALL existing SBAS stations

carrier phase measurements are formed into Ionospheric-Free (IF) combinations such that first order ionospheric delay, the biggest error source in the range measurements, is removed. Although GPS range measurements have additional error sources [12, Chapter 19], Equations (3.2) and (3.3) are sufficient for generating the required orbit and clock product. In the following subsection, we linearize both equations for the KF and discuss each term in detail.

$$\begin{aligned} \rho^{i,j}_{IF,k} &= \frac{f_1^2}{f_1^2-f_2^2}\rho^{i,j}_{1,k} - \frac{f_2^2}{f_1^2-f_2^2}\rho^{i,j}_{2,k} \\ &= r^{i,j}_k + c(dt^j_k - dt^i_k) + T^{i,j}_k + {}^{i,j}e^T_k(APC^j_{IF}+SET^j_k) + DCB^i_{\text{SV}} \\ &\qquad + DCB^j_{\text{RGS}} + GDV^i_{\text{SV}} + GDV^j_{\text{RGS}} \\ &\qquad + \varepsilon_{mp,\rho^{i,j}_{IF}} + \varepsilon_{th,\rho^{i,j}_{IF}} + \delta I^{i,j}_{\rho} \end{aligned} \tag{3.2}$$

where,

c, f_1, f_2	are the speed of light and the two transmission frequencies,
$\rho^{i,j}_{1,k}, \rho^{i,j}_{2,k}$	are code measurements corresponding to f_1 and f_2 frequencies for SV i and RGS j at the time epoch k,
$r^{i,j}_k$	is the true range between transmitting (SV i) and receiving (RGS j) APCs,

dt_k^i, dt_k^j	are the clock biases for SV i and RGS j,
$T_k^{i,j}$	is the tropospheric delay between SV i and RGS j,
${}^{i,j}e_k$	is line-of-sight vector from RGS j to SV i,
APC_{IF}^j	is effective receiver APC displacement vector to the IF signal for RGS j,
SET_k^j	is the Solid Earth Tide (SET) correction vector for RGS j,
DCB_{SV}^i	is the satellite dependent Differential Code group delay Bias (DCB) (constant over a day),
DCB_{RGS}^j	is the receiver dependent DCB (constant over a day),
GDV_{SV}^i	is the satellite antenna dependent code Group Delay Variation (GDV),
GDV_{RGS}^j	is the receiving antenna dependent code GDV,
$\varepsilon_{mp,\rho_{IF}^{i,j}}$	is the time correlated colored multipath on the IF code measurement for SV i and RGS j,
$\varepsilon_{th,\rho_{IF}^{i,j}}$	is the white receiver thermal noise on the IF code measurement for SV i and RGS j,
$\delta I_\rho^{i,j}$	is the higher order ionospheric residual delay on the IF code measurement for SV i and RGS j.

$$
\begin{aligned}
\phi_{IF,k}^{i,j} &= \frac{f_1^2}{f_1^2 - f_2^2}\phi_{1,k}^{i,j} - \frac{f_2^2}{f_1^2 - f_2^2}\phi_{2,k}^{i,j} \\
&= r_k^{i,j} + c(dt_k^j - dt_k^i) + T_k^{i,j} + {}^{i,j}e_k^T(APC_{IF}^j + SET_k^j) + \eta^{i,j} + PWU_k^{i,j} \\
&\qquad + \varepsilon_{mp,\phi_{IF}^{i,j}} + \varepsilon_{th,\phi_{IF}^{i,j}} + \delta I_\phi^{i,j}
\end{aligned}
\tag{3.3}
$$

where,

$\phi_{1,k}^{i,j}, \phi_{2,k}^{i,j}$	are the carrier phase measurements corresponding to f_1 and f_2 frequencies for SV i and RGS j at the time epoch k,
$\eta^{i,j}$	is the cycle ambiguity on the IF carrier signal for SV i and RGS j,
$PWU_k^{i,j}$	is the PWU on the IF carrier measurement for SV i and RGS j,

$\delta I_{\phi}^{i,j}$	is the higher order ionospheric residual delay on the IF carrier measurement for SV i and RGS j,
$\varepsilon_{mp,\phi_{IF}^{i,j}}$	is the time correlated colored multipath on the IF carrier measurement for SV i and RGS j,
$\varepsilon_{th,\phi_{IF}^{i,j}}$	is the white receiver thermal noise on the IF carrier measurement for SV i and RGS j.

3.2.1 Linear measurement model. The 15×1 vector of LNAV parameters (p_i^{orb}) is used to generate the position vector (X_k^i) of SV i at time k, as represented mathematically in Equation (3.4). The description of the non-linear vector function $\mathscr{F}^{orb}$ is provided in [45], and ν_k^{orb} represents the fidelity error of the orbital model. Since the fidelity error of the LNAV parameters ($\sigma_{\nu^{orb}}$ ~0.12 m) makes only a minor contribution to the required orbit and clock product error (σ_{OFM} ~0.5 m), the ν^{orb} term is neglected in the KF design.

$$X_k^i = \mathscr{F}_k^{orb}\left(p_i^{orb}\right) + \nu_k^{orb,i} \tag{3.4}$$

As a first step to implementing the KF, the non-linear terms in Equations (3.2), (3.3), and (3.4) are linearized. Focusing on the range term ($r_k^{i,j}$), an approximate satellite location ($X_k^{*,i}$) is determined using broadcast ephemeris ($p_i^{*,orb}$) and Equation (3.4); an approximate range term ($r_k^{*,i,j}$) is then computed as the location of RGS j is known. The range error due to approximate SV position can be written as a projection of SV position error (δX_k^i) to the line-of-sight vector (${}^{i,j}e_k$). Then, the unknown δX_k^i is transformed into an unknown set of LNAV parameters (δp_i^{orb}) through the Jacobian matrix of $\mathscr{F}_k^{orb}$. Equation (3.5) details the range term in linear form with unknown

LNAV parameter errors δp_i^{orb}.

$$\begin{aligned} r_k^{i,j} &= r_k^{*,i,j} + {}^{i,j}e_k^T \delta X_k^i \\ &= r_k^{*,i,j} + {}^{i,j}e_k^T A_{i,k}^{orb} \delta p_i^{orb} \\ &= r_k^{*,i,j} + \Psi_k^{i,j} \delta p_i^{orb} \end{aligned} \tag{3.5}$$

where, $A_{i,k}^{orb}$ is the 3×15 Jacobian matrix relating the LNAV parameters to the satellite positions. The Jacobian matrix is evaluated numerically using the Richardson extrapolation method for accurate partial derivatives [60]; Appendix A provides required inputs for computing the Jacobian matrix numerically.

$$A_{i,k}^{orb} = \begin{bmatrix} \dfrac{\partial x_{i,k}}{\partial p_1} & \cdots & \dfrac{\partial x_{i,k}}{\partial p_{15}} \\ \\ \dfrac{\partial y_{i,k}}{\partial p_1} & \cdots & \dfrac{\partial y_{i,k}}{\partial p_{15}} \\ \\ \dfrac{\partial z_{i,k}}{\partial p_1} & \cdots & \dfrac{\partial z_{i,k}}{\partial p_{15}} \end{bmatrix}_{3\times 15} ,$$

we then define the product of line-of-sight vector and Jacobian matrix as,

$$\Psi_k^{i,j} \triangleq {}^{i,j}e_k^T A_{i,k}^{orb}.$$

The satellite clock bias (dt_k^i) is the combined effect of three error sources: the actual clock drift over time, a relativistic clock correction and a hardware bias (group delay). In ARAIM OFM, we are mainly interested in the actual clock drift, which is estimated instantaneously and labeled as τ_k^i. Precise relativistic clock corrections ($dt_k^{\mathrm{RC},i}$) can be obtained through an approximate SV position and velocity, and applied at linearization. The hardware bias on the SV is a residual inter-frequency bias between code measurements, which is commonly known as the DCB [12, pp. 613-614]. The CSP provides the Total Group Delay (TGD), an effective DCB_{SV}^i, for GPS L1 frequency user relative to the L1-L2 IF combination. Since DCBs are not observable directly, we assume that effective DCB_{SV}^{i} on the IF code measurement is externally provided for orbit and clock determination. In future work, we will provide our own independently produced DCBs as suggested in [61].

$$cdt_k^i = cdt_k^{\mathrm{RC},i} + \tau_k^i + DCB_{\mathrm{SV}}^i \tag{3.6}$$

where, $dt^{\mathrm{RC},i} = -2\dfrac{X^{*,i} \cdot V^{*,i}}{c^2}$ [45], and SV position $(X^{*,i})$ and velocity $(V^{*,i})$ are computed from broadcast ephemeris $(p_i^{*,orb})$.

For the tropospheric delay term, we use the Global Pressure and Temperature 2 wet (GPT2w) model to predict slant tropospheric delay based on RGS location [62]. In [63], the accuracy of the GPT2w model is validated, and it is shown that residuals of the GPT2w model in the zenith direction can be bounded by a First Order Gauss Markov Process (FOGMP) having a standard deviation of 9 cm and a time-constant of 20 h. Thus, we include Zenith Troposheric Delay (ZTD) as RGS states $(\varepsilon_{tropo,j}^{ZTD})$ to estimate residual errors in the GPT2w modeled vertical delay.

$$T_k^{i,j} = {}^{i,j}T_k^{GPT2w} + \mathbb{M}_T \varepsilon_{tropo,j}^{ZTD} \tag{3.7}$$

where, $\mathbb{M}_T$ is a wet mapping function to convert zenith residual into slant residual [64].

Additional range errors depend on transmitting and receiving antenna characteristics, and frequency of the signal. Usually, these errors are calibrated based on the known antenna types. They are divided into APC offset and GDV. An APC, perceived at receiver's or satellite's antenna, can be different from the geometric center of the antenna. Equation (3.8) shows the effective receiver APC offset correction for IF range measurements using a receiver's APC offsets on the f_1 and f_2 frequencies. Estimated LNAV parameters will be referenced to the effective IF APC of the transmitting SV antenna. In addition, the APC varies depending on the elevation angle but the variation is limited to at most few millimeters, thus, it is neglected here.

$$APC^j_{IF} = \frac{f_1^2}{f_1^2 - f_2^2} APC^j_{f_1} - \frac{f_2^2}{f_1^2 - f_2^2} APC^j_{f_2} \tag{3.8}$$

where, APC_{f_1} and APC_{f_2} are 3×1 pre-calibrated vectors expressed in the Earth-Center Earth-Fixed (ECEF) frame. On top of APC variations, receiver antennas experience daily variations in their positions due to the gravity of the Moon and the Sun, an effect known as the SET [65]. Depending on RGS antenna location, the SET correction vector is computed for any given time as described in [65]. Now, the range errors due to RGS APC offset and the SET are evaluated by projecting the position corrections along the line-of-sight vector (${}^{i,j}e_k$) as

$$ {}^{i,j}\Delta r_k^{\text{ANT}} = {}^{i,j}e_k^T (APC^j_{IF} + SET^j_k) \tag{3.9}$$

where, ${}^{i,j}\Delta r_k^{\text{ANT}}$ is the correction to the IF code measurement applied to RGS j.

The GDV on transmitting and receiving antennas should be calibrated as discussed in [66], and its effects should be corrected at linearization. However, the calibrated GDV model is not readily available for satellites or RGSs. In [66], the contribution of an antenna dependent GDV is demonstrated for some IGS RGSs and GPS satellites to reach up to 1 m on IF code measurements. As a consequence of unavailable GDV models, IF code measurements may experience slowly varying biases which, if unmodeled, can adversely affect the carrier cycle ambiguity estimation in the KF [66]. Moreover, residual biases (decimeter-level) from the DCB exist due to signal deformations in the transmitter and receiver processing chain [67, 68]. These residual biases are usually neglected, but their effects can be significant in a network containing different receiver types [67]. Thus, to compensate for unavailable GDV models and the residual DCBs, we introduce a code bias state (b_{bias}) to acknowledge the presence of remaining uncertainty in code measurements. Section 4.3 will discuss the modeling of the code bias using experimental data, but for now, we will account for the code bias as an additional state for each SV i and RGS j pair, $b_{\text{bias}}^{ij} \sim \mathscr{N}(0, \sigma_{\text{CB}})$, where σ_{CB} is a known standard deviation from the pre-modeling.

Using Equations (3.5), (3.6), (3.7), (3.9), we linearize the IF code measurement—Equation (3.2). Since the receiver clock biases are not required for ARAIM OFM, the $c\delta t_k^j$ and DCB_{RGS}^j terms are estimated together as a single quantity β_k^j. The error contribution of higher order ionospheric delay is currently neglected as the maximum error could reach only 5 cm on a nominal day [69] (the required accuracy of orbit and clock product is 50 cm). However, in future work, it would be prudent to consider higher order ionospheric delays, which could lead to large range errors in the presence of geomagnetic storms.

$$\begin{aligned}
\delta\rho_k^{i,j} &= \rho_{IF,k}^{i,j} - r_k^{*,i,j} - cdt_k^{\text{RC}} - DCB_{\text{SV}}^i - {}^{i,j}T_k^{GPT2w} - {}^{i,j}\Delta r_k^{\text{ANT}} \\
&= \Psi_k^{i,j}\delta p_i^{orb} - \tau_k^i + \underbrace{c\delta t_k^j + DCB_{\text{RGS}}^j}_{\triangleq \beta_k^j} + b_{\text{bias}}^{i,j} + \mathbb{M}_T \varepsilon_{tropo,j}^{ZTD} + \underbrace{\delta I_\rho^{i,j}}_{\approx 0} + \varepsilon_{mp,\rho_{IF}^{i,j}} + \varepsilon_{th,\rho_{IF}^{i,j}} \\
&= \Psi_k^{i,j}\delta p_i^{orb} - \tau_k^i + \beta_k^j + b_{\text{bias}}^{i,j} + \mathbb{M}_T \varepsilon_{tropo,j}^{ZTD} + \varepsilon_{mp,\rho_{IF}^{i,j}} + \varepsilon_{th,\rho_{IF}^{i,j}}.
\end{aligned} \tag{3.10}$$

Multipath error is an elevation dependent colored noise and is typically handled through state augmentation. We represent IF code multipath as the product of an elevation dependent mapping function ($\mathbb{M}_\rho$) and a FOGMP $N_{\rho,mp}$. Subsection 4.2.1 details the code multipath error model using experimental data.

$$\varepsilon_{mp,\rho_{IF,k}^{i,j}} = \mathbb{M}_\rho^j \, N_{\rho,mp,k}^j. \tag{3.11}$$

Equation (3.12) shows the final linear IF code measurement where unknown states are listed as a column vector.

$$\begin{aligned}
\delta\rho_k^{i,j} &= \Psi_k^{i,j}\delta p_i^{orb} - \tau_k^i + \beta_k^j + b_{\text{bias}}^{i,j} + \mathbb{M}_T\varepsilon_{tropo,j}^{ZTD} + \varepsilon_{mp,\rho_{IF}^{i,j}} + \varepsilon_{th,\rho_{IF}^{i,j}} \\
&= \Psi_k^{i,j}\delta p_i^{orb} - \tau_k^i + \beta_k^j + b_{\text{bias}}^{i,j} + \mathbb{M}_T\varepsilon_{tropo,j}^{ZTD} + \mathbb{M}_\rho^j N_{\rho,mp,k}^j + \varepsilon_{th,\rho_{IF}^{i,j}} \\
&= \begin{bmatrix} \Psi_k^{i,j} & -1 & 1 & 1 & \mathbb{M}_T & \mathbb{M}_\rho^j \end{bmatrix} \begin{bmatrix} \delta p_i^{orb} \\ \tau_k^i \\ \beta_k^j \\ b_{\text{bias}}^{i,j} \\ \varepsilon_{tropo,j}^{ZTD} \\ N_{\rho,mp,k}^j \end{bmatrix} + \varepsilon_{th,\rho_{IF}^{i,j}}.
\end{aligned} \tag{3.12}$$

Similarly, the IF carrier phase measurement, Equation (3.3), is linearized as shown in Equation (3.13). The unknown float cycle ambiguity ($\eta^{i,j}$) on the IF carrier signal is estimated as an additional state. Due to the nature of circularly polarized electromagnetic waves, each carrier signal experiences additional range error on top of cycle ambiguity, which is known as the PWU [70]. The computation of PWU correction is straight-forward for a stationary RGS as described in [70]. Note that the PWU correction reaches up to a half carrier cycle during satellite eclipses, making an accurate satellite attitude model necessary [71, 72, 73].

$$
\begin{aligned}
\delta\phi_k^{i,j} &= \phi_{IF,k}^{i,j} - r_k^{*,i,j} - cdt_k^{\mathrm{RC}} - {}^{i,j}T_k^{GPT2w} - {}^{i,j}e_k^{T}(APC_{IF}^{j} + SET_k^{j}) - PWU_k^{i,j} \\
&= \Psi_k^{i,j}\delta p_i^{orb} - \tau_k^i + \beta_k^j + \eta^{i,j} + \mathbb{M}_T\varepsilon_{tropo,j}^{ZTD} + \mathbb{M}_\phi^j\, N_{\phi,mp,k}^j + \varepsilon_{th,\phi_{IF}^{i,j}} \\
&= \begin{bmatrix} \Psi_k^{i,j} & -1 & 1 & 1 & \mathbb{M}_T & \mathbb{M}_\phi^j \end{bmatrix}
\begin{bmatrix} \delta p_i^{orb} \\ \tau_k^i \\ \beta_k^j \\ \eta_{IF}^{i,j} \\ \varepsilon_{tropo,j}^{ZTD} \\ N_{\phi,mp,k}^j \end{bmatrix} + \varepsilon_{th,\phi_{IF}^{i,j}}
\end{aligned}
\tag{3.13}
$$

where,

$\mathbb{M}_\phi$	represents the elevation dependent carrier multipath mapping function,
$N_{\phi,mp}$	is the normalized IF carrier multipath noise.

Now, the linear IF code and carrier phase measurements, Equations (3.12) and (3.13), are stacked as shown in Equation (3.14) to form the input measurement vector for the KF. To describe the structure, Equation (3.14) is specifically written for 32 SVs and 25 RGSs; when an SV is not visible to an RGS, the associated rows and columns of the observation matrix need to be removed. All terms are scalar in Equation (3.14) except δp_i^{orb} (15×1 vector) and $\Psi_k^{i,j}$ (1×15 vector); the first and second superscripts represent SV and RGS indices, respectively. The state vector of the KF is grouped and identified using different colors: green for LNAV parameters, yellow for SV clock biases, gray for RGS clock biases, blue for code biases, cyan for ambiguities, orange for ZTD residuals, pink for normalized code multipath, and brown for normalized carrier multipath.

It may not be obvious at first glance in Equation (3.14) that receiver clock bias state (β_1^{clk}) of 1st RGS is not included. The reason is that satellite and receiver clock biases of a network are observable only differentially. Thus, in our implementation, we consider the first RGS clock as the reference clock ($\beta^1 = 0$), and all estimated satellite and receiver clock biases are with respect to that first RGS clock.

3.2.2 Dynamic model. The dynamics of the state vector are expressed in Equation (3.15) by stacking scalar states of the same color in Equation (3.14) as vectors. The LNAV parameters are constant throughout the filtering-window. Since SV and RGS clock biases are to be estimated instantaneously, infinite process noise is added to both clock bias vectors—this avoids the propagation of clock bias information to the next time-epoch. The code biases and float cycle ambiguities are constant for each satellite trace, but an ambiguity state will be reset if cycle slip occurs. The remaining states, residual ZTD, normalized IF code multipath, and normalized IF carrier multipath, are modeled as FOGMPs with time constants $\mu_T, \mu_\rho, \mu_\phi$ and colored standard deviations $\sigma_T, \sigma_\rho, \sigma_\phi$, respectively. The variances of driving white process noise in the FOGMP is $(1 - e^{-2\Delta T/\mu_{(\cdot)})})\sigma^2_{(\cdot)}$, where ΔT is the sample interval of the KF.

$$
\begin{bmatrix}
\delta\rho^{1,1}\\
\delta\rho^{1,2}\\
\vdots\\
\delta\rho^{1,25}\\
\delta\rho^{2,1}\\
\vdots\\
\delta\rho^{32,25}\\
\delta\phi^{1,1}\\
\vdots\\
\delta\phi^{32,25}
\end{bmatrix}_{\boldsymbol{k}}
=
\begin{bmatrix}
\boldsymbol{\Psi}^{1,1} & \cdots & & 0 & -1 & \cdots & & 0 & 0 & \cdots & 0 & 1 & \cdots & 0 & 0 & \cdots & 0 & \mathbb{M}_{\boldsymbol{T}} & \cdots & & 0 & \mathbb{M}_{\rho}^{0,1} & \cdots & 0 & 0 & \cdots & 0\\
\boldsymbol{\Psi}^{1,2} & \cdots & & 0 & -1 & \cdots & & 0 & 1 & \cdots & 0 & & & & 0 & \cdots & 0 & 0 & \mathbb{M}_{\boldsymbol{T}} & \cdots & 0 & 0 & \cdots & 0 & 0 & \cdots & 0\\
\vdots & & & \vdots & \vdots & \cdots & & \vdots & & \ddots & & & & & \vdots & & \vdots & \vdots & & \ddots & \vdots & \vdots & \ddots & \vdots & \vdots & & \vdots\\
\boldsymbol{\Psi}^{1,25} & \cdots & & 0 & -1 & \cdots & & 0 & 0 & \cdots & 1 & & \ddots & & 0 & \cdots & 0 & 0 & & & \mathbb{M}_{\boldsymbol{T}} & 0 & \cdots & \mathbb{M}_{\rho}^{0,25} & 0 & \cdots & 0\\
0 & \boldsymbol{\Psi}^{2,1} & \cdots & 0 & 0 & -1 & \cdots & 0 & 0 & \cdots & 0 & & & & 0 & \cdots & 0 & \mathbb{M}_{\boldsymbol{T}} & 0 & \cdots & 0 & \mathbb{M}_{\rho}^{0,1} & \cdots & 0 & 0 & \cdots & 0\\
& & \ddots & & & & \ddots & & & \ddots & & & & & \vdots & & \vdots & & & \ddots & & & \ddots & & \vdots & & \vdots\\
0 & \cdots & & \boldsymbol{\Psi}^{32,25} & 0 & & & -1 & 0 & \cdots & 1 & 0 & \cdots & 1 & 0 & \cdots & 0 & 0 & & & \mathbb{M}_{\boldsymbol{T}} & 0 & \cdots & \mathbb{M}_{\rho}^{0,25} & 0 & \cdots & 0\\
\boldsymbol{\Psi}^{1,1} & \cdots & & 0 & -1 & \cdots & & 0 & 0 & \cdots & 0 & 0 & \cdots & 0 & 1 & \cdots & 0 & \mathbb{M}_{\boldsymbol{T}} & \cdots & & 0 & 0 & \cdots & 0 & \mathbb{M}_{\phi}^{0,1} & \cdots & 0\\
& \ddots & & & & \ddots & & & & \ddots & & & \ddots & & & \ddots & & & \ddots & & & & \ddots & & & \ddots & \\
0 & \cdots & & \boldsymbol{\Psi}^{32,25} & 0 & \cdots & & -1 & 0 & \cdots & 1 & 0 & \cdots & 0 & 0 & \cdots & 1 & 0 & & & \mathbb{M}_{\boldsymbol{T}} & 0 & \cdots & 0 & 0 & \cdots & \mathbb{M}_{\phi}^{0,25}
\end{bmatrix}_{\boldsymbol{k}}
\begin{bmatrix}
\boldsymbol{\delta p_1^{orb}}\\
\vdots\\
\boldsymbol{\delta p_{32}^{orb}}\\
\boldsymbol{\tau_1}\\
\vdots\\
\boldsymbol{\tau_{32}}\\
\beta_2^{clk}\\
\vdots\\
\beta_{25}^{clk}\\
\boldsymbol{b}_{\text{bias}}^{1,1}\\
\vdots\\
\boldsymbol{b}_{\text{bias}}^{32,25}\\
\boldsymbol{\eta}^{1,1}\\
\vdots\\
\boldsymbol{\eta}^{32,25}\\
\varepsilon_{tropo,1}^{ZTD}\\
\vdots\\
\varepsilon_{tropo,25}^{ZTD}\\
\boldsymbol{N}_{\rho,mp}^{1,1}\\
\vdots\\
\boldsymbol{N}_{\rho,mp}^{32,25}\\
\boldsymbol{N}_{\phi,mp}^{1,1}\\
\vdots\\
\boldsymbol{N}_{\phi,mp}^{32,25}
\end{bmatrix}_{\boldsymbol{k}}
+
\begin{bmatrix}
\varepsilon_{RNM,\rho_{IF}}^{1,1}\\
\varepsilon_{RNM,\rho_{IF}}^{1,2}\\
\vdots\\
\varepsilon_{RNM,\rho_{IF}}^{1,25}\\
\varepsilon_{RNM,\rho_{IF}}^{2,1}\\
\vdots\\
\varepsilon_{RNM,\rho_{IF}}^{32,25}\\
\varepsilon_{RNM,\phi_{IF}}^{1,1}\\
\vdots\\
\varepsilon_{RNM,\phi_{IF}}^{32,25}
\end{bmatrix}
\tag{3.14}
$$

$$\begin{bmatrix} \boldsymbol{\delta p^{orb}} \\ \boldsymbol{\tau} \\ \boldsymbol{\beta^{clk}} \\ \boldsymbol{b}_{\text{bias}} \\ \boldsymbol{\eta} \\ \boldsymbol{\varepsilon^{ZTD}_{tropo}} \\ \boldsymbol{N_{\rho,mp}} \\ \boldsymbol{N_{\phi,mp}} \end{bmatrix}_{k+1} = \begin{bmatrix} \mathrm{I} & 0 & 0 & 0 & 0 & 0 & 0 & 0 \\ 0 & \mathrm{I} & 0 & 0 & 0 & 0 & 0 & 0 \\ 0 & 0 & \mathrm{I} & 0 & 0 & 0 & 0 & 0 \\ 0 & 0 & 0 & \mathrm{I} & 0 & 0 & 0 & 0 \\ 0 & 0 & 0 & 0 & \mathrm{I} & 0 & 0 & 0 \\ 0 & 0 & 0 & 0 & 0 & e^{-\Delta T/\mu_T}\,\mathrm{I} & 0 & 0 \\ 0 & 0 & 0 & 0 & 0 & 0 & e^{-\Delta T/\mu_\rho}\,\mathrm{I} & 0 \\ 0 & 0 & 0 & 0 & 0 & 0 & 0 & e^{-\Delta T/\mu_\phi}\,\mathrm{I} \end{bmatrix} \begin{bmatrix} \boldsymbol{\delta p^{orb}} \\ \boldsymbol{\tau} \\ \boldsymbol{\beta^{clk}} \\ \boldsymbol{b}_{\text{bias}} \\ \boldsymbol{\eta} \\ \boldsymbol{\varepsilon^{ZTD}_{tropo}} \\ \boldsymbol{N_{\rho,mp}} \\ \boldsymbol{N_{\phi,mp}} \end{bmatrix}_{k} + \begin{bmatrix} 0 & 0 & 0 & 0 & 0 \\ \mathrm{I} & 0 & 0 & 0 & 0 \\ 0 & \mathrm{I} & 0 & 0 & 0 \\ 0 & 0 & 0 & 0 & 0 \\ 0 & 0 & 0 & 0 & 0 \\ 0 & 0 & \mathrm{I} & 0 & 0 \\ 0 & 0 & 0 & \mathrm{I} & 0 \\ 0 & 0 & 0 & 0 & \mathrm{I} \end{bmatrix} \begin{bmatrix} \boldsymbol{\omega^{clk}_{\tau}} \\ \boldsymbol{\omega^{clk}_{\beta}} \\ \boldsymbol{\omega^{ZTD}_{tropo}} \\ \boldsymbol{\omega_{N_{\rho,mp}}} \\ \boldsymbol{\omega_{N_{\phi,mp}}} \end{bmatrix} \tag{3.15}$$

3.2.3 Information Smoother (IS). Equations (3.14) and (3.15) are sufficient to implement the KF but optimal estimates of the instantaneous clock biases will be available for only the last epoch due to infinite process noise on clock bias states. Extracting clock biases during forward filtering is suboptimal because they will be correlated with the LNAV parameter estimates, which will need data from the full filtering window for optimality. To resolve the issue, backward filtering is necessary to obtain optimal clock estimates for any time epoch k. Therefore, we implement the IS with forward- and backward information filters [52, p. 280]. The information filter form also helps to address numerical issue of assigning infinite process noise on the clock states. The initialization process is also simplified as infinite covariance is feasible through the information form; thus, no prior knowledge is required on the state vector. Except residual ZTD, code biases, and normalized multipath states, all other states are initialized without prior knowledge in each filtering-window ($S = 0$).

However, the IS does face two numerical issues. First, the observation matrix is close singular due to no prior knowledge on the eccentricity parameter; the line of apsis and argument of periapsis are undefined when eccentricity is equal to zero. The solution is straightforward by transforming the LNAV parameters to their modified equinoctial elements as discussed in [74, Appendix C]. There is only change in estimated states (no effect in IS), and the required LNAV parameters can be obtained from the estimated modified equinoctial elements. The second issue mainly depends on a processing machine and its ability to invert a large matrix accurately. The state vector of IS contains more than 1500 states and their units are not consistent. Thus, the resulting information matrix (inverse of covariance) becomes ill-conditioned. Obviously, the inverse operation would not be accurate. To address the issue, conditional number of the information matrix (S) is improved by balancing the state vector with a scaling factor. Appendix B provides the scaling factor for the equinoctial elements to improve the conditioning of the information matrix.

At the end, we obtain one set of LNAV parameters for each satellite and its clock biases at each time epoch; the other states are by-products of the error modeling and are not needed for ARAIM OFM. In the following section, we describe the process to validate the estimator output.

3.3 Validation of estimated LNAV parameters and satellite clock biases

In general, to validate an estimator, an estimated state is subtracted from the true state, assuming it is available, and the resulting estimate error is compared with the predicted error covariance. One always wishes to minimize the estimate error but actual performance is limited by input measurement quality.

In our application, the true LNAV parameters are unknown. Moreover, for ARAIM OFM to validate the broadcast range error (σ_{URA}), we are only interested in a resulting *range error* due to the estimate errors in the LNAV parameters and clock biases. Thus, we will assess the resulting range error and its covariance instead of the state estimate error directly. This section demonstrates the procedure to compute range error and covariance for SV i, whose estimated LNAV parameters ($\hat{p}_i^{orb}$) and clock biases ($\hat{\tau}_k^i$) are obtained from the IS with combined covariance matrix $\hat{\Sigma}^i_{k,p^{orb},\tau}$.

First, the covariance $\hat{\Sigma}^i_{k,p^{orb},\tau}$ is transformed to the position domain in satellite's Local Level (LL) frame:

$$\hat{\Sigma}^i_{LL,k} = \begin{bmatrix} \mathscr{R}_{LL,i,k} & 0 \\ 0 & 1 \end{bmatrix}_{4\times4} \mathscr{C}_{i,k} \begin{bmatrix} \hat{\Sigma}^i_{k,p^{orb},\tau} \end{bmatrix}_{16\times16} \mathscr{C}^T_{i,k} \begin{bmatrix} \mathscr{R}_{LL,i,k} & 0 \\ 0 & 1 \end{bmatrix}^T_{4\times4} \tag{3.16}$$

where,

$\mathscr{R}_{LL,i,k}$ is the ECEF to LL rotation matrix, and

$\mathscr{C}_{i,k}$ is defined as

$$\mathscr{C}_{i,k} = \begin{bmatrix} A_{i,k}^{orb} & 0 \\ 0 & 1 \end{bmatrix}_{4\times16} . \tag{3.17}$$

At the same time, the IGS orbit (satellite position) and clock product is utilized as truth to quantify the errors in the satellite position and clock estimates obtained from the estimated $\hat{p}_i^{orb}$ and $\hat{\tau}_k^i$. Equation (3.18) shows the mathematical representation to generate the 4×1 error vector ($\Delta E_{LL,k}^i$) for satellite position and clock bias.

$$\Delta E_{LL,k}^i = \begin{bmatrix} \mathscr{R}_{LL,i,k} & 0 \\ 0 & 1 \end{bmatrix} \begin{bmatrix} X_{k,IGS}^i - \mathscr{F}_k^{orb}(\hat{\delta p}_i^{orb}) \\ \tau_{k,IGS}^i - \hat{\tau}_k^i \end{bmatrix}_{4\times1} \tag{3.18}$$

There are multiple approaches to observe range error from satellite position error [21, 22] that are specifically used to ensure the integrity of broadcast σ_{URA}. In contrast, we are only interested in the *accuracy* of range estimates obtained from the estimated LNAV parameters and clock biases. Thus, we find the maximum covariance by projecting $\hat{\Sigma}_{LL,k}^i$ along lines-of-sight to visible Earth surface locations; we consider a location grid of 5° longitude × 5° latitude on the Earth surface. Figure 3.3 shows an example projection line from m^{th} location grid. The maximum covariance is converted to standard deviation and referred to as a predicted Signal In Space Range Error (SISRE) sigma using Equation (3.19). For the same location where maximum covariance is observed, we evaluate a range error which is the estimate SISRE for SV i—Equation (3.20).

$$\sigma_{SISRE,i,k} = \sqrt{\max_{m=1,\ldots,ALL}(G_{i,m}\hat{\Sigma}_{LL,k}^i G_{i,m}^T)} \tag{3.19}$$

$$\Delta E_{k,SISRE}^i = G_{i,n}\Delta E_{LL,k}^i \tag{3.20}$$

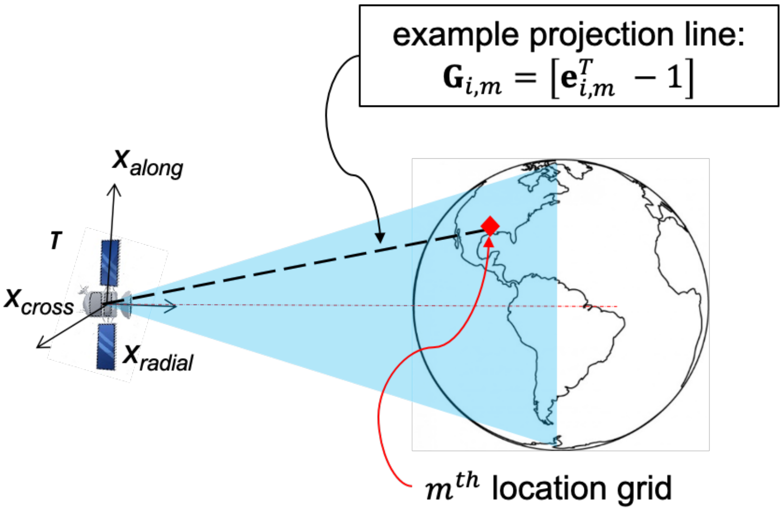

Figure 3.3. Projection of $\hat{\Sigma}^i_{LL,k}$ to the visible Earth surface

where, n is the grid location where maximum predicted σ_{SISRE} is observed.

3.4 Covariance results

This section serves two purposes: (1) as a bridge between prior analysis of [29] to experimental results of the next chapter, and (2) to expose the dependency of IS performance on measurement error models and possible approaches for improvement. Specifically, for end-users, the results of this section provide clear guidelines on which error models would need further refinement for better performance.

The covariance results, observing the predicted σ_{SISRE}, should be the first step in the implementation of IS, as real measurements are not required. Simply by using antenna location, broadcast ephemerides (for linearization), and nominal error models, one can form the observation matrix of Equations (3.14) and (3.15) to predict the σ_{SISRE}. The major advantage of this step is that any unobservable IS states due to lack of RGS diversity, or implementation bugs, can be addressed before introducing real measurements. This is an iterative process, as one can observe that different RGSs were used in [74, 75]. For a clear comparison with Chapter 4, the same 25 final RGSs are used here to illustrate expected IS performance using nominal error models (listed in Table 3.1); details about RGS locations and the used ephemerides are discussed in Section 4.1. The time period 4 to 8 h (GPS time) on January 3, 2016 is considered as an example filtering-window with a 30-s sample interval. Figure 3.4 shows the predicted σ_{SISRE} for 32 PRN (GPS satellites). The majority of σ_{SISRE} values are below 0.45 m, and the higher values (purple and yellow lines) are simply due to poorer satellite observability.

Table 3.1. Nominal GPS measurement error models

Error term	standard deviation, σ (m)	time-constant, μ (s)
IF code multipath	1.5	120
IF carrier multipath	0.03	120
Code bias	0.3	-
IF code thermal noise	0.3	-
IF carrier thermal noise	0.012	-

Obviously, the actual IS performance would be better than the 0.45-m σ_{SISRE} if real measurements are less noisy than the models in Table 3.1. To illustrate the effect of conservative error models on the IS performance, we perform sensitivity analysis in the following subsections. Finally, the last subsection discuss a possible improvement in IS performance.

3.4.1 Sensitivity to multipath error models. Multipath is highly dependent on the environment around an antenna. Depending on the application, antenna design and site location should be considered to reduce multipath effects, although this is not a scope of our development. But in case selection is not possible, for example using an existing SBAS RGS, we must predict its effect on IS performance such that appropriate actions can be taken. For the illustration of noisy multipath,

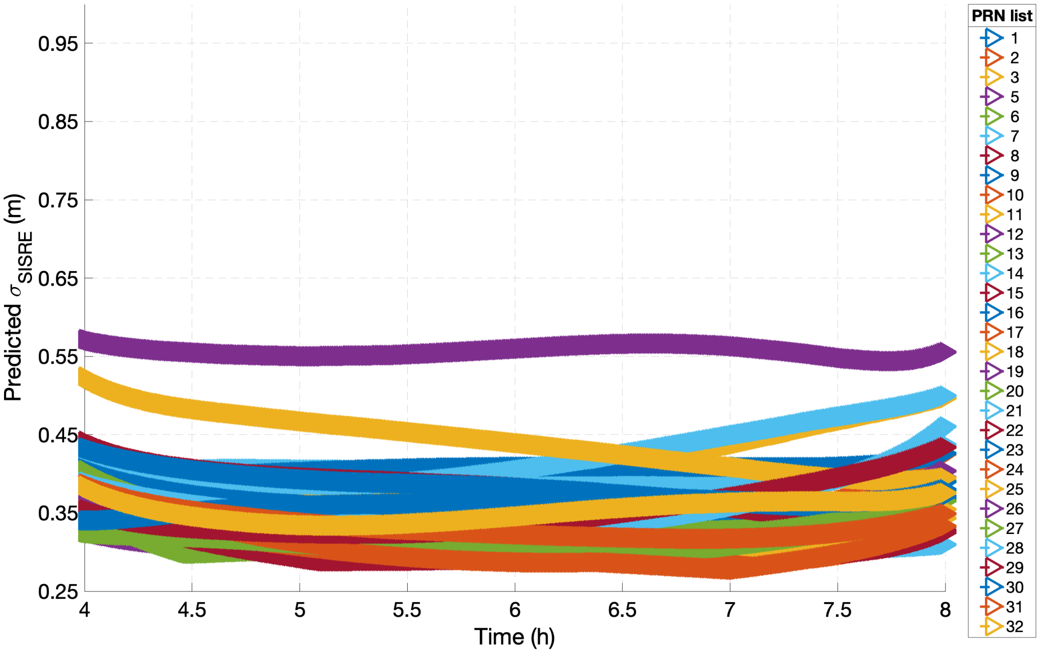

Figure 3.4. Predicted σ_{SISRE} for a worst-case location using nominal error models (Tabel 3.1)

the IF code and carrier multipath models (only σs) are inflated by a factor of three relative to the nominal values, one at a time. Figure 3.5(a) and 3.5(b) show the adverse effects of inflated multipath on IS performance compared to Figure 3.4. By the comparison, IS performance is relatively more sensitive to code multipath than carrier multipath; also, noisy code multipath causes overall increase in the σ_{SISRE} magnitude while noisy carrier multipath only leads to σ_{SISRE} variation especially at the edges. Similar sensitivity results on code and carrier thermal noise can be expected as we only inflated σ in the analysis.

3.4.2 Sensitivity to code bias model. The code bias is a result of the unavailable GDV model and signal deformation effect as discussed in Subsection 3.2.1. By considering the code bias as an additional state, we acknowledge the expected uncertainty in each code measurement. Code biases in real measurements will be observed in Section 4.3, but here we illustrate the possibility of poor performance if code biases

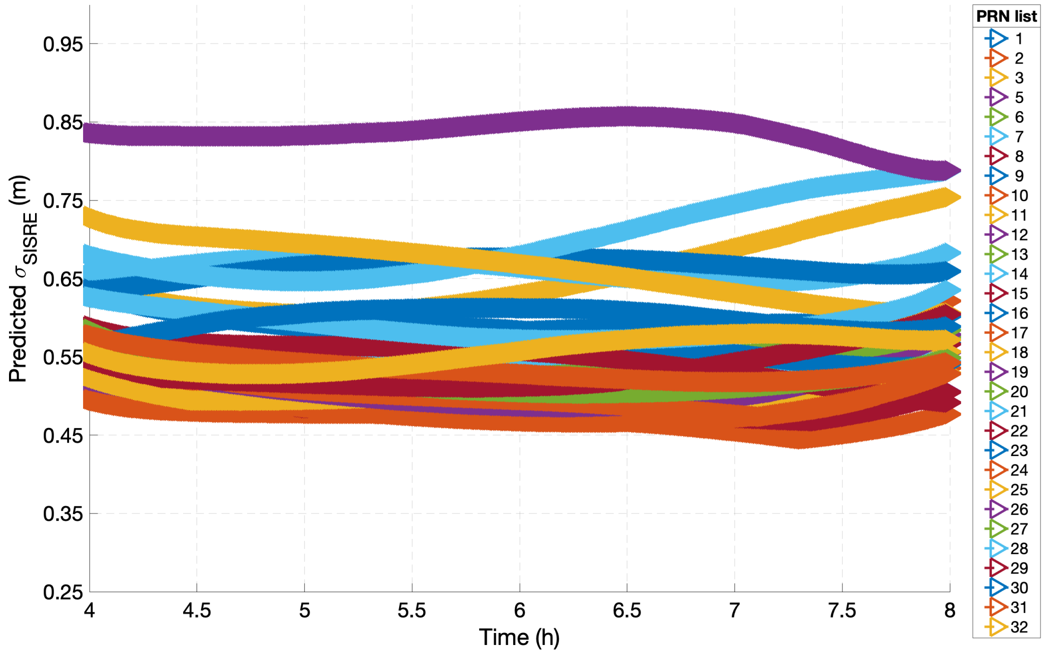

(a) Inflating IF code multipath model ($3 \times \sigma_{\rho_{IF}}$)

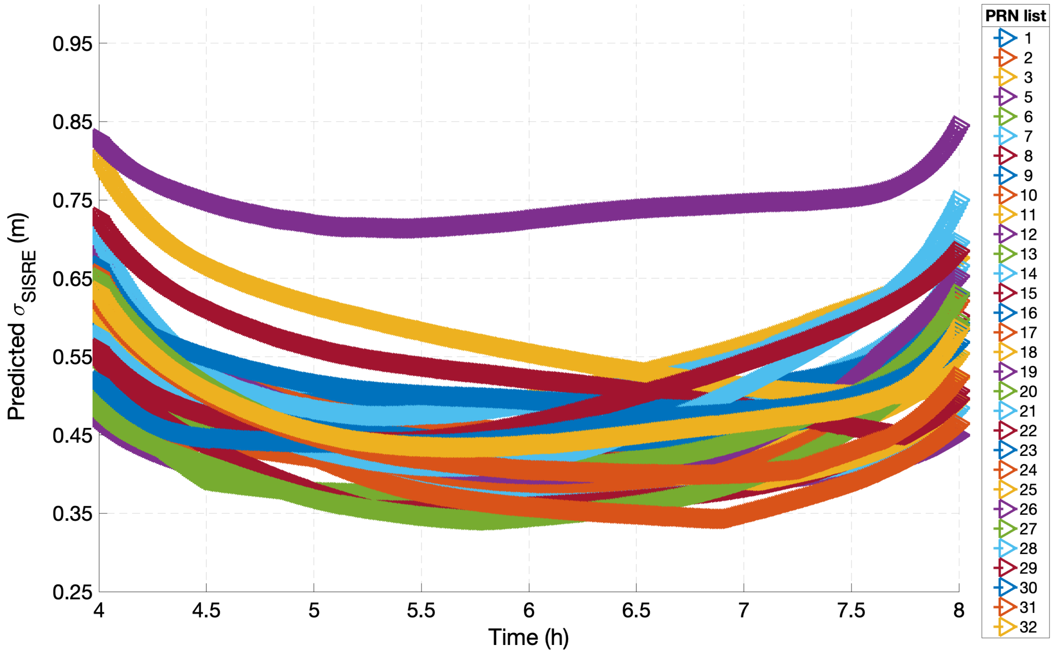

(b) Inflating IF carrier multipath model ($3 \times \sigma_{\phi_{IF}}$)

Figure 3.5. Effect of inflated multipath error model on predicted σ_{SISRE}

are significant. Figure 3.6 indicates the IS performance when the 0.3-m nominal code bias σ_{CB} is increased to 0.9 m. Large predicted σ_{SISRE}s are expected as the code measurement provides direct observability to the satellite range error. Thus, it is highly recommended to invest in the reduction of the code bias model by developing GDV models and selecting high quality receivers (to limit signal deformation effects).

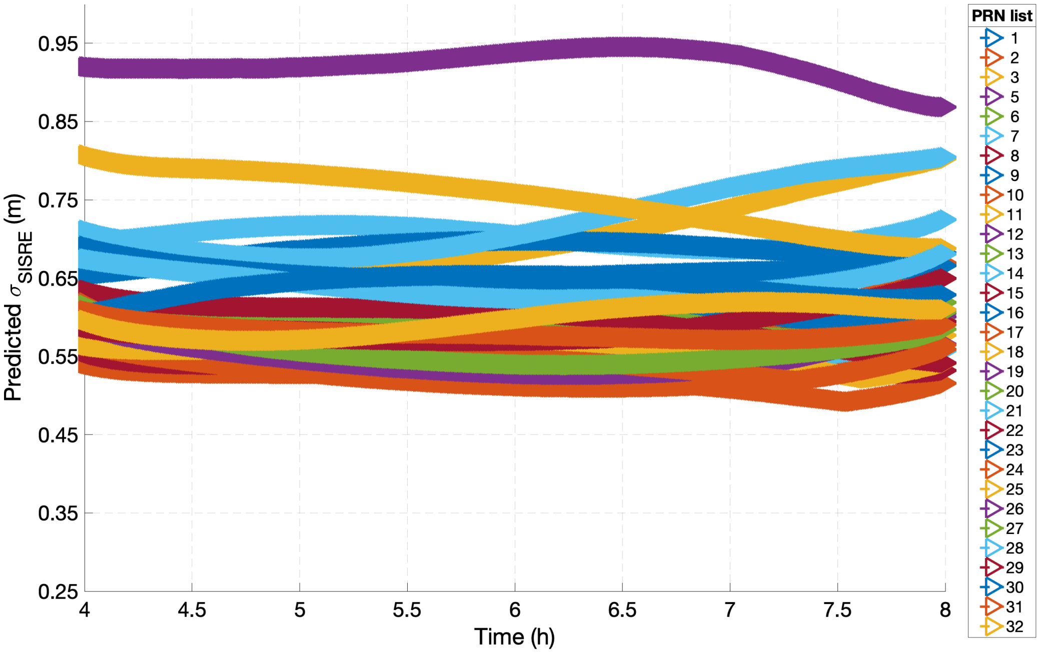

Figure 3.6. Effect of inflated code bias model ($3 \times \sigma_{CB}$) on predicted σ_{SISRE}

3.4.3 Longer length of the filtering-window. In this chapter, we have already assigned 4-h duration for the filtering-window while estimating LNAV parameters due to its fidelity errors. Further increase in the filtering-window is not possible with LNAV parameters, but the Civil NAVigation message (CNAV) parameters have such potential; the details about CNAV parameters are available in [45]. In [29], the fidelity errors of CNAV parameters were shown to be bounded by a 2-cm standard deviation for 4-h filtering window. Since CNAV parameters have better accuracy, increasing 4-h filtering-window is possible. Figure 3.7(a) and 3.7(b) show CNAV model fidelity errors for filtering windows of 4 h and 6 h, respectively. The large fidelity errors at both end edges are expected due to boundary effects. By observing the small errors ($\sigma \leq 20$ cm) during the middle two hours, we consider 6-h filtering window to estimate CNAV parameters and satellite clock bias. Figure 3.8 shows the comparison between the 4-h LNAV filtering-window and a 6-h CNAV filtering-window. In both Figures 3.8(a) and 3.8(b), we consider worst case error models, represented by $3 \times \sigma$ on nominal error models, to demonstrate the advantage of CNAV parameters in the worst case. Overall, the predicted σ_{SISRE} with CNAV parameters are approximately 20% lower than the LNAV σ_{SISRE}. The takeaway is that CNAV parameters will help in σ_{SISRE} reduction, but better error modeling, especially for code biases, is still necessary.

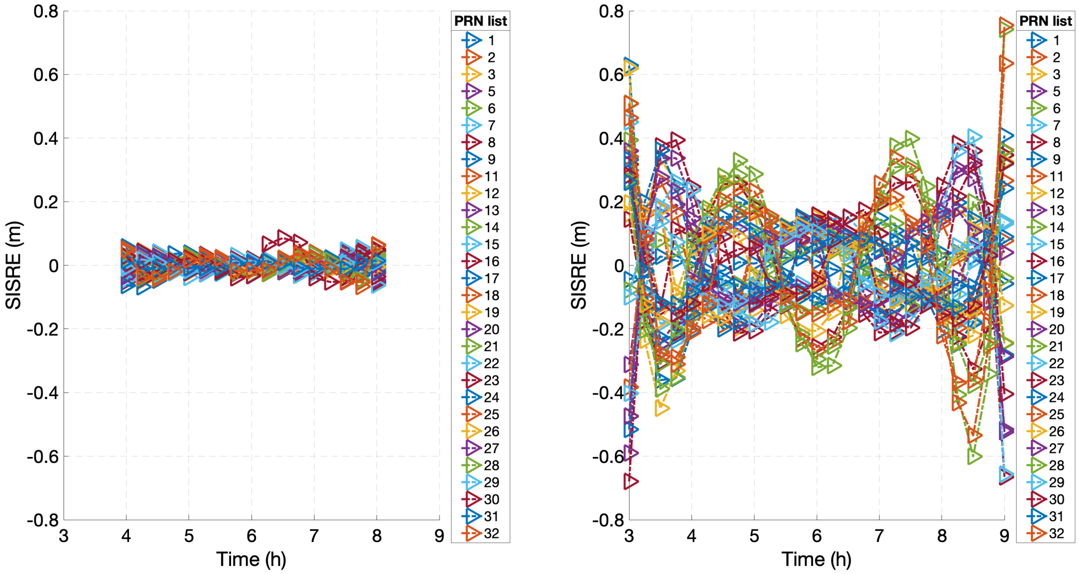

(a) 4-h filtering-window

(b) 6-h filtering-window

Figure 3.7. Fidelity errors of the CNAV parameters

To sum up, this chapter discussed an Information Smoother (IS) designed to estimate satellite position in terms of LNAV parameters and instantaneous satellite

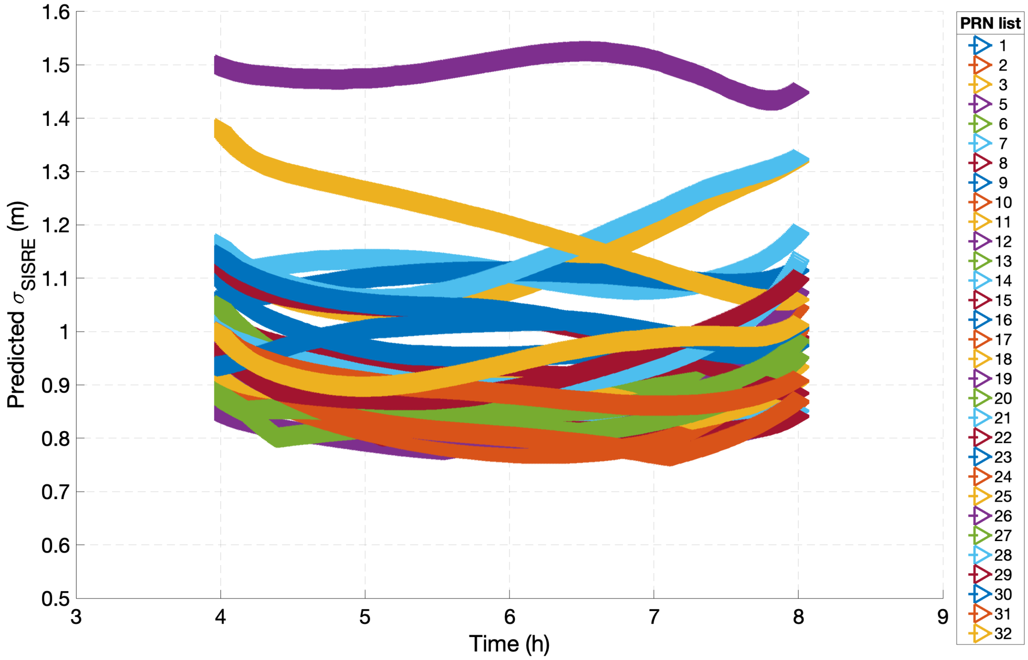

(a) Predicted σ_{SISRE} with 4-h filtering-window and LNAV parameters

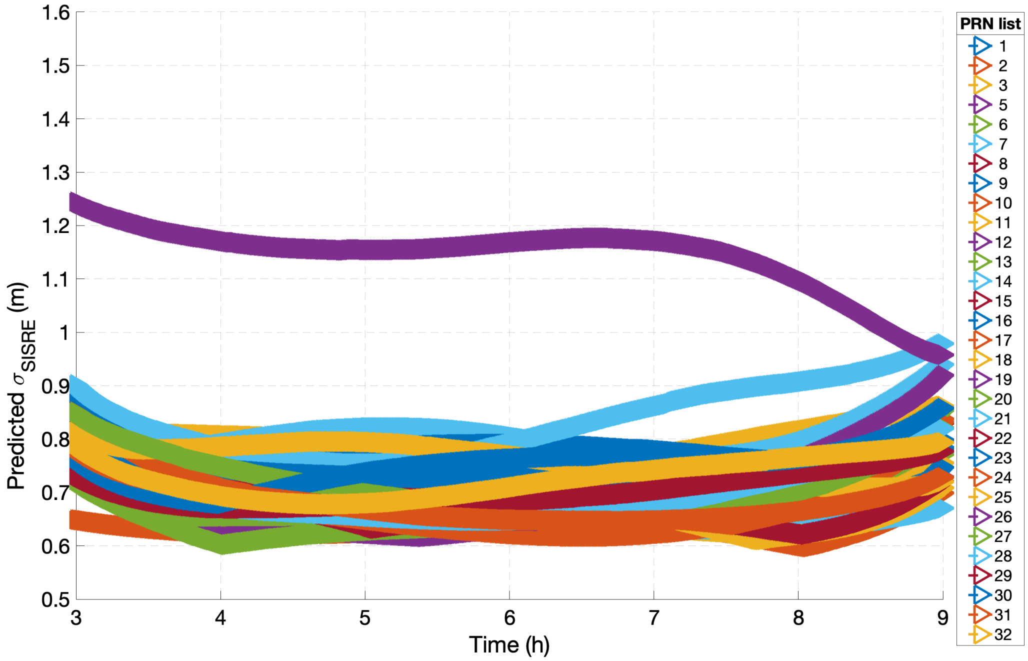

(b) Predicted σ_{SISRE} with 6-h filtering-window and CNAV parameters

Figure 3.8. Effect of longer filtering-window while assuming worst error models ($3\times\sigma$)

clock biases. Since the resulting range errors from the IS are the most important for ARAIM OFM, the necessary validation steps on resulting error are outlined. At the end, the performance of estimated LNAV parameters and satellite clock biases is illustrated through covariance results (σ_{SISRE}) using nominal multipath error and code bias models.

CHAPTER 4

GPS ORBIT AND CLOCK ESTIMATION USING EXPERIMENTAL DATA

This chapter builds a prototype on the previous chapter's concept to provide an independent satellite orbit and clock product. The GPS constellation is used as an example to collect dual-frequency range measurements, develop measurement error models, and estimate satellite orbits and clock biases using the IS. In the future, we expect to implement the concept on other GNSS constellations for ARAIM OFM; this chapter serves as a blueprint.

Keeping future application to other constellations in mind, the four sections of this chapter describe general implementation steps. The first section concerns ground network selection and how to check measurement quality from each RGS. The second and third sections describe how to independently develop error models from raw code and carrier phase measurements. Lastly, the fourth section shows GPS orbit and clock estimates and estimate errors over 10 days[2].

4.1 Background on experimental dataset

Currently, raw code and carrier phase measurements are not publicly accessible from all SBAS networks (Figure 3.2). Therefore, we use the IGS ground network as a surrogate in these experiments. The necessary inputs from each IGS RGS are available through the archive repository at the Crustal Dynamic Data Information System (CDDIS) [76]. First, dual-frequency raw GPS code and carrier phase measurements are retrieved in the Receiver Independent Exchange Format (RINEX) 2.11

---

[2] ©2023 IEEE. Reprinted, with permission, from J. Patel, “Accurate GPS LNAV parameters and clock biases for ARAIM offline monitoring", *IEEE Transactions on Aerospace and Electronic Systems*, Aug 2023. [59].

[76]. Publicly, only single-frequency GPS L1 C/A code measurements are available, but geodesy-grade IGS receivers utilize different processing strategies to extract semi-codeless measurement from the military-purpose-reserve GPS L2 P(Y) code; in the near future, GPS and other constellations will transmit dual-frequency civil signals from all satellites. Second, the antenna location of each IGS RGS is available in the SINEX format [77]. Third, broadcast GPS ephemerides for linearization are retrieved from [76]. Lastly, the calibrated APC offsets and the DCBs are obtained from the IGS [77, 78].

The IGS ground network consists of more than 300 RGSs worldwide. But only a subset of approximately 25 RGSs is sufficient for our orbit and clock estimation. The major issue with IGS RGSs is that they are operated by different independent analysis centers. Thus, huge variations in measurement quality exist due to different antenna/receiver quality and/or poor antenna site location. The selection criteria for an IGS RGS are provided in Appendix C resulting in the selection of the 25 IGS RGSs are shown in Figure 4.1. The receiver clock at the “STK2" RGS is considered as the reference clock and highlighted as blue star in Figure 4.1.

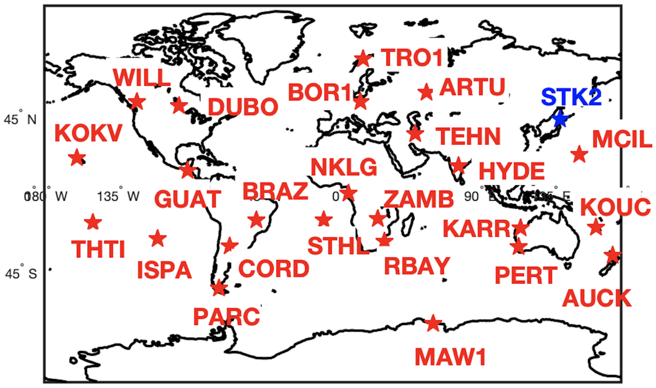

Figure 4.1. The 25 selected IGS stations for prototyping

Once raw code and carrier measurements are available from RINEX, we assign a cutoff value on recorded carrier to noise (C/N_0) and elevation angle for a coarse quality check. In the RINEX 2.11 file, GPS code measurements are labeled as “C1" (C/A code) and “P2" (semi-codeless or cross-correlated), which are modulated on “L1" and “L2" carrier waves, respectively. The L1 signal strength is consistently above a 30 dBHz threshold for almost all stations. However, the L2 signal strength varies considerably, sometimes reaching as low as 10 dBHz. If a threshold on L2 signal is assigned as high as the L1 threshold, the number of usable satellites would be significantly reduced making clock bias states unobservable for instantaneous clock estimation. Therefore, 15 dBHz is assigned as the L2 threshold, but measurements between 15 to 30 dBHz are utilized with significantly increased thermal noise. Increased standard deviations on IF code- and carrier thermal noise are 0.6 m (from 0.3 m) and 0.24 m (from 0.012 m), respectively (a factor of 20 is used for carrier thermal noise to deweight any unexpected outlier). An elevation-angle cutoff of 10 deg is used to limit adverse multipath effects; elevation cutoffs are increased to 20 deg when C/N_0 information is unavailable in RINEX (Tables 4.1 and 4.2).

We consider ten days (3, 4, 5, and 17-23) of January 2016 in our experiments. We confirm the absence of geomagnetic storms and any GPS satellite maneuvers such that our assumptions on higher order ionospheric delay and constant LNAV parameters are valid during the filtering-windows [79, 80, 81]. January 20 and 21, 2016 have minor C-class solar flares during which we are unable to track carrier signals, but the performance of estimated orbit and clock product is still within the requirement.

Table 4.1. Summary of error models with elevation cut-off for 1 to 12 RS

	IGS RS ID	Elevation cut-off (deg)	Normalized code multipath		Normalized carrier multipath		Code bias
			$\sigma_{N_{\rho,IF}}$ (unitless)	$\mu_{N_{\rho,IF}}$ (s)	$\sigma_{N_{\phi,L1mL2}}$ (unitless)	$\mu_{N_{\phi,L1mL2}}$ (s)	σ_{CB} (m)
1	STK2	10	2.4	40	3.2	70	0.5
2	BRAZ	15	2.2	110	6	60	0.55
3	KOUC	10	2.33	35	5	120	0.65
4	TEHN	20	2.33	25	5	120	0.3
5	BOR1	15	2.3	30	5	120	0.65
6	KARR	10	2.6	40	3	60	0.35
7	RBAY	10	2.2	30	3.2	120	0.65
8	TRO1	10	22	35	4.5	120	0.5
9	WILL	10	2	5	4.5	60	0.2
10	MCIL	10	2.3	30	3.0	120	0.6
11	NKLG	10	2.0	30	2.5	90	0.75
12	MAW1	15	2.1	120	3.8	60	0.35

Table 4.2. Summary of error models with elevation cut-off for 13 to 25 RS

	IGS RS ID	Elevation cut-off (deg)	Normalized code multipath $\sigma_{N_{\rho,IF}}$ (unitless)	$\mu_{N_{\rho,IF}}$ (s)	Normalized carrier multipath $\sigma_{N_{\phi,L1mL2}}$ (unitless)	$\mu_{N_{\phi,L1mL2}}$ (s)	Code bias σ_{CB} (m)
13	PARC	10	2	45	3.5	120	0.45
14	ARTU	20	2.2	15	4.5	120	0.375
15	STHL	10	1.9	22	4.5	120	0.25
16	ISPA	10	2	5	4.2	120	0.3
17	HYDE	20	2.2	600	4. 3	120	0.25
18	AUCK	10	1.85	30	4	120	0.3
19	KOKV	10	2.0	5	4	120	0.75
20	GUAT	10	2.1	90	5.6	60	0.3
21	PERT	10	2	20	3	60	0.4
22	DUBO	10	1.9	15	4	60	0.25
23	THTI	10	1.8	15	4	60	0.45
24	ZAMB	10	3	30	4	120	0.3
25	CORD	10	2.1	10	4.2	120	0.25

4.2 Developing multipath error models

In the following two subsections, we develop a multipath error model by processing raw GPS code and carrier phase measurements on January 3, 2016. The proposed methods can be applied to any application as they only require raw range measurements—no need for knowledge of receiver or antenna type.

4.2.1 Code multipath model. Since IF code measurements are utilized in the IS, we directly observe and model IF code multipath instead of code multipath on the individual frequencies. We utilize a well-known Code Minus Carrier (CMC) technique to observe IF code multipath by subtracting Equation (3.3) from (3.2), which eliminates all error sources, and only float ambiguity and IF code multipath are left. The residual of IF CMC contains thermal noise, GDV, and carrier multipath, but their magnitudes are significantly lower than IF code multipath. The float ambiguity on IF CMC is removed by removing the mean of the data—satellites visible less than 30 min are ignored to ensure accurate ambiguity removal. Thus, the residual of IF CMC is treated as the IF code multipath, which will be modeled here. Figure 4.2 shows IF code multipath for example “KOKV" RGS over a 24-h duration at a sample interval of 30 s. The same IF code multipath is shown in Figure 4.3 to observe elevation dependency.

Earlier in Equation (3.11), we introduced a mapping function ($\mathbb{M}_{\rho,IF}$) to capture the elevation dependent variations in standard deviation and a normalized FOGMP IF code multipath model to capture temporal behavior. For the former, the error standard deviations in different elevation-bins (10-15, 15-20, ...) degrees are evaluated and plotted as the blue line in Figure 4.3 using a 3rd order polynomial curve—the mapping function $\mathbb{M}_{\rho,IF}$. For the latter, Figure 4.4, is obtained by normalizing the error using the mapping function $\mathbb{M}_{\rho,IF}$. To develop the FOGMP model, we utilize a recently-developed technique which bounds errors in the frequency domain through the Power Spectral Density (PSD) [82]. The authors of [82] prove that bounding the PSD of an error process is sufficient to capture the overall time-correlation and standard deviation. Using Welch's method, the PSD of normalized code multipath is computed and plotted in Figure 4.5 for multiple PRN (satellite) traces. PSDs from all PRNs are bounded by the red PSD in Figure 4.5 which represents the FOGMP with a time-constant of 5 s and a standard deviation of 2 (unitless). Similarly, IF code multipath is evaluated for the other 24 RGSs to obtain site-dependent mapping functions $\mathbb{M}^{j}_{\rho,IF}$ and FOGMP models. Figure 4.6 shows $\mathbb{M}_{\rho,IF}$ for 25 RGSs, and Tables 4.1 and 4.2 provide the FOGMP model parameters.

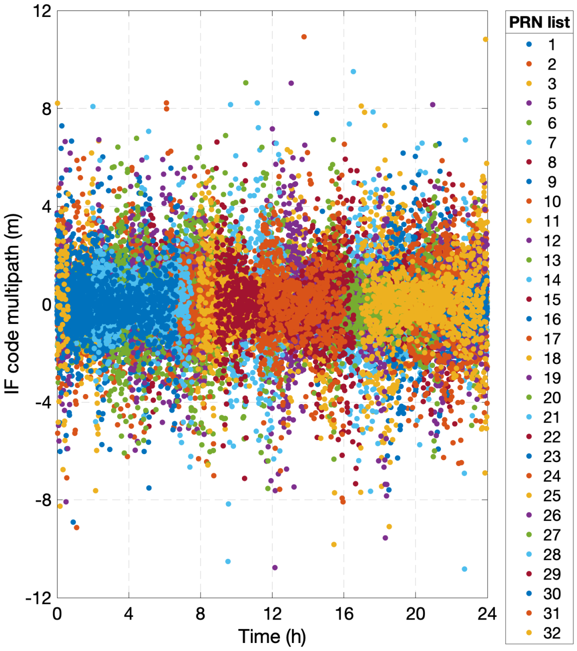

Figure 4.2. IF code multipath for “KOKV" RGS on January 3, 2016

4.2.2 Carrier multipath model. Similar to IF code multipath above, we would like to obtain IF carrier multipath models, but unfortunately existing methods to observe carrier multipath are not suitable for our application. For example, double-difference approaches are inapplicable because only a single antenna is at each RGS.

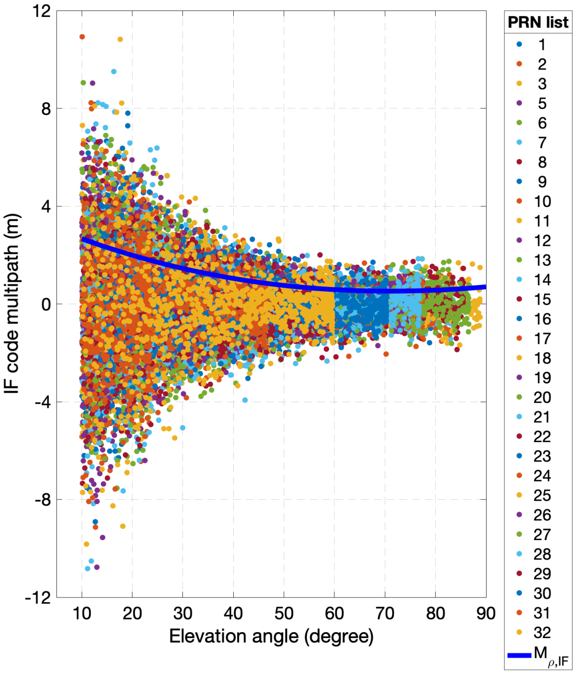

Figure 4.3. IF code residual as a function of elevation angle

Figure 4.4. Normalized IF code multipath using mapping function ($\mathbb{M}_{\rho,IF}$)

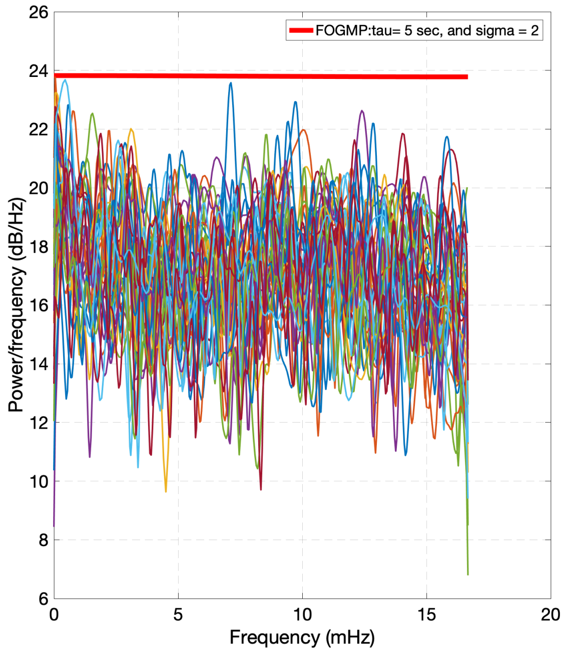

Figure 4.5. Estimated PSD of normalized code multipath at “KOKV" RGS; the red PSD represents the over-bounding FOGMP

Another possible method is to extract carrier multipath from C/N_0 [83]. However, some IGS RGSs do not provide C/N_0 values in the RINEX file. Therefore, we develop a new method to observe carrier multipath. Although the new method is not able to provide absolute carrier multipath, it does enable a way to observe and model the effect of carrier multipath on different RGSs.

Appendix D provides a detailed explanation and validation of the new method to observe carrier multipath. In simple words, we utilize dual frequency carrier measurements to observe differential carrier multipath. In our case, GPS L2 carrier signal is subtracted from GPS L1 carrier signal, removing the majority of range errors, leaving us with ionospheric delay, cycle ambiguity, and differential carrier multipath. A high-pass filter is employed to extract differential carrier multipath from L1 minus L2 (L1mL2) carrier measurements; ionospheric delay and cycle ambiguity are removed being low frequency components. Through the experimental validation, we confirm

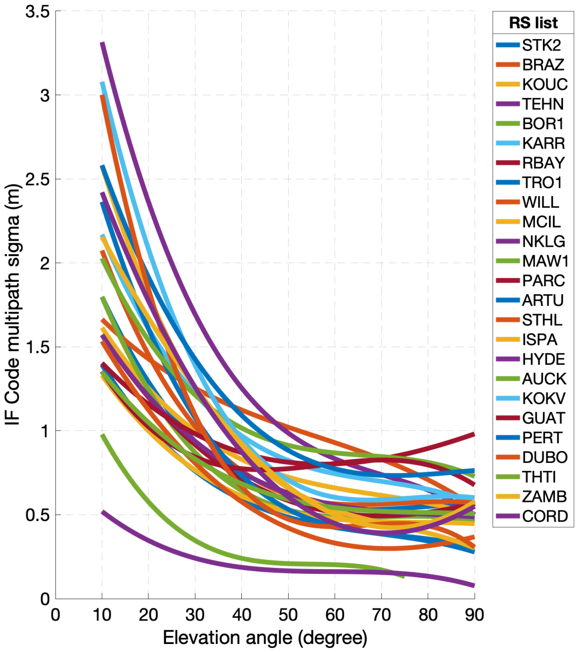

Figure 4.6. Mapping functions ($\mathbb{M}^j_{\rho,IF}$) for the 25 RGSs

that a cut-off frequency of 1.66 mHz (10 min) is sufficient for the high-pass filter (Appendix D). Using the method, differential carrier multipath is evaluated for "KOKV" RGS on January 3, 2016 and shown in Figures 4.7 and 4.8. The observed large multipath around 12 h corresponds to a temporary local effect, likely phase scintillation, which is common at low- and high-latitudes.

Similar to IF code multipath, differential carrier multipath depends on the elevation angle, and we capture variations in the standard deviation through a mapping function ($\mathbb{M}_{\phi,L1mL2}$) and the temporal behavior through a normalized FOGMP carrier multipath model ($N_{\phi,L1mL2}$). The mapping function $\mathbb{M}_{\phi,L1mL2}$ for "KOKV" RGS is shown as the blue line in Figure 4.8—fit to a 3rd order polynomial curve. Then, the normalized differential carrier multipath is obtained as shown in Figure 4.9. The PSD bounding method discussed earlier is applied to the normalized differential carrier multipath to obtain the FOGMP model. Figure 4.10 illustrates the PSD of normalized differential carrier multipath for different PRNs, which are bounded by the FOGMP with a standard deviation of 4 (unitless) and a time-constant of 120 s.

Since IF carrier measurements are utilized in the IS, we need to scale the differential multipath model to IF carrier multipath. Equation (4.1) describes the relation between IF carrier multipath to differential carrier multipath—assuming L1 and L2 carrier signal experience i.i.d. multipath. Figure 4.11 shows the effective mapping function $\mathbb{M}_{\phi,IF}$ for the 25 RGSs; two high latitude ("MAW1" and "TRO1") and one low latitude ("BRAZ") RGSs experience expected nominal ionospheric scintillation for a few hours of a day that ultimately causes larger mapping functions. Tables 4.1 and 4.2 provide FOGMP model parameters to bound normalized differential carrier multipath.

$$\begin{aligned}
\varepsilon_{\phi_{IF},mp} &= \sqrt{\frac{f_{L1}^2}{f_{L1}^2 - f_{L2}^2} + \frac{f_{L2}^2}{f_{L1}^2 - f_{L2}^2}}\ \varepsilon_{\phi_{L1},mp} \\
&= \sqrt{\frac{f_{L1}^2}{f_{L1}^2 - f_{L2}^2} + \frac{f_{L2}^2}{f_{L1}^2 - f_{L2}^2}}\ \frac{\varepsilon_{\phi_{L1mL1},mp}}{\sqrt{2}} \\
&= \sqrt{\frac{f_{L1}^2}{f_{L1}^2 - f_{L2}^2} + \frac{f_{L2}^2}{f_{L1}^2 - f_{L2}^2}}\ \frac{\mathbb{M}_{\phi,L1mL1}}{\sqrt{2}}\ N_{\phi_{L1mL2},mp} \\
&= \mathbb{M}_{\phi,IF}\ N_{\phi_{L1mL2},mp}
\end{aligned} \tag{4.1}$$

where $\mathbb{M}_{\phi,IF}$ is the effective mapping function for IF carrier multipath.

4.3 Developing a code bias model

All GNSS code measurements experience the effects of signal deformation at the transmitting and receiving ends of the signal processing chain resulting in nominal biases [67, 68]. The traditional approach is to separate these biases into purely satellite-dependent and purely receiver-dependent parts—DCB_{SV} and DCB_{RGS}. The DCB_{SV} and DCB_{RGS} corrections remove the majority of signal deformation bias, but decimeter-level residuals exists in each code measurement due to different combinations of receiver front-end bandwidth and employed filters. Usually, these residual

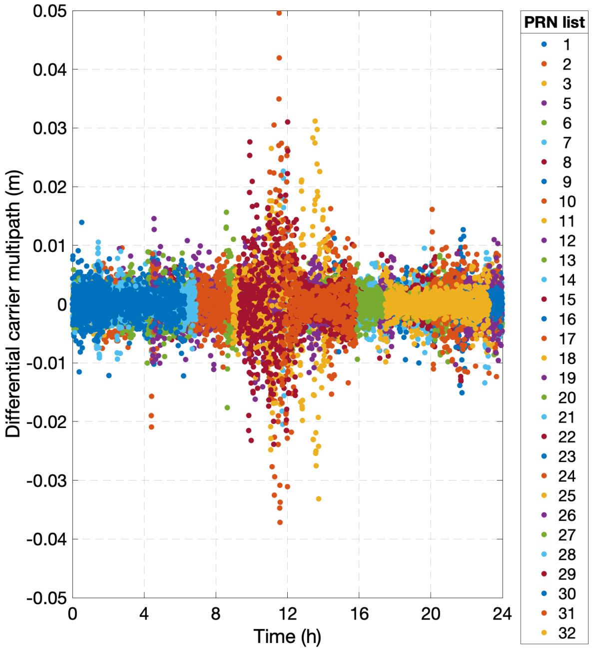

Figure 4.7. Differential carrier multipath at “KOKV" RGS on January 3, 2016

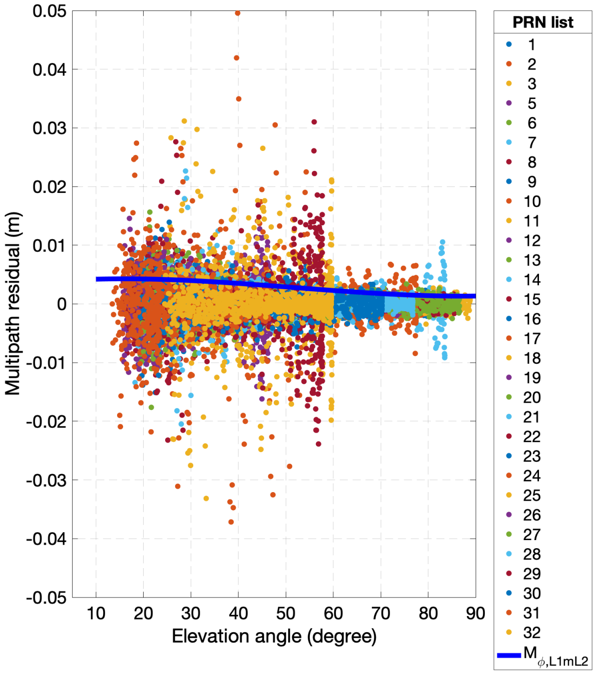

Figure 4.8. Differential carrier multipath as a function of elevation angle

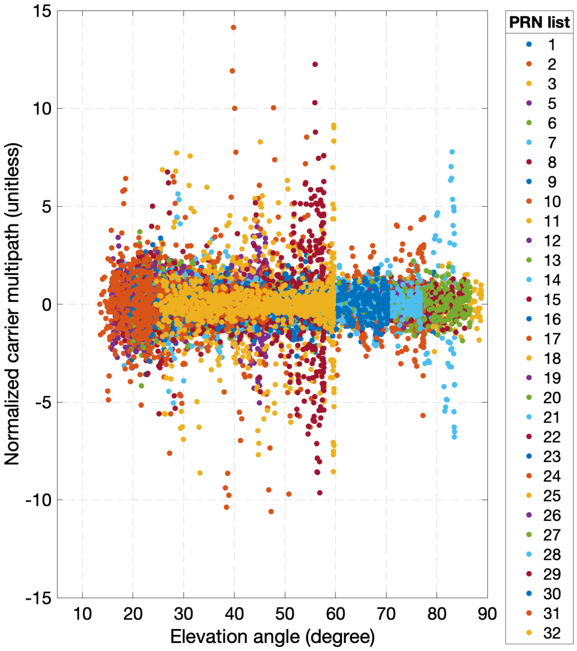

Figure 4.9. Normalized differential carrier multipath (N_{L1mL2}) on January 3, 2016

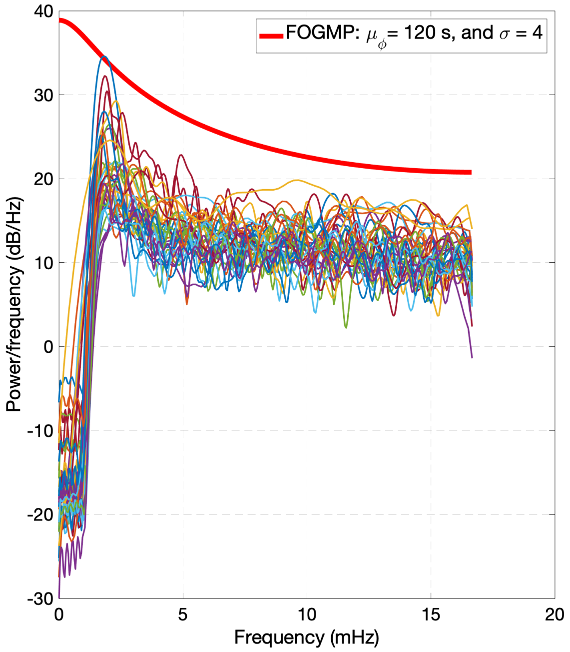

Figure 4.10. Estimated PSD of normalized differential multipath at “KOKV" RGS; the red PSD represents the over-bounding FOGMP

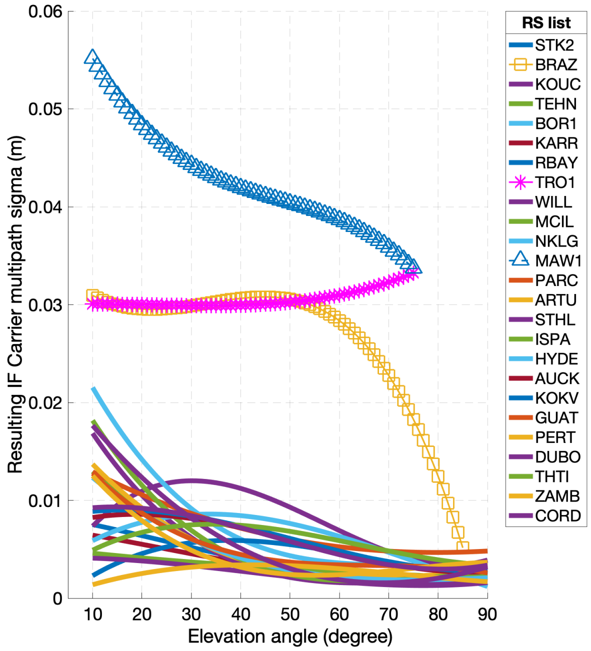

Figure 4.11. Mapping functions ($\mathrm{M}^{j}_{\phi,IF}$) for the 25 RGSs

biases are ignored as code multipath has larger magnitude and dominates them. However, residual biases may reach up to the meter level when different receiver types are employed in the same application [67]. Ultimately, in our application, carrier cycle ambiguity estimation is degraded due to these unexpected large residuals leading to biased orbit and clock estimates. Similarly, the unmodelled GDV discussed in Subsection 3.2.1 may appear as slowly varying biases and affect ambiguity resolution [66].Therefore, in this section, we directly observe effective biases in IF code measurements with aim to model them for the 25 RGSs.

To see code biases, we compute a residual in the IF code measurement (Equation (3.2)) by leveraging different IGS products. The IF code residual is evaluated specifically using the available IGS receiver clock bias, IGS DCB, IGS ZTD, IGS station location, and the GPS orbit and clock products [84, 78, 85, 77]. The first line in Equation (4.2) shows the mathematical expression to compute the IF code residual, and the second line indicates remaining errors in it (Appendix E provides the detailed equations to utilize IGS products). The receiver-side DCB is not available for the majority of IGS RGSs, thus, the IF code residual contains both DCB_{RGS} and code bias which is the combined effect of slowly varying biases due to GDV and residuals from the satellite- and receiver-dependent DCB separation. But, the important fact is that DCB_{RGS} must be same for all PRNs, and therefore, code biases are observed by focusing on variations of means in IF code residuals between different PRNs and days. The contribution of higher order ionospheric delay (∼5 cm) is neglected in this analysis as geomagnetic storms are absent on the selected days.

$$\begin{aligned} \text{IF Code residual} &= \rho^i_{IF,j} - r^i_j - T^i_j - c(\delta t_j - \delta t^i) - DCB^i_{\text{SV}} \\ &= \delta I^i_j + DCB^j_{\text{RGS}} + GDV^i_{\text{SV}} + GDV^j_{\text{RGS}} + \varepsilon_{mp,\rho^{i,j}_{IF}} + \varepsilon_{th,\rho^{i,j}_{IF}} \end{aligned} \tag{4.2}$$

Figure 4.12 shows the computed IF code residuals for example “ZAMB" RGS over January 3, 2016 with a sample rate of 300 s; the IGS receiver clock bias product being available at 300-s intervals prohibits faster rates. The IF code residuals below 15° elevation are neglected in this analysis to avoid large multipath. At first glance, Figure 4.12 seems normal with zero mean and typical multipath, but to see the remaining code biases, PRN 19 and 25 are extracted and plotted separately in Figure 4.13(a). If we focus on the individual satellite traces, PRN 19 has a clear bias while on PRN 25 seems to have a negligible bias. This unexpected behavior is demonstrated in [67] through a controlled experimental setup. To better understand the behavior of the code bias over long duration, we show the IF code residual for the next day in Figure 4.13(b). Clearly, the code biases are not the same for either PRN 19 and 25 on the next day (variation of biases in decimeters). One may argue that the IGS products are not accurate and cause a bias, but if so, the bias must be similar at all IGS RGSs. Figure 4.14 shows the same PRNs over another “HOB2" RGS where the IF code residual is continuously drifting over time for all PRNs—this clearly indicates the dependency on receiver type. To limit our investigation on receiver types for now, an IGS RGS is used in the prototype only if its IF code residual is approximately constant. The histogram of the code biases (means of IF code residuals) for “ZAMB" RGS is shown in Figure 4.15(a) for all SV traces on January 3, 2016, which are randomly distributed over -0.6 to 0.4 m. Histograms of the code bias are then generated over multiple days, Figures 4.15(b), 4.15(c), 4.15(d), and we notice that code biases fall into approximately the same ranges (-0.6 m to 0.4 m) over two weeks. Thus, the range of these code biases are deemed to be constant for “ZAMB" RGS. This preliminary analysis on code biases only conclude that its range depends on a given RGS receiver, and further investigation will be carried out in the future. In summary, we assign $\sigma_{\text{CB}}^{\text{ZAMB}}$ to be 0.3 m to predict uncertainty in IF code measurements at “ZAMB" RGS. Similar investigation is carried out for other 24 RGSs to develop σ_{CB} model, and Tables 4.1 and 4.2 provide the details.

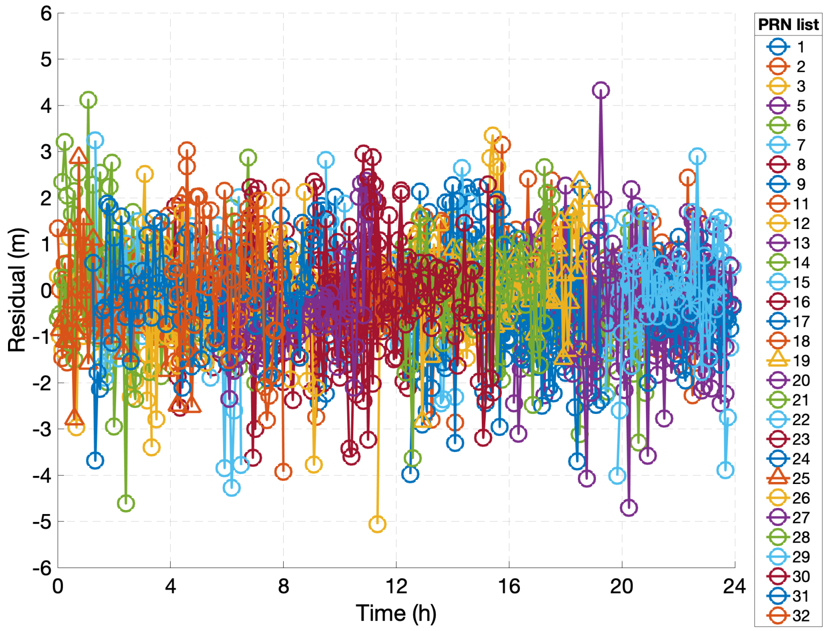

Figure 4.12. IF code residual for all PRNs at “ZAMB" RGS on January 3, 2016

4.4 Quantifying the errors of estimated GPS orbits and clock biases

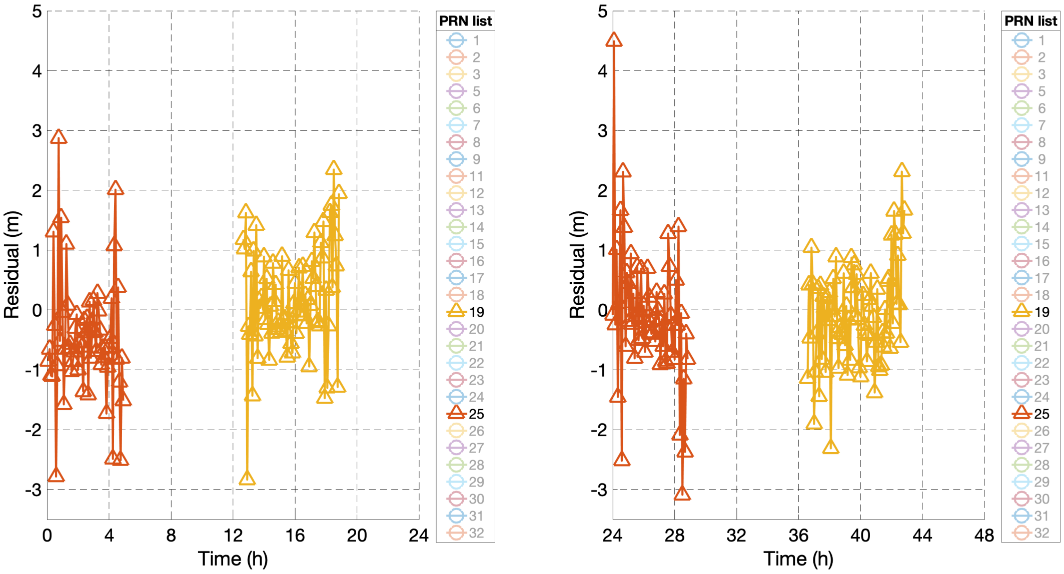

(a) January 3, 2016

(b) January 4, 2016

Figure 4.13. IF code residual for PRN 19 and 25 traces at “ZAMB" RGS

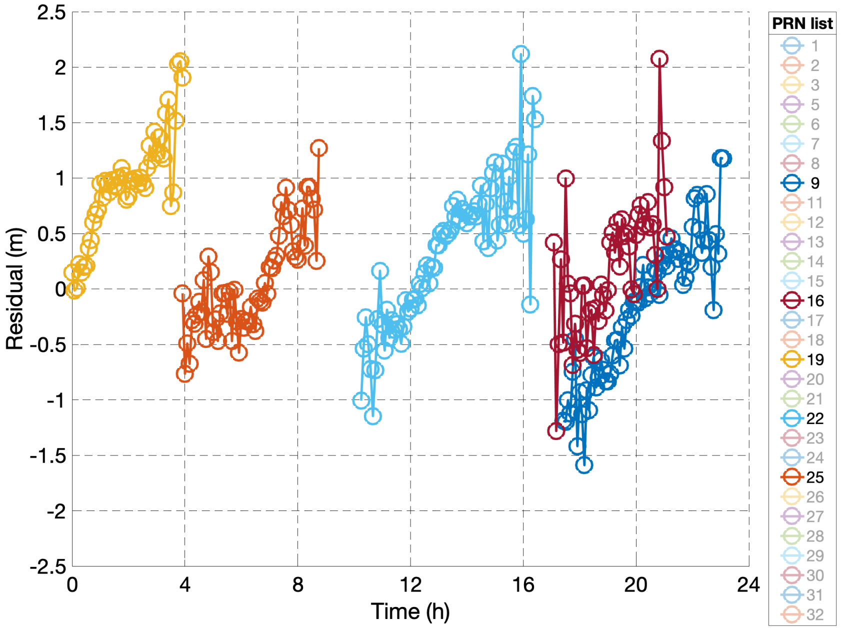

Figure 4.14. IF code residual for “HOB2" RGS on January 3, 2016

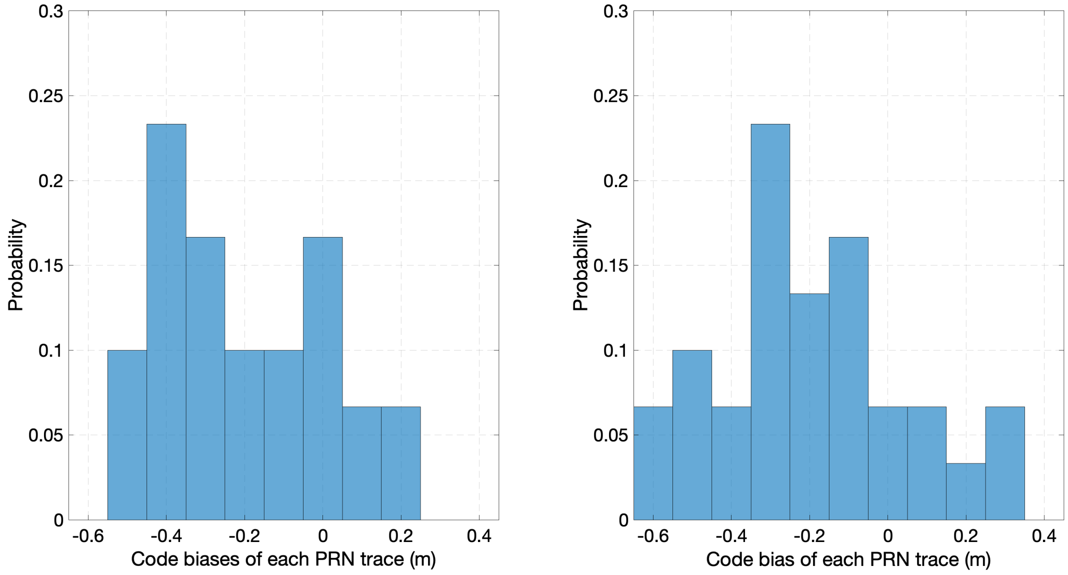

(a) January 3, 2016

(b) January 4, 2016

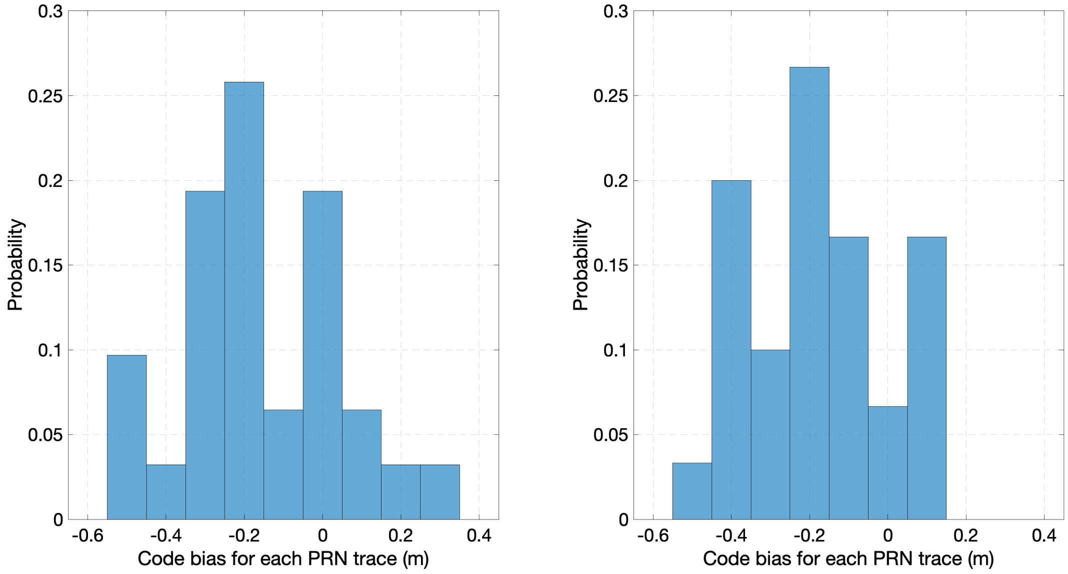

(c) January 5, 2016

(d) January 18, 2016

Figure 4.15. Histogram of the code bias for “ZAMB" RGS

This section discusses the performance of the LNAV orbit parameter and clock bias estimator. A time period 4 to 8 h (GPS time) on January 3, 2016 is first considered as an example filtering-window. The IS (Subsection 3.2.3) is executed with the error models (Sections 4.2, 4.3) to obtain one set of constant LNAV parameters and a series of instantaneous clock biases for each satellite. As discussed in Section 3.3 (validation), the resulting satellite position errors from the estimated LNAV parameters are computed by comparing to the IGS precise orbit product. Although the IS is implemented at a sample rate of 30 s (the available GPS measurement rate), the resulting errors will be displayed, in figures, at each 900 s simply to avoid interpolation of the IGS orbit product. Figures 4.16 and 4.17 show the resulting along- and cross-track errors in the satellite LL frame; thick continuous lines are also plotted for the satellites with maximum and minimum predicted standard deviations. The majority of along- and cross-track errors are within ($\pm 1\sigma$) bounds; the reason behind some of outliers will be discussed later after computing SISRE. Radial error in satellite position is inversely related to the satellite clock bias error, thus to account for their correlation, Radial Plus Clock bias (RPC) errors are displayed. Figure 4.18 shows the RPC errors for all GPS PRNs with $\pm 1\sigma$ bounds. Finally, as discussed in Section 3.3, the estimate SISRE and the predicted σ_{SISRE} are evaluated to illustrate the resulting maximum values. Figure 4.19 is the end result where the estimate SISRE is shown with the ± 1 predicted σ_{SISRE} bounds. Figure 4.20 shows the predicted σ_{SISRE} for all PRNs.

The outliers in Figures 4.16,4.17,4.18,4.19 may emerge from three sources. First, the fidelity error of the LNAV parameters is neglected in the IS. Although the fidelity error is much lower than the predicted σ_{SISRE}, the estimated LNAV parameters would have errors even if the IS output were perfect. Figure 4.21 provides the result of LNAV parameters' fidelity analysis, similar to [29] and in range domain, for the same 4 to 8 h time-window. Considering the fidelity analysis [29], the estimated

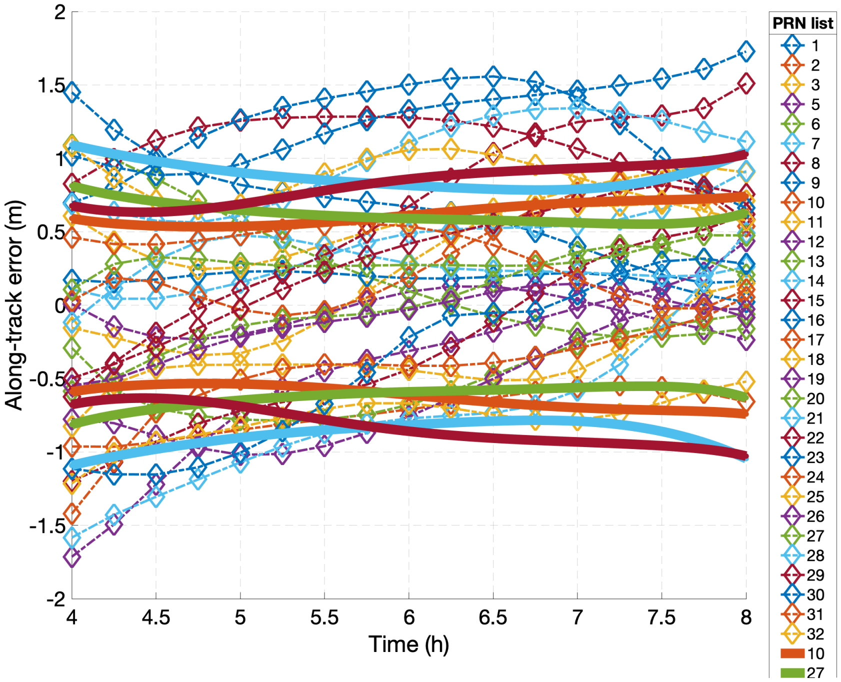

Figure 4.16. Resulting along-track error from 4 to 8 h filtering-window on January 3, 2016

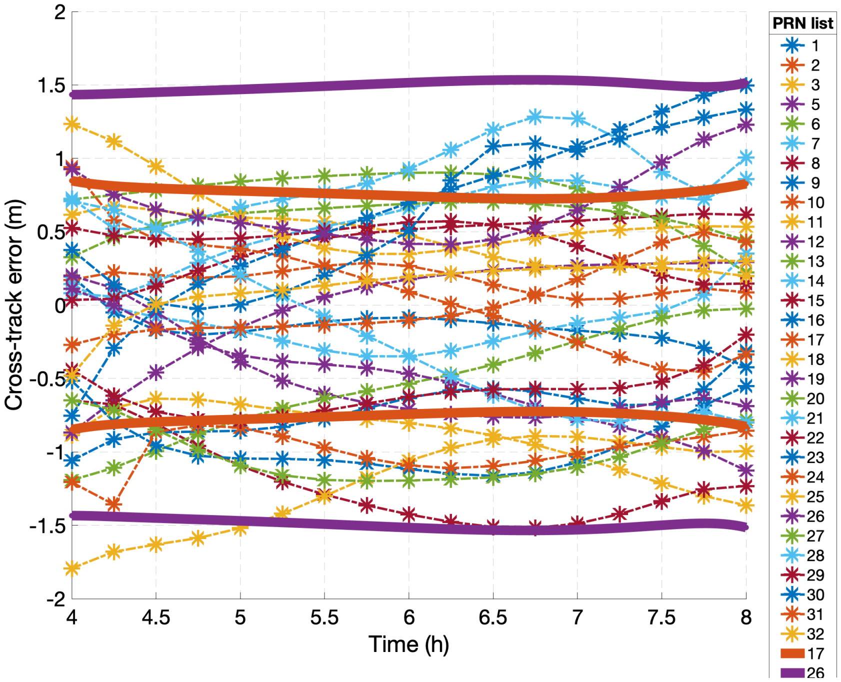

Figure 4.17. Resulting cross-track error from 4 to 8 h filtering-window on January 3, 2016

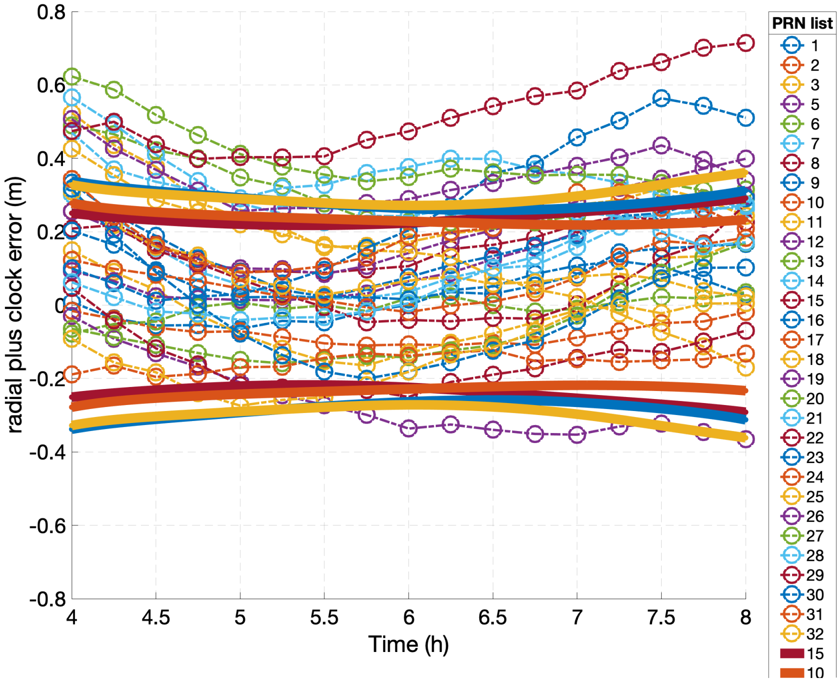

Figure 4.18. Resulting radial plus clock bias error from 4 to 8 h filtering-window on January 3, 2016

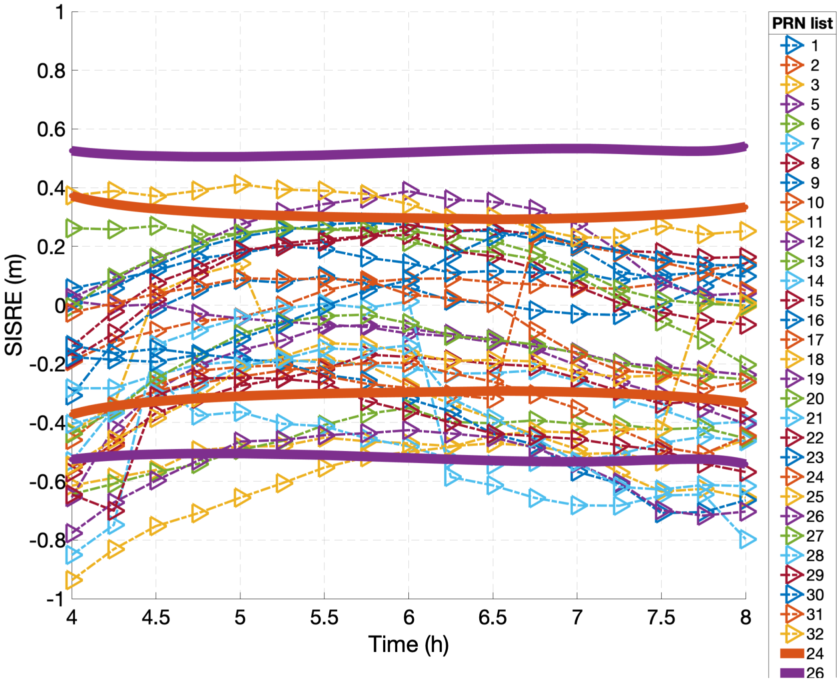

Figure 4.19. The estimate SISRE from 4 to 8 h filtering-window on January 3, 2016

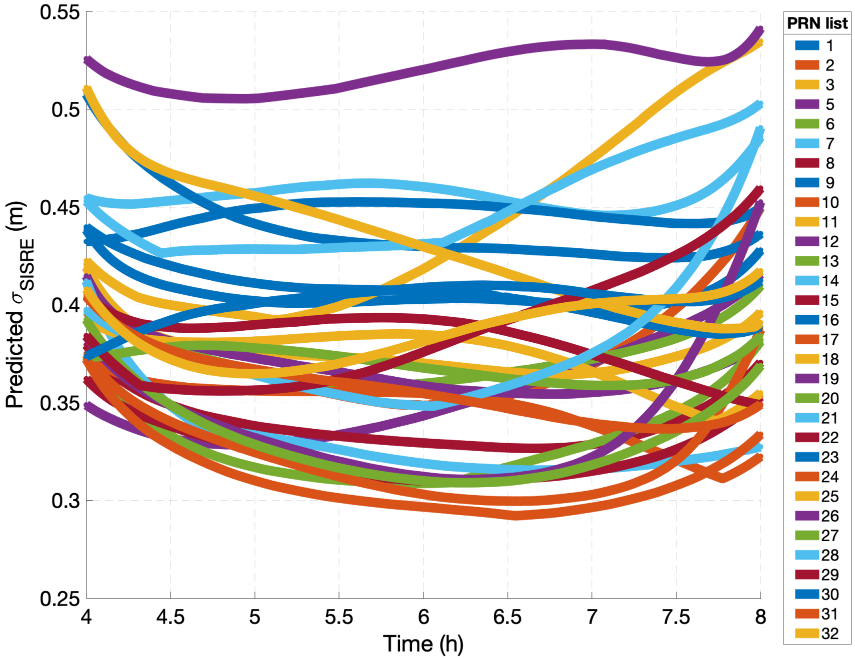

Figure 4.20. Predicted σ_{SISRE} for worst-case location grid from 4 to 8 h filtering-window on January 3, 2016

LNAV parameters are acceptable only for central two-hour period in ARAIM OFM. Second, the precision of the IGS clock product is lower than the IGS orbit product. Figure 4.22 shows a comparison of the IGS product with the corresponding NGA clock product; the NGA product is referenced to the broadcast APC so the necessary transformations are applied to the IGS product [86, 87, 88]. The resulting RPC errors have non-zero mean and cause a bias in the estimate SISRE simply due to inaccurate truth clock bias. Unfortunately, it is not possible to remove the bias because it may be partly or even largely due to biases in the NGA comparison product. The comparison of IGS and NGA satellite position errors is not shown explicitly here but they differ by less than 5 cm. Third, the code bias model developed in Section 4.3 might need refinement. Further investigation on code bias by receiver types may be helpful to enhance the performance.

Having extracted accurate LNAV parameters and SV clock biases for the cen-

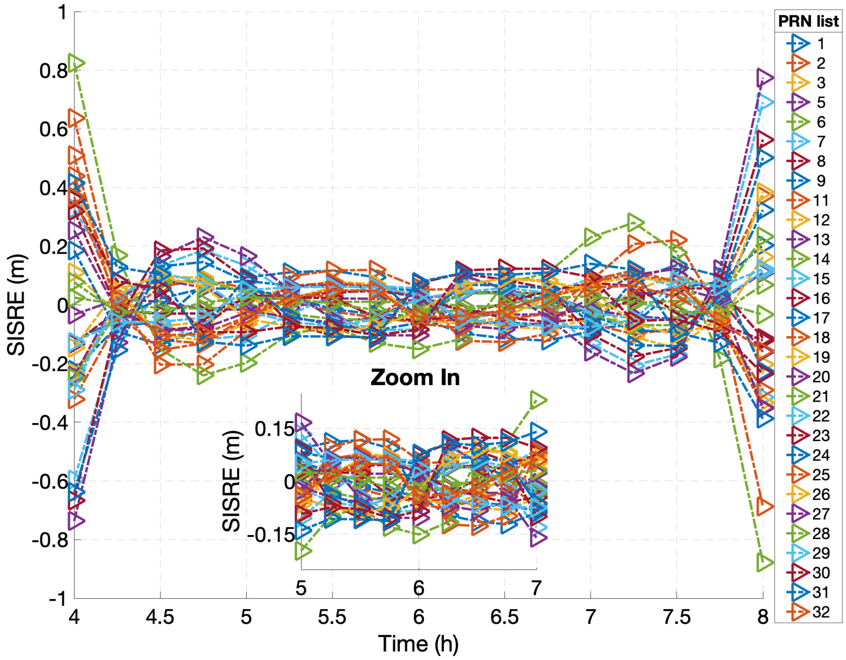

Figure 4.21. Resulting SISREs from fidelity analysis; fitting LNAV parameters to the truth IGS orbit product

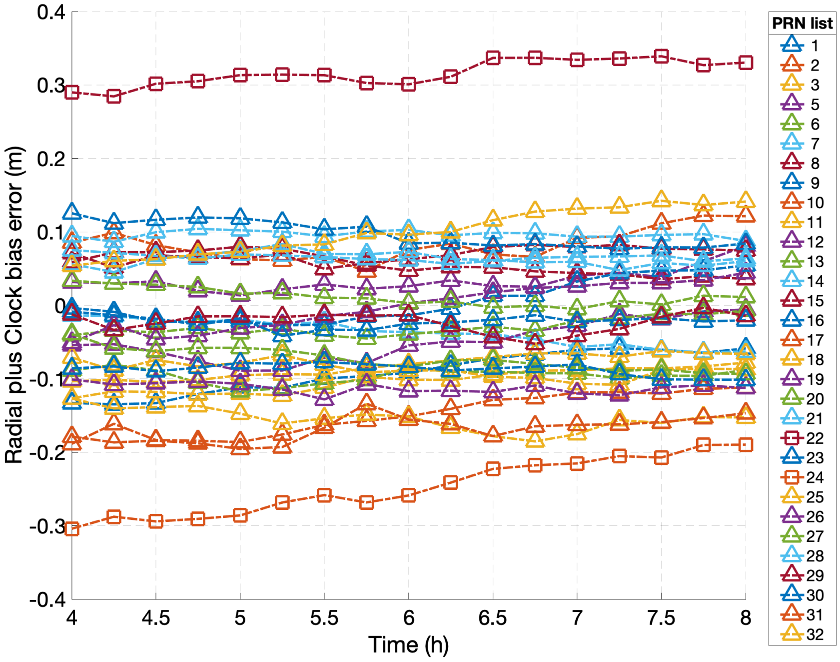

Figure 4.22. Radial plus clock bias error by comparing the IGS and NGA products

tral two hours of the 4-8 h filtering-window, we move the window to another time period, for example, 6-10 h to obtain another set of LNAV parameters and SV clock biases for 7-9 h. Similarly, multiple filtering-windows are employed to achieve sets of LNAV parameters and SV clock biases for the entire day of January 3, 2016, and continuous estimate SISREs are displayed in Figure 4.23 with predicted maximum σ_{SISRE} bounds. Overall, the estimate SISREs are largely within $\pm 1\sigma$ bound and never exceed $\pm 2\sigma$ throughout the day; Figure 4.24 shows the predicted σ_{SISRE} over the same day. Consistency of estimator performance is demonstrated by processing an additional nine days (4, 5, and 17 to 23) in January 2016. Figures 4.25 and 4.26 show the estimate SISREs with $\pm 1\sigma$ bounds for January 4-5 and 17-23 (full GPS week), respectively. The resulting range errors from the estimated LNAV parameters and SV clock biases are accurate up to $\sim$50 cm sigma, and their consistent performance will enable independent ARAIM OFM design.

To sum up, this chapter provides detailed insight to build a prototype for GPS orbit and clock estimation. Using experimental data, the required error models are developed from raw GPS measurements for all selected IGS RGSs. Finally, an estimate error from the estimated LNAV parameters and clock biases is evaluated in satellite position and range domains. Although the current IS has some limitations, SISRE estimate 1-σ accuracy of less than 50 cm is currently achievable.

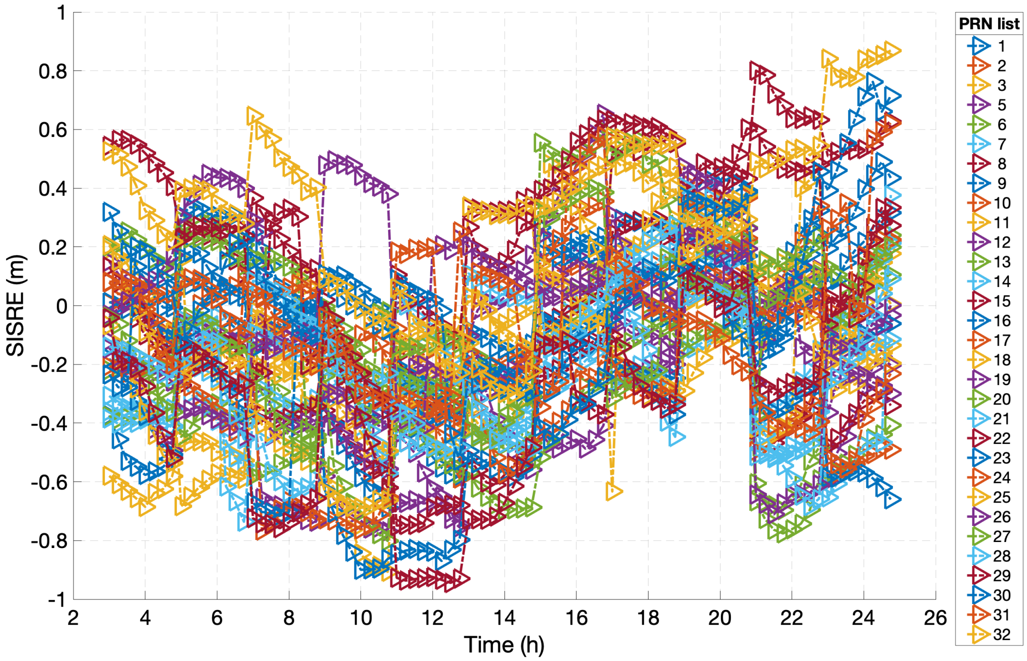

Figure 4.23. Estimate SISREs over January 3, 2016

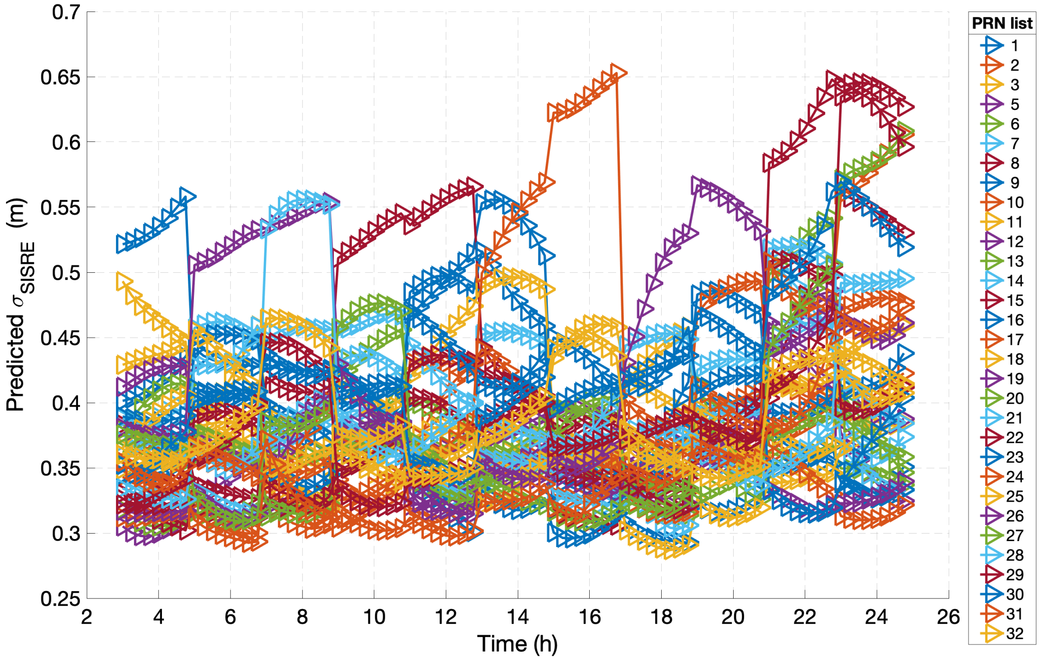

Figure 4.24. Predicted σ_{SISRE} over January 3, 2016

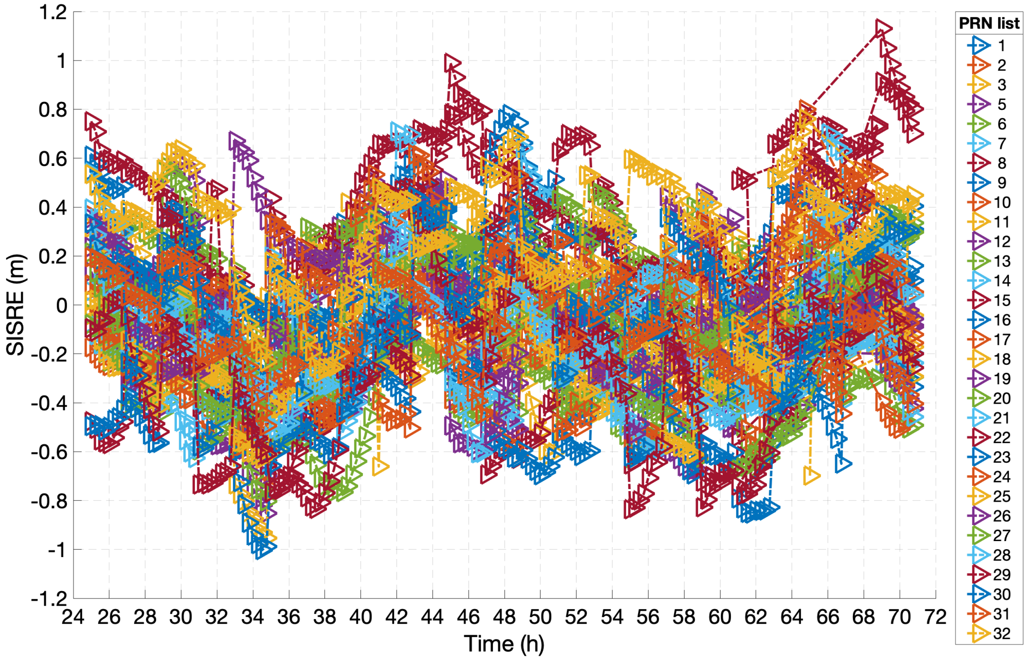

Figure 4.25. Estimate SISREs over January 4-5, 2016

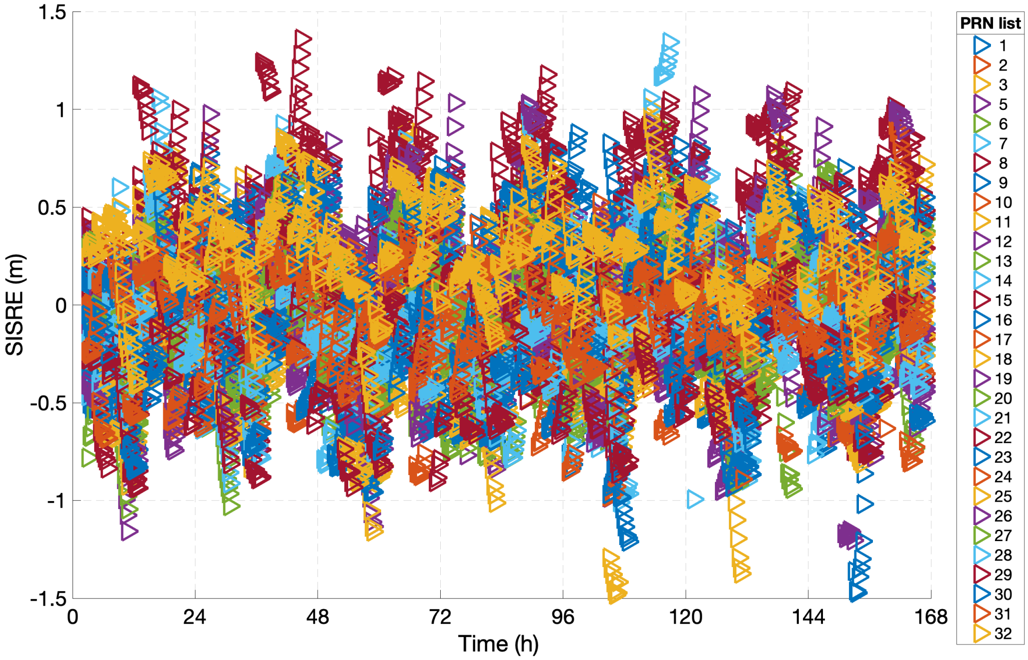

Figure 4.26. Estimate SISREs over January 17 to 23, 2016 (GPS week = 1880)

CHAPTER 5

ANALYZING SATELLITE POSITION ERRORS THROUGH BROADCAST EPHEMERIDES

As part of the ISD, ARAIM OFM is supposed to provide a bias (b_{nom}) and standard deviation (σ_{URA}) for nominal range errors that users will experience. Once the satellite orbit and clock truth product is available, as a secondary step in the OFM, this chapter introduces a new method to extract b_{nom} and σ_{URA}.

Due to previous two chapters, for the first time, we have opportunity to observe errors in the LNAV parameters (GPS ephemeris). This motivates us then to understand ephemeris-error characteristics and underlying nature of range errors. Thus, we comprehensively examine the details of the LNAV parameters in Section 5.1, and then, their behaviors and error characteristics in Section 5.2 and 5.3, respectively. We will see that it is straightforward to capture the temporal behavior of the ephemeris parameter errors. In Section 5.4, a proposed method is outlined to predict the range-error bounds from the observed ephemeris-error characteristics[3].

5.1 Background on broadcast GPS ephemeris (LNAV parameters)

The broadcast navigation message usually contains a set of orbital parameters to allow the computation of an instantaneous satellite position. The CSP selects a specific orbital model by considering the required accuracy in satellite positions. For example, GPS utilizes 15 orbital parameters, which are known as the LNAV parameters (available only in the LNAV message type). Improved sets of orbital

---

[3] ©2020 IEEE. Reprinted, with permission, from J. Patel, "Analyzing satellite orbit error for ARAIM offline monitoring", *IEEE/ION Position, Location, and Navigation Symposium (PLANS)*, April 2020. [89].

parameters exist but we limit our discussion to LNAV parameters as a large amount of historical LNAV messages are available.

In general, orbital parameters describe any celestial body's motion in space. The well-known Keplerian elements contain six parameters to describe overall shape of an orbit and its orientation. For medium Earth orbit GNSS satellites, the Keplerian elements would be accurate up to 100 m only. Therefore, the GPS LNAV message contains an additional nine parameters to enhance broadcast satellite position accuracy to the meter level.

The first six LNAV parameters are the Keplerian elements. The shape and size of an elliptical orbit is described using semi-major axis (A) and eccentricity (e) as shown in Figure 5.1. The position within the orbit is obtained using the mean anomaly (M) parameter, which is directly related to true anomaly (υ). The orientation of the orbit in inertial space is defined by three Euler angles as shown in Figure 5.2. The Ω parameter describes a point where the orbit passes through the equatorial plane while moving northward, which is known as the right ascension of the ascending node. The ω parameter, known as the argument of periapsis, is the angle between the equatorial plane and the point of Earth closest to approach. The last parameter, inclination angle i, provides the angle between the orbital plane and the Earth's equatorial plane. Thus, the satellite position in inertial space is defined by the Keplerian elements $(A, e, M, \Omega, \omega, i)$.

Table 5.1 shows the list of LNAV parameters. Having discussed the first six parameters earlier, the remaining nine parameters are classified into two categories: harmonic corrections and secular corrections. The harmonic corrections come in pairs of cosine and sine terms to improve position in the radial (C_{rc}, C_{rs}), along-track (C_{uc}, C_{us}), and cross-track (C_{ic}, C_{is}) directions. Three rate terms $(\Delta n, \dot{\Omega}, IDOT)$ capture secular drift.

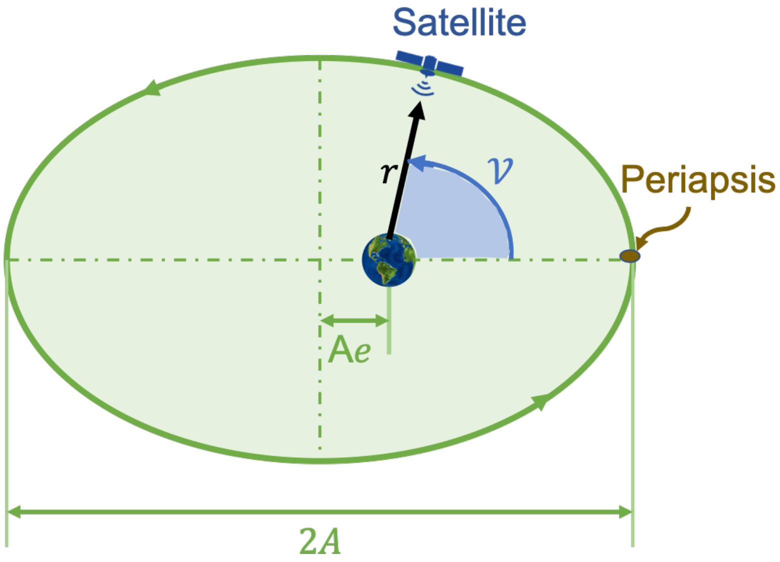

Figure 5.1. The Keplerian elements: A, e describe orbit shape and size

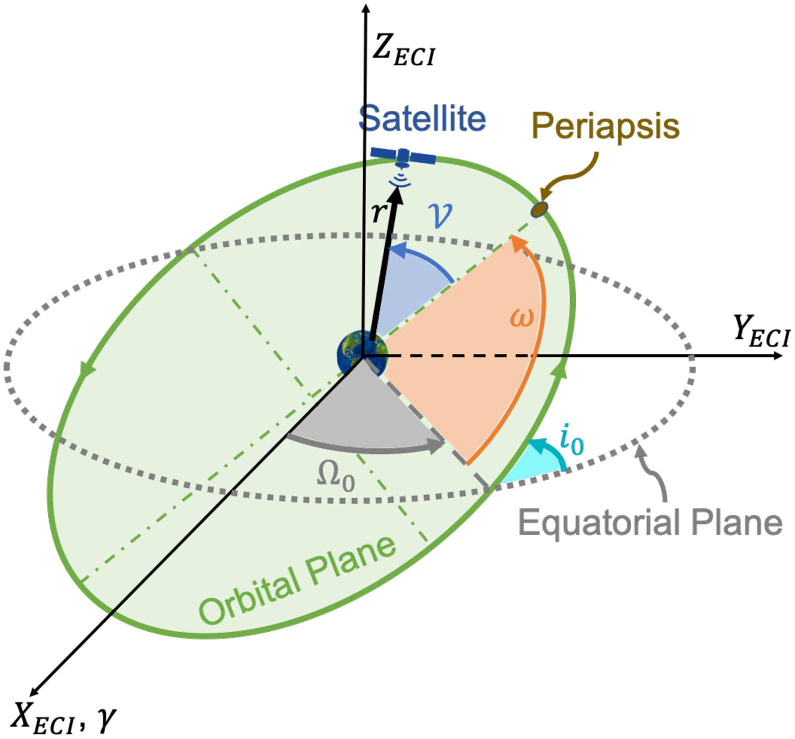

Figure 5.2. The Keplerian elements: ω, Ω and i describe orientation of the orbit in inertia space

The computation of satellite position using LNAV parameters is described in [45]. More detailed description about the GPS ephemeris can be found in [90]. In the following section, we will observe each parameter's behavior and its error over time.

Table 5.1. LNAV parameters in the GPS ephemeris

Parameter	Units	Description
t_{oe}	s	Reference time of ephemeris
$\sqrt{A}$	$\sqrt{m}$	Square root of the semi-major axis
e	dimensionless	Eccentricity
M_0	semi-circle	Mean anomaly at reference time
Ω	semi-circle	Longitude of ascending node of orbit plane at weekly epoch
ω	semi-circle	Argument of perigee
i_0	semi-circle	Inclination angle at reference time
Δn	semi-circle/s	Mean motion difference from computed value
$\dot{\Omega}$	semi-circle/s	Rate of right ascension
$IDOT$	semi-circle/s	Rate of inclination angle
C_{uc}, C_{us}	rad	Amplitude of the cosine and sine harmonic correction terms to the argument of latitude
C_{ic}, C_{is}	rad	Amplitude of the cosine and sine harmonic correction terms to the angle of inclination
C_{rc}, C_{rs}	m	Amplitude of the cosine and sine harmonic correction terms to the orbit radius

Note : semi-circle is converted to rad by multiplying by π

5.2 “Truth" LNAV parameters

Today, different satellite position products exist from the IGS and the NGA with centimeter-level accuracy. For future ARAIM OFM, we assume that truth LNAV parameters will be available from the IS as seen in Chapter 4. However, to determine the viability of the error characterization concept described in this chapter, we will use the readily available IGS position products.

The generation of truth LNAV orbit parameters from a known satellite positions is widely known as orbit fitting. Having accurate satellite positions over a certain period, fitting-window T_{FIT}, a set of LNAV “truth" parameters can be estimated. Of course, the quality of the orbit fitting depends on the fidelity of the LNAV model. In [29], a 4-h fitting-window was considered for fitting LNAV parameters, and the resulting model fidelity errors were bounded by a 12-cm standard deviation in the range domain. We use the 4-h fitting-window ($T_{FIT} = 4$ h) here as well.

The IGS orbit product provides satellite position with reference to satellite's Center of Mass (COM) while the broadcast LNAV parameters are referenced to the transmitting APC [91]. The necessary transformation using the APC offsets [86, 88] is applied to obtain APC referenced satellite positions (X^{IGS}). As shown in Equation (5.1), the known satellite position vector (X^{IGS}) is represented by a nonlinear function $\mathscr{F}^{\text{orb}}$ and an unknown 15-LNAV parameters.

$$X^{\text{IGS}} = \mathscr{F}^{\text{orb}}\left(p^{\text{orb}}\right) + \nu^{\text{orb}} \tag{5.1}$$

where,

p^{orb}	represents the 15-LNAV parameters ($p^{\text{orb}} = [p_1 \ \cdots \ p_{15}]^T$),
ν^{orb}	represents the fidelity errors of LNAV model.

For estimating the parameters for a satellite i, broadcast ephemeris ($p_i^{*,\text{orb}}$) are used to linearize Equation (5.1), and the resulting linear-measurement equation is formed as

$$\begin{aligned} \delta X_{i,k} &= X_{i,k}^{\text{IGS}} - \mathscr{F}_k^{\text{orb}}(p_{i,m}^{*,\text{orb}}) \\ &= J_{i,k}^{\text{orb}} \delta p_{i,m}^{\text{orb}} \end{aligned} \tag{5.2}$$

where,

k represents a time-epoch within the m^{th} fitting-window (T_{FIT}),

$X_{i,k}^{\text{IGS}}$ is a 3×1 position vector at the transmitting APC,

$J_{i,k}^{orb}$ is the 3×15 Jacobian matrix relating the LNAV parameters to satellite position:

$$J_{i,k}^{\text{orb}} = \begin{bmatrix} \frac{\partial x_{i,k}}{\partial p_1} & \cdots & \frac{\partial x_{i,k}}{\partial p_{15}} \\ \frac{\partial y_{i,k}}{\partial p_1} & \cdots & \frac{\partial y_{i,k}}{\partial p_{15}} \\ \frac{\partial z_{i,k}}{\partial p_1} & \cdots & \frac{\partial z_{i,k}}{\partial p_{15}} \end{bmatrix}_{3\times15} . \tag{5.3}$$

Now, for the m^{th} T_{FIT} window, a measurement vector is formed by stacking position vectors over 4 hours:

$$Z_{i,m} = \begin{bmatrix} \delta X_{i,k=0} \\ \vdots \\ \delta X_{i,k=4\text{h}} \end{bmatrix} .$$

The corresponding observation matrix is

$$H_{i,m} = \begin{bmatrix} J_{i,k=0}^{\text{orb}} \\ \vdots \\ J_{i,k=4\text{h}}^{\text{orb}} \end{bmatrix} .$$

Then, least-squares estimation is employed to obtain the unknown parameters as shown in Equation (5.4); a description of least-square estimation is provided in Section 2.2. As a result, a precise set of 15-LNAV parameters ($\hat{p}_{i,m} = p_{i,m}^{*,\text{orb}} + \delta p_{i,m}^{\text{orb}}$) are obtained for the m^{th} fitting-window.

$$\delta p^{\text{orb}}_{i,m} = (H^T_{i,m} H_{i,m})^{-1} H_{i,m} Z_{i,m} \tag{5.4}$$

The estimation procedure is illustrated through Figure 5.3 for an example GPS satellite (PRN 1) on February 1, 2016. For illustration purposes, only the $\sqrt{A}$ parameter is displayed in Figure 5.3. During the first T_{FIT}, PRN 1's positions from 22 to 26 h (GPS time) are processed using Equations (5.2) and (5.4), and the resultant $\sqrt{A}$ is plotted for the 24-h reference time (t_{oe}) (blue circle). For the next T_{FIT}, we slide the 4-h T_{FIT} by 15 min to obtain $\sqrt{A}$ at 24.25 h (the IGS orbit position products are available at 15-min intervals). Similarly, $\sqrt{A}$ is estimated for different reference times 24.5, 24.75, and 25 h using multiple T_{FIT}s in Figure 5.3.

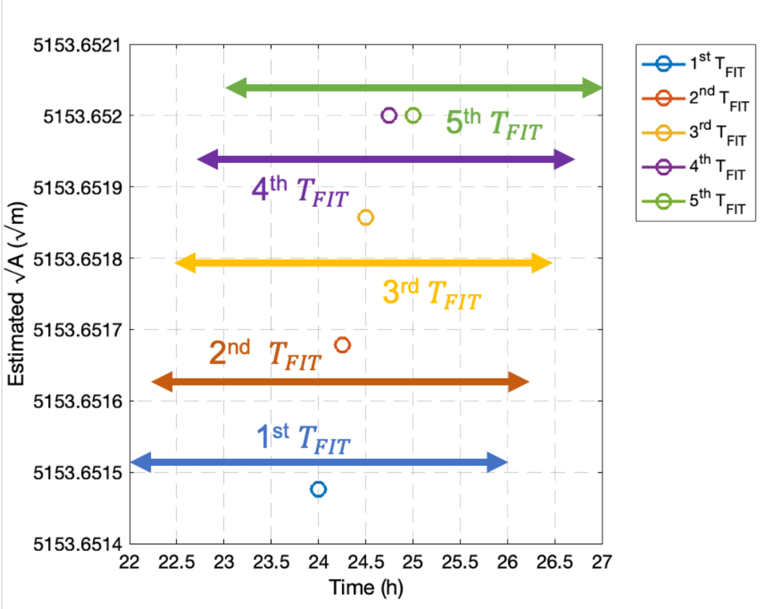

Figure 5.3. Illustration of obtaining LNAV parameters using different fitting-windows (T_{FIT})

Slowly moving T_{FIT} produces LNAV parameters at a high rate leading to smooth variation over time. For example, Figure 5.4 shows the estimated $\sqrt{A}$ for February 1, 2016. We can clearly see the repeated dip at a 12-h interval, which matches the orbital period of GPS satellites. Further, we process four years (February 1, 2016 to January 31, 2020) of PRN 1 positions to observe the variation in $\sqrt{A}$. Figure 5.6 shows the slow overall decrease in $\sqrt{A}$ over time. Moreover, $\sqrt{A}$ contains multiple cyclic behaviors such as satellite orbital period, but we will discuss more about its cyclic nature in the next section. Focusing on Figure 5.6, we see an obvious jump in the middle due to a planned maneuver, which was announced though a Notice Advisory to Navstar Users (NANU) message [92]. Since it was the planned maneuver, we simply ignored the outage period of PRN 1 in our analysis (b_{nom} and σ_{URA} represent nominal range errors).

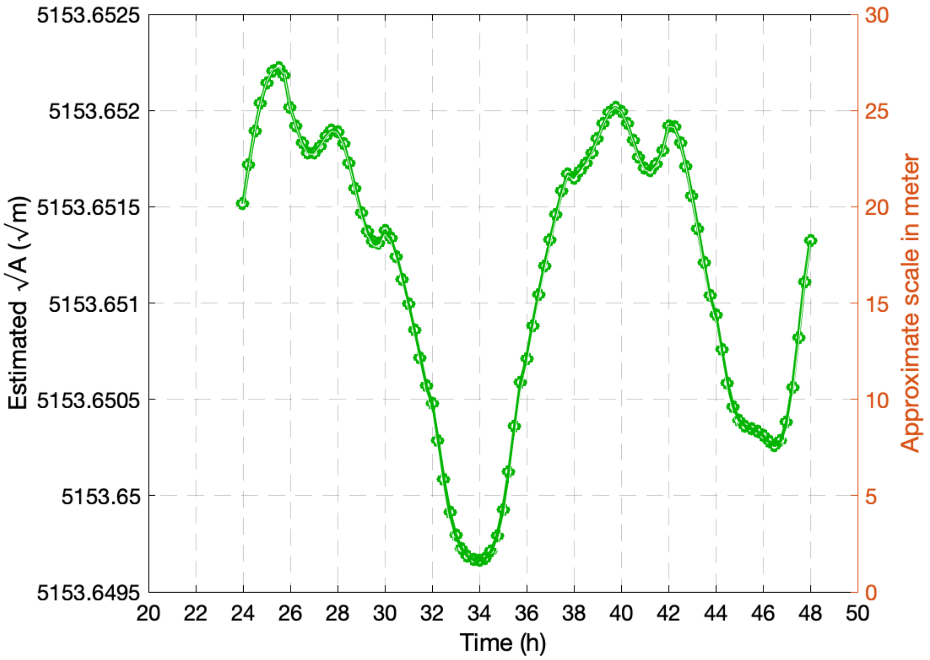

Figure 5.4. Estimated square root of the semi-major axis ($\sqrt{A}$) for PRN 1 on February 1, 2016

The eccentricity (e) parameter behaves inversely relative to $\sqrt{A}$, which can be observed in Figures 5.4 and 5.5. The shapes in the figures are opposite and appear to cancel out each other's variations to make a fixed shape orbit. Figure 5.7 also shows a counter-trend in the eccentricity relative to $\sqrt{A}$ over four years. The remaining

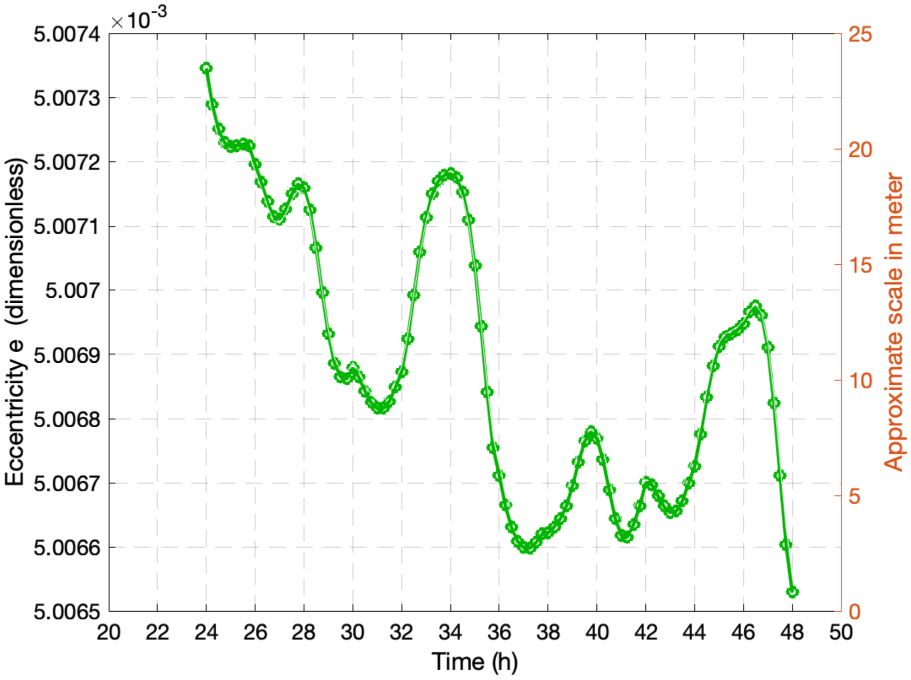

Figure 5.5. Estimated eccentricity e for PRN 1 on February 1, 2016

13-LNAV parameters are shown in Appendix F.

5.3 Errors in broadcast GPS navigation message

Along with the LNAV parameters, GPS navigation message contains a clock bias model to correct for the expected satellite clock error. Any error on the clock bias would directly result in a range error; clock bias error is highly correlated with the radial error of satellite position. Thus, to observe realistic range errors from navigation message, errors in LNAV parameters as well as satellite clock biases are discussed in the following subsections.

5.3.1 Errors in broadcast LNAV parameters. Generally, range errors being experienced by users are analyzed and modeled. But, in this subsection, the goal is to observe the distribution of LNAV parameter errors and find upper bounds on Gaussian mean μ and standard deviation σ. Then, the Gaussian parameters will be

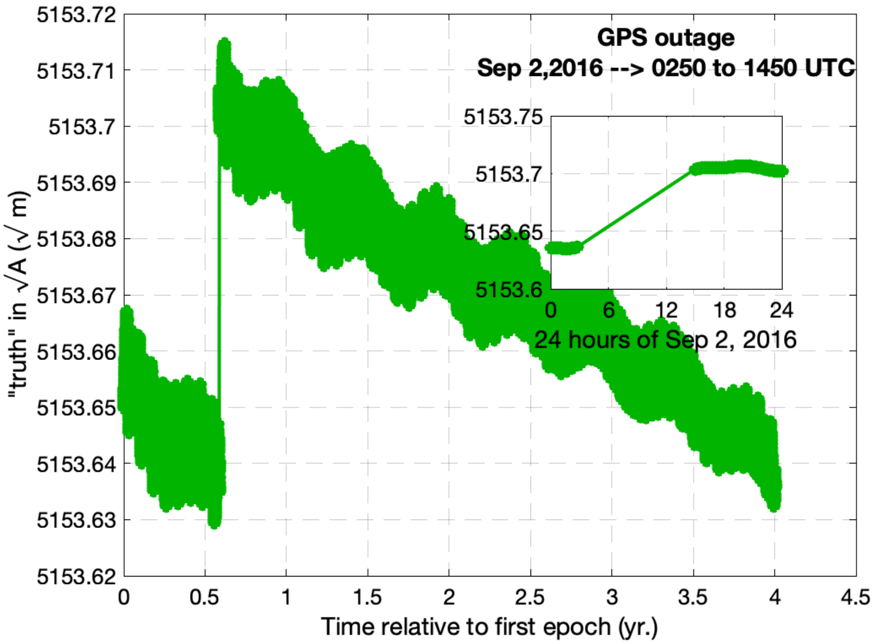

Figure 5.6. Estimated square root of the semi-major axis ($\sqrt{A}$) for PRN 1 over four years (Feb 1, 2016 to Jan 31, 2020)

converted to range domain (in Section 5.4) to bound the range errors. The benefit of our approach will become more clear in Section 5.4.

Observing LNAV parameter error is straightforward by comparing broadcast GPS LNAV parameters [93] with the ones estimated as described in the previous section. Equation (5.5) is a mathematical representation of the LNAV parameter error; estimate errors in truth LNAV parameters (corresponding to ∼ 12 cm satellite position error) are negligible compared to errors in the broadcast ones.

$$\varepsilon_{p^{\mathrm{orb}},k} = p_k^{\mathrm{orb}} - \hat{p}_k^{\mathrm{orb}} \tag{5.5}$$

where,

k	is a sample index (i.e., time),
$\varepsilon_{p^{orb}}$	represents the error in broadcast parameters,
p^{orb}	are broadcast parameters,

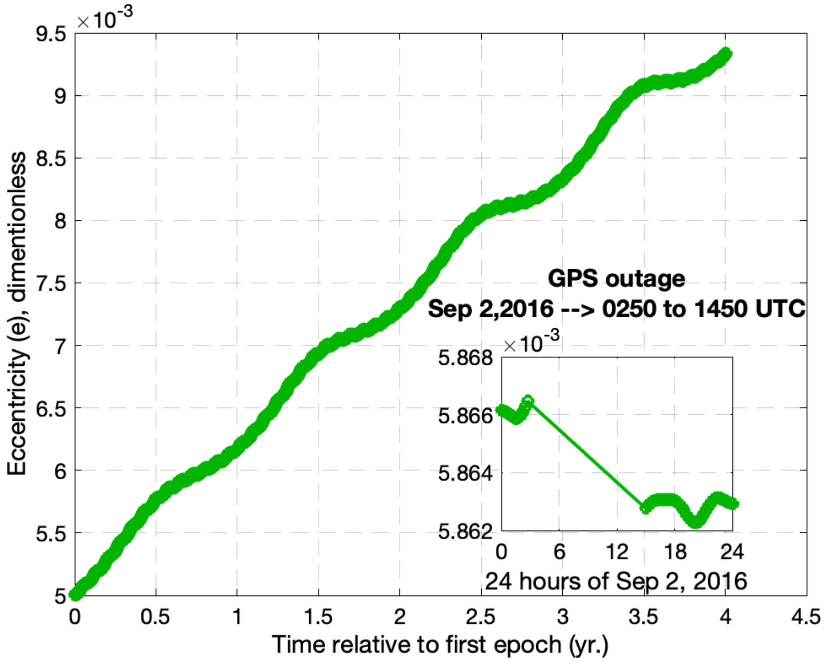

Figure 5.7. Estimated eccentricity e for PRN 1 over four years (Feb 1, 2016 to Jan 31, 2020)

$\hat{p}^{orb}$ are the estimated (truth) parameters.

Figure 5.8 shows the error in the broadcast $\sqrt{A}$ parameter for PRN 1. It is assumed that four years is a sufficiently long period to observe ephemeris-error characteristics. Since broadcast ephemerides are updated at 2-h intervals, higher frequency components in Figures 5.4 and 5.5 will not be visible. Later in this subsection, we will discuss the observable frequency components, but the at present, $\sqrt{A}$ error seems to follow Gaussian distribution with a constant mean and standard deviation. Similarly, the eccentricity ε_e error is shown in Figure 5.9 for PRN 1, which contains a low frequency component close to one year period. Since the ARAIM algorithm takes snapshot for a position fix, the error bounding with the Gaussian distribution is sufficient to describe its instantaneous characteristic. Therefore, the time correlation of ephemeris error will be analyzed in future work, and here, we only focus on capturing Gaussian statistics. Similar to the $\sqrt{A}$ and e errors, Appendix F shows errors for the remaining 13-LNAV parameters.

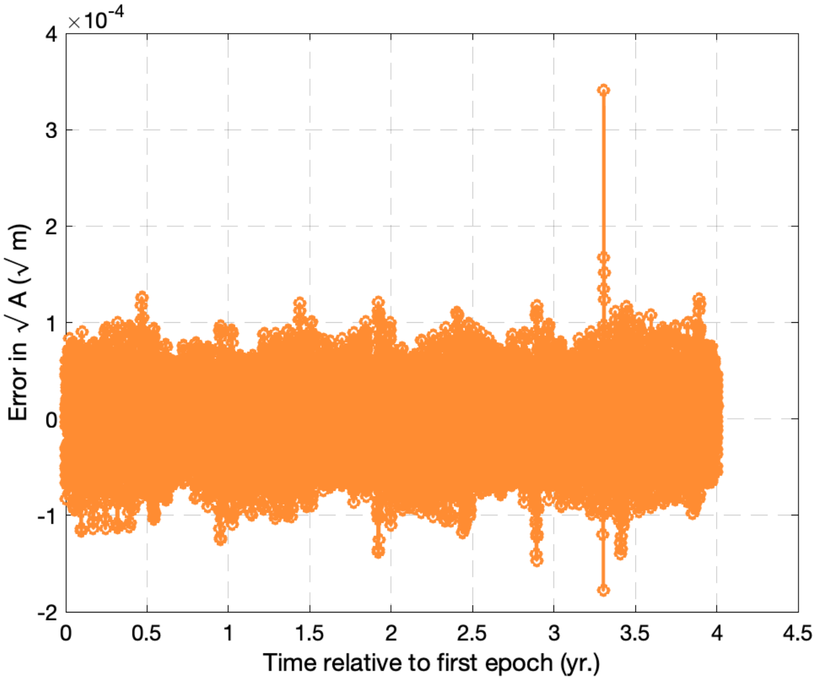

Figure 5.8. Error in broadcast $\sqrt{A}$ for PRN 1 over four years (Feb 1, 2016 to Jan 31, 2020)

The mean value of the $\sqrt{A}$ error is evaluated using Equation (5.6). The mean value is computed similarly for all the other parameter errors, and $\hat{\mu}_{\text{EPH}}$ vector (Equation (5.7)) is obtained to represent overall mean error of LNAV parameters.

$$\hat{\mu}_{\sqrt{A}} = \frac{1}{N} \sum_{k=1}^{k=N} \varepsilon_{\sqrt{A},k} \tag{5.6}$$

where N is total sample size (17518 samples).

$$\hat{\mu}_{\text{EPH}} = \begin{bmatrix} \hat{\mu}_{\sqrt{A}} \\ \hat{\mu}_e \\ \vdots \end{bmatrix}_{15\times 1} \tag{5.7}$$

Equation (5.8) shows an example covariance matrix for the $\sqrt{A}$ and e param-

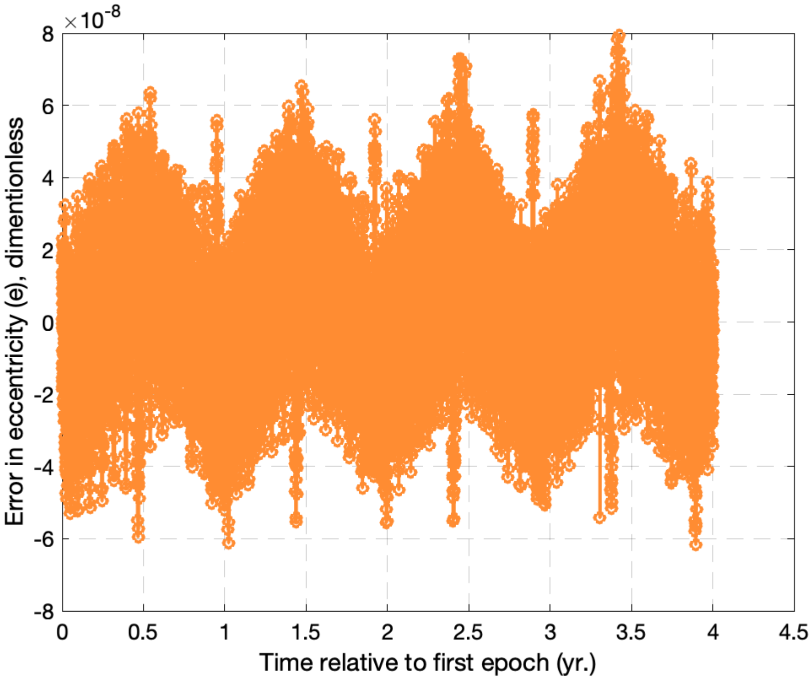

Figure 5.9. Error in broadcast e for PRN 1 over four years (Feb 1, 2016 to Jan 31, 2020)

eters.

$$\hat{\Sigma}_{\sqrt{A}e} = \begin{bmatrix} C_{\sqrt{A}\sqrt{A}}(0) & C_{\sqrt{A}e}(0) \\ \\ C_{\sqrt{A}e}(0) & C_{ee}(0) \end{bmatrix} \tag{5.8}$$

The diagonal terms of the matrix are obtained using the sample auto-covariance function of each parameter, while the non-diagonal terms, representing correlation between two parameters, are obtained using the sample cross-covariance function. Figure 5.10 shows the auto-covariance value for the $\sqrt{A}$ parameter error. As explained earlier, we are currently interested in only the variance of the errors for ARAIM, and $C_{\sqrt{A}\sqrt{A}}(0)$ is the main focused value. Similarly, the $C_{ee}(0)$ value is obtained from Figure 5.11 for the eccentricity-error variance. For the off-diagonal terms in the covariance matrix, the cross-covariance function is computed, and $C_{\sqrt{A}e}(0)$ is obtained. Likewise, the other 13-LNAV parameters are observed through auto-covariance and cross-covariance to achieve the variance ($\hat{\Sigma}_{\text{EPH}}$, 15 × 15 matrix) of the broadcast

GPS ephemeris error. For actual ARAIM OFM, the LNAV parameter errors must be overbounded as suggested in [24, 94]. But, to demonstrate our new approach, we simply use 1-σ covariance here.

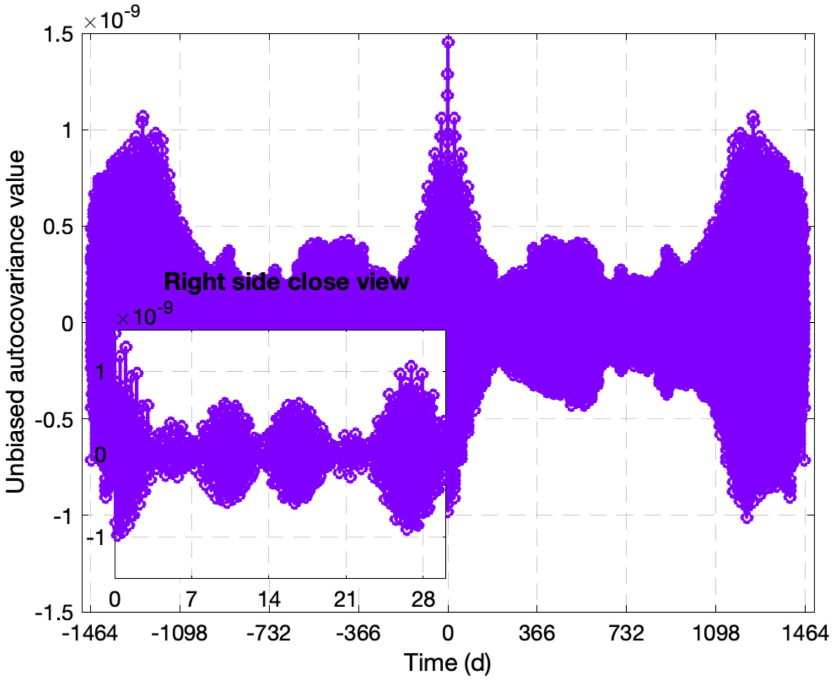

Figure 5.10. Autocovariance plot for the square root of the semi-major axis ($\sqrt{A}$) error

The goal of this subsection is achieved by obtaining the $\hat{\mu}_{\text{EPH}}$ and $\hat{\Sigma}_{\text{EPH}}$ as they capture the joint LNAV-parameter error distribution of 4 years. The following section will show how to predict range error distribution from $\hat{\mu}_{\text{EPH}}$ and $\hat{\Sigma}_{\text{EPH}}$. But, first we draw attention again to our assumption of the sufficiency of a 4-year observation period. There is still an open question of how to determine the observational period to safely bound range errors for ARAIM OFM. In future work, additional analysis will be carried out to define the necessary observational time period. Related to the time period, two interesting trends within Figures 5.10 and 5.11 are noted here for future reference. The first is a slow variation close to the Earth's orbital period (365.256 days): 354.5 days for the e error in Figure 5.11 ($\sqrt{A}$ does not exhibit this

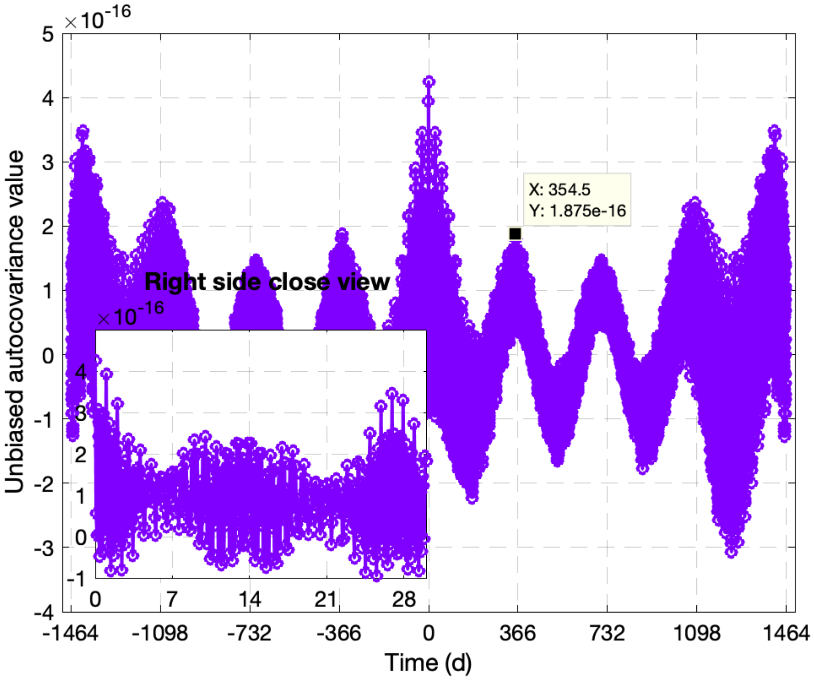

Figure 5.11. Autocovariance plot for the eccentricity (e) error

variation). The second, also a slow variation, is close to the Moon's orbital period (27.3 days): 26.92 days for the $\sqrt{A}$ and e errors in the close-up views in Figures 5.10 and 5.11, respectively.

5.3.2 Errors in broadcast satellite clock bias. Similar to “truth" LNAV parameters, accurate satellite clock biases will be available in the future from the newly-developed IS (Chapter 4), but we rely on the IGS clock product for this analysis. Specifically, we consider the internal clock product from one of the IGS analysis centers, the Center for Orbit Determination in Europe (CODE) [91]; the reason is that the “final" official IGS clock product (.sp3) lacks several time epochs over our selected analysis period.

The GPS navigation message provides satellite clock biases though quadratic parameters (a_{f_0}, a_{f_1} and a_{f_2}) to its users. These parameters are referenced to the time of clock (t_{oc}) parameter (also broadcast) which can be different from the reference time of ephemeris ($t_{oc} \neq t_{oe}$). Equation (5.9) shows the broadcast clock bias (τ_{brd}), in meters, for satellite i using the quadratic parameters [45].

$$\tau^i_{\text{brd}}(t) = c\Big(a_{f_0} + a_{f_1}(t - t_{oc}) + a_{f_2}(t - t_{oc})^2\Big) \tag{5.9}$$

where c is speed of light.

Although the GPS signal is broadcast from a single APC point on the satellite, the realization of APC could differ due to different strategies to estimate satellite position and clock bias. In [86], it is shown that precise IGS clock biases refer to different APCs than the GPS CSP-defined APCs. To make a fair comparison of IGS and broadcast clock bias, the IGS clock bias must first be transformed to the GPS CSP-defined APC as

$$\tilde{\varepsilon}^i_{\text{CLK},k} = \tau^i_{\text{brd},t=k} - \tau^i_{\text{CODE},k} - (\Delta APC^i_{\text{IGS},z} - \Delta APC^i_{\text{GPS},z}) \tag{5.10}$$

where,

$\tau^i_{\text{CODE},k}$	is the truth satellite clock bias from CODE,
$\Delta APC_{\text{IGS},z}$	is the distance between satellite's COM to the IGS-defined APC in radial direction,
$\Delta APC_{\text{GPS},z}$	is distance between satellite's COM to the GPS CSP-defined APC in radial direction.

Since the reference time is synchronized differently in the CODE product and GPS navigation message, clock error $\tilde{\varepsilon}_{CLK,i,k}$ is corrected by removing the constellation mean for each epoch,

$$\varepsilon^i_{\text{CLK},k} = \tilde{\varepsilon}^i_{\text{CLK},k} - \frac{1}{l}\sum_{i=1}^{i=l} \tilde{\varepsilon}^i_{\text{CLK},k} \tag{5.11}$$

where l is total number of satellites in the constellation.

Figure 5.12 shows the broadcast clock bias error for PRN 1 over four years with a 15-min sample rate. On a few occasions, the clock error is drifting over a day, representing upload issues in certain sets of LNAV messages, which are then reset with the next day's updated LNAV message. These events are visible in the figure as eight spikes. Since the error never exceeds the $4.42 \times \sigma_{\text{URA}}$ limit, these are not considered faults. Similar to the previous subsection on position error, the mean and variance of the clock error are evaluated. To incorporate a single covariance matrix for LNAV message errors, the cross-covariance function is evaluated across the LNAV-parameter errors and the clock error. Equations (5.12) and (5.13) show the final Gaussian parameters, $\hat{\mu}_{\text{LNAV}}$ and $\hat{\Sigma}_{\text{LNAV}}$, to represent the four-year error distribution in broadcast GPS LNAV messages.

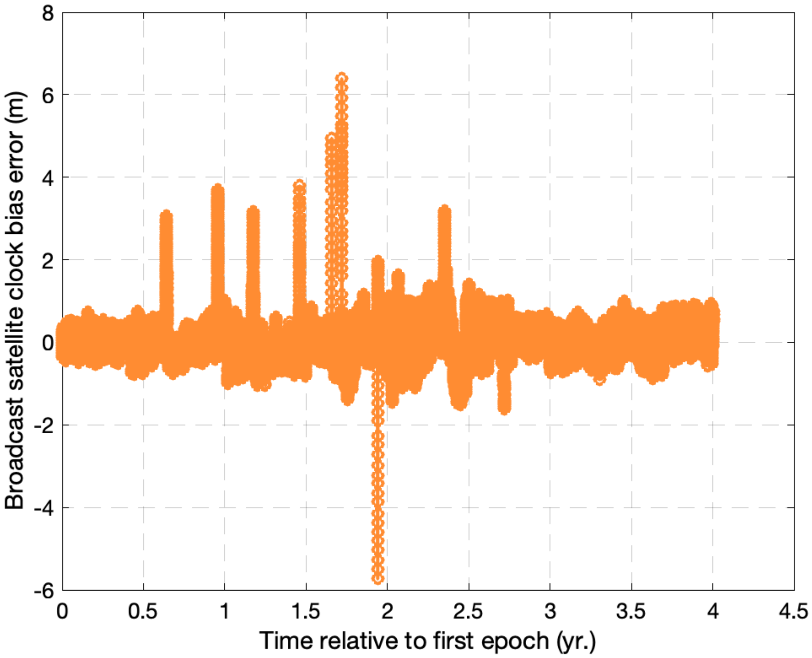

Figure 5.12. Errors in broadcast satellite clock bias for PRN 1 over four years (Feb 1, 2016 to Jan 31, 2020)

$$\hat{\mu}^{i}_{\text{LNAV}} = \begin{bmatrix} \hat{\mu}_{\text{EPH}} \\ \\ \hat{\mu}_{\text{CLK}} \end{bmatrix}_{16\times 1} \tag{5.12}$$

$$\hat{\Sigma}^i_{\text{LNAV}} = \begin{bmatrix} \hat{\Sigma}_{\text{EPH}} & C_{\text{EPH,CLK}}(0) \\ C_{\text{EPH,CLK}}(0) & C_{\text{CLK,CLK}}(0) \end{bmatrix}_{16\times16} \tag{5.13}$$

5.4 Generation of Integrity Support Data (range-error bound)

In general, ARAIM OFM needs to process multiple satellites over a certain observation period to capture the true nature of range errors. At the end, the OFM provides b_{nom} and σ_{URA} parameters for each constellation to bound the distribution of all range errors from its satellites. In the previous section, we developed the $\hat{\mu}_{\text{LNAV}}$ and $\hat{\Sigma}_{\text{LNAV}}$ parameters to bound errors in GPS LNAV messages, and now, in this section, we propose a method to generate the required b_{nom} and σ_{URA} parameters from them. In the first step, we will translate the $\hat{\mu}_{\text{LNAV}}$ and $\hat{\Sigma}_{\text{LNAV}}$ to satellite's position domain and then, to the range domain.

Equation (5.2) indicates that a satellite position error can be expressed as a function of the Jacobian matrix and an error vector from LNAV parameters. Using the same first order approximation, the $\hat{\mu}_{\text{LNAV}}$ and $\hat{\Sigma}_{\text{LNAV}}$ are transformed into the position domain; as discussed in Section 5.2, higher order effects (model fidelity errors) are negligible compared to errors in the broadcast LNAV messages. Equations (5.14) and (5.15) represent the mean and covariance transformed into satellite position domain, which are the predicted mean and variance for satellite position-error bound.

$$\hat{\mu}^i_{\text{LL}}(t) = \begin{bmatrix} \hat{\mu}^i_{\text{along-track}}(t) \\ \hat{\mu}^i_{\text{cross-track}}(t) \\ \hat{\mu}^i_{\text{radial}}(t) \\ \hat{\mu}^i_{\text{CLK}} \end{bmatrix}_{4\times1} = \begin{bmatrix} \mathscr{R}_1(t) \end{bmatrix}_{4\times4} \begin{bmatrix} \mathscr{C}(t) \end{bmatrix}_{4\times16} \begin{bmatrix} \hat{\mu}^i_{\text{EPH}} \\ \hat{\mu}^i_{\text{CLK}} \end{bmatrix}_{16\times1} \tag{5.14}$$

where,

$$\mathscr{R}_1(t) \triangleq \begin{bmatrix} \mathscr{R}_{LL}(t) & 0 \\ 0 & 1 \end{bmatrix}_{4\times4}$$, and $\mathscr{R}_{LL}(t)$ is the ECEF to LL rotation matrix,

$$\mathscr{C}(t) \triangleq \begin{bmatrix} J_i^{orb}(t) & 0 \\ 0 & 1 \end{bmatrix}_{4\times16}$$, and $J_i^{orb}(t)$ is the Jacobian matrix.

$$\hat{\Sigma}^i_{\text{LL}}(t)_{4\times4} = \mathscr{R}_1(t)\,\mathscr{C}(t)\,\hat{\Sigma}_{\text{LNAV}}\,\mathscr{C}^T(t)\,\mathscr{R}_1^T(t). \tag{5.15}$$

Time variable (t) is simply introduced to indicate the variation in the predicted error-bound as a satellite moves along its orbit. Since the orbital period of GPS satellites is 12 h, the Jacobian matrix will be repeated at the 12-h intervals, and any 12-h period is sufficient to predict the GPS satellite position-error bound.

A satellite position error is transformed to the range domain by projecting the position error along the line-of-sight vector. Equations (5.16) and (5.17) show the predicted SIS range-error mean ($\hat{\mu}^i_{\text{SISRE},q}$) and standard deviation ($\hat{\sigma}^i_{\text{SISRE},q}$) for an example location q and satellite i.

$$\hat{\mu}^i_{\text{SISRE},q}(t) = \begin{bmatrix} \mathscr{W}^i_q(t) \end{bmatrix}_{1\times4} \hat{\mu}^i_{\text{LL}}(t)_{4\times1} \tag{5.16}$$

where,

$$\mathscr{W}^i_q(t) \triangleq \begin{bmatrix} e^i_q(t) & 1 \end{bmatrix}_{1\times4}$$, and e^i_q is the line-of-sight vector from location q to satellite i.

$$\hat{\sigma}^i_{\text{SISRE},q}(t) = \sqrt{\mathscr{W}^i_q(t)\,\hat{\Sigma}^i_{LL}(t)\,\mathscr{W}^{i,T}_q(t)}. \tag{5.17}$$

Again, the time variable t is explicitly shown to indicate the error-bound variation as the line-of-sight vector changes due satellite motion. Furthermore, $e^i_q(t)$ is going to be repeated over a 24-h period as GPS satellites will be at the same location over the 24-h Earth rotation. Thus, any 24-h period is sufficient to predict range-error bound for the location q. So far, we have only discussed the SISRE bound, $\hat{\mu}^i_{\text{SISRE},q}$ and

$\hat{\sigma}^{i}_{\mathrm{SISRE},q}$, for arbitrary location q, but ARAIM users can be anywhere on the Earth surface. Therefore, we suggest to compute the SISRE bound for all Earth surface locations and consider the maximum value as a worst case SISRE bound. Equations (5.18) and (5.19) shows the mathematical expressions to provide the worst-case SISRE bound for satellite i.

$$\hat{\mu}^{i}_{\mathrm{SISRE}} = \max_{q=1,\ldots\ \mathrm{all}} \Big(\max_{t} \{ \mid \hat{\mu}^{i}_{\mathrm{SISRE},q}(t) \mid : 0 < t < 24\ \mathrm{h} \} \Big), \tag{5.18}$$

$$\hat{\sigma}^{i}_{\mathrm{SISRE}} = \max_{q=1,\ldots\ \mathrm{all}} \Big(\max_{t} \{ \hat{\sigma}^{i}_{\mathrm{SISRE},q} : 0 < t < 24\ \mathrm{h} \} \Big). \tag{5.19}$$

Once all satellites are analyzed to predict their individual $\hat{\mu}_{\mathrm{SISRE}}$ and $\hat{\sigma}_{\mathrm{SISRE}}$, the OFM must pick the maximum to bound all SISREs. Equations (5.20) and (5.21) show the final output from the OFM to predict nominal range errors for the ARAIM user.

$$b_{\mathrm{nom}} = \max_{i=1,\ldots l} \hat{\mu}^{i}_{\mathrm{SISRE}}, \tag{5.20}$$

$$\sigma_{\mathrm{URA}} = \max_{i=1,\ldots l} \hat{\sigma}^{i}_{\mathrm{SISRE}}, \tag{5.21}$$

where l is the total satellites in a constellation.

From Equations (5.14) to (5.21), the generation of b_{nom} and σ_{URA} is simple and straightforward once the accurate $\hat{\mu}_{\mathrm{LNAV}}$ and $\hat{\Sigma}_{\mathrm{LNAV}}$ are obtained. The key benefit of this approach is that temporal correlation in range errors is accounted for directly orbital parameter domain, which is the origin of the error source, and any spatial correlation in range errors can be avoided.

In this preliminary analysis, range-error bound is illustrated for only PRN 1 to demonstrate the proposed method. Once the required observation period of errors is defined in the future, we can include all satellites in the over-bounding process and provide the final b_{nom} and σ_{URA}. Figures 5.13 and 5.14 show the predicted mean and standard deviation for a Chicago location using the computed $\hat{\mu}_{\mathrm{LNAV}}$ and $\hat{\Sigma}_{\mathrm{LNAV}}$ for PRN 1. Different colors represent the 2-h segments valid for the Jacobian matrix, which is evaluated numerically and causes small discontinuities between two adjacent segments, as seen in Figure 5.14. Both figures show frequencies corresponding to the 12-h orbit period of GPS satellites and the 24-h Earth rotation.

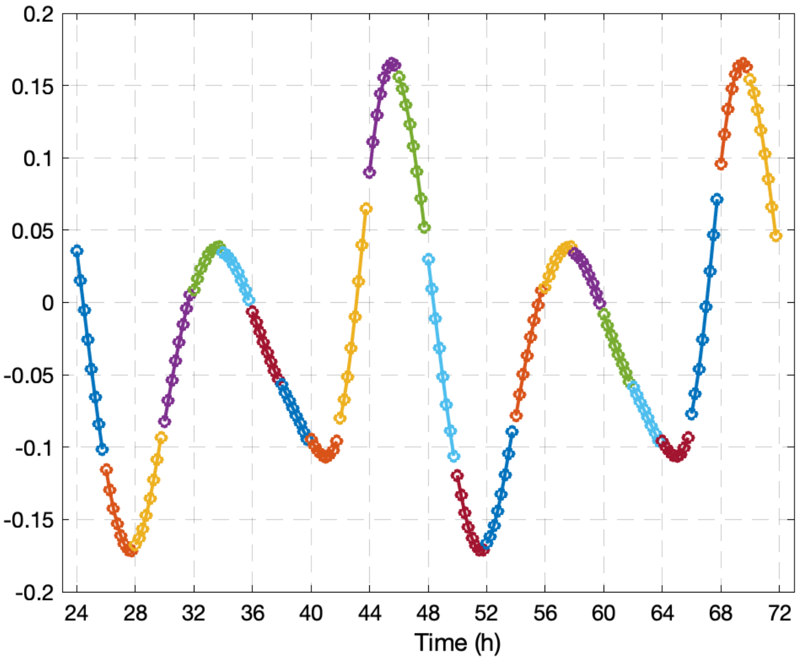

Figure 5.13. Predicted SISRE mean at the Chicago location using the computed $\hat{\mu}_{\text{LNAV}}$

5.4.1 Validation of predicted SISRE bound.

In [22, 24, 95], the GPS constellation performance is evaluated to provide the required b_{nom} and σ_{URA} using independent analyses. When we compare Figure 5.14 with the prior results, $\hat{\sigma}_{\text{SISRE}}$ closely matches, both suggesting a 1-m bound on standard deviation. However, their observed range-error mean is much smaller than in Figure 5.13. Specifically, the variation (-0.17 m to 0.17 m) over a day is quite unexpected as μ_{SISRE} has been assumed to be zero in the past. Thus, two investigations are performed to further to understand the reason behind the μ_{SISRE} variation.

By observing Equations (5.14) and (5.16), one can see that any mis-modeling

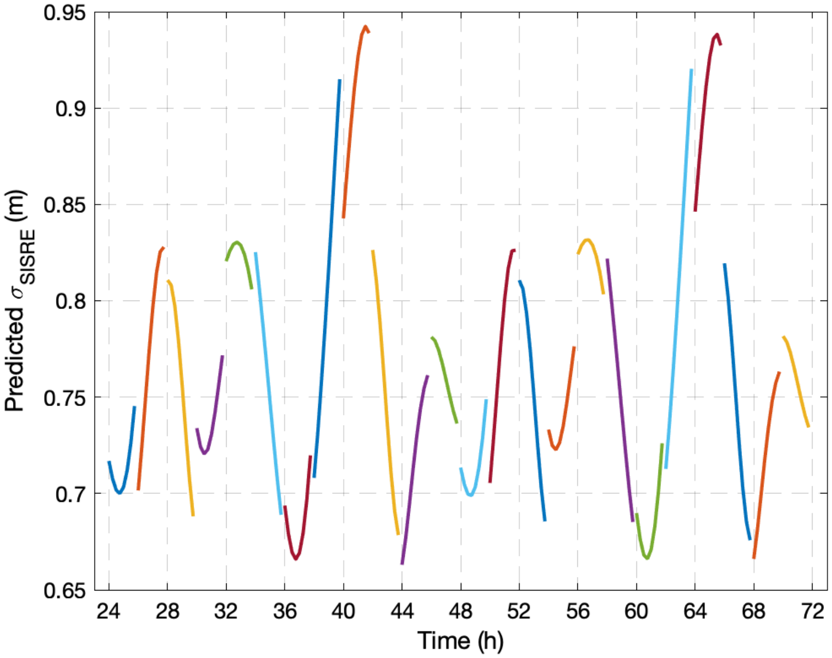

Figure 5.14. Predicted σ_{SISRE} at the Chicago location using the computed $\hat{\Sigma}_{\text{LNAV}}$

of the μ_{LNAV} may result in a μ_{SISRE} error as the Jacobian matrix and line-of-sight vector are simply coordinate transformations and projections. So, in the first investigation, we will illustrate the mean error of each of the LNAV parameters (satellite clock bias errors are not discussed as they have a zero mean). Figure 5.15 shows a running mean of each parameter computed at 10-day intervals; the units of all LNAV parameters are converted approximately to meters to aid in visualizing their convergence. Except M_0, ω, e, Ω_0 and i_0, all other parameter errors converge to a level of just a few centimeters within a one year period. The most notable exception is Ω_0 which converges to an unexpected 0.5 m. This is the main reason behind large fluctuating $\hat{\mu}_{\text{SISRE}}$ in Figure 5.13. The reason behind this divergence in Ω_0 is not clear, so we doubted the sufficiency of our 4-year observation period and considered the possibility of anomaly on PRN 1. However, the divergence is consistent among other GPS satellites even if the observation period is increased to 6 years.

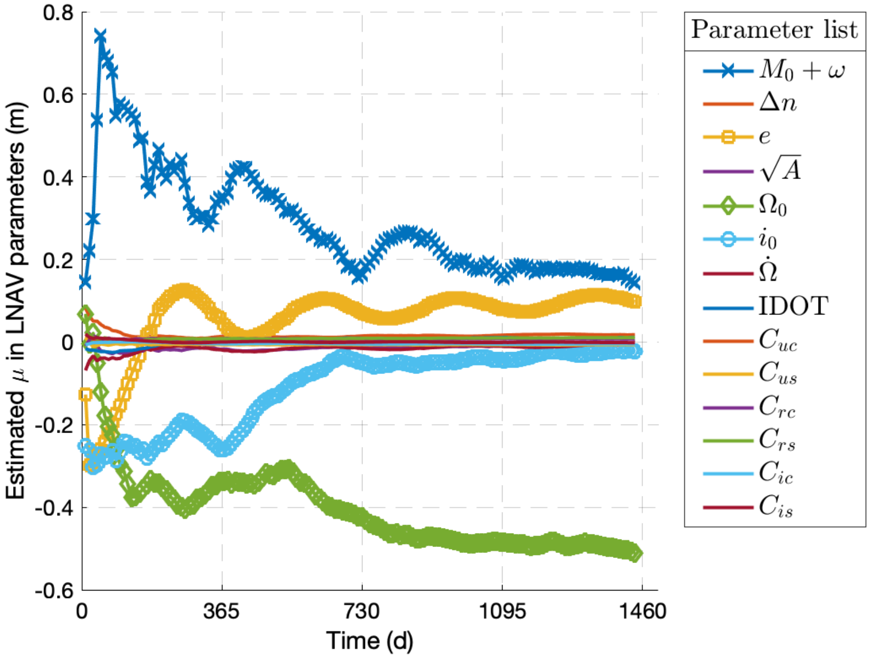

Figure 5.15. Running mean at 10-day intervals for the LNAV-parameter errors (PRN 1)

In the second investigation, we focus on our earlier underlying assumption that each LNAV message contains true random errors. In reality, CSP delivers sets of LNAV parameters to satellites for their future position, and the sets are valid until a new set of LNAV parameters are delivered again. The delivery time is identified using a drop in the IODE and t_{oe} parameters, part of the LNAV message [45], and each drop is labeled as an upload tag. For clear visualization of the upload tag, Figure 5.16 shows the position error of PRN 1 in LL instead of LNAV parameter errors. The cross-track and radial errors look nominal and can be bounded by Gaussian distribution. However, the along-track errors clearly exhibit non-Gaussian behavior (non-symmetric errors). Specifically, a duration of 400 h to 500 h shows the *drifting* along-track errors over four days. This can clearly affect our developed $\hat{\mu}_{\text{LNAV}}$ as LNAV-parameter errors are equally weighted, and it explains the reason behind the unexpected $\hat{\mu}_{\text{SISRE}}$. The same position errors of Figure 5.16 are shown in Figure 5.17

to observe upload-tag dependency.

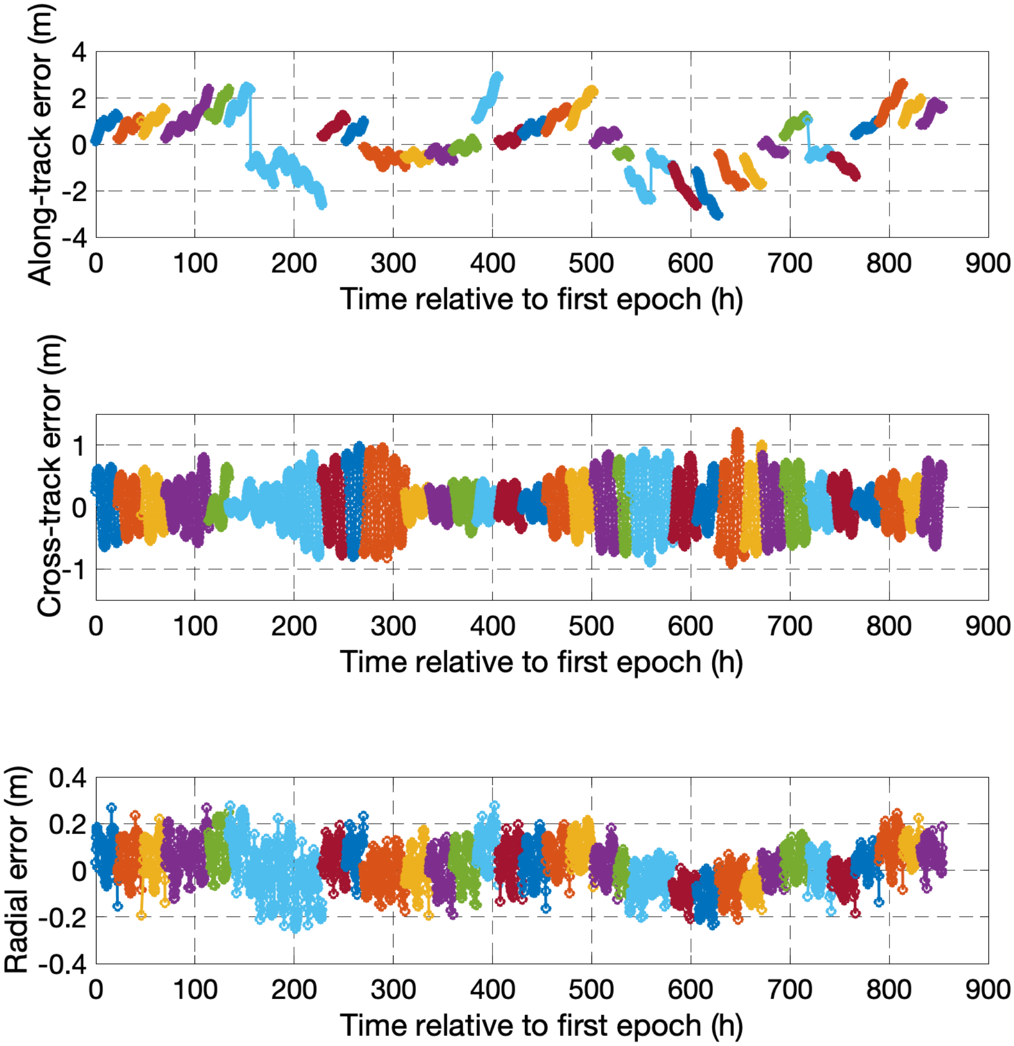

Figure 5.16. Position errors of PRN 1 when categorized by the upload tag (different colors) over April 1, 2016 to May 7, 2016

In future work, we will consider the upload-tag dependency in the development of $\hat{\mu}_{\mathrm{LNAV}}$ and $\hat{\Sigma}_{\mathrm{LNAV}}$, and the proposed method will be demonstrated for the full constellation. Although the data analysis in this chapter is limited to PRN 1, it exposes the underlying error sources in the user-experienced range errors. By understanding

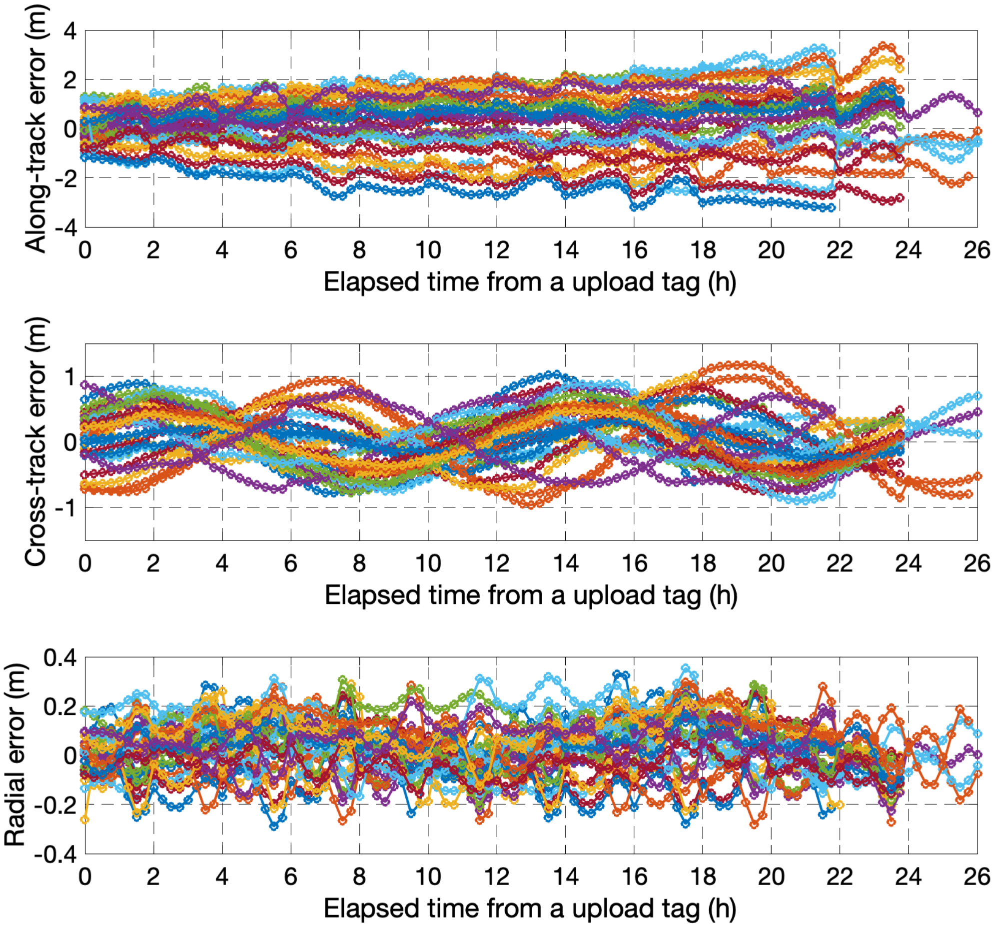

Figure 5.17. Position errors of PRN 1 when plotted against elapsed time from the upload tag over April 1, 2016 to May 7, 2016

the origin of LNAV parameter errors, OFM will have better capability to predict the range-error bound (b_{nom} and σ_{URA}).

To sum up, this chapter discusses a method to generate the Integrity Support Data (ISD) for ARAIM OFM, which is the secondary step after providing an independent satellite orbit and clock truth source. In the first part, we discuss the LNAV parameters, carrying satellite position knowledge in the broadcast GPS navigation message, and develop an error model to bound their errors over 4 years of LNAV messages. Then, the developed error model is converted to the range domain to determine SIS range-error bounds (the ISD). The preliminary SIS range-error bound is shown for PRN 1, and possible approaches for further improvement are discussed at the end.

CHAPTER 6

A SF SPATIAL GRADIENT MONITOR FOR GBAS

This chapter describes a contribution to the GBAS GF located at an airport. Unlike previous chapters addressing an estimation problem, this chapter addresses a fault-detection problem for the GBAS GF. Currently, GBAS is certified for the GPS L1 frequency signal only, and dual-frequency signals will be available in the future. Therefore, this chapter introduces a fault detection monitor concept with a single frequency signal and two antennas at the GBAS GF. The next chapters will incorporate multiple antennas and dual-frequency signals to further enhance monitor performance.

Figure 6.1 illustrates an example scenario where two antennas forming a baseline are installed parallel to the runway. Our goal is to ensure safe landing approach for an aircraft at the decision height (H). Once the GBAS GF approves safe operation, the aircraft flies along a glide path angle (GA) to touch down at glide path intercept point (GPIP). The distance (d_0) between the aircraft at decision height and GPIP varies depending on types of landing categories; 5 km is the maximum expected distance as displayed in Figure 6.1. This chapter introduces a monitor concept to immediately detect spatial gradients caused by ephemeris faults and ionospheric gradients for the example scenario when a satellite is newly acquired or re-acquired by GBAS. Later on, a process to initialize the monitor to achieve desired performance is discussed[4].

---

[4] ©2020 IEEE. Reprinted, with permission, from J. Patel, "Detecting Hazardous Spacial Gradients at Satellite Acquisition in GBAS", *IEEE Transactions on Aerospace and Electronic Systems*, Aug 2020. [96].

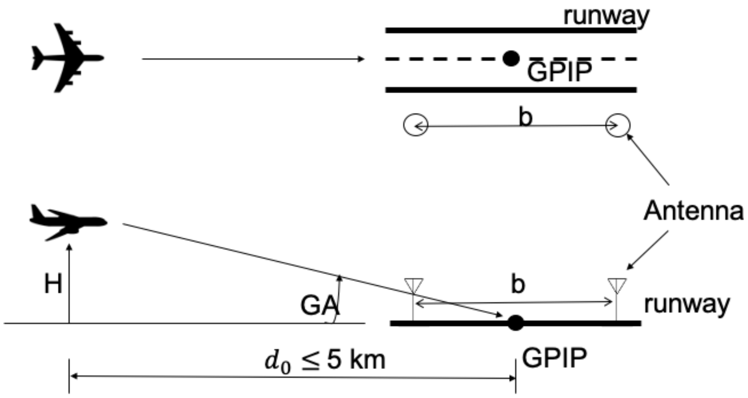

Figure 6.1. Illustration of an aircraft on approach and antenna configurations in GBAS

6.1 SF monitor concept

Since the behavior of the proposed monitors is identical for ephemeris failures and ionospheric gradients, the development of monitors and their results are discussed simultaneously. However, in the real world, two monitors perform fault detection independently to alert for ephemeris failures and ionospheric gradients.

6.1.1 Ephemeris monitor. The probability of multiple ephemeris failures occurring at the same time is lower than the allocated budget in the integrity risk tree. Therefore, the GBAS GF needs to monitor only a single ephemeris failure at any given time. This allows us to assume that other satellite ephemerides are fault-free.

For a faulty satellite i and a fault-free satellite j, the differential carrier phase measurement for antenna 1 is

$$\begin{aligned}\Delta\phi_1^{i,j} &= (r_1^i - r_1^j + \Delta I_1^{i,j} + \Delta T_1^{i,j} + \Delta t_{SD}^{i,j}) + \lambda\Delta n_1^{i,j} + \varepsilon_{\Delta\phi_1^{i,j}} \\ &= \tilde{r}_1^{i,j} + \lambda\Delta n_1 + \Delta\nu_{\phi_1}\end{aligned} \tag{6.1}$$

$$\tilde{r}_1^{i,j} \equiv r_1^i - r_1^j + \Delta I_1^{i,j} + \Delta T_1^{i,j} + \Delta t_{SD}^{i,j} \tag{6.2}$$

where,

r_1^i and r_1^j	are the ranges between antenna 1 and satellites i and j, respectively,
$\Delta I_1^{i,j}$	is the single difference ionospheric error,
$\Delta T_1^{i,j}$	is the single difference tropospheric error,
$\Delta t_{SD}^{i,j}$	is the single difference satellite clock bias,
λ	is the carrier wavelength,
$\Delta n_1^{i,j}$	is the single difference cycle ambiguity for antenna 1,
$\varepsilon_{\Delta\phi_1^{i,j}}$	is the single difference carrier phase thermal noise and multipath error for antenna 1.

Subscripts representing time epoch k and frequency f are dropped as faults are intended to be detected instantaneously using the GPS L1 frequency only.

Receiver antenna phase center variation is corrected in the carrier phase measurement as described in [36], while the millimeter level satellite phase center variation is ignored. A phase wind-up correction is not necessary as the double difference combination, which will ultimately be used in this monitor, cancels out its effect.

Similarly, the differential carrier phase measurement for antenna 2 is written below assuming both antennas are closely located and experience the same nominal ionospheric and tropospheric delay

$$\begin{aligned}\Delta\phi_2 &= (r_2^i - r_2^j + \Delta I_1^{i,j} + \Delta T_1^{i,j} + \Delta t_{SD}^{i,j}) + \lambda\Delta n_2^{i,j} + \varepsilon_{\Delta\phi_2^{i,j}} \\ &= \tilde{r}_1^{i,j} + (r_2^i - r_1^i) - (r_2^j - r_1^j) + \lambda\Delta n_2^{i,j} + \varepsilon_{\Delta\phi_2^{i,j}}.\end{aligned} \tag{6.3}$$

The differential range between the two antennas $(r_2^i - r_1^i)$ is equal to the projection of the true line of sight unit vector from antenna 1 to satellite i $(e_{i,\text{true}})$ onto the baseline displacement vector between the two antennas (b_{12}). If satellite i is faulty, the line of sight unit vector computed from the ephemeris $(e_{i,\text{EPH}})$ will also be faulty. Therefore,

$$r_2^i - r_1^i = b_{12}^T e_{i,\text{true}} = b_{12}^T (e_{i,\text{EPH}} + \delta e_i) \tag{6.4}$$

where,

δe_i	is the 3×1 ephemeris line of sight fault vector, and
b_{12}	is the known 3×1 relative position vector between antennas 1 and 2.

If satellite j is assumed to be fault-free, the true line of sight unit vector between antenna 1 and satellite j is equivalent to the vector computed from the ephemeris, i.e.,

$$r_2^j - r_1^j = b_{12}^T e_{j\text{true}} = b_{12}^T e_{j,\text{EPH}}. \tag{6.5}$$

By substituting Equations (6.4) and (6.5) into Equation (6.3), the measurement received by antenna 2 can be expressed as

$$\begin{aligned} \Delta\phi_2^{i,j} &= \tilde{r}_1^{i,j} + b_{12}^T e_{i,\text{EPH}} + b_{12}^T \delta e_i - b_{12}^T e_{j,\text{EPH}} + \lambda \Delta n_2^{i,j} + \varepsilon_{\Delta\phi_2^{i,j}} \\ &= \tilde{r}_1^{i,j} + b_{12}^T \Delta e^{i,j} + b_{12}^T \delta e_i + \lambda \Delta n_2^{i,j} + \varepsilon_{\Delta\phi_2^{i,j}} \end{aligned} \tag{6.6}$$

where $\Delta e^{i,j} = e_{i,\text{EPH}} - e_{j,\text{EPH}}$.

Taking the difference between the two antennas (to form the double difference),

$$\begin{aligned} \Delta^2\phi_{1,2}^{i,j} &= \Delta\phi_2^{i,j} - \Delta\phi_1^{i,j} \\ &= b_{12}^T \Delta e^{i,j} + b_{12}^T \delta e_i + \lambda(\Delta n_2^{i,j} - \Delta n_1^{i,j}) + \varepsilon_{\Delta^2\phi_{1,2}^{i,j}} \end{aligned} \tag{6.7}$$

where $\varepsilon_{\Delta^2\phi_{1,2}^{i,j}}$ is the double difference carrier phase measurement error.

Assuming that the ambiguities are known, which will be discussed in the following section, and the baseline vector b_{12} is known for a ground antenna installation, the test statistic can be formed as,

$$\begin{aligned} q^{\text{EPH}} &= \Delta^2\phi_{1,2}^{i,j} - b_{12}^T \Delta e^{i,j} - \lambda(\Delta n_2^{i,j} - \Delta n_1^{i,j}) \\ &= b_{12}^T \delta e_i + \varepsilon_{\Delta^2\phi_{1,2}^{i,j}}. \end{aligned} \tag{6.8}$$

Under fault-free conditions, the test statistic q^{EPH} is typically assumed to be bounded by a Gaussian distribution with zero mean and standard deviation of the double difference carrier phase measurement noise $\sigma_{\Delta^2\phi}$ [36]. Due to the low noise in the carrier phase measurements, the test statistic in Equation (6.8) will be sensitive to ephemeris faults, as shown in later sections.

6.1.2 IGM.

In [36], a monitor utilizing differential carrier phase measurements across multiple reference stations was introduced to instantaneously detect ionospheric gradients. The simplified double difference carrier phase measurement model between two antennas for a faulted satellite i and a fault-free satellite j is given by

$$\Delta^2\phi_{1,2}^{i,j} = b_{12}^T\Delta e^{i,j} + \lambda\Delta^2 n_{1,2}^{i,j} + \Delta I_{1,2}^{i,j} + \varepsilon_{\Delta^2\phi_{1,2}^{i,j}} \tag{6.9}$$

where,

$\Delta^2\phi_{1,2}^{i,j}$ is the double difference carrier phase measurement,

$\Delta e^{i,j}$ is the differential user-satellite line of sight unit vector (assuming no ephemeris fault),

$\Delta^2 n_{1,2}^{i,j}$ is the double difference cycle ambiguity, and

$\Delta I_{1,2}^{i,j}$ is the differential ionospheric error between antennas.

The ionospheric anomaly $\Delta I_{1,2}^{i,j}$ is described by the following model [97]

$$\Delta I_{1,2}^{i,j} = b_{12}^T\alpha \tag{6.10}$$

where α is the ionospheric gradient vector.

Therefore, the test statistics can be formed, assuming known ambiguities as we will discuss in the next section, as

$$\begin{aligned} q^{\mathrm{IGM}} &= \Delta^2\phi_{1,2}^{i,j} - b_{12}^T\Delta e^{i,j} - \lambda\Delta^2 n_{1,2}^{i,j} \\ &= b_{12}^T\alpha + \varepsilon_{\Delta^2\phi_{1,2}^{i,j}}. \end{aligned} \tag{6.11}$$

Comparing Equations (6.8) and (6.11), one can see that the monitors are identical and their test statistic sensitivity is directly influenced by the baseline length.

6.2 SF monitor initialization

6.2.1 Resolving the cycle ambiguity for the ephemeris monitor.

The cycle

ambiguity estimation required to compute q in Equation (6.8) needs to be immune to the ephemeris fault itself. We may eliminate the dependency on ephemeris by differencing the pseudorange measurement from the carrier phase:

$$Z^i_{CMC,1} = \phi^i_1 - \rho^i_1 = \lambda n^i_1 - 2I^i_1 + \varepsilon_{\phi^i_1} - \varepsilon_{\rho^i_1}. \tag{6.12}$$

We assume that an ionospheric gradient is absent in the ephemeris monitor as the IGM would alert in the case of ionospheric gradient. Therefore, the effect of ionospheric errors can be largely removed by taking the difference of Z_{CMC} between two antennas as

$$\Delta Z^i_{CMC_{1,2}} = Z^i_{CMC_1} - Z^i_{CMC_2} = \lambda \Delta n^i_{12} - 2\Delta I^i_{1,2} + \varepsilon_{\Delta\phi^i_{1,2}} - \varepsilon_{\Delta\rho^i_{1,2}}. \tag{6.13}$$

The error in $\Delta Z_{CMC_{12}}$ is dominated by thermal noise and multipath errors in $\varepsilon_{\Delta\rho^i_{1,2}}$, which are much larger than the sub-cm level carrier phase noise or the 2-4 mm/km differential ionospheric residual errors. In this analysis, the nominal differential vertical ionospheric errors are conservatively assumed to have a standard deviation of 2 mm/km, which is valid for mid-latitudes (larger values should be used for low latitudes and active ionospheric regions). Filtering of ΔZ_{CMC12} reduces the effect of these errors and allows resolution of the integer ambiguity term Δn_{12} as

$$\Delta \hat{n}^i_{1,2} = \frac{\sum \Delta Z^i_{CMC_{1,2}}}{\mathbb{T}} = \Delta n^i_{12} + \varepsilon_{\Delta \hat{n}^i_{1,2}} \tag{6.14}$$

where,

$\mathbb{T}$ is the number of independent samples and

$$\varepsilon_{\Delta \hat{n}^i_{1,2}} \sim \mathcal{N}\left(0, \frac{\sigma_{\Delta Z^i_{CMC_{1,2}}}}{\sqrt{\mathbb{T}}}\right). \tag{6.15}$$

The time correlation of multipath errors affects the filtering of $\Delta Z_{CMC_{12}}$ since the number of independent samples would be lower for highly correlated errors and vice-versa. Therefore, we analyzed experimental data to quantify the correlation of multipath errors in pseudorange measurements. This data was collected by the Federal Aviation Administration (FAA) Technical Center at their prototype GBAS installation. This GBAS site was installed with Multipath Limiting Antennas (MLA) to attenuate multipath errors. Analyzing the data, a time-constant of 2 s was observed for pseudorange errors and this value is assumed for analyses (Appendix G).

6.2.2 Resolving the cycle ambiguity for the IGM. Similarly, we use the pseudorange measurement to estimate the cycle ambiguity, but in this case, by adding it to carrier phase measurement, to eliminate the ionospheric component

$$\big(\phi + \rho\big)_1^i = 2\big(r_1^i + T_1^i + c(\delta t^i - \delta t_1)\big) + \lambda n_1^i + \varepsilon_{\phi_1^i} + \varepsilon_{\rho_1^i}. \tag{6.16}$$

The effect of nominal tropospheric delay and clock bias errors can be attenuated by taking the double difference of $\phi + \rho$ between two satellites and two antennas—Equation (6.17).

$$\Delta^2\big(\phi + \rho\big)_{1,2}^{i,j} = 2\Delta^2 r_{1,2}^{i,j} + \lambda\Delta^2 n_{1,2}^{i,j} + \varepsilon_{\Delta^2\phi_{1,2}^{i,j}} + \varepsilon_{\Delta^2\rho_{1,2}^{i,j}} \tag{6.17}$$

Since this monitor operates under the fault-free ephemeris hypothesis, the range term $\Delta^2 r_1^i$ is known and is evaluated as $b_{12}^T\Delta e^{i,j}$, which leads to Equation (6.18)

$$\begin{aligned}\Delta^2 Z_{CPC_{1,2}}^{i,j} &= \Delta^2\big(\phi + \rho\big)_{1,2}^{i,j} - 2b_{12}^T\Delta e^{i,j} \\ &= \lambda\Delta^2 n_{1,2}^{i,j} + \varepsilon_{\Delta^2\phi_{1,2}^{i,j}} + \varepsilon_{\Delta^2\rho_{1,2}^{i,j}}.\end{aligned} \tag{6.18}$$

The error in $\Delta^2 Z_{CPC_{1,2}}^{i,j}$ is dominated by thermal noise and multipath errors in $\varepsilon_{\Delta^2\rho_{1,2}^{i,j}}$. Filtering $\Delta^2 Z_{CPC_{1,2}}^{i,j}$ reduces the effect of these errors and allows resolution of the integer ambiguity term $\Delta^2 n_{12}$ as

$$\Delta^2\hat{n}_{1,2}^{i,j} = \frac{\sum\Delta^2 Z_{CPC_{1,2}}^{i,j}}{\mathbb{T}} = \Delta^2 n_{1,2}^{i,j} + \varepsilon_{\Delta^2\hat{n}_{1,2}^{i,j}} \tag{6.19}$$

where,

$\mathbb{T}$ is the number of independent samples considering a time-constant of

2 s (Appendix G) and

$$\varepsilon_{\Delta^2 \hat{n}^{i,j}_{1,2}} \sim \mathcal{N}\left(0, \frac{\sigma_{\Delta^2 Z^{i,j}_{CPC_{1,2}}}}{\sqrt{\mathbb{T}}}\right). \tag{6.20}$$

6.2.3 Impact of the rounding process on test statistics. The error in the float ambiguity estimate must be accounted for in the test statistic q in Equations (6.8) and (6.11). One way to reduce the ambiguity estimate error is to increase the filtering period. However, to reach the level of the carrier phase measurement noise in q and thus have minimal impact on the monitor's detection capabilities, filtering periods of more than 3 h would be necessary—impractical.

Instead, we round the averaged values of $\Delta\hat{n}$ and $\Delta^2\hat{n}$ to the nearest integers much earlier, but in doing so we must also account for the consequences of rounding to the wrong integer. The introduction of rounding eliminates the error in the float ambiguities. As a result, the ideal distribution of test statistics would only be driven by the carrier phase noise. However, the rounding process, which is nonlinear and may result in either correct or incorrect integers, will cause the test statistic to have a mixed Gaussian distribution (Figure 6.2) [98]. Therefore, the probability of rounding to the wrong ambiguity must be accounted for. Since $\Delta Z^{i}_{CMC_{1,2}}$ and $\Delta^2 Z^{i,j}_{CPC_{1,2}}$ are free of ephemeris faults and ionospheric anomalies, only code multipath and thermal noise can cause the ambiguity to be rounded to the wrong integer. Under fault-free conditions, a Wrong Integer Fix (WIF) would cause the test statistic to be biased, which may cause a false alarm. Under the fault hypothesis, this WIF may mask the actual fault and thus result in a MD.

The probability of rounding to the Correct Integer Fix (CIF) or any specific WIF can be computed from the Gaussian CDF given the distributions of $\varepsilon_{\Delta\hat{n}^{i}_{1,2}}$ and $\varepsilon_{\Delta^2\hat{n}^{i,j}_{1,2}}$ in Equations (6.15) and (6.20), respectively. For example, Figure 6.3 highlights the regions corresponding to CIF and WIF of ±1 integer cycle.

Since the monitor runs in the background to detect spatial gradients while the GF generates the differential corrections, it is assumed that any external cycle slip detection by the GF will be accessible to the monitor and result in a reset of the monitor filters.

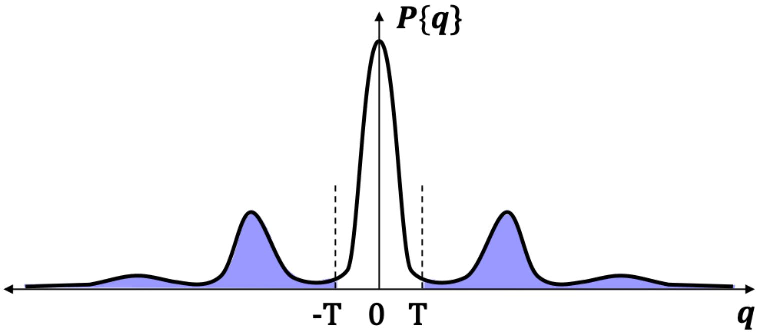

Figure 6.2. Illustration of the mixed Gaussian distribution of the test statistic q as a result of rounding

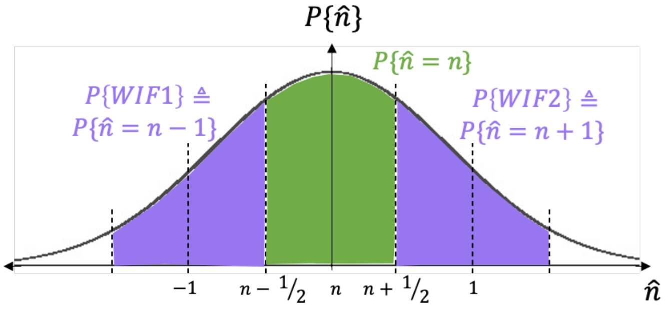

Figure 6.3. The probability density function for obtaining the correct and wrong cycle ambiguity

6.3 Analytical expression of monitor's FA and MD

Given that the CIF and all WIF events are mutually exclusive and exhaustive events, and using the law of total probability, we may express the FA probability under the null hypothesis H_0 (fault-free) as

$$\begin{aligned} P_{\mathrm{FA}} &= P\{q > T \mid H_0\} \\ &= P\{q > T \mid H_0, CIF\}P\{CIF\} + P\{q > T \mid H_0, WIF\}P\{WIF\}. \end{aligned} \tag{6.21}$$

For simplicity, at this stage, we temporarily assume that all WIF events will result in false alarms ($P\{q > T \mid H_0, WIF\} = 1$), which is a conservative assumption. Since WIF and CIF events are mutually exclusive and exhaustive, $P\{WIF\} = 1 - P\{CIF\}$. As a result, the probability of FA in Equation (6.21) is upper bounded as

$$P_{\mathrm{FA}} \leq P\{q > T \mid H_0, CIF\}P\{CIF\} + (1 - P\{CIF\}). \tag{6.22}$$

Equation (6.22) illustrates that the probability of a CIF must be high enough such that the term $(1 - P\{CIF\})$ is smaller than the allocated FA probability (on the order of 10^{-8} for the GBAS Category III landing). To achieve such a low probability, the float ambiguity estimates in Equations (6.14) and (6.19) need to be filtered for at least 3 h. Instead, we provide a tighter bound on the FA probability in Equation (6.22) by precisely accounting for the impact of a limited number of WIFs on the test statistic, while bounding the effect of the remaining WIFs [99, 100].

WIF events in Equation (6.21) include an infinite number of mutually exclusive possibilities, and when expanded we can rewrite Equation (6.21) as

$$P_{\mathrm{FA}} = P\{q > T \mid H_0, CIF\}P\{CIF\} + \sum_{i=1}^{\infty} P\{q > T \mid H_0, WIF_i\}P\{WIF_i\}. \tag{6.23}$$

Now, we will use the same bounding technique as in Equation (6.22), but only for a subset of WIFs $(n + 1) : \infty$ [100]

$$\begin{aligned} P_{\mathrm{FA}} \leq & P\{q > T \mid H_0, CIF\}P\{CIF\} \\ &+ \sum_{i=1}^{n} P\{q > T \mid H_0, WIF_i\}P\{WIF_i\} + \Big(1 - P\{CIF\} - \sum_{i=1}^{n} P\{WIF_i\}\Big). \end{aligned} \tag{6.24}$$

Even if many terms are computed in the series term in Equation (6.24) to provide a tight bound, we may still need to filter for prolonged periods before meeting the required level of P_{FA}, because each WIF generates a bias in the test statistic and will result in a FA. Instead, we will consider only ±1 WIFs and introduce multiple threshold regions, as illustrated in Figure 6.4. If the test statistic lies inside the region corresponding to the CIF, or the regions corresponding to ±1 cycle ambiguity, no alarm is triggered. The multiple threshold regions introduce a significant change in our prior assumption that a WIF of ±1 cycle will result in a FA.

Equation (6.25) provides a mathematical definition of the threshold regions

$$\{|q| \succ T\} \triangleq \{T < |q| < \lambda - T\} \cup \{|q| > \lambda + T\}. \tag{6.25}$$

Using the definition in Equation (6.25), we may rewrite P_{FA} in Equation (6.24) as

$$\begin{aligned} P_{\text{FA}} \leq & P\{q \succ T \mid H_0, CIF\}P\{CIF\} \\ & + \sum_{i=1}^{2} P\{q \succ T \mid H_0, WIF_i\}P\{WIF_i\} \\ & + \Big(1 - P\{CIF\} - \sum_{i=1}^{2} P\{WIF_i\}\Big). \end{aligned} \tag{6.26}$$

Now, a MD occurs if the test statistic is inside the threshold regions under the fault hypothesis H_f (Figure 6.4). The first two terms of Equation (6.27) bound the MD risk due to spatial gradients, while the last term bounds the MD risks due to WIF beyond ±1 integer

$$\begin{aligned} P_{\text{MD}} \leq & P\{q \prec T \mid H_f, CIF\}P\{CIF\} \\ & + \sum_{i=1}^{2} P\{q \prec T \mid H_f, WIF_i\}P\{WIF_i\} \\ & + \Big(1 - P\{CIF\} - \sum_{i=1}^{2} P\{WIF_i\}\Big). \end{aligned} \tag{6.27}$$

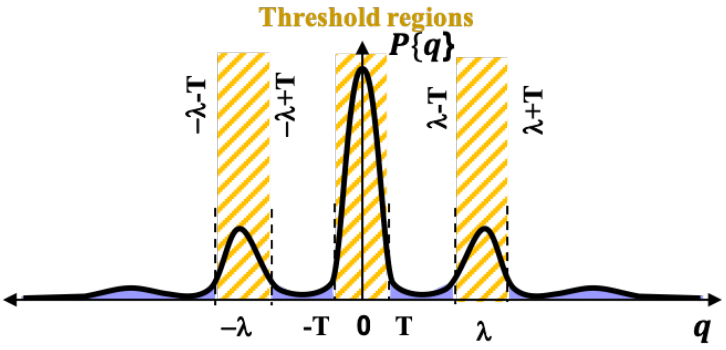

Figure 6.4. Illustration of the threshold regions defined in Equation (6.25)

6.4 Requirements on GBAS ephemeris monitor and IGM

Utilizing the same baseline for the ephemeris monitor and the IGM causes highly correlated test statistics under the fault-free condition. Nevertheless, the GBAS continuity risk of 10^{-8} is conservatively allocated to each monitor separately as the false alarm requirement.

6.4.1 Ephemeris monitor. For a GAST-D Category III landing, the current Standards and Recommended Practices (SARP) has no requirement specifically placed on the ephemeris monitor. However, two general requirements apply to the post-monitoring error in the corrected pseudorange [41]. The first requirement, termed the “limit case" requirement, shown in Figure 6.5, specifies thee minimum required probability of missed detection of a ranging source fault as a function of the ranging error $|E_r|$. The second requirement, known as the “malfunction case" requirement, shown in Figure 6.6, applies to all faults that have a prior probability of occurrence greater than 10^{-9}. It stipulates that the probability of an undetected fault leading to a differential ranging error greater than 1.8 m must not exceed 10^{-9}. Details behind the origin of these two requirements are outside the scope of this work, but the interested reader can find them in [101] and [102]. The P_{MD} of the ephemeris monitor must satisfy both requirements.

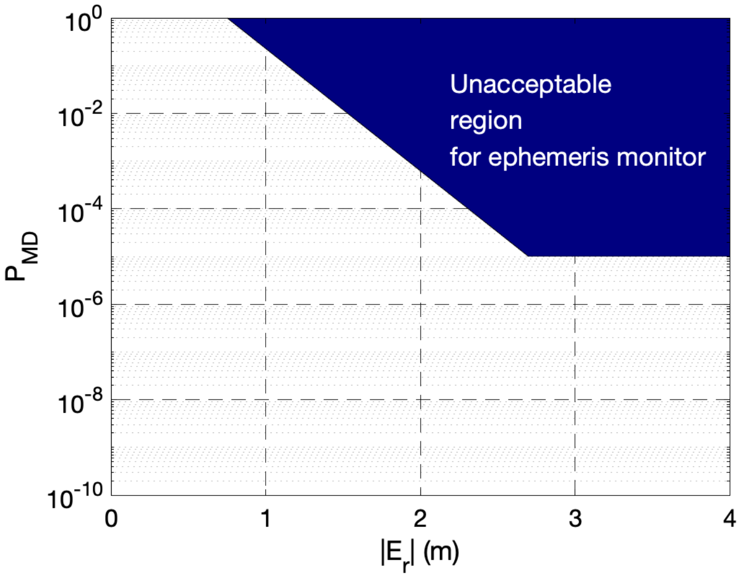

Figure 6.5. Integrity requirement for ephemeris monitor: “limit case"

6.4.2 IGM. In a GAST-D Category III landing, the probability of an undetected ionospheric front leading to a differential ranging error greater than 2.75 meters must not exceed 10^{-9} [41]. It is presumed that the prior probability of a potentially hazardous ionospheric front is 10^{-3} [103]. Thus, the IGM needs to meet a MD probability of 10^{-6}. This requirement applies to the post-monitoring error in the corrected pseudorange as depicted in Figure 6.7.

Based on the experimental analysis of data collected at the FAA Technical Center, it was shown in [104] that the CDF of the double difference carrier phase measurement error is overbounded by a zero-mean Gaussian distribution with a standard deviation of 6 mm, and the double difference pseudorange errors are bounded by a standard deviation of 84 cm.

In computing the ambiguities for the ephemeris monitor, a nominal differential vertical ionospheric error standard deviation of 2 mm/km is assumed based on the results in [105], which is then converted to a conservative range error using the

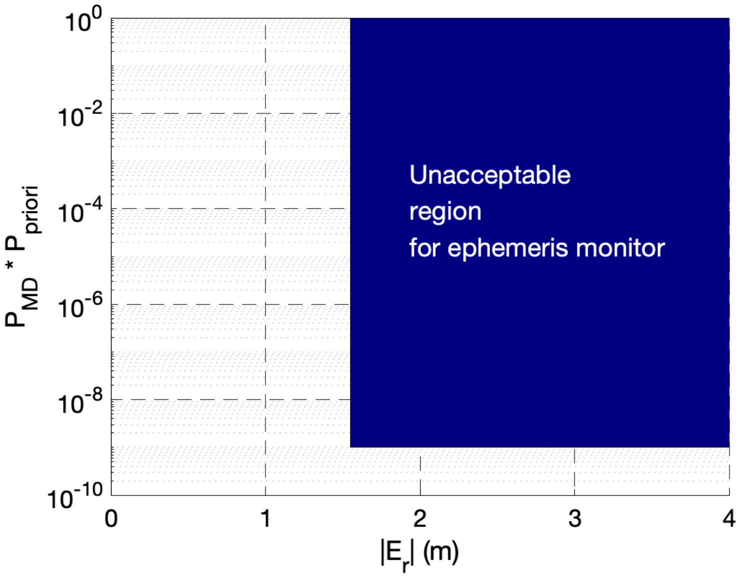

Figure 6.6. Integrity requirement for ephemeris monitor: “malfunction case"

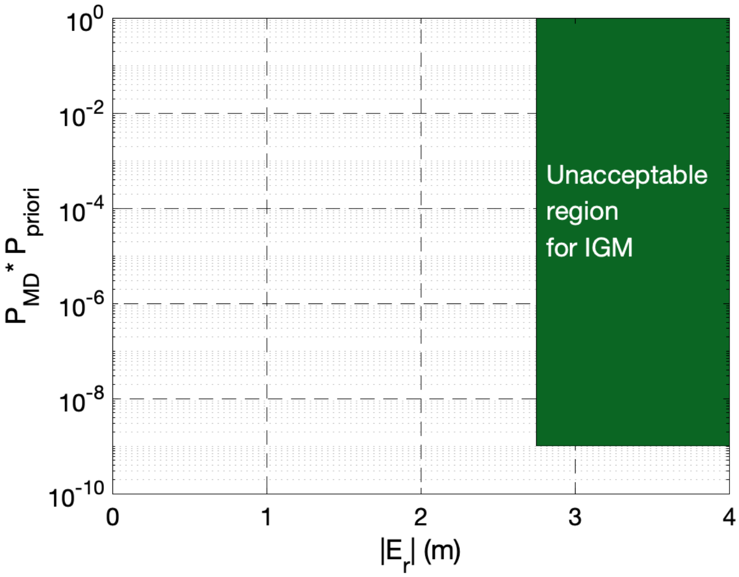

Figure 6.7. Integrity requirement for IGM weighted by prior fault probability

obliquity factor for a 3° elevation angle satellite.

6.5 Performance evaluation using an example single baseline

The proposed ephemeris monitor (Equation (6.8)) and the IGM (Equation (6.11)) are both sensitive to the baseline length, which is one of the design parameters for a GBAS site. The monitors need to initialize over a certain filtering period, a second design parameter, to obtain cycle ambiguities. Both design parameters are discussed in detail for an example single baseline scenario (Figure 6.1).

6.5.1 Filtering period. Filtering is applied initially to get the ambiguities needed to compute the test statistics. Therefore, the longer the filtering period, the higher the probability of CIF but, the longer the monitor has to wait to compute a test statistic and start monitoring for spatial gradients. During this time, the GBAS GF would not broadcast corrections for the satellite until they are validated by both monitors. In the forthcoming analysis, we will use the three threshold regions introduced in Section (6.3).

In the ephemeris monitor, it is assumed that the reference satellite was previously validated, having been tracked for a far longer period than the newly acquired one being tested. A filtering time of 5400 s (1.5 h) is assumed for the reference satellite; this is a conservative assumption because the average time-in-view for GPS satellites is considerably longer. In a FA analysis, Equation (6.26) is used to compute a threshold to meet the required probability of FA. Since CIF and WIF are related to ambiguity resolution, we filter Equations (6.14) and (6.19) to obtain sufficient $P\{CIF\}$ and $P\{WIF\}$. Based on the FA analysis, a filtering period of 605 s (10 min) and a threshold of 38 mm are adequate to meet 10^{-8} (P_{FA}) using a 1-km baseline. To evaluate P_{MD}, different ephemeris fault gradients were considered. The ranging error resulting from an ephemeris fault is computed by multiplying the ephemeris fault gradient by 5 km, which corresponds to the maximum distance between a landing aircraft and the geographic centroid of the reference stations as shown in Figure 6.1. This process is then repeated for all gradient values. Figure 6.8 shows the resulting

P_{MD}, where the highlighted area illustrates the ephemeris monitor requirements as shown in Figures 6.5 and 6.6. The pink diamond curve represents the probability of MD conditioned on a CIF and weighted by the probability of CIF—the first term of Equation (6.27). The green square and blue circle curves represent the terms of Equation (6.27) corresponding to -1 and +1 WIF terms, respectively. The sum of all three curves, the red curve, shows the total probability of MD on the ephemeris monitor, which does not satisfy the requirements using the arbitrarily selected 1-km baseline.

As for the IGM, a filtering period of 1138 s (19 min) and a threshold of 40 mm are adequate to satisfy the probability of FA requirement using a 1-km baseline. Different ionospheric gradients have been simulated to evaluate P_{MD}. In prior work [36], the IGM requirements were allocated in the gradient domain as a minimum detectable gradient of 300 mm/km. Recently, the requirements have been updated to be in the range domain as shown in Figure 6.7. Because the airborne system utilizes carrier smoothed pseudorange for positioning, an ionospheric anomaly that occurred before the decision height, H in Figure 6.1, may still affect the aircraft position estimate, which is not true for an ephemeris fault. The effective distance for monitoring must be $d_0 + 2v\tau$, where v is an aircraft approach speed, and τ is a time constant used in the smoothing filter. If the aircraft speed during the approach is 131 kn [106], and a time constant of 30 s is utilized for carrier smoothed pseudorange, the aircraft is being impacted by the ionospheric front earlier than reaching decision height H for a travel distance of 4 km. Therefore, 9 km is used as a distance between the reference station and aircraft for the computation of P_{MD}. Similar to Figure 6.8, the pink diamond, the green square, and the blue circle in Figure 6.9 represent the three terms of Equation (6.27) corresponding to the CIF ambiguity, -1 WIF ambiguity, and +1 WIF ambiguity, respectively. The red curve shows the resultant P_{MD} for the IGM, which illustrates that the requirement is not satisfied given the chosen baseline length and filtering period.

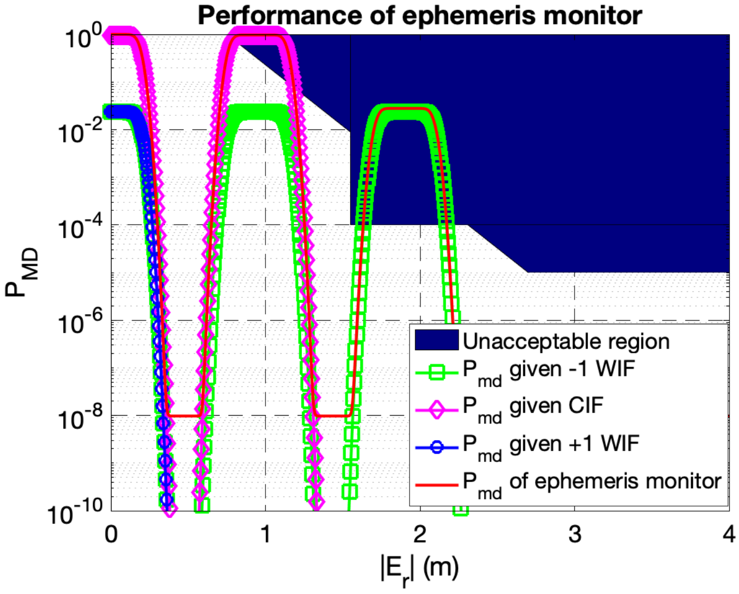

Figure 6.8. P_{MD} vs ranging error for the ephemeris monitor using 1-km baseline while considering the likelihood of ± 1 WIF ambiguity

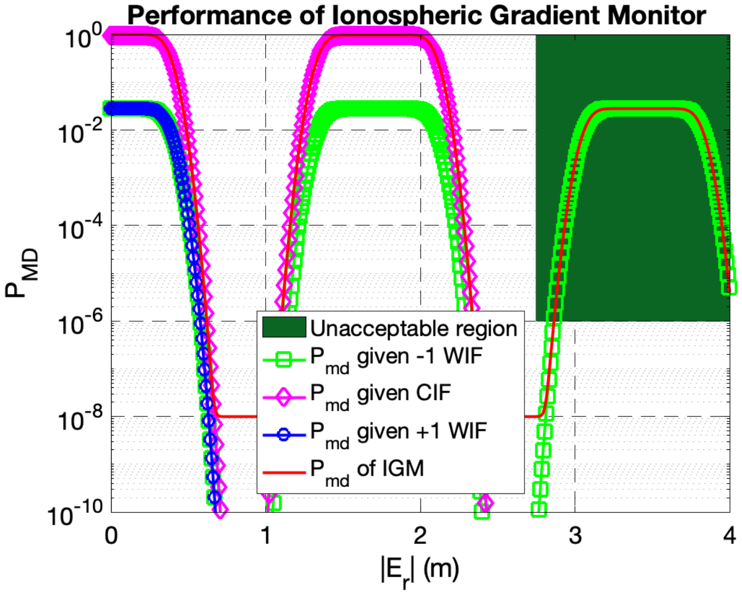

Figure 6.9. P_{MD} vs ranging error for the IGM using 1-km baseline while considering the likelihood of ± 1 WIF ambiguity

For the ephemeris monitor, an increase in the filtering period reduces the probability levels in the third peak of the green curve in Figure 6.8 (-1 WIF term). However, it does not reduce the probability levels of the second peak corresponding to the CIF probability (the pink curve). Therefore, even if greatly extended filtering periods are used, the resulting P_{MD} does not meet the requirements.

6.5.2 Baseline length. This section investigates the effect of baseline length on the monitor performance. Observing the test statistics in Equations (6.8) and (6.11), one can see that the test statistic is proportional to the baseline length under fault conditions. Thus, increasing the baseline length allows the monitor to detect smaller fault gradients. For example, an increase in the 1-km baseline would shift the red curve in Figures 6.8 and 6.9 to the left. For the ephemeris monitor, Figure 6.10 shows the probability of MD for an example baseline length of 1.5 km with a filtering period of 656 s and a threshold of 38 mm, which meets the FA requirements. Notice that the filtering period was increased to reduce the effect of code noise and multipath to accommodate the additional differential ionospheric error that is proportional to the baseline length in Equation (6.13). For the IGM, Figure 6.11 shows the probability of MD for the same baseline length of 1.5 km and a filtering period of 1138 s, which also meets the FA requirements.

To sum up, this chapter proposes a differential carrier phase based ephemeris monitor and IGM to detect instantaneous spatial gradients when a satellite is newly acquired or re-acquired in the GBAS. In the example scenario of Figure 6.1, test statistics are formed using a single baseline for the proposed monitor; sufficient knowledge of carrier cycle ambiguities is also achieved. It is determined that the minimum required baseline length is 1.5 km. The GBAS GF needs to wait 656 s for the ephemeris monitor and 1138 s for the IGM to initialize and broadcast differential corrections. In the following chapter, we will discuss how to reduce the filtering period and baseline for the SF ephemeris monitor and IGM.

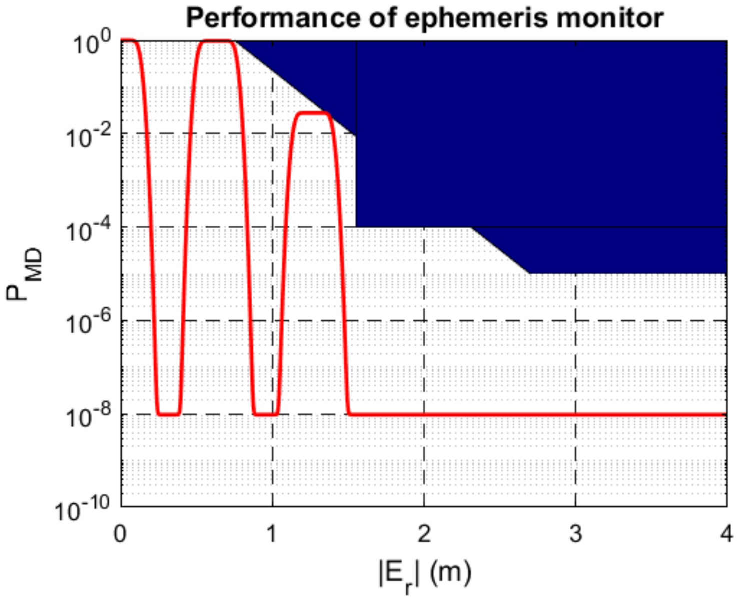

Figure 6.10. P_{MD} vs ranging error for the ephemeris monitor using 1.5 km-baseline while considering the likelihood of ± 1 WIF

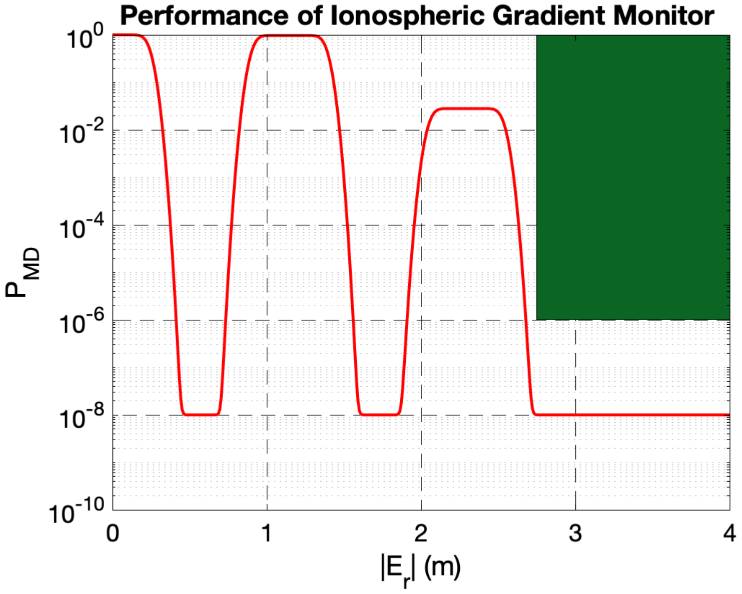

Figure 6.11. P_{MD} vs ranging error for the IGM using 1.5-km baseline while considering the likelihood of ± 1 WIF

CHAPTER 7

MULTI-BASELINE SF SPATIAL GRADIENTS MONITORS

In Chapter 6, a new ephemeris monitor and IGM were proposed to detect spatial gradients even for new satellites at acquisition. The performance requirements were met, but there were restrictions on monitor initialization time and antenna siting. For example, an IGM using 1.5-km baseline length between antennas needed at least 1138 s to resolve the cycle ambiguities before the monitor could start detecting faults. It is desired to reduce the initialization period and baseline length to improve system availability and airport siting limitations, respectively. In response, in this chapter, we investigate the effects of adding more antennas or baselines and the reduction of filtering period on monitor performance[5].

7.1 Exploiting multiple baselines to reduce single baseline length

In this section, we specifically focus on reducing the 1.5-km baseline length. Since the GBAS GF has multiple antennas for redundancy, an additional antenna can be utilized to form a second baseline. The second baseline is also installed parallel to the runway; both baselines are displayed in Figure 7.1. In this configuration, the monitor computes two different test statistics, one for each baseline, and triggers an alarm if *either* test statistic exceeds the threshold.

---

[5] ©2020 IEEE. Reprinted, with permission, from J. Patel, “Detecting Hazardous Spacial Gradients at Satellite Acquisition in GBAS", *IEEE Transactions on Aerospace and Electronic Systems*, Aug 2020. [96].

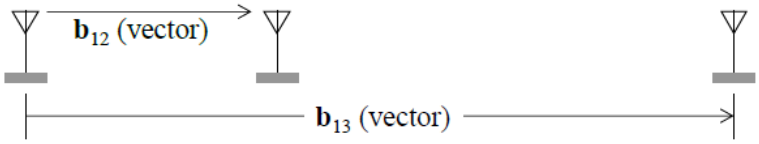

Figure 7.1. Illustration of two baselines at the GBAS GF along the runway

For the ephemeris monitor, the test statistics are defined as,

$$\begin{aligned} q_1^{\text{EPH}} &= \Delta^2\phi_{1,2}^{i,j} - b_{12}^T\Delta e^{i,j} - \lambda(\Delta n_{1,2}^i - \Delta n_{1,2}^j) = b_{12}^T\delta e_i + \varepsilon_{\Delta^2\phi_{1,2}^{i,j}} \\ q_2^{\text{EPH}} &= \Delta^2\phi_{1,3}^{i,j} - b_{13}^T\Delta e^{i,j} - \lambda(\Delta n_{1,3}^i - \Delta n_{1,3}^j) = b_{13}^T\delta e_i + \varepsilon_{\Delta^2\phi_{1,3}^{i,j}} \end{aligned} \tag{7.1}$$

and the detection rule is

$$\text{if} \quad \{q_1^{\text{EPH}} \succ T^{\text{EPH}}\} \cup \{q_2^{\text{EPH}} \succ T^{\text{EPH}}\} \quad \rightarrow \quad \text{alarm.}$$

Similarly the test statistics for the IGM are defined as,

$$\begin{aligned} q_1^{\text{IGM}} &= \Delta^2\phi_{1,2}^{i,j} - b_{12}^T\Delta e^{i,j} - \lambda\Delta^2 n_{12}^{ij} = b_{12}^T\alpha + \varepsilon_{\Delta^2\phi_{1,2}^{i,j}} \\ q_2^{\text{IGM}} &= \Delta^2\phi_{1,3}^{i,j} - b_{13}^T\Delta e^{i,j} - \lambda\Delta^2 n_{13}^{ij} = b_{13}^T\alpha + \varepsilon_{\Delta^2\phi_{1,3}^{i,j}} \end{aligned} \tag{7.2}$$

with the same detection rule

$$\text{if} \quad \{q_1^{\text{IGM}} \succ T^{\text{IGM}}\} \cup \{q_2^{\text{IGM}} \succ T^{\text{IGM}}\} \quad \rightarrow \quad \text{alarm.}$$

The test statistics q_1 and q_2 are correlated due to usage of the same antenna (1). The correlation can be captured in the measurement noise covariance matrix. The monitor's test statistics can be described by a multidimensional mixed Gaussian distribution. Figure 7.2 illustrates a probability contour plot of the distribution and the threshold regions of such a monitor. The FA probability corresponding to the integration of the distribution over the non-highlighted regions is written as

$$P_{\text{FA}} = P\{q_1 \succ T \cup q_2 \succ T \mid H_0\} \;\; \leq P\{q_1 \succ T \mid H_0\} + P\{q_2 \succ T \mid H_0\}. \tag{7.3}$$

A tighter upper bound on P_{FA} can be derived as shown in Equation (6.26).

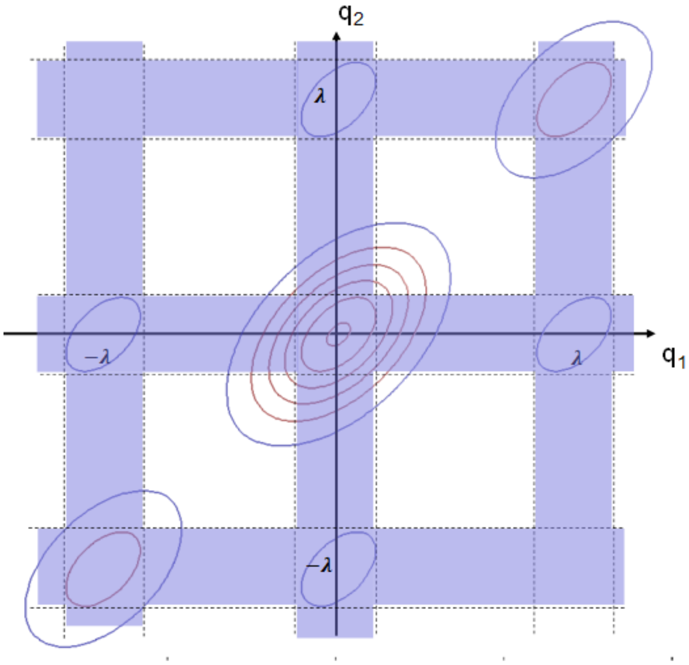

Figure 7.2. Contour plot showing the multivariate mixed Gaussian distribution corresponding to the dual baseline monitor and the threshold regions

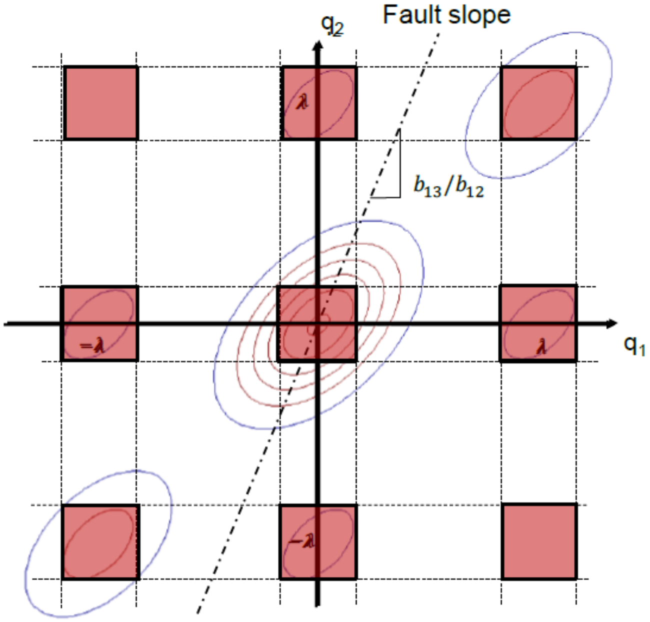

Figure 7.3. Contour plot showing the multivariate mixed Gaussian distribution corresponding to the dual baseline monitor, the missed detection regions, and the fault slope

On the other hand, a MD occurs if both test statistics are inside of the threshold regions (Figure 7.3).

$$P_{\text{MD}} = P\{q_1 \prec T \cap q_2 \prec T | H_f\}. \tag{7.4}$$

Similar to the FA probability, Equation (7.4) can be bounded as,

$$\begin{aligned} P\{q_1 \prec T \cap q_2 \prec T \mid H_f\} \leq\ & P\{q_1 \prec T \cap q_2 \prec T \mid H_f, CIF_{1\cap 2}\}P\{CIF_{1\cap 2}\} \\ & + \sum_{k=1}^{l} P\{q_{1k} \prec T \cap q_{2k} \prec T \mid H_f, WIF_k\}P\{WIF_k\} \\ & + \left(1 - P\{CIF_{1\cap 2} - \sum_{k=1}^{l} P\{WIF_k\}\right). \end{aligned} \tag{7.5}$$

Under fault conditions, the "mean" (which corresponds to the maximum peak of the distribution) of the multivariate mixed Gaussian distribution moves along a fixed fault slope. For example, Figure 7.3 shows the fault slope when cycle ambiguities are correctly resolved. It can be easily shown from Equation (7.1) that the fault slope, the ratio of q_2/q_1, is equal to b_{13}/b_{12}.

Next, the performance of the monitors is illustrated for an example with two baselines of 228 m and 800 m; the multidimensional mixed Gaussian distribution is evaluated using the MATLAB function "mvncdf". For the ephemeris monitor, a filtering period of 709 s and a threshold of 36.9 mm are adequate to meet the required FA probability. Figure 7.4 shows the resultant P_{MD} of the dual baseline monitor. Unlike Figure 6.8, where two peaks among three are penetrating through the highlighted requirement region, use of two baselines allow the fault slope to avoid the third threshold region, and only two peaks are observed.

For the IGM, a filtering period of 1190 s and a threshold of 37.6 mm are adequate to meet the required FA probability. Similar to the ephemeris monitor, only two peaks show up in the P_{MD} curve (Figure 7.5).

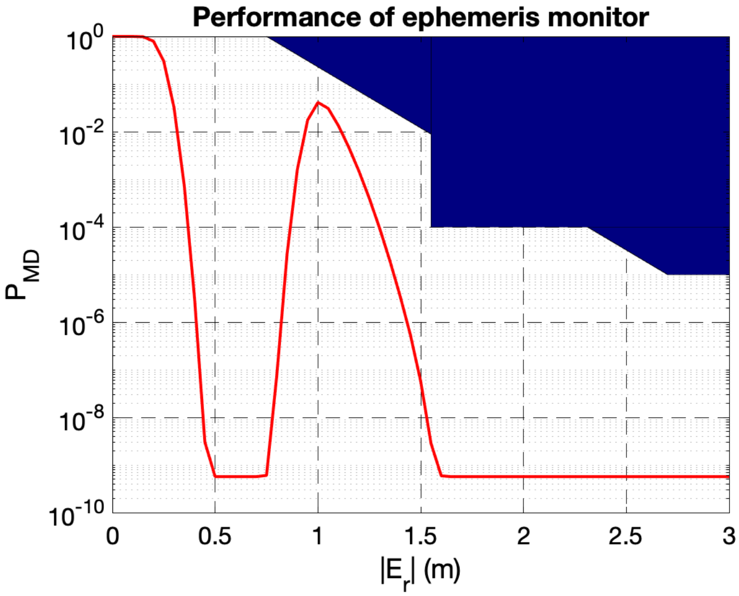

Figure 7.4. P_{MD} vs ranging error for the ephemeris monitor using 228-m and 800-m baselines while considering the likelihood of ± 1 WIF

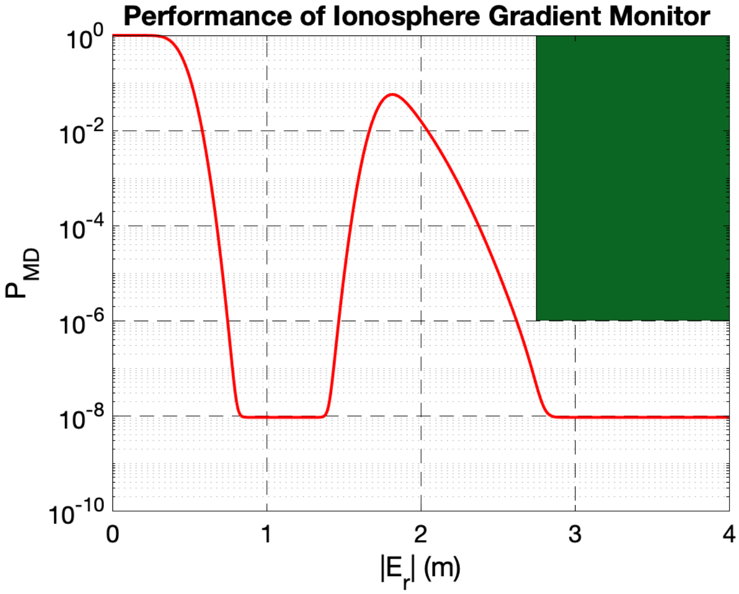

Figure 7.5. P_{MD} vs ranging error for the IGM using 228-m and 800-m baselines while considering the likelihood of ± 1 WIF

7.1.1 Changing the baseline lengths while preserving the baseline ratio.

Previously, for the single baseline case in Subsection 6.5.2, we saw that increasing the baseline length moves the P_{MD} curve to the left. To illustrate this effect, we have increased the longer baseline length to 1 km, while keeping the ratio of both baselines the same at 2/7, which results in a second baseline of 285 m. Figure 7.6 shows the resultant P_{MD} curve for the IGM. This example baseline combination also shifts the P_{MD} curve of the ephemeris monitor to the left.

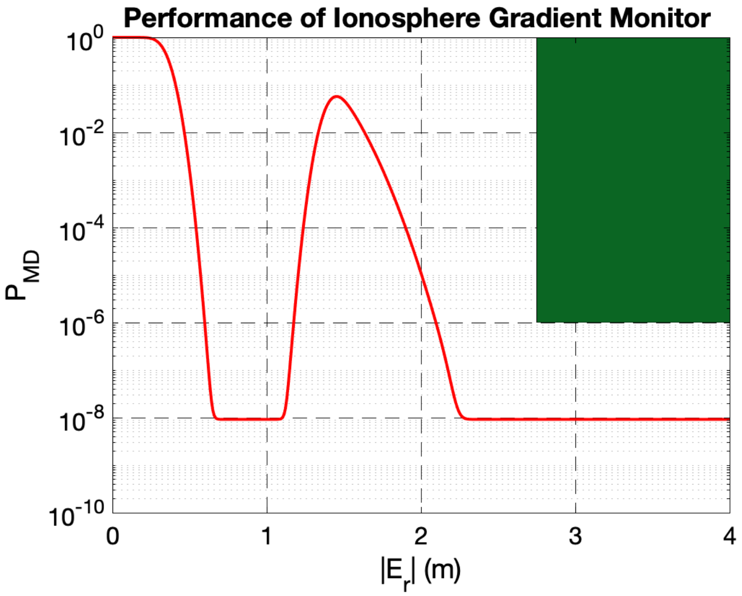

Figure 7.6. P_{MD} vs ranging error for the IGM using 285-m and 1-km baselines while considering the likelihood of ± 1 WIF

7.2 Modified threshold regions to reduce the initialization period

In this section, we focus on reducing the initialization period, which is simply the filtering period needed for resolving the cycle ambiguities. This filtering period is higher for the IGM compared to the ephemeris monitor. Therefore, the reduction of filtering period is demonstrated on the IGM as an example. Specifically, we consider expanding the threshold regions to include ±2 WIF ambiguities. As discussed in Subsection 6.2.3, tolerating more WIF ambiguities allows for a reduction of the filtering period by accounting for additional threshold regions, but detection performance is degraded. For the single baseline monitor, the inclusion of ±2 WIF is inapplicable due to the appearance of two additional peaks in Figure 6.11; the IGM thus no longer meets the MD requirement. The dual-baseline monitor will be able to handle ±2 WIF.

The introduction of ± 2 WIF requires additional threshold regions to avoid FAs as discussed in Section 6.3. For a single baseline case, the five threshold regions are illustrated in Figure 7.7 and written mathematically in Equation (7.6). For a dual baseline case, the probability of FA and probability of MD are expressed as Equations (7.7) and (7.8), by simply replacing the three-threshold definition (Equation (6.25)) with the five-threshold definition (Equation (7.6)) in Equations (7.3) and (7.4). Figure 7.8 illustrates the threshold regions resulting from the dual baseline configuration.

$$\{|q| \gtrdot T\} \triangleq \{T < |q| < \lambda - T\} \cup \{\lambda + T < |q| < 2\lambda - T\} \cup \{|q| > 2\lambda + T\} \tag{7.6}$$

$$P_{\text{FA}} = P\{q_1 \gtrdot T \cup q_2 \gtrdot T \mid H_0\} \leq \; P\{q_1 \gtrdot T \mid H_0\} + P\{q_2 \gtrdot T \mid H_0\} \tag{7.7}$$

$$P_{\text{MD}} = P\{q_1 \lessdot T \cap q_2 \lessdot T | H_f\} \tag{7.8}$$

When implemented, the filtering period for the IGM is reduced to 439 s using Equation (7.7) while meeting the required FA probability with a 36-mm threshold. Using two baseline lengths of 1 km and 285 m, the probability of MD is plotted in Figure 7.9. As expected, two additional peaks are observed in the P_{MD} curve because of the two additional threshold regions. Therefore, the P_{MD} requirement is not met for the current configuration, but the improvement in detection performance is achieved in the following Subsection 7.2.1. In summary, the introduction of five threshold regions is currently helpful in reducing the initialization period but degrades fault detection performance as shown in the P_{MD} curve.

7.2.1 Effect of baseline length ratio. In this subsection, we investigate the effect of the baseline ratio on the probability of MD. Starting with the configuration used earlier of the 285-m and 1-km baselines, the means of the test statistics for varying fault magnitude are plotted in Figure 7.10. Comparing Figure 7.10 to Figure 7.9 for

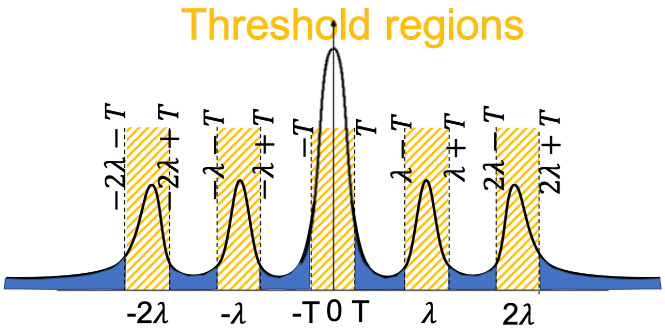

Figure 7.7. Five threshold regions for a single baseline monitor

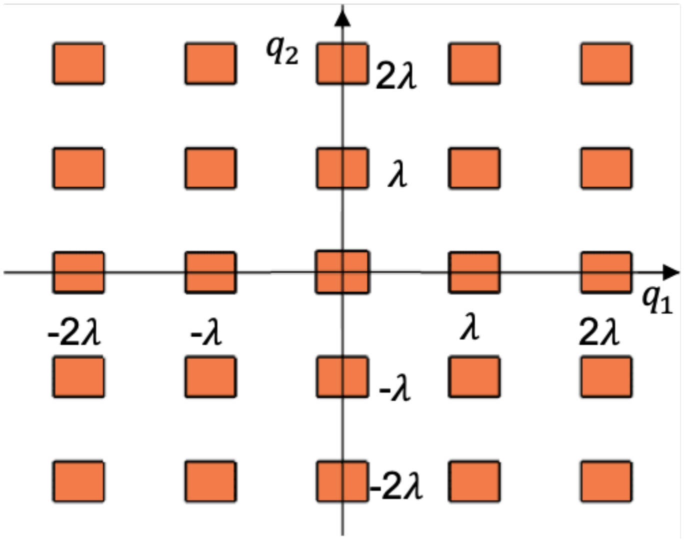

Figure 7.8. 25 threshold regions for a dual baseline monitor

different fault magnitudes, one concludes that as the fault magnitude slides along the fault slope in Figure 7.10, P_{MD} increases or peaks whenever the fault mean is close to or penetrates the threshold regions, respectively. Since the fault slope is proportional to baseline length ratio, we can vary the baseline lengths such that the fault slope avoids passing through the threshold regions in Figure 7.10. By optimization, it was found that baseline lengths of 176 m and 1 km result in a P_{MD} that meets the requirement (Figures 7.11 and 7.12). For this baseline combination, the required P_{FA} is achieved using a 439-s filtering period and a 36-mm threshold. The expansion

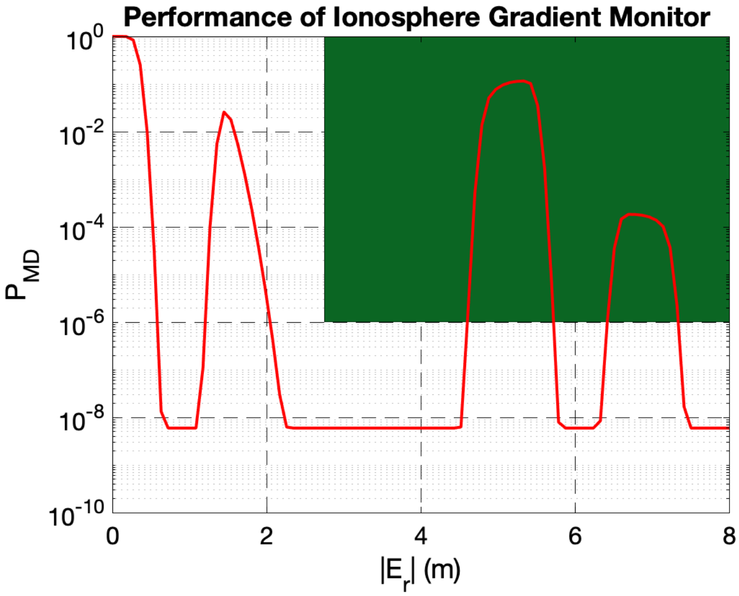

Figure 7.9. P_{MD} vs ranging error for the IGM using 285-m and 1-km baselines while considering the likelihood of ± 2 WIF

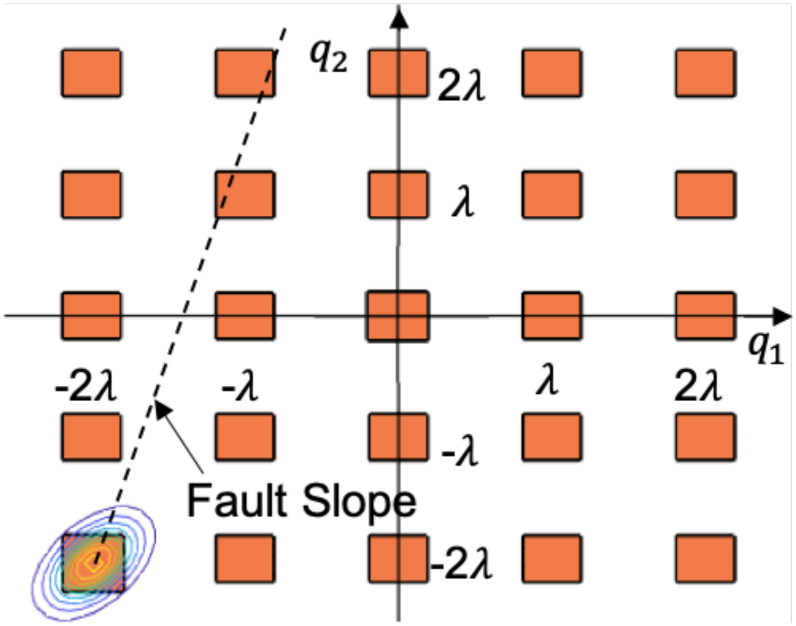

Figure 7.10. Fault slope in 285-m and 1-km baselines monitor for -2 WIF

of the threshold regions can also be applied to the ephemeris monitor. Only one optimized baseline length ratio (0.176) satisfies the required P_{MD} for IGM using the five threshold regions, but more options of baseline length ratio are possible for the

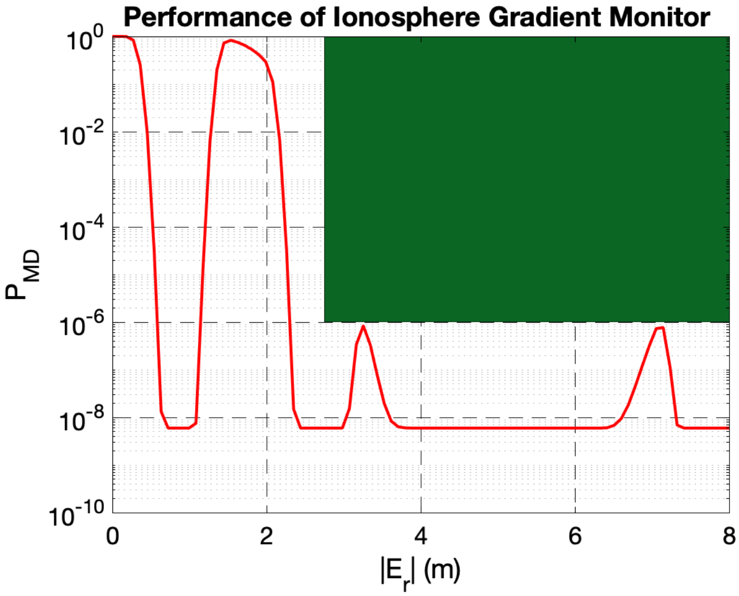

Figure 7.11. P_{MD} vs ranging error for the IGM using 176-m and 1-km baselines while considering the likelihood of ± 2 WIF

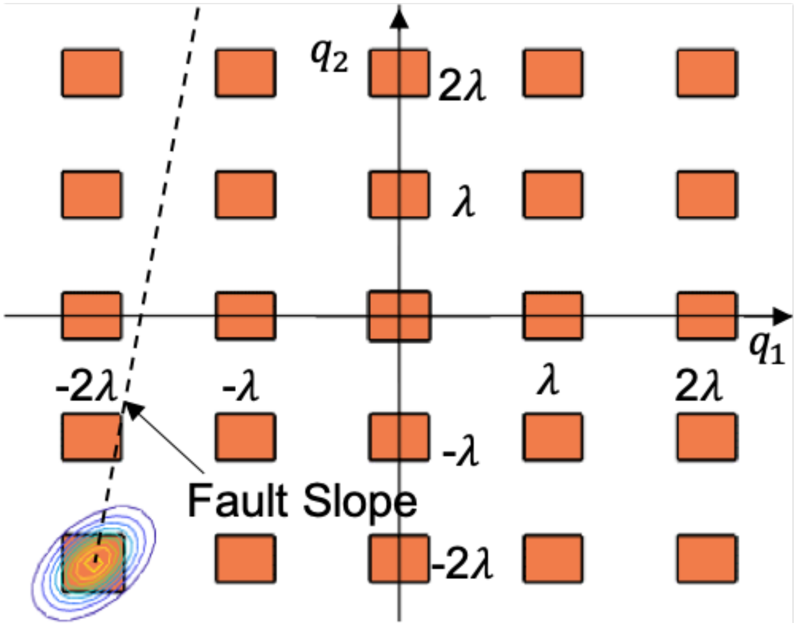

Figure 7.12. Optimal fault slope by selecting 176-m and 1-km baselines and illustrated for -2 WIF

ephemeris monitor. In contrast, the three threshold regions provide broader flexibility in the baseline length ratio (in the range of 0.24 to 0.32) at the expense of more extended filtering periods.

7.3 The SF monitor in the presence of tropospheric turbulence

The SF ephemeris monitor and IGM of Chapter 6 assume a nominal tropospheric delay that cancels out in the double difference carrier phase measurement. However, in recent years, short-duration localized neutral atmospheric disturbances, known as tropospheric turbulence, have been observed at multiple GBAS sites [107]. The nominal troposphere delay assumption fails in the presence of tropospheric turbulence, and it appears as a gradient in the test statistic. This means that even if ephemeris failures or ionospheric gradients are absent, the monitors may alarm simply due to the tropospheric turbulence. It is worth noting, however, that GBAS users are not affected by the small magnitude of tropospheric turbulence, but the GF must consider monitor triggers due to the extreme sensitivity of the carrier phase measurements.

There have been extensive studies on the behavior of tropospheric turbulence and its influence on the GBAS GF [108, 109]. It can be caused by multiple reasons such as strong wind shears, temperature gradients, unbalanced flow, mountain-waves, and gravity wave wind shear [110, 111]. In [112], the effect of tropospheric turbulence was observed to cause up to 10-cm residual error in differential carrier phase measurement. This residual error triggers an alarm in the double-difference carrier phase monitor [107]. Typically, tropospheric anomalies exist in the lower atmosphere and only affect small areas, and unlike ionospheric gradients, they do not scale with (baseline) distance.

Since tropospheric turbulence is a local effect, we propose using a replica baseline configuration (again, parallel to runway), but at a larger distance than the scale of tropospheric turbulence structures. For the dual-baseline configuration (b_{12} and

b_{13}) of Figure 7.1, a duplicate-baseline configuration (b_{45} and b_{46}) is utilized at an example 1-km distance (Figure 7.13). This orthogonal separation of 1 km allows us to assume tentatively that the tropospheric anomaly affects only one baseline configuration at a time; thus, the monitor is designed to alarm only if *both* configurations alarm:

$$\begin{aligned}
q_1^{\mathrm{IGM}} &= \Delta^2\phi_{1,2}^{i,j} - b_{12}^T\Delta e^{i,j} - \lambda\Delta^2 n_{12}^{ij} = b_{12}^T\alpha + \varepsilon_{\Delta^2\phi_{1,2}^{i,j}} \\
q_2^{\mathrm{IGM}} &= \Delta^2\phi_{1,3}^{i,j} - b_{13}^T\Delta e^{i,j} - \lambda\Delta^2 n_{13}^{ij} = b_{13}^T\alpha + \varepsilon_{\Delta^2\phi_{1,3}^{i,j}} \\
q_3^{\mathrm{IGM}} &= \Delta^2\phi_{4,5}^{i,j} - b_{45}^T\Delta e^{i,j} - \lambda\Delta^2 n_{45}^{ij} = b_{45}^T\alpha + \varepsilon_{\Delta^2\phi_{4,5}^{i,j}} \\
q_4^{\mathrm{IGM}} &= \Delta^2\phi_{4,6}^{i,j} - b_{46}^T\Delta e^{i,j} - \lambda\Delta^2 n_{46}^{ij} = b_{46}^T\alpha + \varepsilon_{\Delta^2\phi_{4,6}^{i,j}}
\end{aligned} \tag{7.9}$$

and the detection rule is

$$\text{if}\left\{\{q_1^{\mathrm{IGM}} \succ T\} \cup \{q_2^{\mathrm{IGM}} \succ T\}\right\} \cap \left\{\{q_3^{\mathrm{IGM}} \succ T\} \cup \{q_4^{\mathrm{IGM}} \succ T\}\right\} \rightarrow \text{alarm.}$$

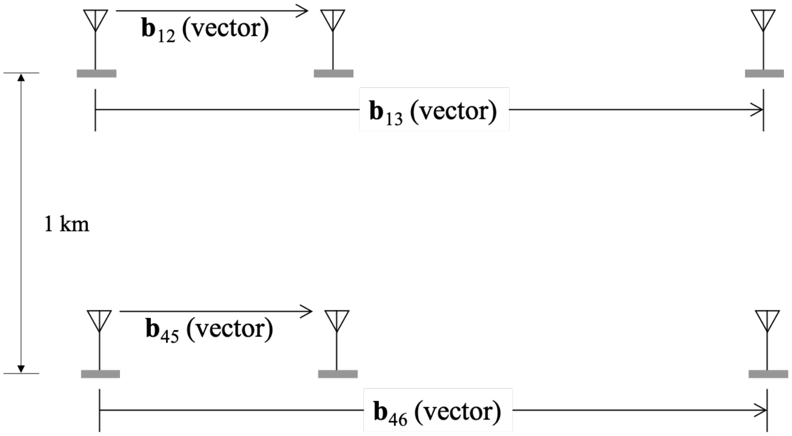

Figure 7.13. Illustration of the duplicate baselines to tackle tropospheric turbulence

The cycle ambiguity resolution within the ephemeris monitor is not impacted by tropospheric turbulence because it is eliminated in the difference between carrier and code phase measurements (Equation (6.12)). However, this is not the case for the IGM as ambiguities are resolved using carrier-plus-code measurements (Equation (6.16)). To account for tropospheric error in the ambiguity resolution, it is assumed that the differential error standard deviation due to tropospheric anomalies can be bounded by a Gaussian distribution with an example standard deviation of 15 mm. This 15 mm is used in computing the post-filtering ambiguity standard deviation that is then used in subsequent results. The example 15-mm σ needs to be validated, and in the case of increased number, it only affects the filtering period to get ambiguities.

The probability of FA and MD are given as

$$\begin{aligned} P_{\text{FA}} &= P\Big\{\big\{q_1 \succ T \cup q_2 \succ T\big\} \cap \big\{q_3 \succ T \cup q_4 \succ T\big\} \mid H_0\Big\} \\ &= P\Big\{q_1 \succ T \cup q_2 \succ T \mid H_0\Big\} P\Big\{q_3 \succ T \cup q_4 \succ T \mid H_0\Big\}, \end{aligned} \tag{7.10}$$

$$\begin{aligned} P_{\text{MD}} &= P\Big\{\big\{q_1 \prec T \cap q_2 \prec T\big\} \cup \big\{q_3 \prec T \cap q_4 \prec T\big\} \mid H_f\Big\} \\ &\leq P\Big\{q_1 \prec T \cap q_2 \prec T \mid H_f\Big\} + P\Big\{q_3 \prec T \cap q_4 \prec T \mid H_f\Big\}. \end{aligned} \tag{7.11}$$

Although the original and duplicate configurations are spatially separated, nominal ionospheric effects can cause correlation between the test statistics. However, in the FA analysis, we conservatively assume that test statistics q_1 and q_2 are independent from q_3 and q_4. The bounds for these probabilities can be derived similarly to Equations (7.3) and (7.4). The addition of a replica baseline configuration reduces the FA probability as the tropospheric turbulence is local and only impacts one of the two baselines, but the additional baseline impacts the probability of MD as illustrated in Equation (7.11). The resultant P_{MD} is larger in Equation (7.11) compared to Equation (7.11) due to the additional test statistics from the second configuration that might mis-detect.

Using Equation (7.10), a filtering period of 600 s is sufficient to meet the required P_{FA} for 285-m and 1-km baselines. However, the additional terms in Equation

(7.11) will cause the low probability portion of P_{MD} to be greater than the requirement. Therefore, increasing the filtering period to 1100 s is necessary to satisfy the MD requirement (Figure 7.14). The same baseline configuration with a 425-s filtering period was sufficient to meet the ephemeris monitor requirement as shown in Figure 7.15.

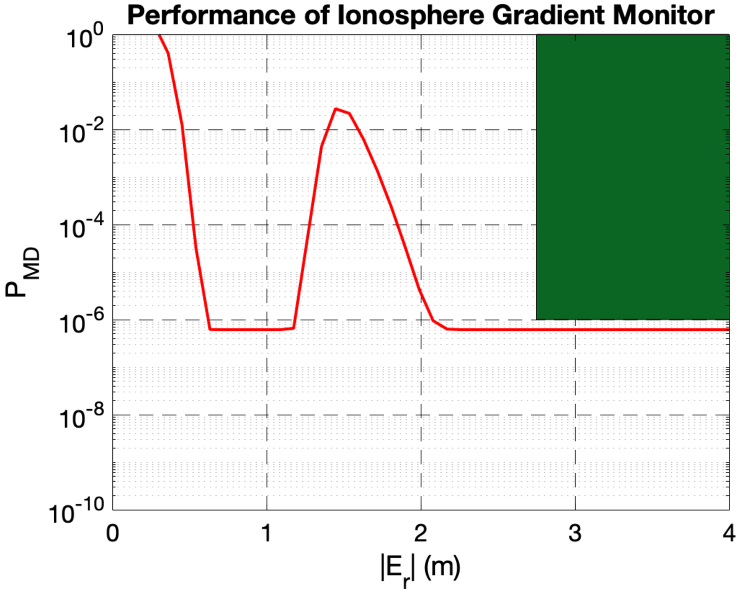

Figure 7.14. P_{MD} vs ranging error for the IGM under tropospheric turbulence using 285-m and 1-km baselines while considering the likelihood of ± 1 WIF

To sum up, this chapter provides detailed analysis of the SF ephemeris monitor and IGM. Depending on the GBAS site and performance requirements, baseline length and filtering period should be selected for a case of single long-baseline or dual short-baselines. The presence of troposphere turbulence is a rare event, but the proposed monitor is still able to perform fault detection efficiently.

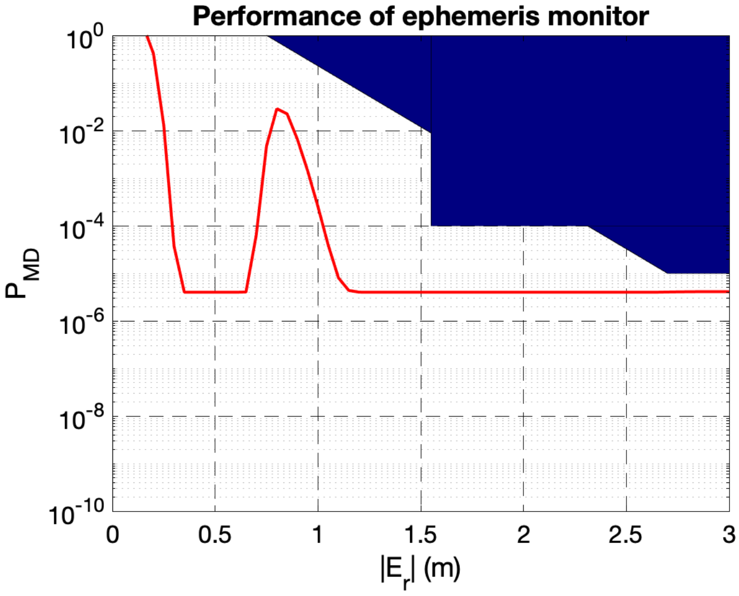

Figure 7.15. P_{MD} vs ranging error for the ephemeris monitor under tropospheric turbulence using 285-m and 1-km baselines pair while considering the likelihood of ± 1 WIF

CHAPTER 8

DF SPATIAL GRADIENT MONITOR FOR GBAS

This chapter investigates the effect of the upcoming GPS L5 frequency on improving the performance of SF spatial gradient monitors in Chapters 6 and 7. As discussed in the introduction, multiple constellations with dual-frequency (DF) signals will be operational in the near future and they have great potential to improve GBAS performance. Using only the GPS L1 and L5 signals, this chapter demonstrates the significant improvement it brings to gradient detection.

The introduction of dual frequency signals enables the removal of first order ionospheric delay at GBAS users without any support needed from the GBAS GF. However, it comes at a significant cost in the position solution as the resulting IF signal is noisier than the SF signal [113]. Thus, in order to service both SF and DF users, it will be assumed that SF is utilized for positioning by airborne users and the second frequency is used only for gradient detection at the GF [114]. Assuming GBAS users are relying on SF, this chapter describes how to use DF to detect ephemeris failures and ionospheric gradients for rising, newly acquired, and re-acquired satellites[6].

8.1 DF monitor concept

The double difference carrier phase measurement for satellites i and j using antennas k and l can be written, from Equations (6.1) and (6.7), as

$$\Delta^2\phi_{k,l}^{i,j} = \Delta^2 r_{k,l}^{i,j} + \Delta^2 T_{kl}^{ij} - \Delta^2 I_{kl}^{ij} + \lambda\Delta^2 n_{kl}^{ij} + \varepsilon_{\Delta^2\phi_{k,l}^{i,j}}. \tag{8.1}$$

---

[6] ©2020 IEEE. Reprinted, with permission, from J. Patel, “Detecting Hazardous Spacial Gradients at Satellite Acquisition in GBAS", *IEEE Transactions on Aerospace and Electronic Systems*, Aug 2020. [96].

Now, the measurement equations for L1 and L5 frequencies are written in units of cycles as

$$\Delta^2\varphi^{i,j}_{L1,k,l} = \frac{\Delta^2\phi^{i,j}_{L1,k,l}}{\lambda_{L1}} = \frac{1}{\lambda_{L1}}(\Delta^2 r^{i,j}_{k,l} + \Delta^2 T^{ij}_{kl} - \Delta^2 I^{ij}_{L1,kl}) + \Delta^2 n^{ij}_{L1,kl} + \frac{\varepsilon_{\Delta^2\phi^{i,j}_{L1,k,l}}}{\lambda_{L1}} \quad (8.2)$$

$$\Delta^2\varphi^{i,j}_{L5,k,l} = \frac{\Delta^2\phi^{i,j}_{L5,k,l}}{\lambda_{L5}} = \frac{1}{\lambda_{L5}}(\Delta^2 r^{i,j}_{k,l} + \Delta^2 T^{ij}_{kl} - \Delta^2 I^{ij}_{L5,kl}) + \Delta^2 n^{ij}_{L5,kl} + \frac{\varepsilon_{\Delta^2\phi^{i,j}_{L5,k,l}}}{\lambda_{L5}} \quad (8.3)$$

where, we assume that $\sigma(\varepsilon_{\Delta^2\phi^{i,j}_{L1,k,l}}) \approx \sigma(\varepsilon_{\Delta^2\phi^{i,j}_{L5,k,l}}) = \sigma(\varepsilon_{\Delta^2\phi^{ij}_{kl}})$, and $\sigma(\varepsilon_{\Delta^2\phi^{ij}_{kl}})$ is the standard deviation of the differential L1 carrier phase measurement error.

The so-called “widelane" measurement is constructed by subtracting Equation (8.3) from (8.2)

$$\begin{aligned} \Delta^2\varphi^{i,j}_{w,k,l} &\equiv \Delta^2\varphi^{i,j}_{L1,k,l} - \Delta^2\varphi^{ij}_{L5,kl} \\ &= \frac{1}{\lambda_w}(\Delta^2 r^{i,j}_{k,l} + \Delta^2 T^{ij}_{kl} + \frac{\lambda_{L5}}{\lambda_{L1}}\Delta^2 I^{ij}_{L1,kl}) + \Delta^2 n^{ij}_{w,kl} + \frac{1}{\lambda_w}\varepsilon_{\Delta^2\phi^{i,j}_{w,k,l}} \end{aligned} \quad (8.4)$$

where $\sigma(\varepsilon_{\Delta^2\phi^{i,j}_{w,k,l}}) = \sqrt{2}\sigma(\varepsilon_{\Delta^2\phi^{i,j}_{k,l}})$, and the wavelength of the widelane signal, about four times longer than the L1, is

$$\lambda_w = \frac{1}{\frac{1}{\lambda_{L1}} - \frac{1}{\lambda_{L5}}} = \frac{\lambda_{L1}\lambda_{L5}}{\lambda_{L5} - \lambda_{L1}} = 75.14 \text{ cm}.$$

Rewriting the widelane measurement in meters,

$$\Delta^2\phi^{i,j}_{w,k,l} = \lambda_w\Delta^2\varphi^{i,j}_{w,k,l} = \Delta^2 r^{i,j}_{k,l} + \Delta^2 T^{ij}_{kl} + \frac{\lambda_{L5}}{\lambda_{L1}}\Delta^2 I^{ij}_{L1,kl} + \lambda_w\Delta^2 n^{ij}_{w,kl} + \varepsilon_{\Delta^2\phi^{i,j}_{w,k,l}}. \quad (8.5)$$

8.1.1 DF ephemeris monitor. As stated in Subsection 6.1.1, the GF needs to detect only one satellite ephemeris failure at any given time. For example, a satellite i is considered as faulty while satellite j is fault-free, and the widelane measurement is written for antennas 1 and 2 as

$$\Delta^2\phi^{i,j}_{w,1,2} = b^T_{12}\Delta e^{i,j} + b^T_{12}\delta e_i + \Delta^2 T^{ij}_{12} + \lambda_w\Delta^2 n^{ij}_{w,12} + \varepsilon_{\Delta^2\phi^{i,j}_{w,1,2}}. \quad (8.6)$$

Similar to Equation (6.7), the differential range term is written as a function of the ephemeris fault vector, baseline length, and line of sight unit vector. The differential ionospheric delay is assumed nominal under the faulted ephemeris hypothesis. Assuming that the widelane ambiguities are known, which will be discussed in the following subsection, the test statistic can be formed as

$$\begin{aligned} q^{\text{EPH,DF}} &= \Delta^2\phi^{i,j}_{w,1,2} - b^T_{12}\Delta e^{i,j} - \lambda_w \Delta^2 n^{ij}_{w,12} \\ &= b^T_{12}\delta e_i + \Delta^2 T^{ij}_{12} + \varepsilon_{\Delta^2\phi^{i,j}_{w,1,2}} \\ &= b^T_{12}\delta e_i + \varepsilon_q \end{aligned} \tag{8.7}$$

In the development of the SF monitor, we presumed nominal troposphere and then added a parallel replica monitor to resolve tropospheric turbulence issues (Section 7.3). Here, in this DF monitor development, we will treat differential troposphere effects explicitly. The term ε_q represents the differential carrier phase error in the presence of a tropospheric anomaly.

8.1.2 DF IGM. Similarly, the widelane measurement, Equation (8.5), is utilized to detect instantaneous ionospheric gradients. Considering an affected satellite i and an unaffected satellite j, between antennas 1 and 2, the measurement equation becomes:

$$\Delta^2\phi^{i,j}_{w,1,2} = b^T_{12}\Delta e^{i,j} + \Delta^2 T^{ij}_{12} + \frac{\lambda_{L5}}{\lambda_{L1}}\Delta I^i_{L1} + \lambda_w \Delta^2 n^{ij}_{w,12} + \varepsilon_{\Delta^2\phi^{i,j}_{w,1,2}} \tag{8.8}$$

where ΔI^i_{L1} is the differential ionospheric error between antennas which is modeled using Equation (6.10). Therefore, the test statistics can be formed, assuming known ambiguities from Subsection (8.2), as

$$\begin{aligned} q^{\text{IGM,DF}} &= \Delta^2\phi^{i,j}_{w,1,2} - b^T_{12}\Delta e^{i,j} - \lambda_w \Delta^2 n^{ij}_{w,12} \\ &= \frac{\lambda_{L5}}{\lambda_{L1}} b^T_{12}\alpha + \Delta^2 T^{ij}_{12} + \varepsilon_{\Delta^2\phi^{ij}_{w,12}} \\ &= \frac{\lambda_{L5}}{\lambda_{L1}} b^T_{12}\alpha + \varepsilon_q . \end{aligned} \tag{8.9}$$

Comparing Equations (6.11) and (8.9), we can see that the test statistic $q^{\mathrm{IGM,DF}}$ benefits from a gain factor $\lambda_{L5}/\lambda_{L1}$ when the ionospheric front is present. However, the effect of tropospheric turbulence is considered directly in the distribution of fault-free test statistics, and $q^{\mathrm{IGM,DF}}$ will be less sensitive to spatial gradients compared to $q^{\mathrm{IGM,SF}}$.

8.2 DF monitor initialization

The widelane cycle ambiguity estimation must be constructed such that it is immune to ephemeris and ionospheric faults. Here, we seek the widelane ambiguity to compute test statistics in Equations (8.7) and (8.9). To get the widelane ambiguities, the “narrowlane" code is subtracted from the widelane carrier to form a geometry-free IF observable [115, 116].

$$\begin{aligned}\rho^i_{nr,k} =&\Big(\frac{\rho^i_{L1,k}}{\lambda_{L1}}+\frac{\rho^i_{L5,k}}{\lambda_{L5}}\Big)\Big(\frac{\lambda_{L1}\lambda_{L5}}{\lambda_{L1}+\lambda_{L5}}\Big)\\ =&r^i_k+dt^i+dt_k+T^i_k+\frac{\lambda_{L5}}{\lambda_{L1}}I^i_{L1,k}\\ &+\Big(\frac{\lambda_{L1}}{\lambda_{L1}+\lambda_{L5}}\Big)d^i_{f,\rho,k}+\Big(\frac{\lambda_{L1}\lambda_{L5}}{\lambda_{L1}+\lambda_{L5}}\Big)\Big(\frac{\varepsilon^i_{\rho_{L1,k}}}{\lambda_{L1}}+\frac{\varepsilon_{\rho^i_{L5,k}}}{\lambda_{L5}}\Big)\end{aligned} \tag{8.10}$$

$$\begin{aligned}\phi^i_{wr,k} =&\Big(\frac{\phi^i_{L1,k}}{\lambda_{L1}}-\frac{\phi^i_{L5,k}}{\lambda_{L5}}\Big)\Big(\frac{\lambda_{L1}\lambda_{L5}}{\lambda_{L5}-\lambda_{L1}}\Big)\\ =&r^i_k+dt^i+dt_k+T^i_k+\frac{\lambda_{L5}}{\lambda_{L1}}I^i_{L1,k}\\ &+\Big(\frac{\lambda_{L1}\lambda_{L5}}{\lambda_{L5}-\lambda_{L1}}\Big)(n^i_{L1,k}-n^i_{L5,k})-\Big(\frac{\lambda_{L1}}{\lambda_{L5}-\lambda_{L1}}\Big)d^i_{f,\phi,k}\\ &+\Big(\frac{\lambda_{L1}\lambda_{L5}}{\lambda_{L5}-\lambda_{L1}}\Big)\Big(\frac{\varepsilon^i_{\phi_{L1,k}}}{\lambda_{L1}}-\frac{\varepsilon_{\phi^i_{L5,k}}}{\lambda_{L5}}\Big)\end{aligned} \tag{8.11}$$

where,

r^i_k	is the true range from receiver k to satellite i,
dt^i	is i^{th} satellite's clock bias,
dt_k	is receiver k clock bias,
T^i_k	is tropospheric delay error,

$I^i_{L1,k}$ is L1-ionospheric delay error and,

$d^i_{f,\rho,k}$ & $d^i_{f,\phi,k}$ are inter-frequency biases for the code and carrier phase measurements, respectively, and

ε_{ρ_k} is raw code measurement error for receiver k.

$$\begin{aligned} Z^i_{\mathrm{GF},k} &= \phi^i_{wr,k} - \rho^i_{nr,k} \\ &= \left(\frac{\lambda_{L1}\lambda_{L5}}{\lambda_{L5}-\lambda_{L1}}\right)(n^i_{L1,k} - n^i_{L5,k}) + d^i_{\mathrm{GF},k} + \varepsilon_{Z^i_{\mathrm{GF},k}} \qquad (8.12) \\ &= \lambda_w n^i_{w,k} + d^i_{\mathrm{GF},k} + \varepsilon_{Z^i_{\mathrm{GF},k}} \end{aligned}$$

where,

$Z^i_{\mathrm{GF},k}$ is a geometry-free IF measurement for satellite i and antenna k,

$d^i_{\mathrm{GF},k}$ is a geometry-free IF inter-frequency bias;

$$d^i_{\mathrm{GF},k} = \left(\frac{\lambda_{L1}}{\lambda_{L1}-\lambda_{L5}}\right)d^i_{f,\phi,k} - \left(\frac{\lambda_{L1}}{\lambda_{L1}+\lambda_{L5}}\right)d^i_{f,\rho,k},$$

$\varepsilon_{Z^i_{\mathrm{GF},k}}$ accounts for the multipath and other error in the measurement with a variance ($\sigma^2_{Z_{\mathrm{GF}}}$). In this analysis, we assume that the measurement errors on L1 and L5 are independent.

$$\sigma^2_{Z_{\mathrm{GF}}} = \lambda_w^2\left[\left(\frac{\sigma^2_{\phi_{L1}}}{\lambda^2_{L1}} + \frac{\sigma^2_{\phi_{L5}}}{\lambda^2_{L5}}\right) + \left(\frac{\lambda_{L5}-\lambda_{L1}}{\lambda_{L1}+\lambda_{L5}}\right)^2\left(\frac{\sigma^2_{\rho_{L1}}}{\lambda^2_{L1}} + \frac{\sigma^2_{\rho_{L5}}}{\lambda^2_{L5}}\right)\right]$$

where,

$\sigma^2_{Z_{\mathrm{GF}}}$ is the geometry free variance,

$\sigma^2_{\phi_{L1}}, \sigma^2_{\phi_{L5}}$ are the L1 and L5 raw carrier phase noise variances,

$\sigma^2_{\rho_{L1}}, \sigma^2_{\rho_{L5}}$ are L1 and L5 raw code phase noise variances.

The inter-frequency bias term in Equation (8.12) can be eliminated using double differencing between two satellites and two antennas. Thus, the geometry-free measurement for faulty satellite i and fault-free (previously monitor-validated) satellite j using antennas k and l is written as

$$\Delta^2 Z^{i,j}_{\mathrm{GF},k,l} = \lambda_w \Delta^2 n^{i,j}_{w,k,l} + \varepsilon_{\Delta^2 Z^{i,j}_{\mathrm{GF},k,l}} \tag{8.13}$$

and its variance as

$$\sigma^2_{\Delta^2 Z_{\mathrm{GF}}} = \lambda_w^2 \left[\left(\frac{\sigma^2_{\Delta^2 \phi_{L1}}}{\lambda^2_{L1}} + \frac{\sigma^2_{\Delta^2 \phi_{L5}}}{\lambda^2_{L5}} \right) + \left(\frac{\lambda_{L5} - \lambda_{L1}}{\lambda_{L1} + \lambda_{L5}} \right)^2 \left(\frac{\sigma^2_{\Delta^2 \rho_{L1}}}{\lambda^2_{L1}} + \frac{\sigma^2_{\Delta^2 \rho_{L5}}}{\lambda^2_{L5}} \right) \right]. \tag{8.14}$$

Filtering $\Delta^2 Z_{GF}$ reduces the effect of measurement errors and may allow resolution of the widelane ambiguity term in Equation (8.13). Due to the longer wavelength compared to the SF case, a shorter filtering period is sufficient to get acceptable correct widelane ambiguities.

$$\Delta^2 \hat{n}^{i,j}_{w,k,l} = \frac{\sum \Delta^2 Z^{i,,j}_{\mathrm{GF},k,l}}{\mathbb{T}} = \Delta^2 n^{i,j}_{w,k,l} + \varepsilon_{\Delta^2 \hat{n}_w} \tag{8.15}$$

where $\mathbb{T}$ is the number of independent samples considering an error correlation time of 2 s (Appendix G) and

$$\varepsilon_{\Delta^2 \hat{n}^{i,j}_{w,k,l}} \sim \mathcal{N}\left(0, \frac{\sigma_{\Delta^2 Z_{GF}}}{\sqrt{\mathbb{T}}}\right). \tag{8.16}$$

8.3 Performance Evaluation of DF monitors

Since the test statistics of the DF monitor behave similarly to the SF monitor in the event of spatial gradients, the derivation of FA and MD probabilities can be retrieved from Subsection 6.3. The key difference in the DF monitor is that test statistics require the widelane cycle ambiguity. Since the wavelength of the widelane signal is much larger (approximately four times) than the L1 frequency, the resolution of the widelane cycle ambiguity is much faster than the L1 cycle ambiguity. Using the same measurement error models as the L1 frequency, the likelihood is high that CIF is sufficient to meet FA requirements for the DF monitor—no need for multiple threshold regions. Finally, FA and MD probabilities of the DF monitor can be expressed as shown in Equations (6.22) and (8.17), respectively.

$$P_{\mathrm{MD}} \leq P\Big\{q < T \mid H_f, CIF\Big\} P\{CIF\} + \Big(1 - P\{CIF\}\Big) \tag{8.17}$$

In this analysis, we evaluated the DF monitor performance relative to the same GAST-D requirements as before for ephemeris faults and ionospheric fronts (Subsection 6.4). Actual DF GBAS requirements have not been developed yet and may differ. For the future L5 frequency, we utilized the same error model as the one used for the L1 frequency: the CDF of the double difference carrier phase measurement error can be overbounded by a zero-mean Gaussian distribution with a standard deviation of 6 mm, and the double difference pseudorange is bounded by a standard deviation of 84 cm with autocorrelation time constant of 2 s [104]. To also account for potential tropospheric turbulence, we assume that ε_q in Equations (8.7) and (8.9) is bounded by a zero-mean Gaussian distribution with a standard deviation of 15 mm. This will result in a larger threshold to meet FA requirements. Also, the cycle resolution step is inherently immune to tropospheric delay in the DF approach.

To illustrate the performance of the DF monitor, a 600-m baseline is used as an example. Under the fault-free hypothesis, Equations (8.7) and (8.9) are identical. Thus, using Equation (6.22), a filtering period of 337 s and a threshold of 94 mm are adequate to meet the probability of FA requirement.

Under the fault hypothesis, P_{MD} of the DF ephemeris monitor is evaluated and shown in Figure 8.1. Compared to the SF ephemeris monitor, a single shorter baseline is sufficient to meet P_{MD} requirements. Figure 8.2 shows the DF monitor performance when a longer baseline of 1 km is used (as in the SF case).

Similarly, the DF IGM also outperforms the SF monitor as illustrated in Figures 8.3 and 8.4 for the same two example baselines used in Figures 8.1 and 8.2. Overall, the benefit of the DF monitor is obvious as observed in faster cycle ambigu-

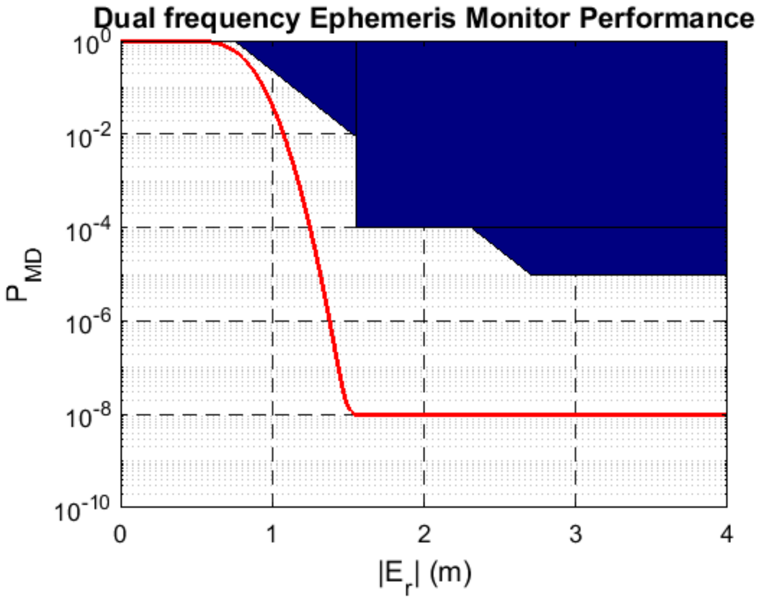

Figure 8.1. P_{MD} vs ranging error for the ephemeris monitor using 600-m baseline and $\sigma_q \sim \mathcal{N}(0, 15 \text{ mm})$

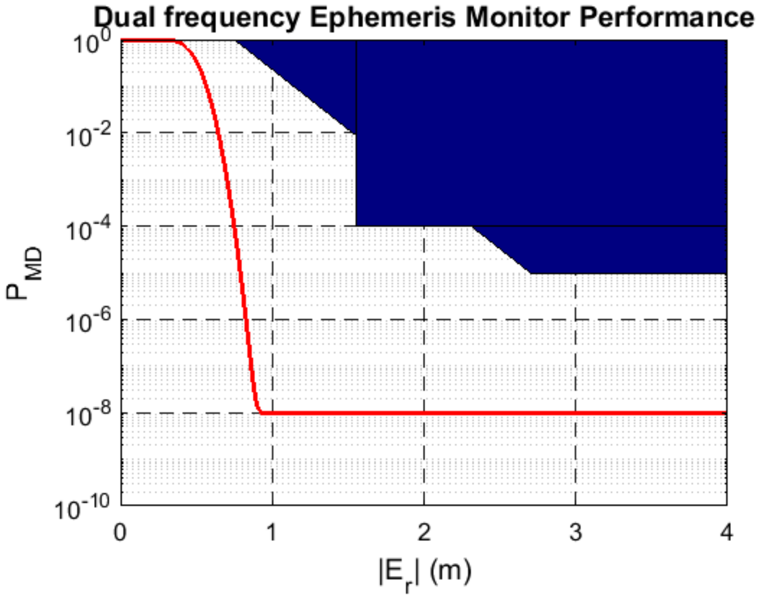

Figure 8.2. P_{MD} vs ranging error for the ephemeris monitor using 1-km baseline and $\sigma_q \sim \mathcal{N}(0, 15 \text{ mm})$

ity resolution and no need for additional threshold regions. If one wishes to further reduce filtering time in the DF implementation, the multiple threshold idea can be utilized.

These results are based on our assumption that ε_q is bounded with a standard deviation of 15 mm. This assumption must be validated for GBAS by post-processing measurements collected in the presence of tropospheric turbulence. To illustrate the monitor's sensitivity to this parameter, the standard deviation of the residual error is increased from 15 mm to 30 mm. In this case, a filtering period of 420 s with an increased threshold of 172 mm are sufficient to satisfy the FA requirements for the ephemeris monitor as well as IGM. The probability of MD for a 1-km baseline is shown in Figures (8.5) and (8.6) for the ephemeris monitor and IGM, respectively. Although the performance is degraded compared to Figures (8.2) and (8.4), the detection requirements are still satisfied.

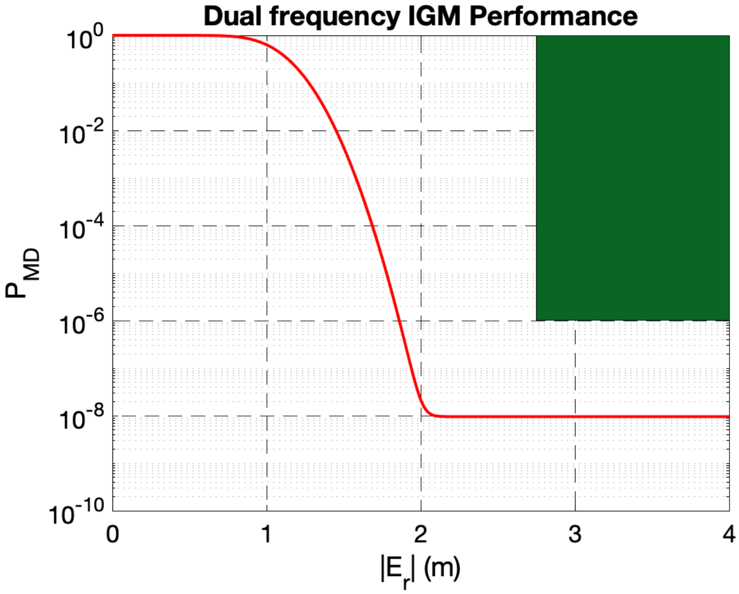

Figure 8.3. P_{MD} vs ranging error for the IGM using 600-m baseline and $\sigma_q \sim \mathcal{N}(0, 15\text{ mm})$

To sum up, the availability of DF measurements at the GBAS GF leads to significant monitor performance and operational benefits. The mitigation of FAs due to tropospheric turbulence is handled directly by the test statistics via an increased threshold.

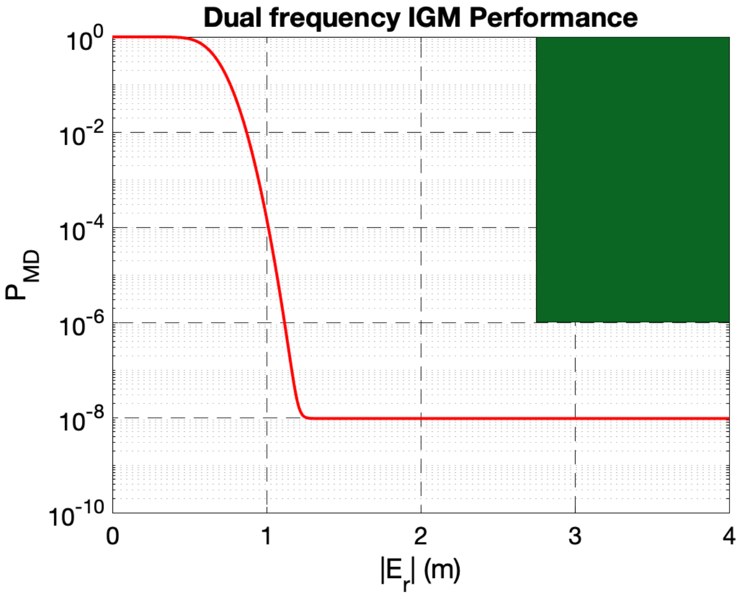

Figure 8.4. P_{MD} vs ranging error for the IGM using 1-km baseline and $\sigma_q \sim \mathscr{N}(0, 15\ \mathrm{mm})$

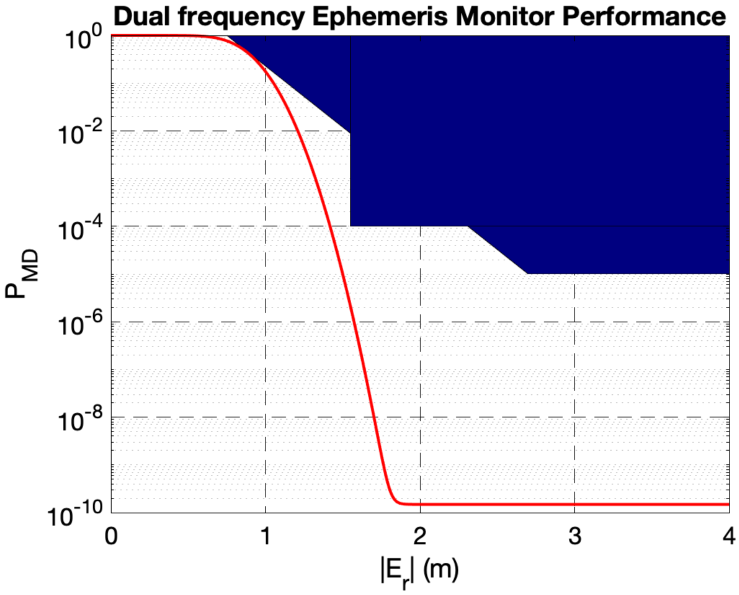

Figure 8.5. P_{MD} vs ranging error for the ephemeris monitor using 1-km baseline for $\sigma_q \sim \mathscr{N}(0, 30\ \mathrm{mm})$

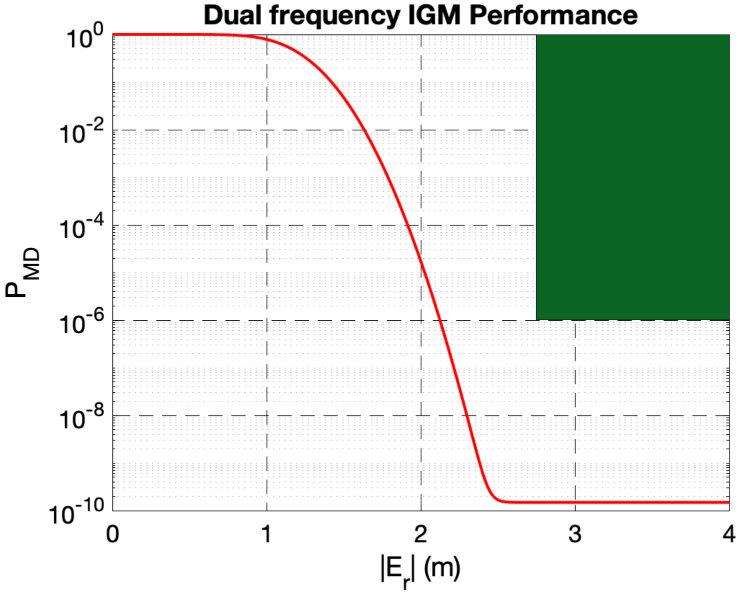

Figure 8.6. P_{MD} vs ranging error for the IGM using 1-km baseline for $\sigma_q \sim \mathscr{N}(0, 30\text{ mm})$

CHAPTER 9

CONCLUSION

As seen in Chapter 2, GNSS is self-sufficient to provide worldwide navigation. GNSS users simply decode broadcast signals from satellites and are able to determine their position. This dissertation specifically focuses on aircraft navigation for precision approach and landing where integrity of obtained aircraft positions is critical. The dissertation contributions enhance ground operations of ARAIM and GBAS to ultimately support critical approach and landing phases of aircraft.

9.1 Summary of accomplishments for ARAIM OFM

The ARAIM algorithm is inspired from operational RAIM which supports the en route phase of aircraft flight using single-frequency GPS signals. Since multiple constellations with dual-frequencies have emerged in the past decade, ARAIM is intended to exploit largely available GNSS measurements and to support precision approach and landing operations. The core principle of ARAIM and RAIM is to perform consistency checks among all collected GNSS signals to detect any outliers in them, i.e., provides fault-free position solutions. In traditional RAIM, CSP provided statistics of ranging errors were hardcoded in receivers, while ARAIM will have that necessary information via the Integrity Support Message (ISM). The ISM is generated via dedicated OFM at ground and updated periodically to satellites whenever needed.

Two dissertation contributions enable the operation of ARAIM OFM which shares a responsibility to provide statistics of range errors caused by satellite position and clock errors. This includes Gaussian parameters ($b_{\mathrm{nom}}, \sigma_{\mathrm{URA}}$) to provide realistic bounds on range errors and fault probabilities ($P_{\mathrm{SAT}}, P_{\mathrm{CONST}}$) to consider the failure of a satellite and a constellation; all terms together are known as Integrity Support

Data (ISD). ARAIM OFM analyzes all historical broadcast navigation messages to characterize range errors for each constellation and generates ISD. Since OFM is not connected to ARAIM users in real time, OFM needs to ensure that generated ISD will be valid over a certain period. In the first contribution, a new method is developed to estimate accurate satellite position and clock bias such that the historical broadcast navigation message can be evaluated. In the second contribution, a new approach is proposed to characterize satellite position errors directly from broadcast ephemeris errors.

9.1.1 Estimation of accurate GPS satellite position and clock bias . Unlike traditional cumbersome satellite-orbit determination, a simple and transparent estimator is developed and demonstrated to provide a truth satellite position and clock reference for ARAIM OFM. A computationally efficient Information Smoother (IS) is designed to estimate satellite position, in terms of ephemeris parameters and clock biases. The IS relies only on GNSS range measurements, collected from a sparsely distributed global reference receiver network, and a few error models; the necessary error models are developed and validated using experimental data. The IS is prototyped for the GPS constellation with experimental data, which includes step-by-step guidance for extension to other constellations. The estimated GPS LNAV ephemeris parameters and satellite clock biases are compared to IGS's provided orbit and clock product for its validation. The resulting estimate errors in satellite position, clock bias and range are explained in detail and are evaluated over ten days. Statistically, the range errors produced by the estimated LNAV ephemeris parameters and clock biases are consistently accurate up to 50 cm ($\pm 1\sigma$), tightly matching with the predicted covariance from the IS.

9.1.2 Analysis of broadcast GPS ephemeris errors. Once precise satellite positions and clock biases are available in ARAIM OFM, this contribution demonstrates how to evaluate the nominal range error characteristic (b_{nom}, σ_{URA}). For the first time, there is a possibility to have truth ephemeris parameters due to the first contribution. Thus, an effort is made to understand the nature of range error caused by orbital-ephemeris-parameter errors directly. As an example, one GPS satellite is discussed in more detail to understand the behavior of LNAV ephemeris and to characterize the resulting LNAV ephemeris errors. A simple LNAV ephemeris model ($b_{\text{LNAV}}, \sigma_{\text{LNAV}}$) is generated from observed LNAV ephemeris errors, and then a new method is proposed to predict range-error bounds from the developed b_{LNAV} and σ_{LNAV} parameters. In this preliminary analysis, the predicted σ_{URA} closely matches prior works.

9.2 Summary of accomplishments for GBAS

GBAS is designed to support the landing phase of aircraft navigation with minimum ground infrastructures. Specifically, this dissertation helps to enable the Category III landing phase. At a GBAS Ground Facility (GF), GNSS antennas are placed at a precisely surveyed location to collect range measurements. Then, differential corrections are generated and broadcast to close-proximity aircraft to improve their position estimate during landing operation. At the same time, GF locally monitors any threats which could cause unreliable aircraft position estimates due to GNSS or GBAS failures. In this dissertation, two major threats are detected in real-time. The first is due to an inaccurate satellite position in a broadcast navigation message. The second is a hazardous ionospheric front caused by intense ionospheric activity in a small region.

9.2.1 Detection of inaccurate satellite position and hazardous ionospheric fronts. Through this dissertation, for the first time, GBAS GF has a methodology to ensure fault-free satellite acquisition in GBAS. Prior methods had a blind spot in detection due to carrier phase cycle ambiguity, but here, a cycle ambiguity resolution is proposed for each fault type such that obtained ambiguities are immune to faults.

Ambiguity resolution with high integrity requires at least ten minutes to start monitoring fault events. The core idea is to obtain limited knowledge of cycle ambiguities in a short time and handle them through a unique fault-monitor design.

In the first part of development, GBAS GF is assumed to have single frequency GNSS range measurements through multiple spatially separated ground antennas. The limited single frequency measurements help to demonstrate different practical limitations in GBAS, and all feasible design choices are presented. The proposed monitor uses differential carrier phase measurements to form a test statistic. Satellite-position failures and ionospheric fronts will have two separate test statistics to monitor both fault events in real-time. The advantage of the proposed solutions is that both fault events are monitored using the same ground infrastructure; only the signal processing scheme is different, and the necessary correlation is considered in the design. Detailed analysis is performed to optimize design parameters, such as ambiguity resolution time and a baseline distance between two antennas. It allows each GBAS GF to make unique decisions in implementation for worldwide airports; for example, some airports may have geographical space limitations. Later, the availability of dual-frequency ranging measurements illustrates the reduced complexity compared to single-frequency monitors. The dual-frequency monitor design is slightly different and provides significant improvement in fault-detection.

9.3 Recommended topics for Future Research

A number of recommendations for future work are given in the following subsections for further enhancement of each contribution.

9.3.1 Enhancing the concept of estimating satellite position and clock biases. The first contribution is an initial step to demonstrate the feasibility of a simple estimator (IS) without involving a complex orbit determination process. The achieved range accuracy of estimated satellite positions and clock biases ($\sigma_{\mathrm{OFM}} = 0.5$ m) is remarkable with simple GNSS measurements and the LNAV orbital model. However, a few additional approaches can be considered to improve the estimation performance. The list below provides future research directions which can be investigated separately, and then integrated into IS.

1) If the filtering-window of IS is extended for a longer period, estimation accuracy can be further improved. For example, Subsection 3.4.3 demonstrates the benefits of CNAV ephemeris parameters through covariance analysis. The next immediate step is to incorporate the CNAV model. One can also explore an alternative model to represent full satellite orbit. Being an offline estimation process, there is no constraint on number of orbital parameters or using unconventional orbit models.

2) IS mainly relies on code measurements to get absolute range information. If any un-modeled or systematic error exists in code measurement, it would negatively impact estimated orbit and clock biases. For example, Section 4.3 demonstrates the DCB residual which causes an additional code bias. The initial study in the current work only demonstrates its presence and acknowledges it in IS. However, given the goal of OFM to reduce b_{nom} as much as possible, it is highly recommended to characterize the DCB residuals based on receiver design such that they can be corrected in IS. [117] provides a study of characterizing DCB residuals for IGS stations.

3) In the current IS implementation, Differential Code group delay Bias (DCB) is obtained from IGS for demonstrating the estimation concept. However, any dependence on external organizations should be avoided for ANSP. [118] explains the methodology used in producing the IGS DCB product. Thus, the same network of estimating orbit and clock bias can be used for generating DCB estimates in OFM. The challenge could be to achieve an accurate DCB with limited RGS compared to IGS stations. It is recommended to perform covariance analysis first to demonstrate

the feasibility of independent DCB estimates.

4) The selected Reference Ground Stations (RGSs) are simply picked from the IGS station list to cover the visibility of GPS satellites. A separate study would be necessary for optimal placement of RGS worldwide; especially, when ANSP would have a choice in placing RGSs. This selection is more critical for estimating satellite clock biases as they are estimated instantaneously for each epoch. Thus, any unavailable measurements from RGS would directly impact the ability to estimate clock biases; the performance of orbit estimation would degrade, but at least continuous orbit is possible through the orbital model.

5) Based on this experience of analyzing GPS measurements from GBAS ground stations, the quality of IGS measurements are relatively poor. If ANSP has a choice, they should pick a consistent antenna and receiver pair in a ground network which would provide better measurement quality. One can simply check the covariance analysis (Section 3.4) to see potential benefits. Also, the earlier discussed DCB residuals could be reduced if a network has similar receivers [117].

9.3.2 ISD generation in ARAIM OFM. Methodologies are available for generating ISD once the truth satellite position and clock biases are available for large datasets, but quantifying and capturing the distribution of range errors is challenging in the short-operational period of satellites. In addition, ISD must be valid for a certain future time-period as OFM is not connected to ARAIM users in real-time. If any anomaly occurs, a methodology is required to efficiently update ISD as quickly as possible within a necessary observation period. That is why effort is made in this dissertation to understand the true nature of range errors from broadcast ephemeris parameter errors. A few open questions are listed below that could be helpful in enhancing the understanding of range errors, and ultimately result in better design choice in ARAIM OFM.

1) In this dissertation, broadcast ephemeris errors are evaluated for four years, and then the error model is generated. However, for ARAIM OFM, a methodology is needed to pick an observation period to generate the ephemeris error model. [28, Chapter 5] showed that satellite position errors are correlated over a day, which may not provide sufficient knowledge due to limited sample points of ephemeris errors. Thus, a method is required to quantify the accuracy of the ephemeris error model and to find out the necessary observation period in modeling.

2) CSP predicts satellite orbit and generates a set of ephemerides to represent satellite orbit. Then, the sets of ephemerides are uploaded to the satellite and are broadcast to GNSS users one by one. Since ephemerides are uploaded together, they may have correlation in user-experienced range errors. Figures 5.16 and 5.17 discussed the preliminary results to demonstrate the effect on range errors against elapsed time from upload. It appears that range errors are correlated within an uploaded ephemerides set, but detailed investigation is needed to explore the relationship.

3) Since the prediction methodology of satellite orbit is unknown from CSP, we are not able to claim anything about how ephemeris sets are correlated from one satellite to another. In this dissertation, a methodology is proposed with an assumption that ephemerides are independent among satellites. It is recommended to verify this assumption. The worst-case scenario could be a faulty ephemeris contributing its residual to other satellites on top of their nominal ephemeris errors.

9.3.3 Improvement in spatial-fault detection. The GBAS contributions are focused to enhance fault detection capability for an ideal single runway. Different design parameters and antenna placements are optimized for this single runway. However, GBAS is aimed to support multiple runways in any direction with a few antennas in place. Thus, there is a need to expand the proposed fault-detection monitor to support aircraft landing on multiple runways simultaneously. This will be more favorable for GBAS operations such as curved flight approach and efficient air-traffic management.

One of the major dissertation contributions is to resolve carrier phase cycle ambiguities in a short period to quickly start monitoring faults. It was shown that limited knowledge on ambiguity resolution can be used for efficient fault monitoring. Until the ambiguity resolution process has completed for a satellite, GBAS GF has to wait for monitoring, and the satellite may not be used by GBAS users. Thus, it is ideal to reduce ambiguity resolution time as much as possible with different techniques. For example, the LAMBDA method can be considered instead of the used rounding approach.

Tropospheric turbulence is a nuisance event which significantly causes false-alarm in carrier-phase measurement based monitors. Here, in this dissertation, available information of tropospheric turbulence is used to make an educated assumption. Given the scope of GBAS to worldwide airports, more quantitative knowledge is needed for different regions to characterize the nature of tropospheric turbulence in worst-case scenarios.

APPENDIX A

COMPUTING THE NUMERICAL JACOBIAN MATRIX OF THE LNAV MODEL

We consider a numerical approach to compute the Jacobian matrix due to its simplicity compared to the theoretical derivation; one can refer to [119, pp 185-189] for a theoretical approach. However, the derivative using the Newton's difference quotient method (two-point estimation) requires a small deviation as an input which directly contributes to derivative errors. To minimize derivative errors, we use Equation (A.1) which is known as the four-point estimation [120, pp 100-101].

$$\frac{df}{dp} = \frac{f(p - 2\Delta p) - 8f(p - \Delta p) + 8f(p + \Delta p) - f(p + 2\Delta p)}{12\Delta p} \tag{A.1}$$

where, p is an orbital parameter, and Δp is an input small deviation.

Moreover, choosing an appropriate small deviation (Δp) is also crucial. If we choose a larger Δp, it will produce an inaccurate derivative. On the other hand, choosing a very small value introduces rounding errors. Instead, we utilize the Richardson extrapolation method to achieve precise derivatives [121]. In this method, we input Δp and a required precision limit (ϵ) on the derivative, and Δp is automatically adjusted to achieve the precise derivative. The suitable input Δp for the LNAV model is validated and listed in Table A.1.

Table A.1. Inputs (small deviation) to compute Jacobian matrix using the Richardson extrapolation method

	orbital parameter	Δp	ϵ
1	M_0	10^{-2}	10^{-3}
2	Δn	10^{-6}	100
3	e	10^{-5}	1
4	$\sqrt{A}$	1	10^{-1}
5	Ω_0	10^{-2}	10^{-3}
6	i_0	10^{-2}	10^{-3}
7	ω	10^{-2}	10^{-3}
8	$\dot{\Omega}$	10^{-6}	1
9	IDOT	10^{-6}	1
10	Cuc	10^{-2}	1
11	Cus	10^{-2}	1
12	Crc	1	10^{-7}
13	Crs	1	10^{-7}
14	Cic	10^{-2}	1
15	Cis	10^{-2}	1

APPENDIX B

IMPROVING THE CONDITIONING OF THE INFORMATION MATRIX

As discussed in Subsection 3.2.3, the Information Smoother (IS) faces numerical issues while inverting the information matrix due to its ill-condition. The solution is that the state vector corresponding to orbital parameters is scaled using Table B.1 such that the information matrix will have better conditioning for the inverse operation. At the end of IS, the orbital parameters of interest are obtained by dividing the same scaling factor into the estimated orbital state vector.

Table B.1. Scaling Factor (multiplier) to modified equinoctial elements

	Parameter	Scaling Factor
1	L	3×10^6
2	Δn	13×10^9
3	e_X	5×10^6
4	$\sqrt{A}$	16×10^2
5	Ω	2.5×10^6
6	i_0	2.3×10^6
7	e_Y	5×10^6
8	$\dot{\Omega}$	1.1×10^{10}
9	IDOT	9×10^9
10	Cuc	2×10^6
11	Cus	2×10^6
12	Crc	8×10^{-2}
13	Crs	8×10^{-2}
14	Cic	1.5×10^6
15	Cis	1.5×10^6

APPENDIX C

SELECTION CRITERIA FOR AN IGS STATION IN ARAIM OFM

The following steps are suggested to include an IGS station. The first few steps are a quick check from the IGS website to get a rough estimate of measurement quality, and then the additional steps will help us to make a final decision by observing specific errors.

Step (1): Select a site which has an RMS multipath value lower than 0.5 m for each frequency [122]. An RMS multipath value can be accepted up to 1 m if there is no other site nearby.

Step (2): Ensure the availability of antenna location and its phase center offset values in the SINEX file for the selected site [77].

Step (3): After fulfilling the previous two steps, download the RINEX 2.11 file containing raw ranging measurements. Ensure the availability of interested measurement types and notice the $\mathrm{C/N_0}$ values in the file. The L1 signal must roughly measure above 35 dBHz to indicate good quality of recorded measurements. In the absent of $\mathrm{C/N_0}$ or lower values, the first suggestion is to avoid the site, but if one must consider the site, only accept it after observing code and carrier phase multipath.

Step (4): Compute IF code multipath as suggested in Subsection 4.2.1. Ensure that code multipath values are close to the expected RMS value from Step 1. If code multipath is significantly high, specifically below 20-deg elevation angle, avoid the site.

Step (5): Currently, a model for the site dependent code GDV is not available. So, select the site having an antenna type from [66] such that its effects are minimum and known. Once the GDV model is available, this step can be avoided.

Step (6): Since the effect of signal deformation on code measurements is still under investigation for different receiver types, we suggested an alternative analysis in Section 4.3 to observe resulting code biases. Perform the similar analysis and ensure consistent code biases for a new site. If a transient bias exists (like Figure 4.14), avoid the site as it will have adverse effects in the estimation.

Step (7): This step is mainly to ensure measurement quality from low and high latitude sites. Both locations are susceptible to ionospheric scintillation on a regular basis, which leads to poor tracking and recording of measurements. Thus, in this step, carrier multipath is observed for a quality check. The magnitude of carrier multipath is not important, but any unexpected large number, more than a quarter of the carrier wavelength, would indicate the poor receiver quality.

APPENDIX D

HIGH-PASS FILTER FOR OBSERVING DIFFERENTIAL CARRIER MULTIPATH

Usually, carrier multipath is observed by computing double-difference (DD) carrier phase measurements, which are the combination between two closely-located antennas and two satellites. However, the IGS network has mostly single antenna sites. Thus, observing DD carrier multipath is not possible for IGS RGSs. Instead, we propose a highpass filter to observe differential carrier multipath by leveraging dual-frequency carrier measurements. Specifically, the GPS L1 carrier signal is subtracted from the GPS L2 carrier signal to remove the majority of range errors, and we are left with ionospheric delay, cycle ambiguity, and differential carrier multipath. Then, the digital highpass filter with a cut-off frequency (f_c) of 1.66 mHz (10 min) is employed to extract differential carrier multipath from L1 minus L2 (L1mL2) carrier measurements. In the following paragraph, we consider a specific site which has dual-frequency measurements from two closely-located antennas such that conventional DD and differential carrier multipath can be evaluated and compared. The last paragraph discusses the reason behind selecting the 1.66-mHz cut-off frequency.

From prior work [50], dual-frequency GPS measurements collected from 82-m separated (two) antennas are used here. As discussed in [50], DD carrier multipath is computed between two satellites and two antennas for GPS L1 carrier phase measurement and shown in Figure D.1; Figure D.3 shows the same DD carrier multipath depending on elevation angle. Now, the proposed highpass filter (f_c=1.66 mHz) is implemented on GPS L1 minus GPS L2 carrier phase measurements. As a result, differential carrier multipath is obtained and shown in Figure D.2. By comparing Figures D.1 and D.2, we conclude that both methods produce closely matching carrier multipath. Furthermore, the comparison with elevation angle is also shown in Figures D.3 and D.4. The only limitation of the highpass filter method is that the low frequency content of antenna phase center is removed, but the magnitude of carrier multipath is still observable.

Differential carrier multipath using the highpass filter method has only one designed variable: cut-off frequency (f_c). The selection of f_c is crucial as incorrect f_c would lead to either ionospheric content in differential carrier multipath or removal of actual carrier multipath. We analyzed multiple stations for the selection of 1.66-mHz f_c, and here we show the effect on differential carrier multipath by reducing f_c. Figure D.5 shows carrier multipath on PRN 31 using three approaches: a reduced f_c of 1.11 mHz, the final f_c of 1.66 mHz, and the DD method. Clearly, carrier multipath using the DD method and the 1.66 mHz f_c are closely matching, whereas carrier multipath using the 1.11-mHz f_c has slightly higher magnitude with low-frequency content. The higher magnitude using 1.11 mHz f_c could be acceptable as being close to typical carrier multipath, but carrier multipath usually lasts for a short period unlike the hours shown in Figure D.5. Moreover, the same carrier mutlipath of PRN 31 is plotted against the elevation angle in Figure D.6, where the low-frequency content lasts up to a 40-deg elevation angle. Therefore, we conclude that carrier multipath using the 1.11-mHz f_c has minor ionospheric residuals, and the 1.11-mHz f_c is unacceptable.

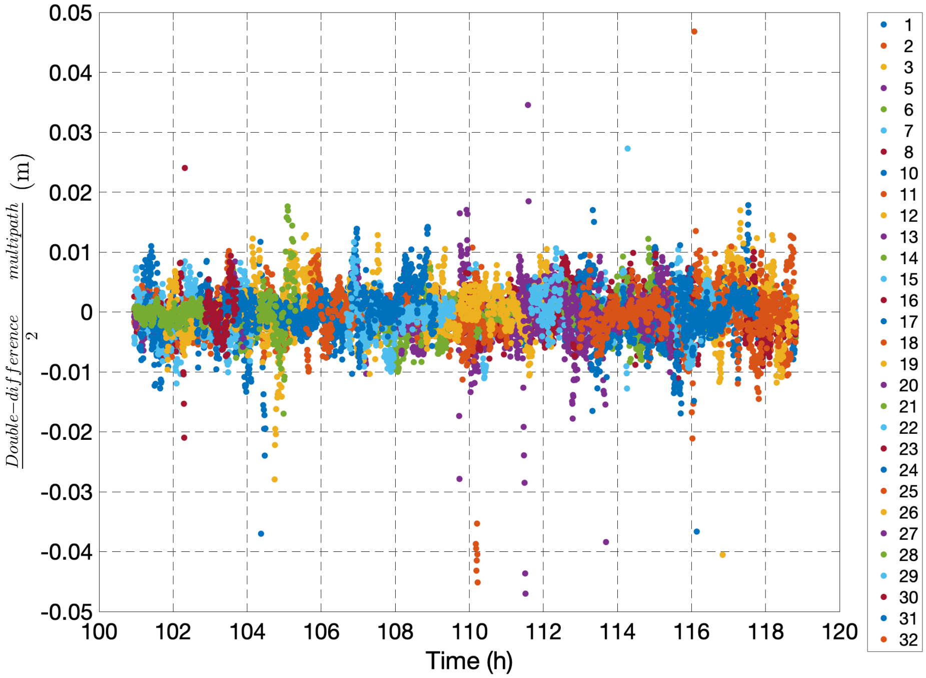

Figure D.1. DD carrier multipath on GPS L1 signal

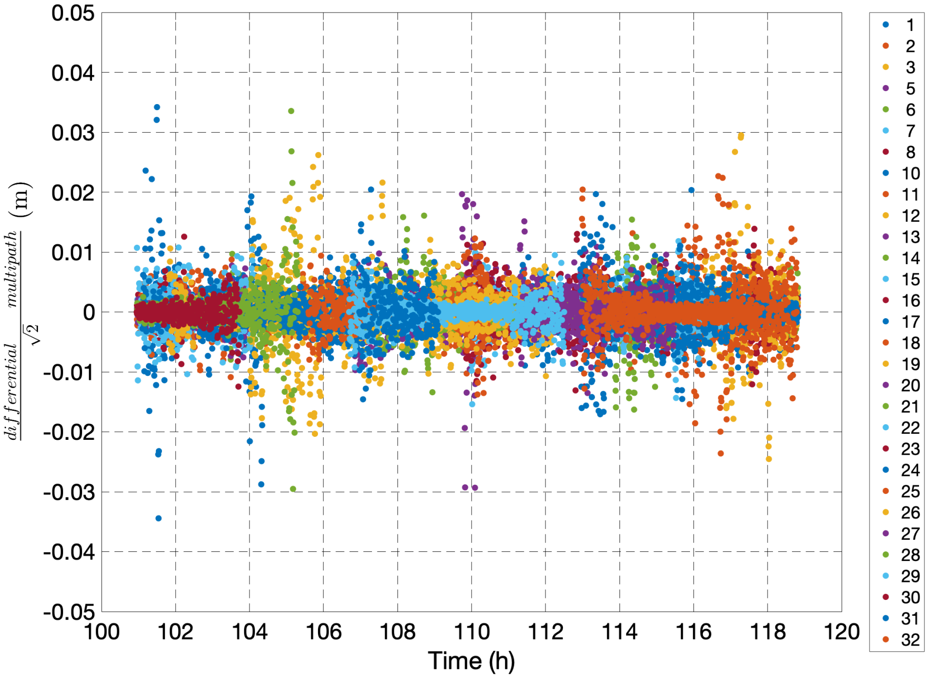

Figure D.2. Differential carrier multipath on L1 minus L2 signal

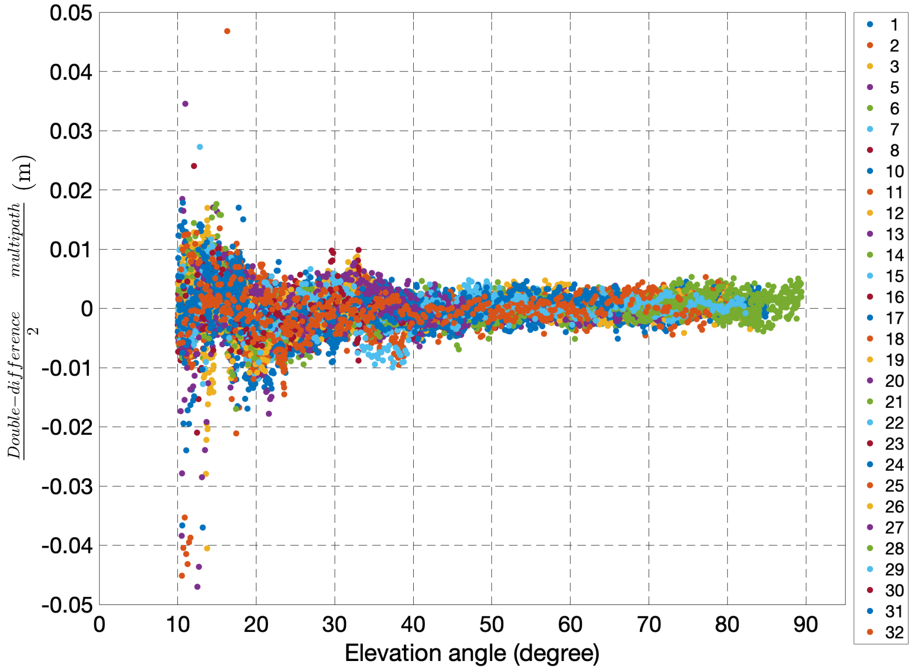

Figure D.3. DD carrier multipath as a function of elevation angle on GPS L1 signal

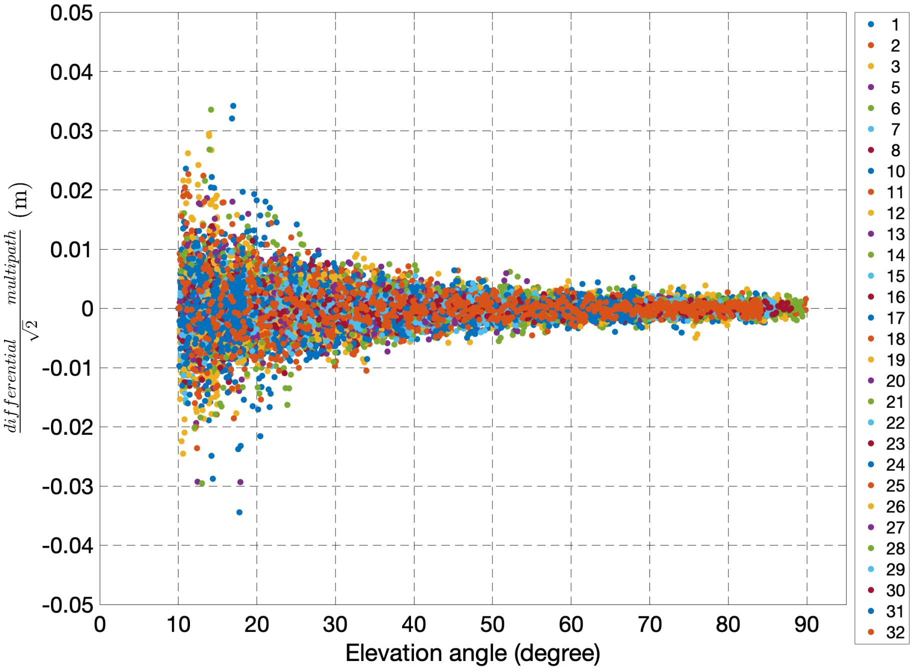

Figure D.4. Differential carrier multipath as a function of elevation angle on L1 minus L2 signal

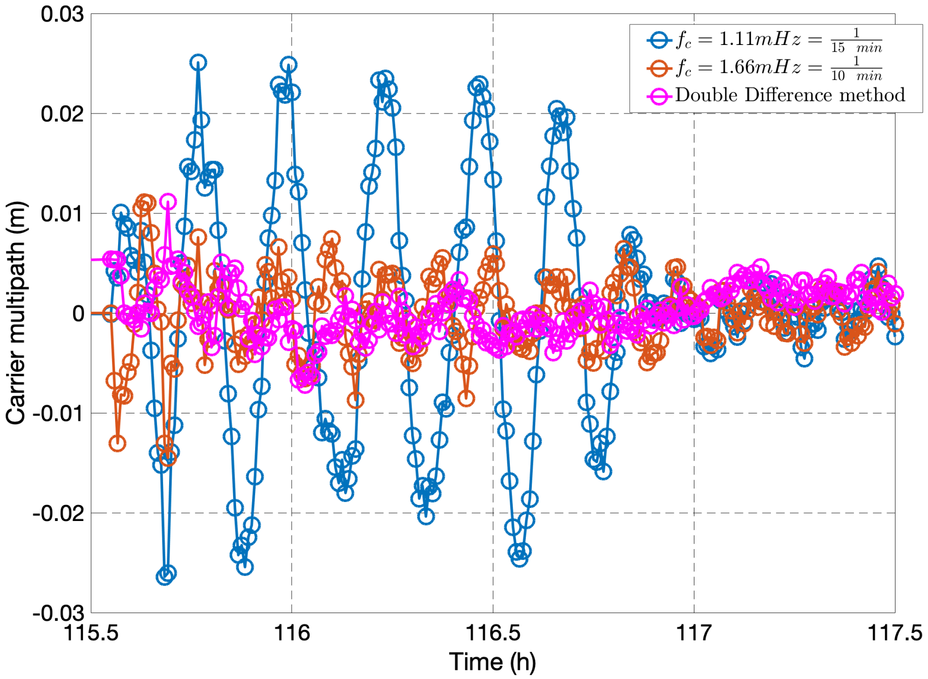

Figure D.5. Carrier multipath on PRN31 trace using different methods

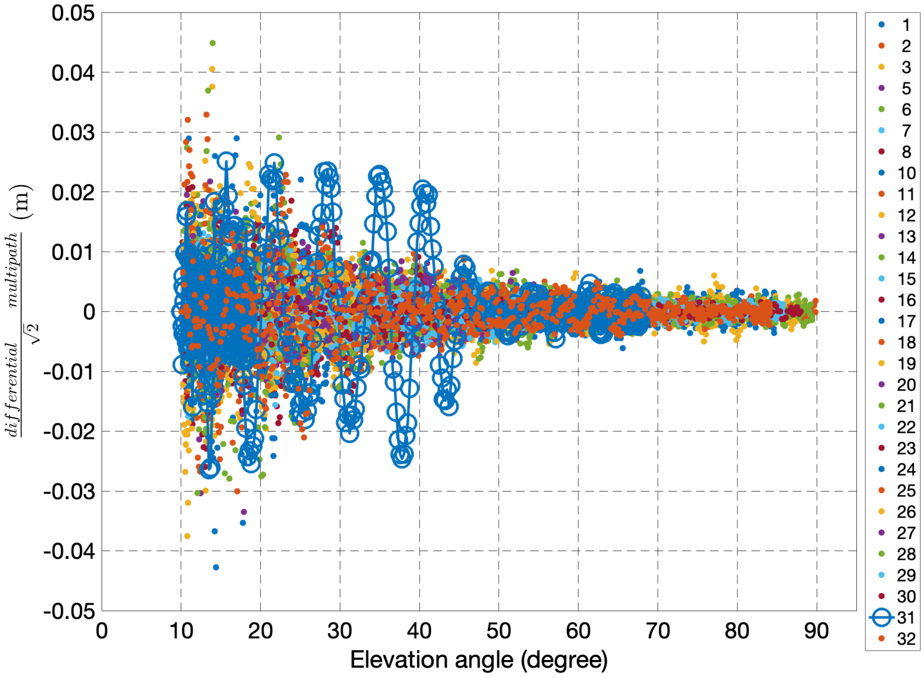

Figure D.6. Differential carrier multipath when f_c is reduced to *unacceptable* 1.11 mHz

APPENDIX E

PRECISE CODE MEASUREMENT TERMS FOR CALCULATING IONO-FREE CODE RESIDUAL

The precise range between transmitting (satellite i) and receiving (IGS RGS j) antenna phase center is

$$r_k^{i,j} = \|X^j - X_k^i\| - {}^{i,j}e_k^T \left(ARP^j + SET_k^j + \frac{f_{L1}^2}{f_{L1}^2 - f_{L2}^2} APC_{L1}^j - \frac{f_{L2}^2}{f_{L1}^2 - f_{L2}^2} APC_{L2}^j \right) \tag{E.1}$$

where,

X^j	is the Monument Marker (MM) location vector for the IGS station [77],
X_k^i	is satellite position vector from the IGS orbit product after considering signal traveling time and the Sagnac effect,
ARP^j	is the Antenna Reference Point (ARP) vector describing antenna mounted location from the MM,
APC_{L1}^j, APC_{L2}^j	are pre-calibrated APC vector for GPS L1 and L2 frequency signals.

Note that all vectors are in the ECEF frame.

The receiver clock bias (δt^j) for IGS stations is available at 300-s sample intervals in [84]. The same file also includes GPS satellite clock biases. Since IGS employs a different convention to define their APC compared to the GPS control segment defined APC [86], the IGS satellite clock needs to be transformed at GPS control segment defined APC as

$$\delta t_k^i = \delta t_{k,IGS}^i + \frac{1}{c}(\text{IGS APC offset}^i - \text{Navigation APC offset}^i) + \delta t^{\mathrm{RC},i} \tag{E.2}$$

where,

δt_{IGS}^i	is satellite clock bias available directly from the IGS clock product [84],
IGS APC offset^i	is a radial offset of IGS defined APC from COM and obtained from [87], and
Navigation APC offset^i	is a radial offset of GPS control segment defined APC from COM and obtained from [88].

For the troposphere delay term, IGS provides the Zenith Troposheric Delay

(ZTD) product for their stations [85]. This ZTD product is utilized with wet vienna mapping functions 1 (VMF1) to obtain slant tropospheric delay [64].

Equation (E.3) indicates the effective DCB correction (derivation is available in [75, Appendix A]) for the IF code measurement generated from GPS C1 and P2 code measurements.

$$DCB^{i}_{\mathrm{SV}} = \frac{f_{L1}^2}{f_{L1}^2 - f_{L2}^2} DCB_{C1-P1} \tag{E.3}$$

where, DCB_{C1-P1} is available in [78], and the notation of C1 and P1 is consistent with RINEX 2.11.

APPENDIX F

BROADCAST EPHEMERIS ERRORS AND TRUTH EPHEMERIS VIA ORBIT-FITTING

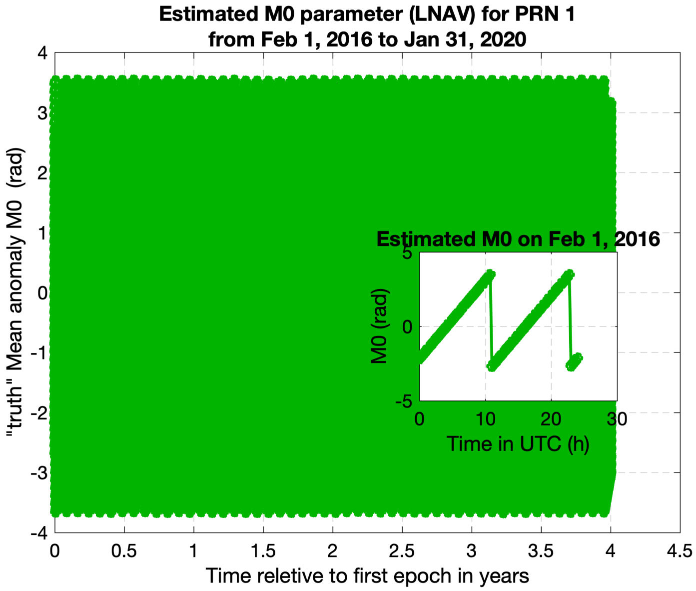

(a) Estimated mean anomaly during 4 years

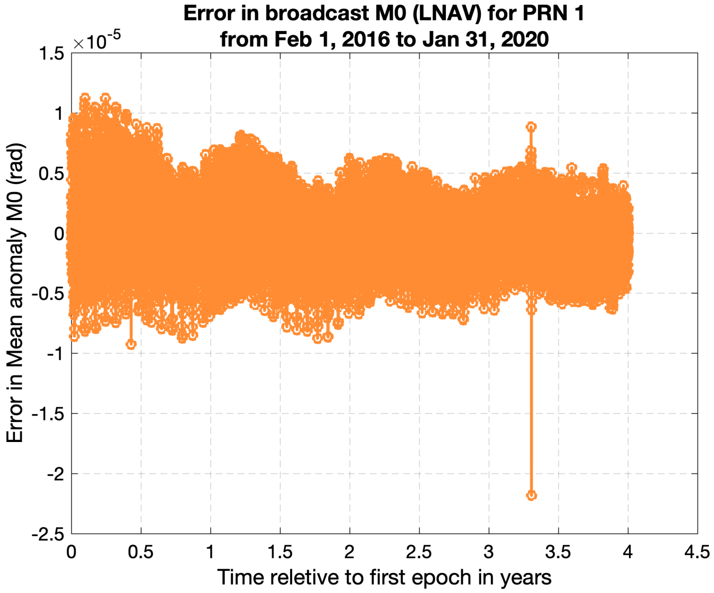

(b) Error in mean anomaly during 4 years

Figure F.1. Mean anomaly (M_0)

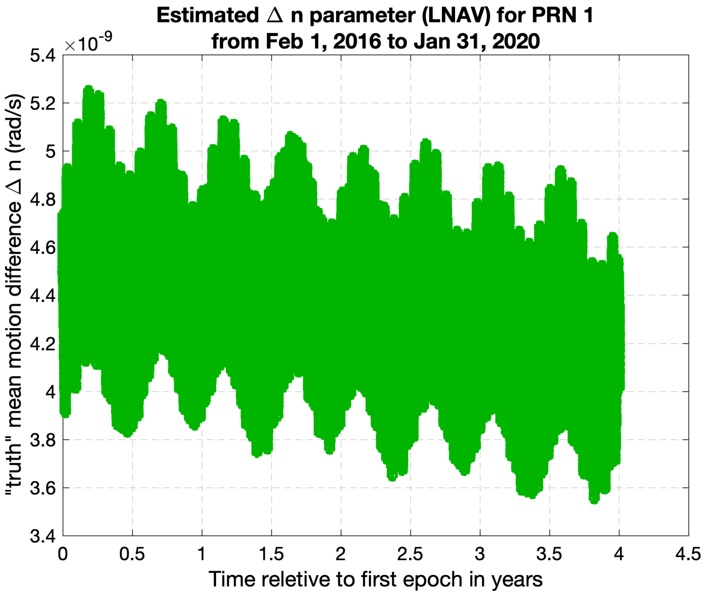

(a) Estimated mean motion difference during 4 years

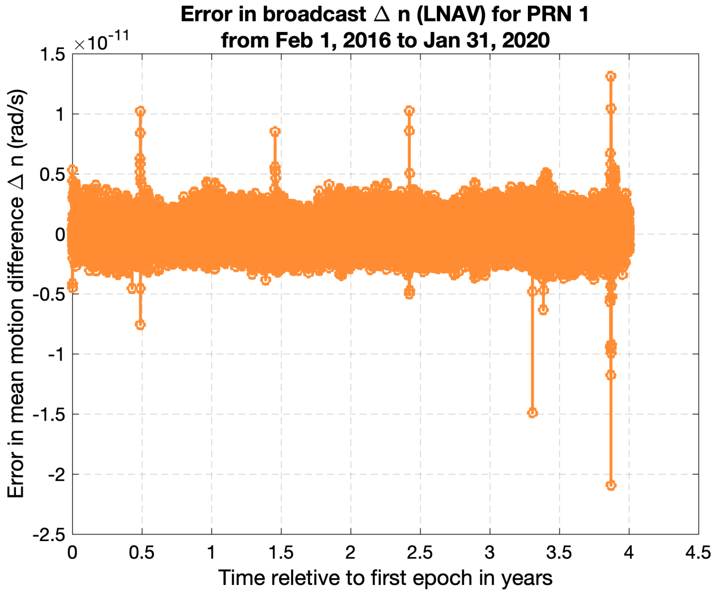

(b) Error in mean motion difference during 4 years

Figure F.2. Mean motion difference (Δn)

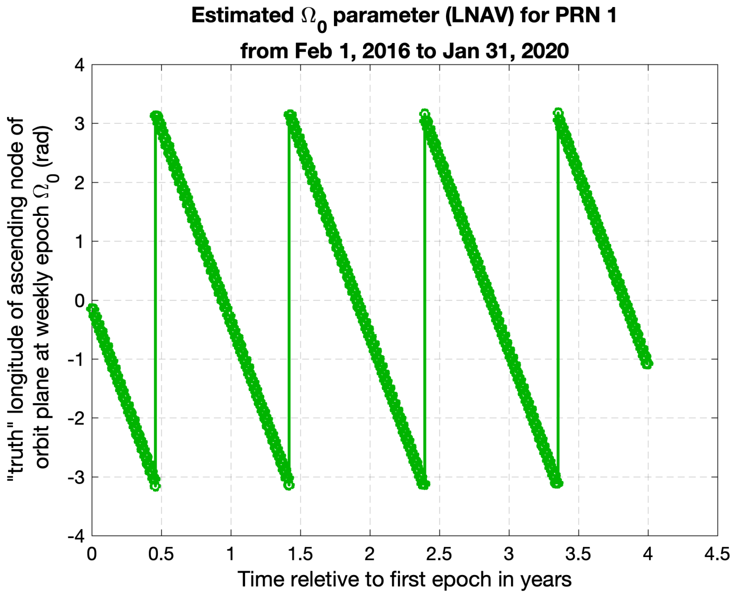

(a) Estimated longitude of ascending node during 4 years

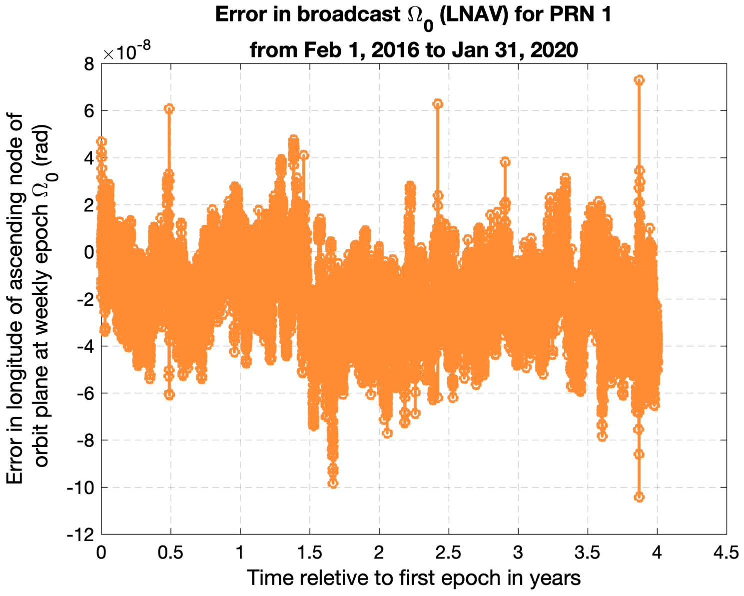

(b) Error in longitude of ascending node during 4 years

Figure F.3. Longitude of ascending node (Ω_0)

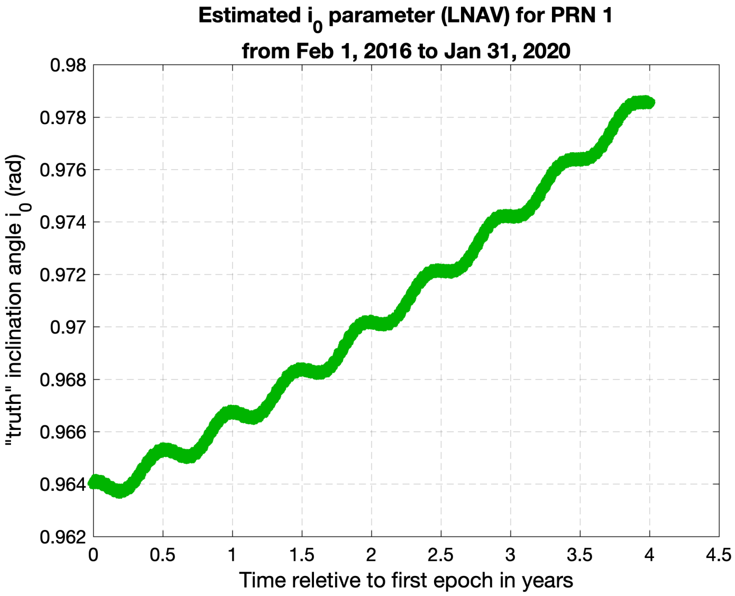

(a) Estimated inclination angle during 4 years

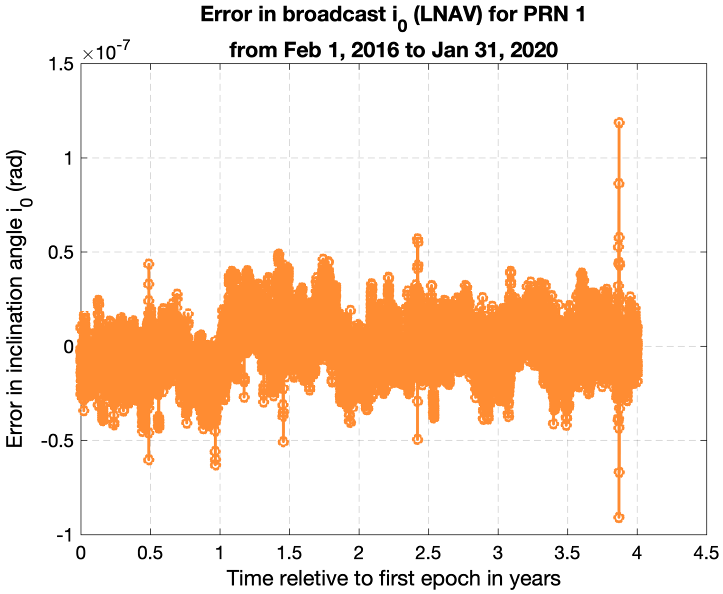

(b) Error in inclination angle during 4 years

Figure F.4. Inclination angle (i_0)

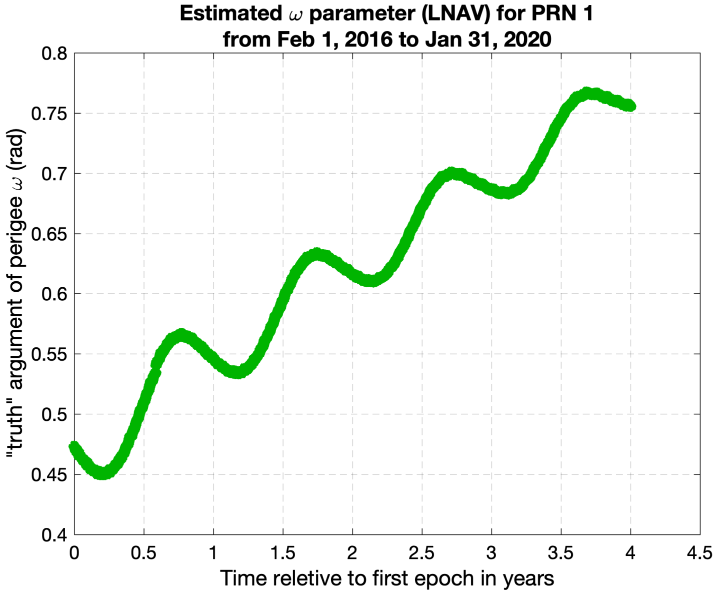

(a) Estimated argument of perigee during 4 years

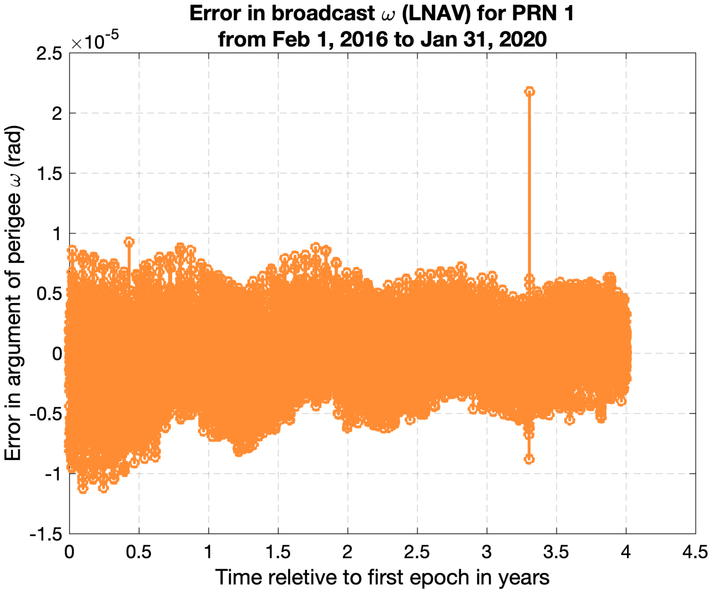

(b) Error in argument of perigee during 4 years

Figure F.5. Argument of perigee (ω)

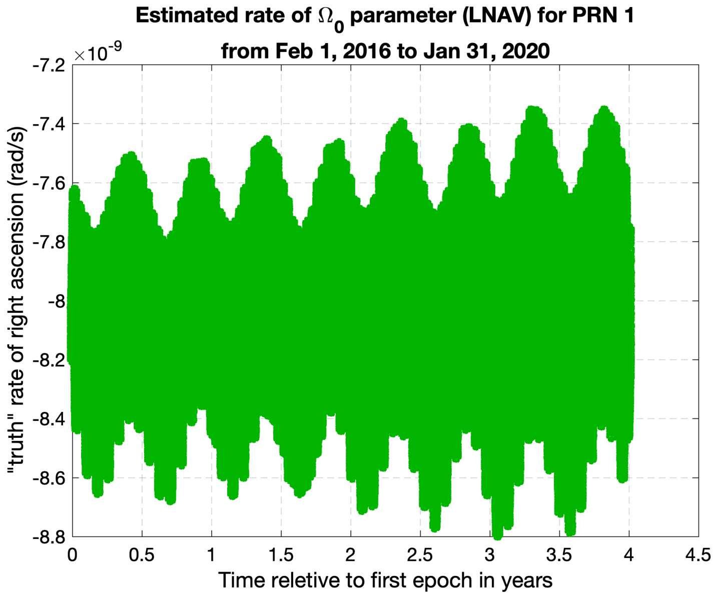

(a) Estimated rate of right ascension during 4 years

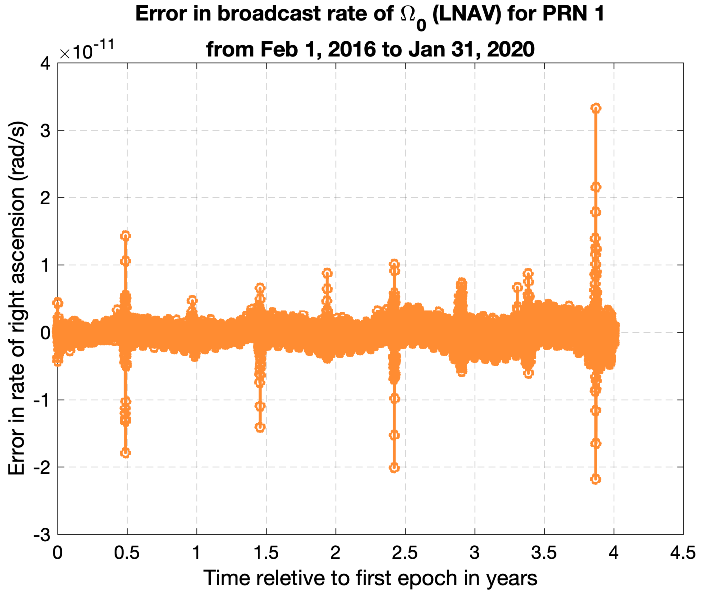

(b) Error rate of right ascension during 4 years

Figure F.6. Rate of right ascension node ($\hat{\Omega}_0$)

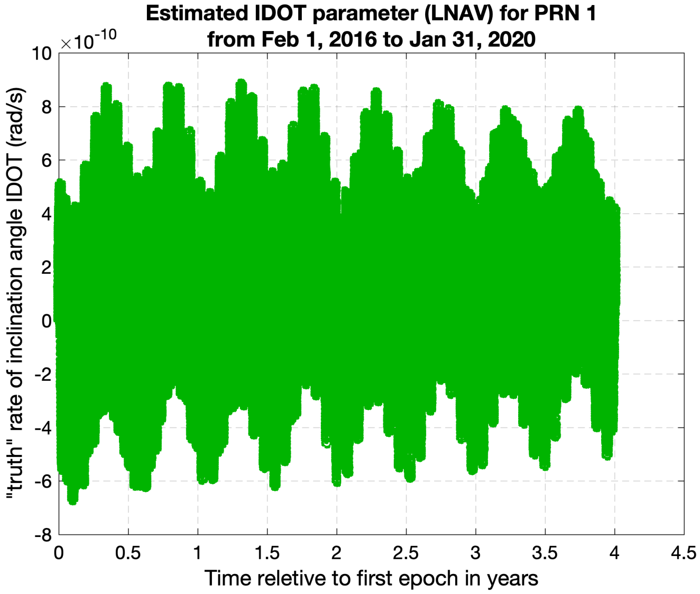

(a) Estimated rate of inclination angle during 4 years

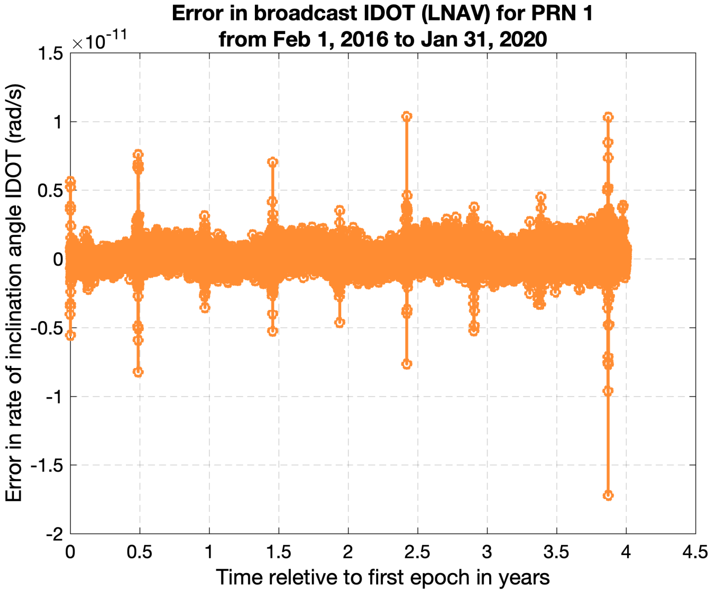

(b) Error in rate of inclination angle during 4 years

Figure F.7. Rate of inclination angle (IDOT)

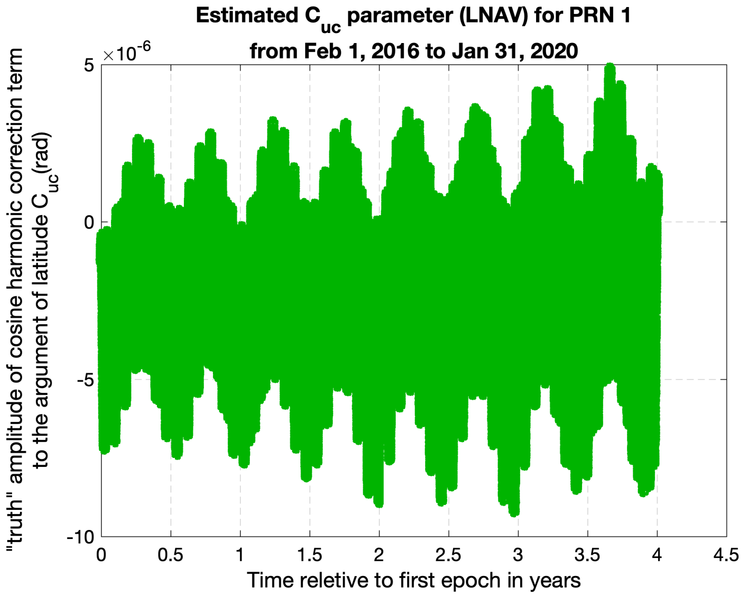

(a) Estimated amplitude of the cosine correction term to the argument of latitude during 4 years

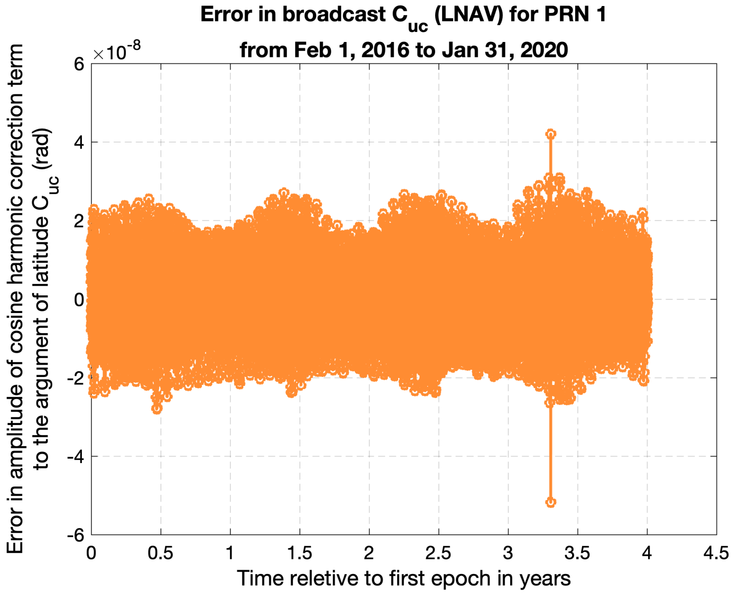

(b) Error in amplitude of the cosine correction term to the argument of latitude during 4 years

Figure F.8. Amplitude of the cosine correction term to the argument of latitude (C_{uc})

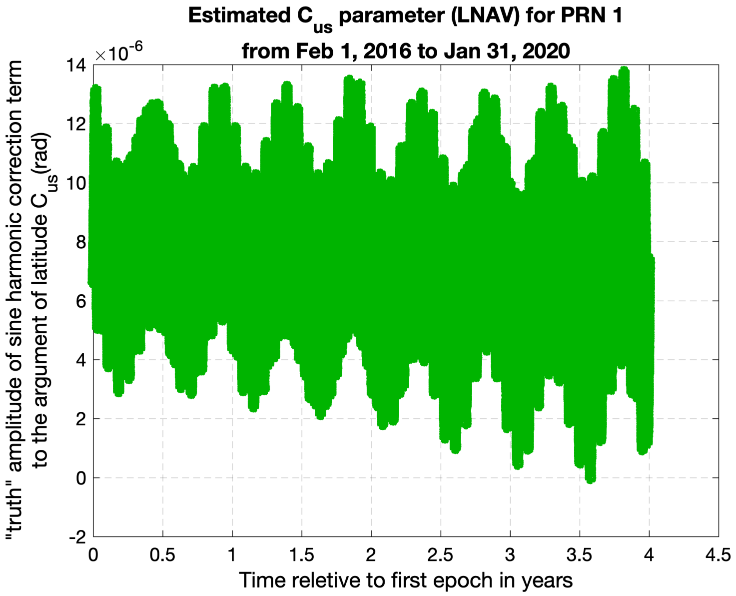

(a) Estimated amplitude of the sine correction term to the argument of latitude during 4 years

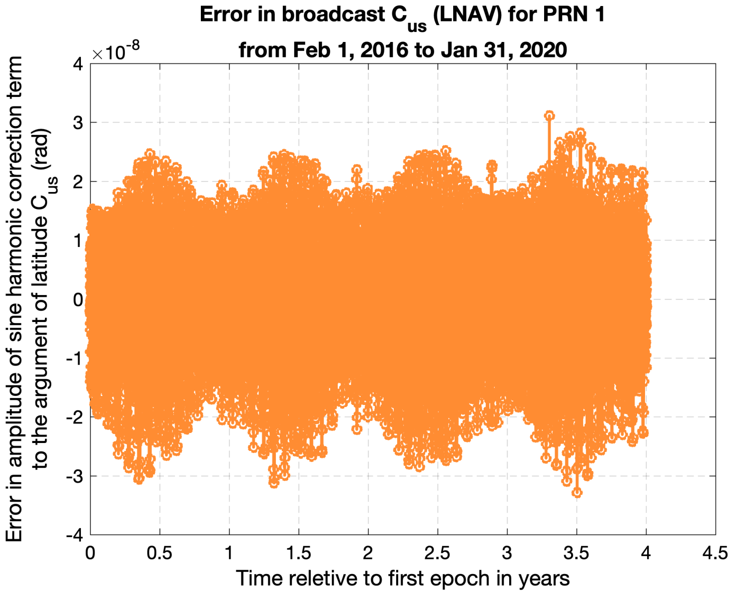

(b) Error in amplitude of the sine correction term to the argument of latitude during 4 years

Figure F.9. Amplitude of the sine correction term to the argument of latitude (C_{us})

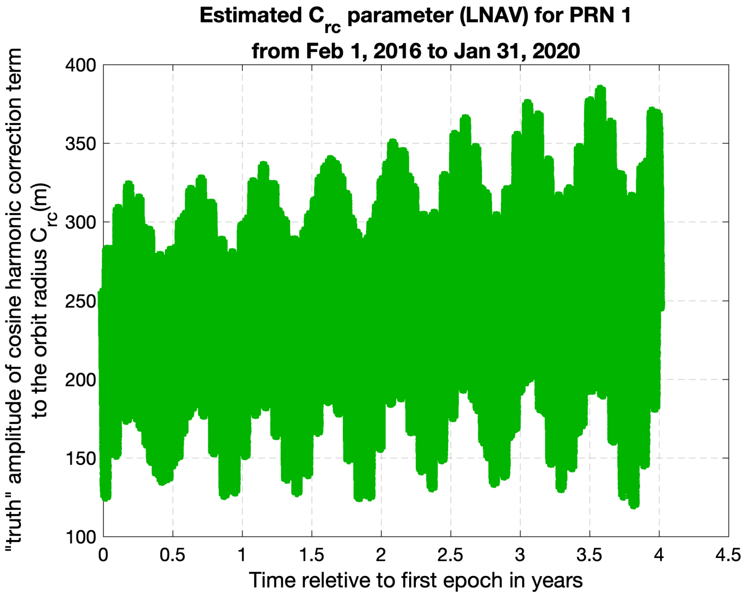

(a) Estimated amplitude of the cosine correction term to the orbit radius during 4 years

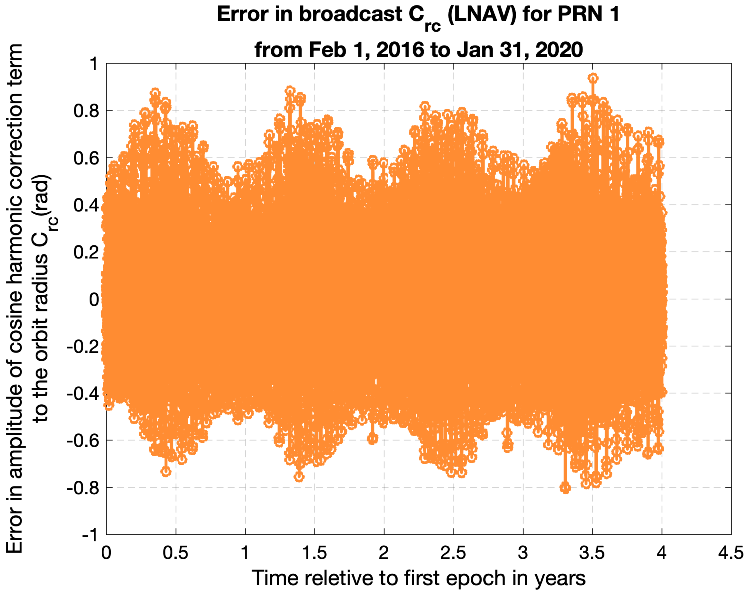

(b) Error in amplitude of the cosine correction term to the orbit radius during 4 years

Figure F.10. Amplitude of the cosine correction term to the orbit radius (C_{rc})

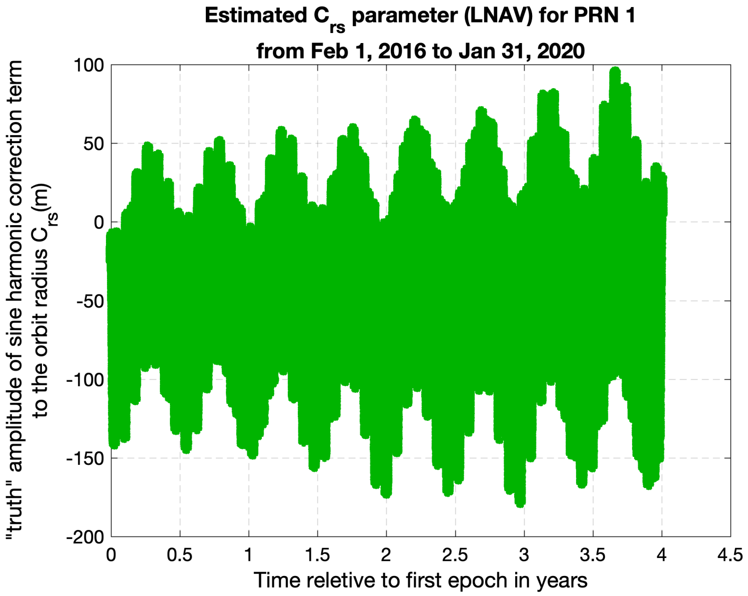

(a) Estimated amplitude of the sine correction term to the orbit radius during 4 years

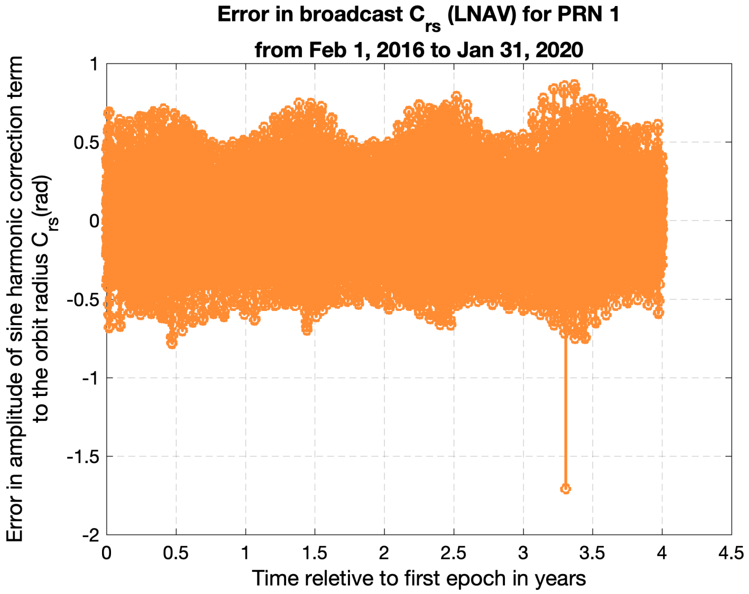

(b) Error in amplitude of the sine correction term to the orbit radius during 4 years

Figure F.11. Amplitude of the sine correction term to the orbit radius (C_{rs})

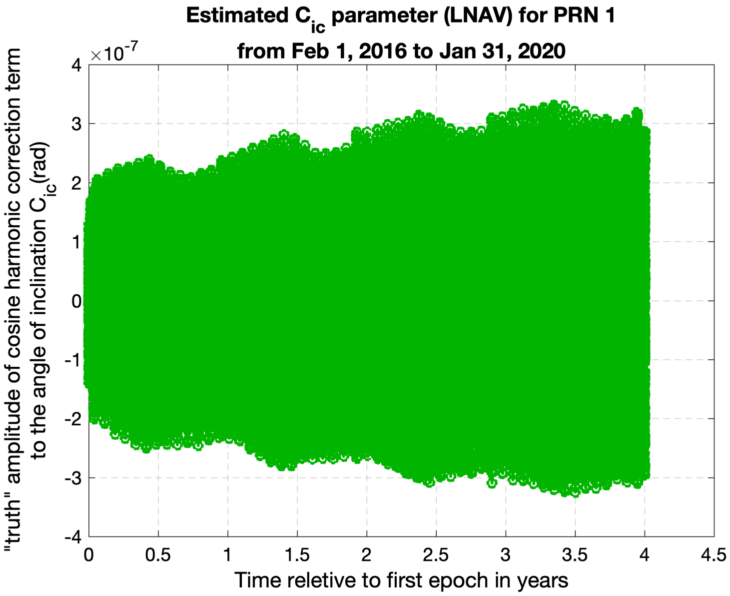

(a) Estimated amplitude of the cosine correction term to the angle of inclination during 4 years

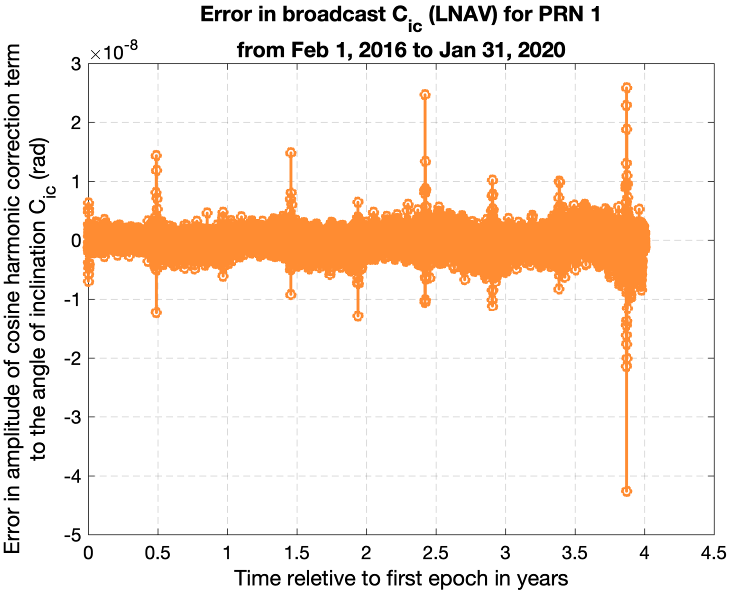

(b) Error in amplitude of the cosine correction term to the angle of inclination during 4 years

Figure F.12. Amplitude of the cosine correction term to the angle of inclination (C_{ic})

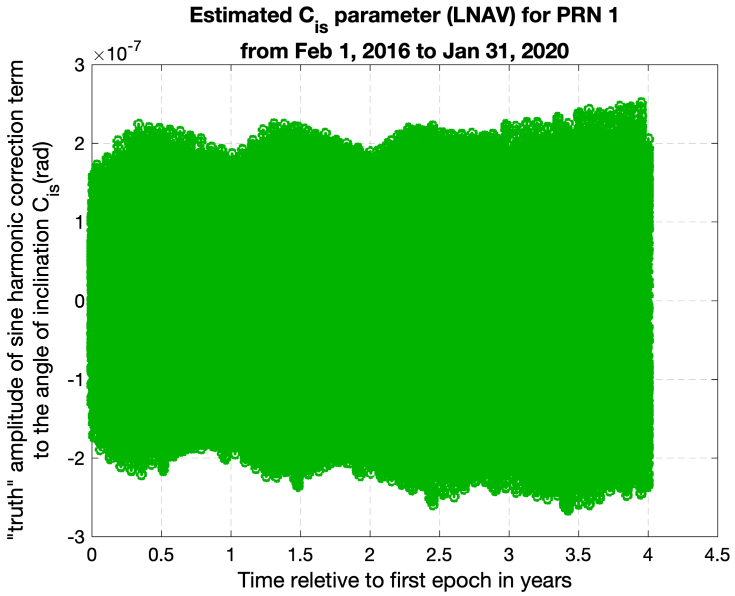

(a) Estimated amplitude of the sine correction term to the angle of inclination during 4 years

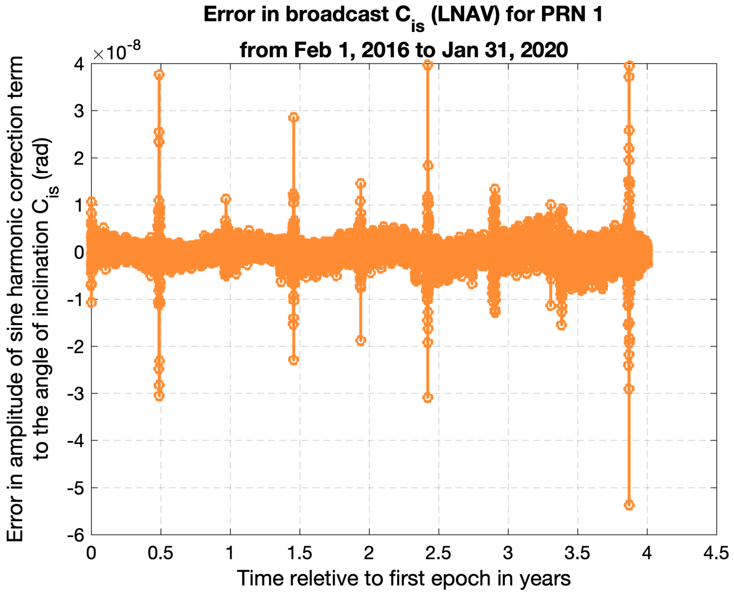

(b) Error in amplitude of the sine correction term to the angle of inclination during 4 years

Figure F.13. Amplitude of the sine correction term to the angle of inclination (C_{is})

APPENDIX G

EXPERIMENTAL VALIDATION OF GBAS ANTENNA

Raw pseudorange and carrier phase measurements were collected from the GBAS Test facility in Newark Liberty International Airport (EWR). A Multipath Limiting Antenna (MLA) is an array antenna that rejects multipath while meeting the signal-to-noise ratio requirements at low elevation. The characterization of pseudorange measurement error can be carried out in two ways: computing pseudorange minus carrier, or computing the double difference pseudorange residual. Since we rely on single and double difference for ambiguity resolution in Chapters 6, 7, and 8, we opted for the double difference approach. Similar to the carrier phase residual development in Equations (6.1) to (6.7), the double difference pseudorange residual error between two receivers (k & l) and two satellites (i &j) is computed using the line of sight vectors (e^i and e^j) and baseline b_{kl} as

$$r_{\Delta^2_\rho} = \rho^i_k - \rho^i_l - (\rho^j_k - \rho^j_l) - b^T_{kl}(\Delta e_i - \Delta e_j) = \varepsilon_{\Delta^2 \rho^{ij}_{kl}}. \tag{G.1}$$

Figure G.1 shows the residual in Equation (G.1) computed for a 27-h period of EWR data starting from 90.5 h to 118 h of GPS week 1887. In [104], we showed that the double difference pesudorange residual errors are overbounded by a zero-mean Gaussian distribution with a standard deviation of 84 cm. Since the time correlation of this residual is crucial for ambiguity resolution, here we illustrate the auto-correlation function for one of the processed satellites (PRN 26). Figure G.2 shows the autocorrelation value for a 2.4-h-long residual set. To find a time-constant, we draw the exp(-1) line on the figure, which is shown as a red horizontal line. Now, the lag at which the red line intersects the auto-correlation function is the FOGMP time constant (it is assumed that FOGMP is an adequate model for colored multipath noise behavior). From the close-up view of Figure G.2, we can see resultant time constant of 0.88 s. Similarly, we computed the time constant for all pseudorange residual sets and concluded that a 2-s time constant is conservative for ambiguity resolution [104].

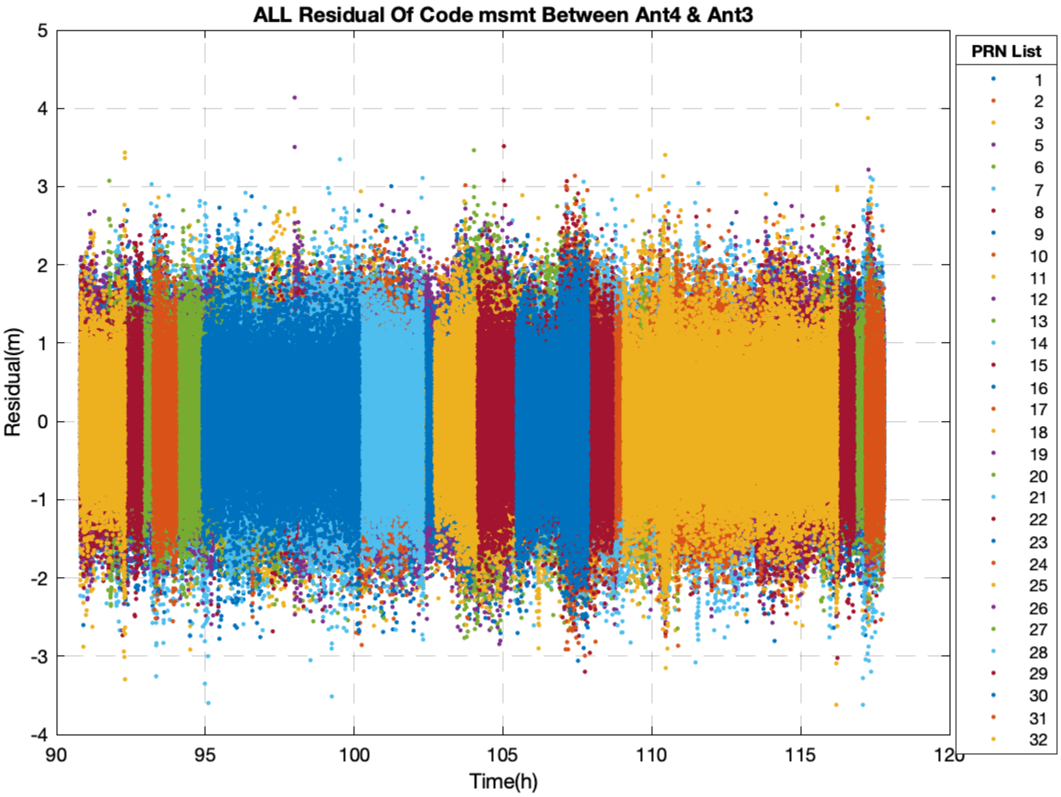

Figure G.1. Double-difference pseudorange residual

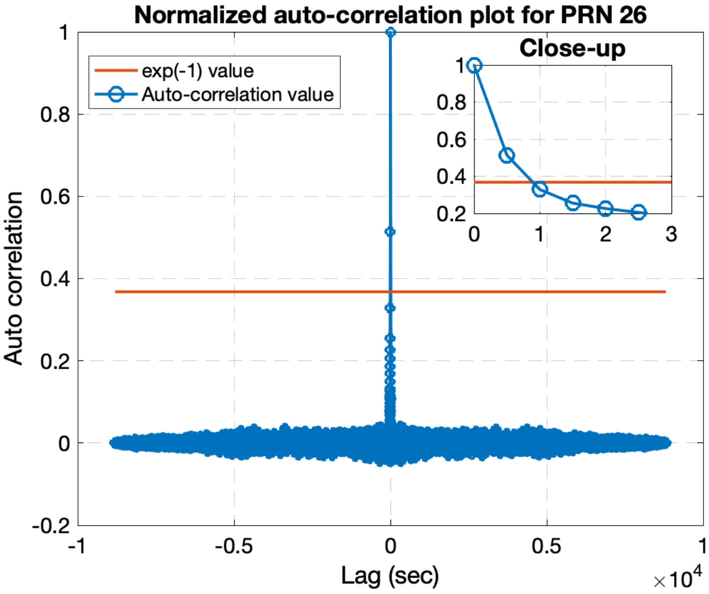

Figure G.2. Example of normalized auto-correlation with exp(-1) line in red

BIBLIOGRAPHY

[1] *Annex 10 - Aeronautical Telecommunications - Volume I - Radio Navigational Aids*, 6th ed., International Civil Aviation Organization (ICAO), July 2006.

[2] *Minimum Aviation System Performance Standards for Local Area Augmentation System (LAAS)*, Do-245 ed., Radio Technical Commission for Aeronautics (RTCA), December 2004.

[3] T. Walter, P. Enge, J. Blanch, and B. Pervan, "Worldwide vertical guidance of aircraft based on modernized GPS and new integrity augmentations," *Proceedings of the IEEE*, vol. 96, no. 12, pp. 1918–1935, 2008.

[4] Y. C. Lee, "Analysis of range and position comparison methods as a means to provide GPS integrity in the user receiver," in *Proceedings of the 42nd Annual Meeting of The Institute of Navigation (1986)*, Seattle, WA, June 1986, pp. 1–4.

[5] B. W. Parkinson and P. Axelrad, "Autonomous GPS integrity monitoring using the pseudorange residual," *NAVIGATION, Journal of The Institute of Navigation*, vol. 35, no. 2, pp. 255–274, 1988.

[6] *Minimum Operational Performance Standards for Airborne Supplemental Navigation Equipment Using Global Positioning System (GPS)*, Do-208 ed., Radio Technical Commission for Aeronautics (RTCA), July 1991.

[7] J. Blanch, T. Walker, P. Enge, Y. Lee, B. Pervan, M. Rippl, A. Spletter, and V. Kropp, "Baseline advanced RAIM user algorithm and possible improvements," *IEEE Transactions on Aerospace and Electronic Systems*, vol. 51, no. 1, pp. 713–732, January 2015.

[8] *Phase II of the GNSS Evolutionary Architecture Study*, February 2010.

[9] *EU-U.S. Cooperation on Satellite Navigation Working Group C, ARAIM Technical Subgroup*, Interim report, issue 1.0 ed., December 2012. [Online]. Available: https://www.gps.gov/policy/cooperation/europe/2013/working-group-c/ARAIM-report-1.0.pdf

[10] *EU-U.S. Cooperation on Satellite Navigation Working Group C, ARAIM Technical Subgroup*, Milestone 2 report, final version ed., February 2015. [Online]. Available: https://www.gps.gov/policy/cooperation/europe/2015/working-group-c/ARAIM-milestone-2-report.pdf

[11] J. Blanch, T. Walter, P. Enge, S. Wallner, F. A. Fernandez, R. Dellago, R. Ioannides, I. F. Hernandez, B. Belabbas, A. Spletter, and M. Rippl, "Critical elements for a multi-constellation advanced RAIM," *NAVIGATION, Journal of The Institute of Navigation*, vol. 60, no. 1, pp. 53–69, 2013.

[12] P. J. Teunissen and O. Montenbruck, *Springer Handbook of Global Navigation Satellite Systems*, 1st ed. Springer, Cham. [Online]. Available: https://doi.org/10.1007/978-3-319-42928-1

[13] "GNSS user technology report-2020." [Online]. Available: https://www.euspa.europa.eu/sites/default/files/uploads/technology_report_2020.pdf

[14] D. Lawrence, D. Bunce, N. G. Mathur, and C. E. Sigler, "Wide area augmentation system (WAAS) - program status," in *Proceedings of the 20th International Technical Meeting of the Satellite Division of The Institute of Navigation (ION GNSS 2007)*, Fort Worth, TX, September 2007, pp. 892–899.

[15] R. Braff, "Description of the FAA's local area augmentation system (LAAS)*," *NAVIGATION*, vol. 44, no. 4, pp. 411–423, 1997. [Online]. Available: https://onlinelibrary.wiley.com/doi/abs/10.1002/j.2161-4296.1997.tb02357.x

[16] *Minimum Operational Performance Standards for GPS Ground-based Regional Augmentation System Airborne Equipment*, Do-310 ed., Radio Technical Commission for Aeronautics (RTCA), March 2008.

[17] *Specification: Performance Type One Local Area Augmentation System Ground Facility*, FAA-E-2937A ed., US Federal Aviation Administration, Washington DC, April 2002.

[18] J. Blanch, T. Walter, P. Enge, Y. Lee, B. Pervan, M. Rippl, and A. Spletter, "A framework for analyzing architectures that support ARAIM," in *Proceedings of the 25th International Technical Meeting of the Satellite Division of The Institute of Navigation (ION GNSS 2012)*, Nashville, TN, September 2012, pp. 2850–2857.

[19] J. Blanch, T. Walter, P. Enge, B. Pervan, M. Joerger, S. Khanafseh, J. Burns, K. Alexander, J. P. Boyero, Y. Lee, V. Kropp, C. Milner, C. Macabiau, N. Suard, G. Berz, and M. Rippl, "Architectures for advanced RAIM: Offline and online," in *Proceedings of the 27th International Technical Meeting of the Satellite Division of The Institute of Navigation (ION GNSS+ 2014)*, Tampa, FL, September 2014, pp. 787–804.

[20] M. Joerger, Y. Zhai, and B. Pervan, "Online monitor against clock and orbit ephemeris faults in ARAIM," in *Proceedings of the ION 2015 Pacific PNT Meeting*, Honolulu, HI, April 2015, pp. 932–945.

[21] T. Walter and J. Blanch, "KEYNOTE - characterization of GNSS clock and ephemeris errors to support ARAIM," in *Proceedings of the ION 2015 Pacific PNT Meeting*, Honolulu, HI, April 2015, pp. 920–931.

[22] S. Perea, M. Meurer, M. Rippl, B. Belabbas, and M. Joerger, "URA/SISA analysis for GPS and Galileo to support ARAIM," *NAVIGATION*, vol. 64, no. 2, pp. 237–254, 2017. [Online]. Available: https://onlinelibrary.wiley.com/doi/abs/10.1002/navi.199

[23] T. Walter, K. Gunning, and J. Blanch, "KEYNOTE: Validation of the unfaulted error bounds for ARAIM," in *Proceedings of the ION 2017 Pacific PNT Meeting*, Honolulu, HI, May 2017, pp. 1–19. [Online]. Available: https://doi.org/10.33012/2017.15047

[24] K. Gunning, T. Walter, and P. Enge, "Multi-GNSS constellation anomaly detection and performance monitoring," in *Proceedings of the 30th International Technical Meeting of the Satellite Division of The Institute of Navigation (ION GNSS+ 2017)*, Portland, OR, September 2017, pp. 1051–1062. [Online]. Available: https://doi.org/10.33012/2017.15174

[25] T. Walter, J. Blanch, K. Gunning, M. Joerger, and B. Pervan, "Determination of fault probabilities for ARAIM," *IEEE Transactions on Aerospace and Electronic Systems*, vol. 55, no. 6, pp. 3505–3516, 2019.

[26] Y. C. Lee and B. Bian, "Advanced RAIM performance sensitivity to deviation of ISM parameter values," in *Proceedings of the 30th International Technical Meeting of the Satellite Division of The Institute of Navigation (ION GNSS+ 2017)*, Portland, OR, September 2017, pp. 2338–2358. [Online]. Available: https://doi.org/10.33012/2017.15192

[27] I. Martini and M. Sgammini, "Integrity support message generation algorithm prototype," in *Proceedings of the 32nd International Technical Meeting of the Satellite Division of The Institute of Navigation (ION GNSS+ 2019)*, Miami, FL, September 2019, pp. 552–572. [Online]. Available: https://doi.org/10.33012/2019.16866

[28] S. Perea Diaz, "Design of an integrity support message for offline advanced RAIM," PhD dissertation, Rheinisch-Westfälische Technische Hochschule (RWTH) Aachen University, May 2019. [Online]. Available: https://publications.rwth-aachen.de/record/762736/files/762736.pdf

[29] Y. Zhai, J. Patel, X. Zhan, M. Joerger, and B. Pervan, "An advanced receiver autonomous integrity monitoring (ARAIM) ground monitor design to estimate satellite orbits and clocks," *Journal of Navigation*, vol. 73, no. 5, p. 1087–1105, 2020. [Online]. Available: https://doi.org/10.1017/S0373463320000181

[30] S. Perea, M. Meurer, and B. Pervan, "Impact of sample correlation on SISRE overbound for ARAIM," *NAVIGATION*, vol. 67, no. 1, pp. 197–212, 2020. [Online]. Available: https://onlinelibrary.wiley.com/doi/abs/10.1002/navi.346

[31] B. Pervan and F.-C. Chan, "Detecting global positioning satellite orbit errors using short-baseline carrier-phase measurements," *Journal of Guidance, Control, and Dynamics*, vol. 26, no. 1, pp. 122–131, 2003. [Online]. Available: https://doi.org/10.2514/2.5022

[32] H. Tang, S. Pullen, P. Enge, L. Gratton, B. Pervan, M. Brenner, J. Scheitlin, and P. Kline, "Ephemeris type A fault analysis and mitigation for LAAS," in *IEEE/ION Position, Location and Navigation Symposium*, Indian Wells, CA, May 2010, pp. 654–666.

[33] B. Pervan and L. Gratton, "Orbit ephemeris monitors for local area differential GPS," *IEEE Transactions on Aerospace and Electronic Systems*, vol. 41, no. 2, pp. 449–460, April 2005.

[34] S. Pullen, J. Lee, M. Luo, B. Pervan, F.-C. Chan, and L. Gratton, "Ephemeris protection level equations and monitor algorithms for GBAS," in *Proceedings of the 14th International Technical Meeting of the Satellite Division of the Institute of Navigation (ION GPS 2001)*, Salt Lake City, UT, September 2001, pp. 1738–1749.

[35] J. Jing, S. Khanafseh, S. Langel, F. C. Chan, and B. Pervan, "Null space ephemeris monitor for GBAS," in *Proceedings of the ION 2013 Pacific PNT Meeting*, Honolulu, HI, April 2013, pp. 978–985.

[36] S. Khanafseh, S. Pullen, and J. Warburton, "Carrier phase ionospheric gradient ground monitor for GBAS with experimental validation," *NAVIGATION*, vol. 59, no. 1, pp. 51–60, 2012. [Online]. Available: https://onlinelibrary.wiley.com/doi/abs/10.1002/navi.3

[37] S. Pullen, Y. S. Park, and P. Enge, "Impact and mitigation of ionospheric anomalies on ground-based augmentation of GNSS," *Radio Science*, vol. 44, no. 1, 2009. [Online]. Available: https://agupubs.onlinelibrary.wiley.com/doi/abs/10.1029/2008RS004084

[38] S. Pullen, R. Cassell, B. Johnson, M. Brenner, D. Weed, L. Cypriano, M. Topland, M. Stakkeland, B. Pervan, M. Harris, S. Saito, J. Lee, B. Clark, S. Beauchamp, and J. Dennis, "Impact of ionospheric anomalies on GBAS GAST D service and validation of relevant ICAO SARPs requirements," in *Proceedings of the 30th International Technical Meeting of the Satellite Division of the Institute of Navigation (ION GNSS+ 2017)*, Portland, OR, September 2017, pp. 2085–2105. [Online]. Available: https://doi.org/10.33012/2017.15135

[39] J. R. I. Christie, P.-Y. Ko, A. Hansen, D. Dai, S. Pullen, B. S. Pervan, and B. W. Parkinson, "The effects of local ionospheric decorrelation on LAAS: Theory and experimental results," in *Proceedings of the 1999 National Technical Meeting of The Institute of Navigation*, San Diego, CA, January 1999, pp. 769–777.

[40] M. Luo, S. Pullen, T. Walter, and P. Enge, "Ionosphere spatial gradient threat for LAAS: Mitigation and tolerable threat space," in *Proceedings of the 2004 National Technical Meeting of The Institute of Navigation*, San Diego, CA, January, p. 490–501.

[41] *Annex 10 - Aeronautical Telecommunications - Volume I - Radio Navigational Aids*, 7th ed., International Civil Aviation Organization (ICAO), July 2018.

[42] M. Yoon, J. Lee, S. Pullen, J. Gillespie, N. Mathur, R. Cole, J. R. de Souza, P. Doherty, and R. Pradipta, "Equatorial plasma bubble threat parameterization to support GBAS operations in the brazilian region," *NAVIGATION*, vol. 64, no. 3, pp. 309–321, 2017. [Online]. Available: https://onlinelibrary.wiley.com/doi/abs/10.1002/navi.203

[43] J. Jing, S. Khanafseh, F. C. Chan, S. Langel, and B. Pervan, "Detecting ionospheric gradients for GBAS using a null space monitor," in *Proceedings of IEEE/ION PLANS 2012*, Myrtle Beach, SC, April 2012, pp. 1125–1133.

[44] J. Jing, S. Khanafseh, S. Langel, and B. Pervan, "Detection and isolation of ionospheric fronts for GBAS," in *Proceedings of the 27th International Technical Meeting of the Satellite Division of the Institute of Navigation (ION GNSS+ 2014)*, Tampa, FL, September 2014, pp. 3526–3531.

[45] *Global Positioning System Directorate Systems Engineering and Integration*, IS-GPS-200H ed., 2013. [Online]. Available: http://www.gps.gov/technical/icwg/IS-GPS-200H.pdf

[46] GPS modernization: New civil signals. [Online]. Available: https://www.gps.gov/systems/gps/modernization/civilsignals/

[47] R. Leandro, M. Santos, and R. B. Langley, "UNB neutral atmosphere models: Development and performance," in *Proceedings of the 2006 National Technical Meeting of The Institute of Navigation*, Monterey, CA, January 2006, pp. 564–573.

[48] P. Misra and P. Enge, "Global positioning system: Signals, measurements and performance (lincoln, ma: Ganga," *Global Positioning System: Signals, Measurements and Performance Lincoln, MA: Ganga*, 2006.

[49] B. Park, C. Lim, Y. Yun, E. Kim, and C. Kee, "Optimal divergence-free hatch filter for GNSS single-frequency measurement," *Sensors*, vol. 17, no. 3, 2017. [Online]. Available: https://www.mdpi.com/1424-8220/17/3/448

[50] S. Khanafseh, B. Kujur, M. Joerger, T. Walter, S. Pullen, J. Blanch, K. Doherty, L. Norman, L. de Groot, and B. Pervan, "GNSS multipath error modeling for automotive applications," in *Proceedings of the 31st International Technical Meeting of the Satellite Division of The Institute of Navigation (ION GNSS+ 2018)*, September 2018, pp. 1573–1589. [Online]. Available: https://doi.org/10.33012/2018.16107

[51] G. A. McGraw, T. Murphy, M. Brenner, S. Pullen, and A. J. Van Dierendonck, "Development of the LAAS accuracy models," in *Proceedings of the 13th International Technical Meeting of the Satellite Division of The Institute of Navigation (ION GPS 2000)*, Salt Lake City, UT, September 2000, pp. 1212–1223.

[52] D. Simon, "Optimal state estimation, kalman and nonlinear approaches, a john wiley & sons," *Inc., Hoboken, New Jersey*, p. 129, 2006.

[53] *Minimum Operational Performance Standards (MOPS) for GPS/ABAS airborne equipment*. [Online]. Available: https://standards.globalspec.com/std/1199977/RTCA%20DO-316

[54] *Minimum Operational Performance Standards (MOPS) for GPS/SBAS airborne equipment*. [Online]. Available: https://standards.globalspec.com/std/14281994/RTCA%20DO-229

[55] *Minimum Operational Performance Standard for Global Navigation Satellite Ground Based Augmentation System Ground Equipment to Support Precision Approach and Landing*. [Online]. Available: https://standards.globalspec.com/std/13497674/eurocae-ed-114

[56] J. Blanch, T. Walter, C. Milner, M. Joerger, B. Pervan, and D. Bouvet, "Baseline advanced RAIM user algorithm: Proposed updates," in *Proceedings of the 2022 International Technical Meeting of The Institute of Navigation*, Long Beach, CA, January 2022, pp. 229–251. [Online]. Available: https://doi.org/10.33012/2022.18254

[57] T. Walter and J. Blanch, "KEYNOTE - characterization of GNSS clock and ephemeris errors to support ARAIM," in *Proceedings of the ION 2015 Pacific PNT Meeting*, Honolulu, Hawaii, April 2015, pp. 920–931.

[58] M. Joerger, F.-C. Chan, and B. Pervan, "Solution separation versus residual-based raim," *NAVIGATION*, vol. 61, no. 4, pp. 273–291, 2014. [Online]. Available: https://onlinelibrary.wiley.com/doi/abs/10.1002/navi.71

[59] J. Patel and B. Pervan, "Accurate GPS LNAV parameters and clock biases for ARAIM offline monitoring," *IEEE Transactions on Aerospace and Electronic Systems*, vol. 59, no. 4, pp. 4313–4332, 2023.

[60] L. F. Richardson and R. T. Glazebrook, "The approximate arithmetical solution by finite differences of physical problems involving differential equations, with an application to the stresses in a masonry dam," *Philosophical Transactions of the Royal Society of London. Series A, Containing Papers of a Mathematical or Physical Character*, vol. 210, no. 459-470, pp. 307–357, 1911. [Online]. Available: https://royalsocietypublishing.org/doi/abs/10.1098/rsta.1911.0009

[61] N. Wang, Y. Yuan, Z. Li, O. Montenbruck, and B. Tan, "Determination of differential code biases with multi-GNSS observations," *Journal of Geodesy*, vol. 90, no. 3, pp. 209–228, 2016. [Online]. Available: https://doi.org/10.1007/s00190-015-0867-4

[62] J. Böhm, G. Möller, M. Schindelegger, G. Pain, and R. Weber, "Development of an improved empirical model for slant delays in the troposphere (GPT2w)," *GPS Solutions*, vol. 19, no. 3, pp. 433–441, 2015. [Online]. Available: https://doi.org/10.1007/s10291-014-0403-7

[63] E. Gallon, M. Joerger, and B. Pervan, "Robust modeling of GNSS tropospheric delay dynamics," *IEEE Transactions on Aerospace and Electronic Systems*, vol. 57, no. 5, pp. 2992–3003, 2021.

[64] J. Boehm, B. Werl, and H. Schuh, "Troposphere mapping functions for GPS and very long baseline interferometry from European Centre for medium-range weather forecasts operational analysis data," *Journal of Geophysical Research: Solid Earth*, vol. 111, no. B2, 2006. [Online]. Available: https://agupubs.onlinelibrary.wiley.com/doi/abs/10.1029/2005JB003629

[65] G. Petitl and B. Luzum, "International earth rotation and reference systems service (IERS) conventions, technical note no. 36," Tech. Rep., 2010.

[66] L. Wanninger, H. Sumaya, and S. Beer, "Group delay variations of GPS transmitting and receiving antennas," *Journal of Geodesy*, vol. 91, no. 9, pp. 1099–1116, 2017. [Online]. Available: https://doi.org/10.1007/s00190-017-1012-3

[67] A. Hauschild and O. Montenbruck, "A study on the dependency of GNSS pseudorange biases on correlator spacing," *GPS Solutions*, vol. 20, no. 2, pp. 159–171, 2016. [Online]. Available: https://doi.org/10.1007/s10291-014-0426-0

[68] X. Ye, W. Xiao, W. Liu, S. Ni, and F. Wang, "Influence of pseudorange biases on single epoch GNSS integer ambiguity resolution," *IEEE Access*, vol. 8, pp. 112 496–112 506, 2020.

[69] S. Datta-Barua, T. Walter, J. Blanch, and P. Enge, "Bounding higher order ionosphere errors for the dual frequency GPS user," in *Proceedings of the 19th International Technical Meeting of the Satellite Division of The Institute of Navigation (ION GNSS 2006)*, Fort Worth, TX, September 2006, pp. 1377–1392.

[70] J.-T. Wu, S.-C. Wu, G. Hajj, W. Bertiger, and S. M. Lichten, "Effects of antenna orientation on GPS carrier phase," in *IN: Astrodynamics 1991; Proceedings of the AAS/AIAA Astrodynamics Conference*.

[71] Y. E. Bar-Sever, "A new model for GPS yaw attitude," *Journal of Geodesy*, vol. 70, no. 11, pp. 714–723, 1996. [Online]. Available: https://doi.org/10.1007/BF00867149

[72] F. Dilssner, "GPS IIF-1 satellite," Inside GNSS, September 2010. [Online]. Available: https://www.insidegnss.com/auto/sep10-Dilssner.pdf

[73] J. Kouba, "A simplified yaw-attitude model for eclipsing GPS satellites," *GPS Solutions*, vol. 13, no. 1, pp. 1–12, 2009. [Online]. Available: https://doi.org/10.1007/s10291-008-0092-1

[74] J. Patel, Y. Zhai, S. Kiarash, S. Khanafseh, M. Joerger, and B. Pervan, "Prototyping an ARAIM offline ground monitor using experimental data," in *Proceedings of the 31st International Technical Meeting of the Satellite Division of The Institute of Navigation (ION GNSS+ 2018)*, Miami, FL, September 2018, pp. 2583–2597. [Online]. Available: https://doi.org/10.33012/2018.16023

[75] J. Patel, S. Khanafseh, and B. Pervan, "GNSS satellite orbit and clock truth generation for ARAIM offline monitoring," in *Proceedings of the ION 2019 Pacific PNT Meeting*, Honolulu, HI, April 2019, pp. 942–955. [Online]. Available: https://doi.org/10.33012/2019.16850

[76] About the crustal dynamic data information system (CDDIS) GNSS data and products archive. [Online]. Available: https://cddis.nasa.gov/Data_and_Derived_Products/GNSS/GNSS_data_and_product_archive.html

[77] GNSS station position products. [Online]. Available: https://cddis.nasa.gov/Data_and_Derived_Products/GNSS/station_position_products.html

[78] GNSS differential code bias product. [Online]. Available: https://cddis.nasa.gov/Data_and_Derived_Products/GNSS/gnss_differential_code_bias_product.html

[79] The Kp index in january 2016. [Online]. Available: https://www.spaceweatherlive.com/en/archive/2016/01.html

[80] The Dst number in january 2016. [Online]. Available: http://wdc.kugi.kyoto-u.ac.jp/dst_provisional/201601/index.html

[81] Notice advisory to navstar users (NANU). [Online]. Available: https://celestrak.com/GPS/NANU/2016/

[82] S. Langel, O. G. Crespillo, and M. Joerger, "A new approach for modeling correlated gaussian errors using frequency domain overbounding," in *2020 IEEE/ION Position, Location and Navigation Symposium (PLANS)*, April 2020, pp. 868–876.

[83] A. Bilich, P. Axelrad, and K. M. Larson, "Scientific utility of the signal-to-noise ratio (SNR) reported by geodetic gps receivers," in *Proceedings of the 20th International Technical Meeting of the Satellite Division of The Institute of Navigation (ION GNSS 2007)*, Fort Worth, TX, September 2007, pp. 1999–2010.

[84] Station and satellilte clock products. [Online]. Available: https://cddis.nasa.gov/Data_and_Derived_Products/GNSS/clock_products.html

[85] GNSS atmospheric products: zenith tropospheric delay. [Online]. Available: https://cddis.nasa.gov/Data_and_Derived_Products/GNSS/atmospheric_products.html

[86] O. Montenbruck, P. Steigenberger, and A. Hauschild, "Broadcast versus precise ephemerides: a multi-GNSS perspective," *GPS Solutions*, vol. 19, no. 2, pp. 321–333, 2015. [Online]. Available: https://doi.org/10.1007/s10291-014-0390-8

[87] IGS antenna working group : ANTEX file. [Online]. Available: https://www.igs.org/wg/antenna/#documents

[88] Antenna information from NGA GNSS division : WGS 84(G2139).pdf. [Online]. Available: https://earth-info.nga.mil/index.php?dir=gnss&action=gnss

[89] J. Patel and B. Pervan, "Analyzing satellite orbit error for ARAIM offline monitoring," in *2020 IEEE/ION Position, Location and Navigation Symposium (PLANS)*, Portland, OR, April 2020, pp. 490–501.

[90] A. J. Van Dierendonck, S. S. Russell, E. R. Kopitzke, and M. Birnbaum, "The GPS navigation message," *NAVIGATION*, vol. 25, no. 2, pp. 147–165, 1978. [Online]. Available: https://onlinelibrary.wiley.com/doi/abs/10.1002/j.2161-4296.1978.tb01326.x

[91] "International GNSS service (IGS) orbit product," visited on October 26, 2021. [Online]. Available: https://cddis.nasa.gov/Data_and_Derived_Products/GNSS/orbit_products.html

[92] "Notice advisory to navstar users (NANU) for PRN 01," visited on October 26, 2021. [Online]. Available: https://celestrak.com/GPS/NANU/2016/nanu.2016059.txt

[93] "Broadcast ephemeris data for GPS constellation," visited on October 26, 2021. [Online]. Available: https://cddis.nasa.gov/Data_and_Derived_Products/GNSS/broadcast_ephemeris_data.html

[94] S. Perea, M. Meurer, l. Martini, M. Rippl, M. Joerger, and B. Pervan, "Nominal range error analysis to support ARAIM," in *Proceedings of the 29th International Technical Meeting of the Satellite Division of The Institute of Navigation (ION GNSS+ 2016)*, Portland, OR, September 2016, pp. 1726–1735. [Online]. Available: https://doi.org/10.33012/2016.14861

[95] E. Gallon, M. Joerger, and B. Pervan, "Frequency-domain modeling of orbit and clock errors for sequential positioning," in *Proceedings of the 33rd International Technical Meeting of the Satellite Division of The Institute of Navigation (ION GNSS+ 2020)*, September 2020, pp. 1041–1053. [Online]. Available: https://doi.org/10.33012/2020.17542

[96] J. Patel, S. Khanafseh, and B. Pervan, "Detecting hazardous spatial gradients at satellite acquisition in GBAS," *IEEE Transactions on Aerospace and Electronic Systems*, vol. 56, no. 4, pp. 3214–3230, 2020.

[97] M. Luo, S. Pullen, S. Datta-Barua, G. Zhang, T. Walter, and P. Enge, "LAAS study of slow-moving ionosphere anomalies and their potential impacts," in *Proceedings of the 18th International Technical Meeting of the Satellite Division of The Institute of Navigation (ION GNSS 2005)*, Long Beach, CA, September 2005, pp. 2337–2349.

[98] J.-M. Marin, K. Mengersen, and C. P. Robert, "Bayesian modelling and inference on mixtures of distributions," in *Bayesian Thinking*, ser. Handbook of Statistics, D. Dey and C. Rao, Eds. Elsevier, 2005, vol. 25, pp. 459–507. [Online]. Available: https://www.sciencedirect.com/science/article/pii/S0169716105250162

[99] S. Khanafseh and S. Langel, "Implementation and experimental validation of cycle ambiguity resolution with position domain integrity risk constraints," *NAVIGATION*, vol. 58, no. 1, pp. 45–58, 2011. [Online]. Available: https://onlinelibrary.wiley.com/doi/abs/10.1002/j.2161-4296.2011.tb01791.x

[100] S. Khanafseh and B. Pervan, “New approach for calculating position domain integrity risk for cycle resolution in carrier phase navigation systems,” *IEEE Transactions on Aerospace and Electronic Systems*, vol. 46, no. 1, pp. 296–307, 2010.

[101] C. A. Shively, “Treatment of faulted navigation sensor error when assessing risk of unsafe landing for CAT IIIB LAAS,” in *Proceedings of the 19th International Technical Meeting of the Satellite Division of The Institute of Navigation (ION GNSS 2006)*, Fort Worth, TX, September 2006, pp. 477–491.

[102] ——, “Comparison of alternative methods for deriving ground monitor requirements for CAT IIIB LAAS,” in *Proceedings of the 2007 National Technical Meeting of The Institute of Navigation*, San Diego, CA, January 2007, pp. 267–284.

[103] M. Yoon, J. Lee, and S. Pullen, “Integrity risk evaluation of impact of ionospheric anomalies on GAST D GBAS,” *NAVIGATION*, vol. 67, no. 2, pp. 223–234, 2020. [Online]. Available: https://onlinelibrary.wiley.com/doi/abs/10.1002/navi.339

[104] S. Khanafseh, J. Patel, and B. Pervan, “Ephemeris monitor for GBAS using multiple baseline antennas with experimental validation,” in *Proceedings of the 30th International Technical Meeting of the Satellite Division of the Institute of Navigation (ION GNSS+ 2017)*, Portland, OR, September 2017, pp. 4197–4209. [Online]. Available: https://doi.org/10.33012/2017.15380

[105] J. Lee, S. Pullen, S. Datta-Barua, and P. Enge, “Assessment of ionosphere spatial decorrelation for global positioning system-based aircraft landing systems,” *Journal of Aircraft*, vol. 44, no. 5, pp. 1662–1669, 2007. [Online]. Available: https://doi.org/10.2514/1.28199

[106] R. K. Heffley and W. F. Jewell, *Aircraft handling qualities data.* NASA-CR-2144, 1972.

[107] K. Alexander, “Observed nominal atmospheric behavior using honeywell’s GAST D ionosphere gradient monitor,” Navigation Systems Panel (NSP) CAT II/III Subgroup (CSG), Montreal, Canada, Tech. Rep., May 2014.

[108] J. Y. N. Cho, R. E. Newell, B. E. Anderson, J. D. W. Barrick, and K. L. Thornhill, “Characterizations of tropospheric turbulence and stability layers from aircraft observations,” *Journal of Geophysical Research: Atmospheres*, vol. 108, no. D20, 2003. [Online]. Available: https://agupubs.onlinelibrary.wiley.com/doi/abs/10.1029/2002JD002820

[109] S. Jin, L. Han, and J. Cho, “Lower atmospheric anomalies following the 2008 wenchuan earthquake observed by GPS measurements,” *Journal of Atmospheric and Solar-Terrestrial Physics*, vol. 73, no. 7, pp. 810–814, 2011. [Online]. Available: https://www.sciencedirect.com/science/article/pii/S1364682611000332

[110] R. D. Sharman, S. B. Trier, T. P. Lane, and J. D. Doyle, “Sources and dynamics of turbulence in the upper troposphere and lower stratosphere: A review,” *Geophysical Research Letters*, vol. 39, no. 12, 2012. [Online]. Available: https://agupubs.onlinelibrary.wiley.com/doi/abs/10.1029/2012GL051996

[111] A. Mahalov, *3D Dynamics and Turbulence Induced By Mountain and Inertia-Gravity Waves in the Upper Troposphere and Lower Stratosphere (UTLS)*. [Online]. Available: https://arc.aiaa.org/doi/abs/10.2514/6.2011-3930

[112] Y. Ahn, D. Kim, and P. Dare, "Local tropospheric anomaly effects on GPS RTK performance," in *Proceedings of the 19th International Technical Meeting of the Satellite Division of The Institute of Navigation (ION GNSS 2006)*, Fort Worth, TX, September 2006, pp. 1925–1935.

[113] M.-S. Circiu, M. Felux, B. Belabbas, M. Meurer, J. Lee, M. Kim, and S. Pullen, "Evaluation of GPS L5, Galileo E1 and Galileo E5a performance in flight trials for multi frequency multi constellation GBAS," in *Proceedings of the 28th International Technical Meeting of the Satellite Division of The Institute of Navigation (ION GNSS+ 2015)*, Tampa, FL, September 2015, pp. 897–906.

[114] M. Felux, M.-S. Circiu, J. Lee, and F. Holzapfel, "Ionospheric gradient threat mitigation in future dual frequency GBAS," vol. 2017, 2007. [Online]. Available: https://doi.org/10.1155/2017/4326018

[115] S. Khanafseh, "GPS navigation algorithms for autonomous airborne refueling of unmanned air vehicles," PhD dissertation, Illinois Institute of Technology, May 2008.

[116] S. M. Khanafseh and B. Pervan, "Autonomous airborne refueling of unmanned air vehicles using the global positioning system," *Journal of Aircraft*, vol. 44, no. 5, pp. 1670–1682, 2007. [Online]. Available: https://doi.org/10.2514/1.28195

[117] Q. Ai, B. Zhang, Y. Yuan, T. Xu, Y. Chen, and B. Tan, "Evaluation and mitigation of the influence of pseudorange biases on GNSS satellite clock offset estimation," *Measurement*, vol. 193, p. 111015, 2022. [Online]. Available: https://www.sciencedirect.com/science/article/pii/S0263224122002834

[118] N. Wang, Y. Yuan, Z. Li, O. Montenbruck, and B. Tan, "Determination of differential code biases with multi-GNSS observations," *Journal of Geodesy*, vol. 90, no. 3, pp. 209–228, 2016. [Online]. Available: https://doi.org/10.1007/s00190-015-0867-4

[119] T. Reid, "Orbital diversity for global navigation satellite systems," PhD dissertation, Stanford University, June 2017. [Online]. Available: https://web.stanford.edu/group/scpnt/gpslab/pubs/theses/TylerReidThesis2017.pdf

[120] G. W. I. Collins, *Fundamental Numerical Methods and Data Analysis*. [Online]. Available: https://ds.amu.edu.et/xmlui/bitstream/handle/123456789/2935/1006840.pdf?sequence=1&isAllowed=y

[121] L. F. Richardson and R. T. Glazebrook, "Ix. the approximate arithmetical solution by finite differences of physical problems involving differential equations, with an application to the stresses in a masonry dam," *Philosophical Transactions of the Royal Society of London. Series A, Containing Papers of a Mathematical or Physical Character*, vol. 210, no. 459-470, pp. 307–357, 1911. [Online]. Available: https://royalsocietypublishing.org/doi/abs/10.1098/rsta.1911.0009

[122] IGS network map with antenna and receiver details for all sites. [Online]. Available: https://igs.org/network/#station-map-list